ISBN 978-82-326-0702-0 (printed version)
ISBN 978-82-326-0703-7 (electronic version)
ISSN 1503-8181

Doctoral theses at NTNU, 2015:16

Eirik Bøckmann

Wave Propulsion of Ships

NTNU
Norwegian University of
Science and Technology
Faculty of Engineering
Science and Technology
Department of Marine Technology

NTNU – Trondheim
Norwegian University of
Science and Technology

Doctoral theses at NTNU, 2015:16

NTNU

NTNU – Trondheim
Norwegian University of
Science and Technology

Eirik Bøckmann

Wave Propulsion of Ships

Thesis for the degree of Philosophiae Doctor

Trondheim, February 2015

Norwegian University of Science and Technology
Faculty of Engineering Science and Technology
Department of Marine Technology

NTNU – Trondheim
Norwegian University of
Science and Technology

NTNU
Norwegian University of Science and Technology

Thesis for the degree of Philosophiae Doctor

Faculty of Engineering Science and Technology
Department of Marine Technology

ISBN 978-82-326-0702-0 (printed version)
ISBN 978-82-326-0703-7 (electronic version)
ISSN 1503-8181

Doctoral theses at NTNU, 2015:16

Printed by Skipnes Kommunikasjon as

Abstract

Propelling a boat forward by converting wave energy into propulsive thrust was first proposed in 1858 and first successfully done in practice in the 1890s – to the author's knowledge. Several experimenters have since demonstrated the feasibility of wave-powered boats, both in model and full scale. The most common type of wave-powered boat, and also the type studied in this thesis, is a boat with foils that convert the vertical motion in waves into propulsive thrust. In addition to saving fuel, another benefit of these foils, called wavefoils in this thesis, is that they significantly reduce the most violent vessel motions.

Previous theoretical models of wavefoils have neglected the effect of stall, which is reasonable only for small wave height and/or if the ship speed is high. To be able to simulate all wave conditions in real-time or faster, a slightly modified version of the Leishman-Beddoes dynamic stall model for the wavefoil forces was implemented in the time-domain ship simulator VeSim from MARINTEK. This model was compared with experiments and was found to give good estimates of the average foil thrust, although the experimental force histories were not always well reproduced by the model.

The drawback of a spring-loaded wavefoil, which is commonly used to reduce the maximum angle of attack below the stall limit, is that the spring stiffness needs to be tuned for the instantaneous wave condition. In this thesis, two experiments where the foil was pitched automatically by a motor – so-called active pitch control – are presented. A model of a platform supply vessel was outfitted with a wavefoil with pressure sensors on and near the leading edge. The purpose of the pressure sensors was to relate the leading-edge pressure to the angle of attack. The actively pitch-controlled foil resulted in less ship resistance in waves than the fixed foil in some cases but could potentially have performed better with a stiffer pitch actuation mechanism. Another method of pitch control, where freely-rotating vanes near the foil detected the angle of attack, was also tested, with an improved pitch actuation mechanism. This method of pitch control relies on the value of a parameter in the control algorithm to result in reduced ship resistance, and this was also observed in the experiments.

A spring-loaded foil was tested without the ship model and produced higher thrust than the actively pitch-controlled foil with angle of attack vanes. The added mass force is believed to have caused a more beneficial pitch motion for the spring-loaded foil than for the vane-based pitch-controlled foil.

The experiments were compared with simulations in VeSim. Foil thrust and ship motions agreed fairly well in simulations and experiments, but there was less agreement for the ship resistance. At moderate speed, pitching the foil, either actively with a motor or passively with a spring, was shown to only be important for the wave periods producing the most violent ship motions. Simulated fuel savings for the vessel operating in irregular waves, with one wave height and three wave periods commonly found in the North Sea, were well above 30% when sailing at 8 knots for several wave directions but decreased with increasing speed.

A ship entirely powered by renewable energy was proposed and simulated. The ship was propelled by wind and wave energy using wingsails and wavefoils, while

solar panels provided the necessary electricity for onboard use. Sailing between the Azores and Madeira, round-trip, the expected ship speed was 5-6 knots with a standard deviation of approximately 4 knots, for all four seasons.

Experiments were performed with a small radio-controlled ship model, outfitted with a spring-loaded wavefoil underneath the bulb. The influence of the spring-stiffness on the ship speed was small in the experiments, and this was also found in simulations. Although the wavefoil was only beneficial for two of the three wave periods tested in the experiments, and only in head seas, simulations showed that the wavefoil is much more beneficial in full scale.

Acknowledgments

I would like to thank my supervisor, Professor Sverre Steen, for his academic advice and moral support during the work with this thesis. Not only is Sverre an excellent academic advisor, but he is also a fun and inspiring person whom I have thoroughly enjoyed being around for some years now. Thanks also to my co-supervisor, Professor Dag Myrhaug, who has always been very available for questions and has shown keen interest in whatever problems I have presented to him.

Thanks to all my friends and colleagues for giving me advice and suggestions when needed. Dr. Erin Bachynski has without doubt received the most questions from me, and she has done an outstanding job trying to answer them all. Vegard Longva, Dr. Øyvind Ygre Rogne, Morten Dinhoff Pedersen, Mats Thorsen, and Håkon Strandenes have also been very helpful. Dr. Fredrik Dukan and Martin Storheim have contributed with moral support and awesome lunch discussions.

During the fall of 2011 and spring of 2012 I had the pleasure and benefit of working together with master's student Fridtjof Eitzen, for which I am grateful. My thanks also go to Jarle Kramer for many fruitful conversations and for sharing the fun of building a wave-powered model boat during the spring of 2014. Håvard Holm helped us with all the equipment and tips we needed to build that boat.

Dariusz Fathi at MARINTEK has been instrumental for the VeSim simulations, and Torgeir Wahl at NTNU for the experiments. A special thank-you goes to Einar Jakobsen and his daughter, Ingvil Bjørnæs, for providing me with information on Jakobsen's pioneering work.

My deepest gratitude goes to my parents, Gerd and Bernt, and brother Arne with family, for encouraging and motivating me through this chapter in life.

The experiments performed in this doctoral study have been generously funded by the Rolls-Royce University Technology Centre at NTNU and Anders Jahre's Fund for the Promotion of Science.

Trondheim, October 2014
Eirik Bøckmann

Nomenclature

Abbreviations

2D	Two-dimensional
3D	Three-dimensional
AP	Aft perpendicular
BL	Baseline
CDF	Cumulative distribution function
CFD	Computational fluid dynamics
L-B	Leishman-Beddoes
RAO	Response Amplitude Operator

Greek Letters

α	Angle of attack
α_0	Zero-lift angle of attack
α_A	Angle of attack amplitude
α_E	Effective angle of attack
α_f	Equivalent angle of attack, defined in Eq. 3.43
α_v	Angle of attack where leading-edge vortex shedding begins
$\alpha_{A,c}$	Complex angle of attack amplitude
α_{max}	Maximum angle of attack for a pitch-controlled foil, maximum quasi-steady angle of attack in Sections 4.7 and 5.7
α_{opt}	Optimal angle of attack
β	Apparent wind angle

δ	Foil pitch, Dirac delta function in Section 3.2.2, parameter determining wave short-crestedness in Section 6.4
δ_A	Foil pitch amplitude
$\delta_{A,c}$	Complex foil pitch amplitude
δ_{opt}	Optimal foil pitch
δ_{ws}	Wingsail angle
η	Efficiency
η_C	Leading-edge suction recovery factor
γ_b	Bound vorticity
γ_w	Wake vorticity
Λ	Aspect ratio
λ	Wave length, scale factor
ω	Angular wave frequency, angular frequency for an oscillating foil
ω_e	Angular frequency of encounter
$\omega_{e,r}$	Reduced frequency in Section 5.6
Φ	Variable in MARINTEK's expression for the form factor
ϕ	Inflow angle
$\phi(s)$	Wagner function
ϕ_E	Effective inflow angle
ρ	Water density
σ	Dummy time variable of integration, standard deviation
$\sigma_{\overline{C_T}}$	Standard deviation of the mean value of the thrust coefficient
σ_{C_T}	Standard deviation of the thrust coefficient
τ	Leading-edge vortex travel parameter
θ	Primary direction of wave propagation
ζ_A	Wave amplitude

Mathematical Symbols

$\boldsymbol{\eta}$	Vector with ship positions and Euler angles in n-frame
$\boldsymbol{\nu}$	Vector with ship velocities in b-frame

$\boldsymbol{\nu}_r$	Vector with ship velocities in b-frame including ocean currents
$\boldsymbol{\tau}_{FK+d}$	Vector containing Froude-Krylov and diffraction forces
$\boldsymbol{\xi}$	Vector with ship motions in s-frame
$\ddot{z}$	Water acceleration perpendicular to foil
ΔS	Nondimensional time step
Δt	Time step
δu	Wave-induced vessel velocities in x_b-direction
δw	Wave-induced vessel velocities in z_b-direction
$\Im$	Imaginary part
$\mathbf{A}$	Added mass matrix
$\mathbf{B}_{total}$	Damping matrix, including both potential and viscous damping
$\mathbf{C}^*_{RB}$	Coriolis matrix
$\mathbf{e}_1$	Unit vector in x_b-direction
$\mathbf{G}$	Restoring force matrix
$\mathbf{K}(t)$	Matrix of retardation functions
$\mathbf{M}_{RB}$	Rigid body mass matrix
$\mathcal{L}$	Laplace transform
$\mathcal{L}^{-1}$	Inverse Laplace transform
$\overline{C_H}$	Mean horizontal force coefficient
$\overline{F_H}$	Average foil thrust during a cycle
$\Re$	Real part
$\underline{\xi_A}$	Vector containing complex motion amplitudes
$\underline{F_A}$	Vector containing complex amplitudes of the wave excitation forces and moments
$\underline{F_{fA}}$	Foil wave excitation force amplitude vector
$\underline{F_{foil}}$	Vector containing complex amplitudes of the foil forces
$\underline{\underline{A_f}}$	Foil added mass matrix
$\underline{\underline{A}}$	Added mass matrix

$\underline{\underline{B_f}}$ Foil damping mass matrix

$\underline{\underline{B}}$ Damping matrix

$\underline{\underline{C_f}}$ Foil restoring matrix

$\underline{\underline{C}}$ Restoring matrix

$\underline{\underline{M}}$ Mass matrix

Latin Letters

A Wake width in definition of Strouhal number

a Pitch axis location relative to the mid-chord measured in semi-chords in Section 3.2, distance from where N_f attacks to the quarter-chord in Section 5.3

A_1 Constant in Wagner function curve fit, Eq. 3.10

A_2 Constant in Wagner function curve fit, Eq. 3.10

B Breadth of ship hull

b Semi-chord length

b_1 Constant in Wagner function curve fit, Eq. 3.10

b_2 Constant in Wagner function curve fit, Eq. 3.10

c Chord length

$C(k)$ Theodorsen function

C_B Block coefficient

C_C Chordwise force coefficent

C_C^{static} Static chordwise force coefficient

C_D Drag coefficient

C_F Frictional resistance coefficient

C_L Lift coefficient

C_L^C Circulatory part of the lift coefficient

C_N Normal force coefficient

C'_N Normal force coefficient after pressure delay

C_N^C Circulatory normal force coefficient

C_N^f	Normal force coefficient incorporating both pressure and viscous lags
C_N^I	Noncirculatory normal force coefficient
C_N^p	Sum of circulatory and noncirculatory force coefficients
C_N^V	Vortex-induced normal force coefficient
C_P	Power coefficient
C_R	Residual resistance coefficient
C_T	Thrust coefficient, total resistance coefficient of ship
C_V	Increment in vortex-induced normal force coefficient due to a leading-edge vortex
$C_{D,i}$	Induced drag coefficient
$C_{D,v}$	Viscous drag coefficient
C_{D0}	Viscous drag coefficient at zero lift
C_{L_α}	Lift coefficient slope
c_{max}	Maximum chord length
C_{N_α}	Normal force coefficient slope
C_N^{static}	Static normal force coefficient
C_{strip}	Stripwise chordwise foil force
CP_V	Nondimensional center of pressure due to leading-edge vortex
D	Foil drag, deficiency function in Appendix A
d	Distance from spring clamp to foil pivot point
$D(\theta)$	Wave spreading function
D_f	Deficiency function for the degree of attachment
D_p	Attached flow deficiency function
$D_{i,strip}$	Induced drag contribution from a foil strip
D_{strip}	Stripwise foil drag
ds	Foil strip width
$E[U]$	Expected value of ship speed
f	Degree of attachment in Section 3.3, example function in Appendix A
f'	Degree of attachment calculated from α_f

f''	Delayed f' due to boundary layer delay
f''_C	Delayed f'_C due to boundary layer delay
f'_C	Degree of attachment defined in Eq. 3.58
$F(u)$	Cumulative distribution function for vessel speed
F_V	Vertical foil force
f_{lag}	Delayed f in Appendix A
g	Acceleration of gravity
H	Wave height
h	Foil heave motion
h_A	Foil heave amplitude
H_s	Significant wave height
$h_{A,c}$	Complex foil heave amplitude
$H_{s,sw}$	H_s due to swell-dominated sea
$H_{s,w}$	H_s due to wind-dominated sea
I	Moment of inertia, integral in the calculation of deficiency functions
i	Imaginary unit
k	Reduced frequency, wave number in Section 5.6, variable in MARINTEK's expression for the form factor
k_s	Spring constant
L	Foil lift
L_{PP}	Length between perpendiculars
L_{strip}	Stripwise foil lift
L_{WL}	Waterline length
M	Foil pitching moment (about quarter-chord if not otherwise specified)
M_{spring}	Moment about a spring-loaded foil's pivot point produced by the spring
N	Normal foil force, number of repeated tests in Appendix B
N_f	Normal force associated with C_N^f
N_V	Normal force associated with C_N^V
N_{AM}	Noncirculatory normal foil force

N_{strip}	Stripwise normal foil force
o_b	Origin in b-frame
o_n	Origin in n-frame
o_s	Origin in s-frame
P	Average input power to the foil during a cycle in Chapter 4, total engine power in Section 5.5
p_k	Pressure at pressure sensor k
P_M	Power consumed by the electric motor in Chapter 7
P_T	Propeller power
$P_{\overline{C_T}}$	Precision limit for the mean value of the thrust coefficient
P_{C_T}	Precision limit for the thrust coefficient
R	Ship resistance
Re	Reynolds number
S	Leading-edge suction force in Section 3.2.5, projected area of the foil
s	Number of semi-chords traveled at time t
St	Strouhal number with the double heave amplitude as the wake width
St_{TE}	Strouhal number with the trailing edge motion as the wake width
T	Motion period, wave period, foil thrust, ship draft, nondimensional time constant in Appendix A
t	Time, t-value in the Student's t-distribution in Appendix B
t'_C	Parameter defined in Eq. 3.57
t'_N	Parameter defined in Eq. 3.45
T_f	Nondimensional time constant for boundary layer delay
T_p	Nondimensional time constant for pressure delay, peak wave period
T_v	Nondimensional time constant for vortex delay
T_{m02}	Mean zero-crossing period
$T_{p,sw}$	Peak period due to swell-dominated sea
$T_{p,w}$	Peak period due to wind-dominated sea
U	Ship speed or horizontal foil speed

V	Inflow speed to the foil
V_W	Wind speed
w	Vertical wave particle velocity
w_{pc}	Pitch-control parameter
X	Deficiency function, defined in Eq. 3.20
$x_b y_b z_b$	Body-fixed reference frame (b-frame)
x_f	Horizontal foil location relative to coordinate system in Figure 5.26
$x_n y_n z_n$	North-East-Down reference frame (n-frame)
x_p	Distance from leading edge to pivot point of foil
$x_s y_s z_s$	Seakeeping reference frame (s-frame)
x_{cp}	Distance from leading edge to center of pressure of foil
Y	Deficiency function, defined in Eq. 3.21
z_f	Vertical foil location relative to coordinate system in Figure 5.26

Contents

List of Tables

List of Figures

Chapter 1

Introduction

1.1 Motivation

Propelling a boat using wave energy sounds almost too good to be true. Yet, as outlined in Section 1.2.1, wave-powered boats have been around since the 1890s and were proposed as early as in 1858. Knowing this, one might wonder why the concept has yet to be put to use on larger ships.

During the oil crisis in the late 1970s, interest in wind-augmented ship propulsion skyrocketed as a result of the sudden rise in oil price. Two conferences on wind-assisted ship propulsion were arranged in the UK: The Symposium on Wind Propulsion of Commercial Ships held by The Royal Institution of Naval Architects (RINA) in 1980 and the International Symposium on Windship Technology (Windtech '85) in 1985. As the oil price declined through the 1980s, however, interest in wind-augmented ship propulsion faded and remained low through the cheap-oil era of the 1990s.

Although less research was done on wave propulsion of ships, the same trend was seen: interest depended heavily on the oil price. In recent years, oil has been relatively expensive, except for a brief downturn after the financial crisis hit in 2008. Today, the economic motivation for using less fossil fuel for ship propulsion is accompanied by a general concern over the environment, and over global warming in particular. Consequently, there is currently renewed interest in renewable energy for supplementary propulsion of ships.

In 2012, the 31 m long vessel MS *Tûranor PlanetSolar* became the first vessel to circumnavigate the world using only solar power for propulsion. It is also the world's largest solar-powered boat (PlanetSolar, 2013). A ship entirely powered by solar power will need a large area covered with solar panels and a hull with extremely low resistance, as in *Tûranor PlanetSolar*'s case. For a more conventional ship, however, solar energy can only provide a fraction of the necessary power for propulsion, as exemplified by the 160 kW (215 hp) generated by the solar panel-covered deck of the 200 m long car carrier *Emerald Ace* (Mitsui O.S.K. Lines, 2012). Wind and wave energy, on the other hand, can provide a significant part of the required propulsive power (Smulders, 1985; Veritec, 1985, 1986; Angvik, 2009;

Borgen, 2010).

One advantage of wave energy over wind energy for ship propulsion is that it is generally less variable, as waves spread out across the oceans after being generated by distant storms. The simplest and most common type of wave-powered boat uses foils, called wavefoils in this thesis, which convert the relative motion between the foil and the water into propulsive thrust. While this concept has been analyzed by others, see Section 1.2.2, the effect of wavefoil stall has not been properly accounted for. Spring-loaded wavefoils have been employed by earlier experimenters (e.g., Jakobsen (1981) and Terao and Isshiki (1991)). These foils are free to pitch, but their pitch angle is limited by a spring. Active pitch control of the foil has been suggested in order to increase the foil thrust (Naito and Isshiki, 2005; Angvik, 2009; Borgen, 2010; Politis and Politis, 2014; Belibassakis and Politis, 2012, 2013), but the author found only one previous experiment in the literature suggesting a practical way of achieving this (Naito and Isshiki, 2005).

The starting point for the work presented in this thesis was the idea that actively controlled foil pitch could improve the performance of wavefoils. The objective of the thesis was therefore to develop solutions for using actively pitch-controlled foils to significantly reduce the fuel consumption of ships traveling in waves. To reach this objective, it was found necessary to predict the performance of ships with foil systems in an efficient and reliable manner.

The performance of an actively pitch-controlled foil must be compared with the performance of a fixed foil, which may stall. Therefore, implementing a method for simulating dynamic stall with acceptable accuracy was desired. It was also of interest to compare fixed and actively pitch-controlled foils with a spring-loaded foil. The overall motivation behind this was to investigate the fuel saving potential of ships employing wavefoils for auxiliary propulsion, as well as studying the performance of a ship harnessing all of its propulsive power from renewable energy.

1.2 Previous work on partly and fully wave-powered boats

1.2.1 Full-scale vessels and notable model boats

The content of this section, in its current form and in previous versions, has been published at `www.wavepropulsion.com` *– a website written by the author to inform the general public about wave-powered boats.*

Using waves to propel a boat forward is far from a new idea. It is known that whalers throughout history cut off the flukes of the whales they had killed, as it was observed that a dead whale propelled itself forward at a speed of about 1 knot due to the action of the sea (Bose and Lien, 1990). It is not unthinkable that this could have sparked the idea of using the same principle to propel a boat against the waves.

The earliest known document describing a wave-powered boat is a US patent by Daniel Vrooman (Vrooman, 1858) of Hudson, Ohio, from 1858. In his patent, see Figure 1.1 he describes "[...] a new and useful improvement in ships and other vessels for enabling their up and down motion from the rolling of the sea and other causes and the corresponding movement of the water to aid in propelling them on their course [...]". Vrooman explains how this can be achieved by attaching elastic fins or wings to the ship. It appears, however, that Vrooman did not build his wave-powered boat, as his patent reads: "To enable others skilled in the art to make and use my invention, I will proceed to describe its construction and operation." It is not known whether or not anyone actually built Vrooman's boat.

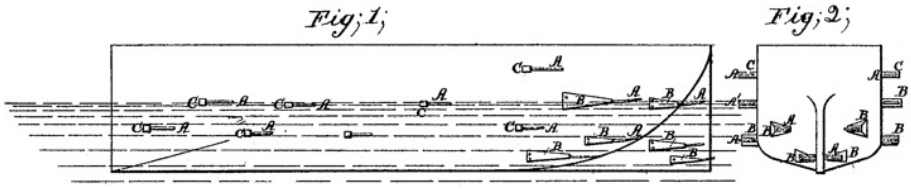

Figure 1.1: Drawings from Vrooman's patent specification (Vrooman, 1858). Side view of the hull to the left, stern view of the hull to the right.

Hermann Linden of the Zoological Station in Naples, Italy, filed a British patent (Linden, 1895) for a wave-powered boat in 1895, see Figure 1.2. Linden built a 13 ft long boat named *Autonaut* (Burnett, 1979), see Figure 1.3, which moved against the waves at three to four miles per hour, powered purely by the energy of the waves. The boat obtained its thrust from two underwater steel plates – one at the bow and one at the stern. The plates were fixed at one end and feathered like fish fins as the boat moved up and down due to the waves. Linden proceeded to build a 24 ft long boat being able to tow two 10 ft boats, each containing two passengers, at nearly four miles per hour.

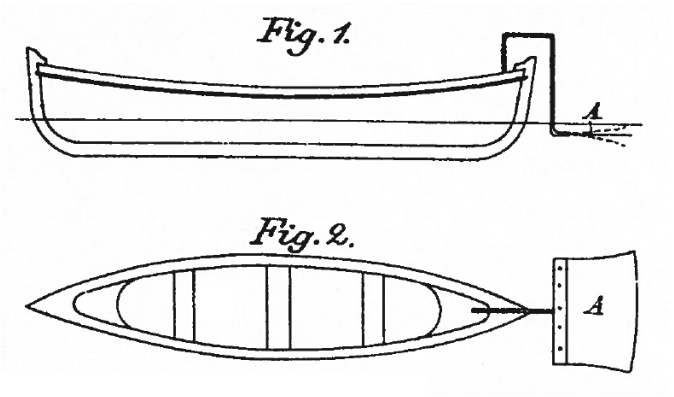

Figure 1.2: Drawings from Linden's patent specification (Linden, 1895)

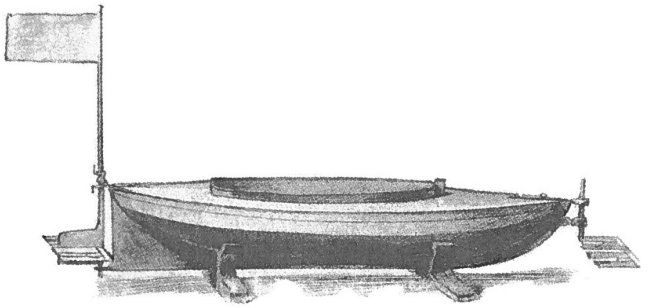

Figure 1.3: Drawing of the *Autonaut* from Pearson's Magazine, December 1898 (Burnett, 1979)

Wave propulsion methods other than using fins directly were also conceived more than 100 years ago. Otto Schulze of Brooklyn, New York, thought of using the wave-induced vertical motion of buoys along the hull of the boat to drive an ordinary propeller at the stern (Schulze, 1911), see Figure 1.4. Schulze also considered using the wave energy to generate electricity for later use, either for driving the propeller, or for other purposes. Again, it is not known whether or not the boat was built.

Although it received praise in the contemporary newspapers from New York (The New York Times, 1898) to New Zealand (Ashburton Guardian, 1897), Linden's boat must have been forgotten by the scientific community. In 1935, Popular Science claims that "it remained for a Long Beach, Calif., inventor to design a wave-operated mechanism to propel a boat" (Popular Science, 1935), see Figure 1.5. The inventor's name is not mentioned, though. Two fins in the bow and one fin in the stern attached to flexible joints provided the propulsion. The 18-inch model built by the inventor, see Figure 1.6, could reportedly attain a pace of five

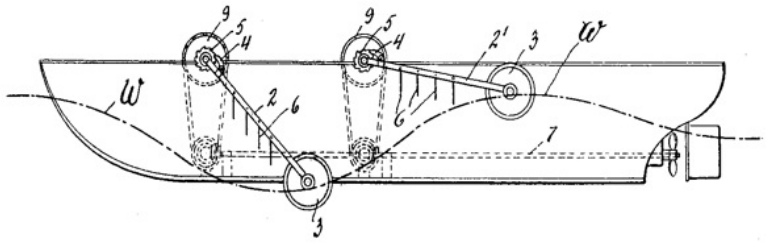

Figure 1.4: Drawing from Schulze's patent specification (Schulze, 1911)

miles per hour, which seems unrealistically fast compared to other experiments described in this section.

Figure 1.5: The unnamed inventor of Long Beach with his wave-powered model boat in 1935 (Popular Science, 1935)

In the latter half of the 20th century, more stories about people that had built wave-powered boats appeared. These people include John S. McCubbin of Victoria, Australia (Popular Science, 1950), see Figure 1.7, and Joseph A. Gause of Burlington, Ontario, Canada (Mechanix Illustrated, 1972). Gause filed his first patent for a wave-powered boat in 1966 (Gause, 1966). Gause's 34 ft boat, *Gausefin I*, see Figure 1.8, attained a top speed of 5 mph on Lake Ontario, using wave energy only, witnessed by five Canadian Government officials who were cruising alongside. *Gausefin I* had three pairs of fixed fins rigidly attached to the hull. The fins were thickest at the root and gradually tapered outward toward a thin trailing edge allowing for the fins to flex when hit by a wave. According to the Mechanix Ilustrated

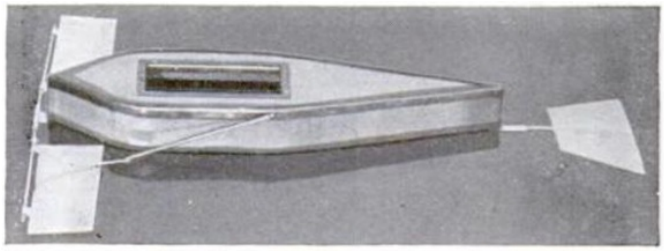

Close-up of model, showing fins that gather energy from waves

Figure 1.6: Close-up view of the wave-powered model boat of 1935 (Popular Science, 1935)

article (Mechanix Illustrated, 1972), "[...] the size, angle, thickness and flexibility of the fins were arrived at through guesstimating." Gause, a sculptor and painter, certainly knew the historical background of wave-powered boats, as he cites both Vrooman and the Popular Science article of 1950 in one of his four patents (Gause, 1967).

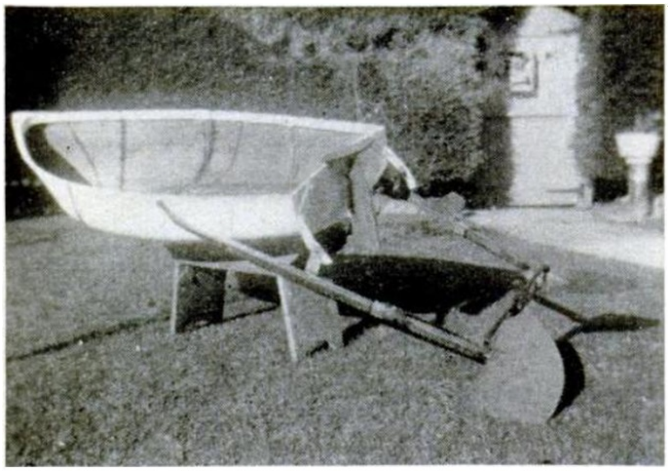

Figure 1.7: John S. McCubbin's boat of 1950 (Popular Science, 1950)

Einar Jakobsen started his experiments on wave-powered boats in Norway in 1978. In 1981, he presented results (Jakobsen, 1981) from experiments performed at the Norwegian Hydrodynamics Laboratories (today MARINTEK) in Trondheim, Norway. Jakobsen's model boat of length 1.025 m moved at a speed of 0.824 m/s in regular head sea waves with height 0.05 m and period 1.2 s, according to the report on the experiments (Kjærland, 1980), but figures in the same report indicate that the speed in this condition was in fact about 0.55 m/s. The model had a spring-loaded foil on an extension out from the bow, and another spring-loaded foil on an extension aft of the stern. Einar Jakobsen termed the device a "foilpropeller".

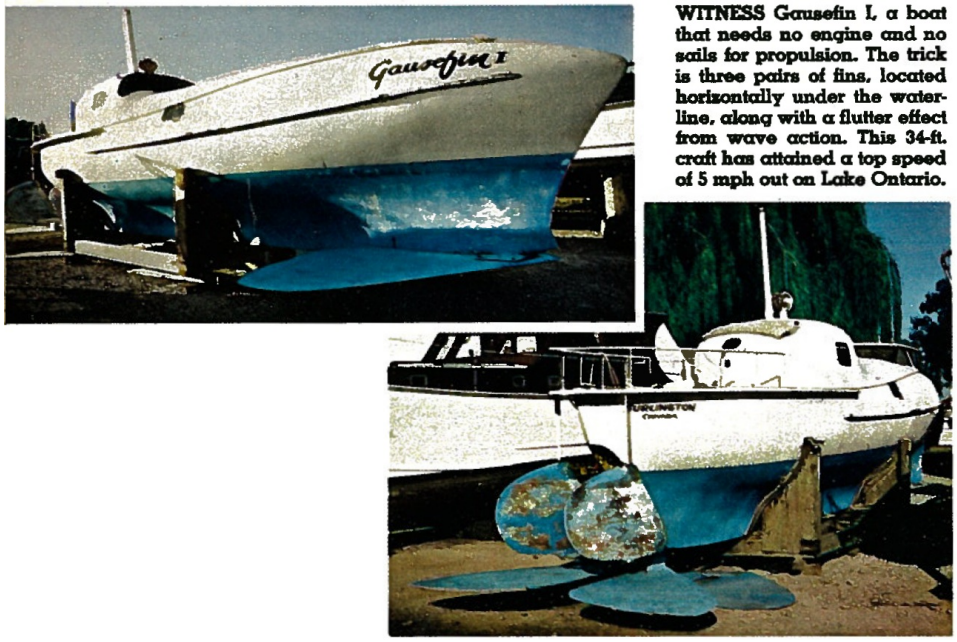

Figure 1.8: The *Gausefin I* (Mechanix Illustrated, 1972)

Jakobsen and his Wave Control Company used combinations of two and four foils, each measuring 0.5 m^2 on a 7.5 m long sailboat hull (Anon., 1983), see Figure 1.9. A maximum speed of six knots was recorded on one occasion. The Norwegian government sponsored NOK 450,000 to fit the fishing research vessel *Kystfangst* (20 m long and 180 tonnes), owned by the Institute of Fishery Technology Research, with a bulbous bow and two foils with a total area of 3 m^2 (Anon., 1983; Berg, 1985), see Figure 1.10. In a seastate of about 3 m significant wave height, the foils produced a propulsive force corresponding to 16-22% of the vessel's estimated resistance (Berg, 1985), or 8-16% when accounting for the strut resistance. The vessel speed was 4-8 knots. Reduced pitching motion of the vessel in head seas and reduced rolling motion in following seas were observed.

The wave periods of 7-7.5 seconds that *Kystfangst* was tested in give wavelengths of about 80 m, or 4 times the length of *Kystfangst*. Model tests (Kjærland, 1979; Nagata et al., 2010) have shown that the largest speeds of wave-powered ships occur when the wave length is about 1.1-1.2 times the ship length in beam and following seas, and 1.5-2.2 times the ship length in head seas. Lai et al. (1993) studied a model of a racing yacht equipped with a flexible-armed rigid foil for wave propulsion in head seas and also found that maximum foil thrust was obtained in waves 1.5 to 2.0 times longer than the vessel. In other words, *Kystfangst* would have benefited more from the foils had she been longer.

Simultaneously with Jakobsen's work, Hiroshi Isshiki of the Technical Research Institute, Hitachi Shipbuilding & Engineering Co., Ltd. in Osaka, Japan began

Figure 1.9: The bow of the 7.5 m hull used in tests on Wave Control Company's "foilpropeller" (Anon., 1983)

Figure 1.10: *Kystfangst* (Dybdahl, 1988)

a thorough theoretical and experimental study of wave-powered boats (Isshiki, 1982a,b; Isshiki and Murakami, 1983, 1984). Isshiki used the term "wave devouring propulsion", allegedly proposed by Prof. T. Y. Wu of the California Institute of Technology in 1980. Yutaka Terao of Tokai University in Japan was also working on

"wave devouring propulsion" at the time (Terao, 1982). In 1991, Isshiki and Terao presented results from full scale tests on a 15.7 m long fishing vessel (Terao and Isshiki, 1991), see Figure 1.11. The projected hydrofoil area was 7.4% of the ship's waterline area. Using the bow foil resulted in reduced pitching motion, reduced bow slamming, and increased speed in waves.

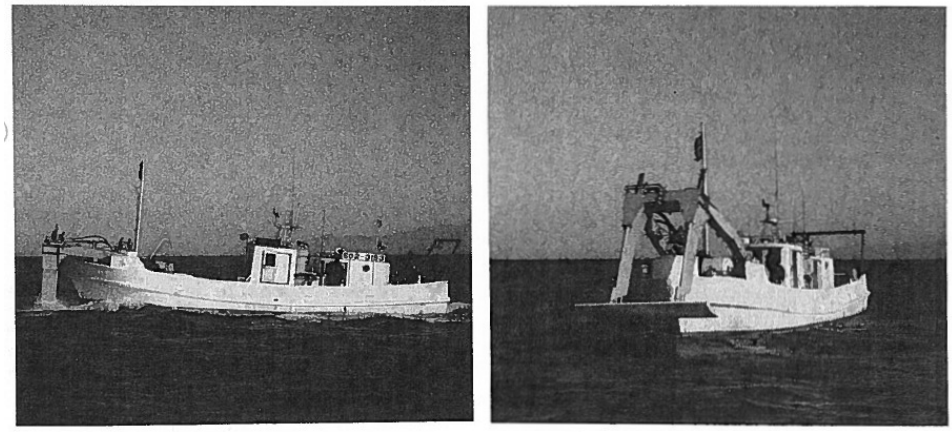

Figure 1.11: The 20-ton fishing vessel equipped with a bow foil tested in 1988/89 (Terao and Isshiki, 1991)

In 2008, Japanese sailor and environmentalist Kenichi Horie sailed the wave-powered catamaran *Suntory Mermaid II* from Honolulu, Hawaii, to the Kii Channel, Japan (Geoghegan, 2008b), see Figure 1.12. The boat's propulsion system, see Figure 1.13 was designed by Yutaka Terao. The journey took 110 days, which was longer than planned, due to unusually good weather and calm seas. The journey is to date the longest known voyage by a manned wave-powered boat. The *Suntory Mermaid II* was widely, yet wrongly, described on the Internet as "the world's first wave-powered boat".

Nagata et al. (2010) performed model tests of a 2 m long model of an 80 m long container ship. The ship was equipped with a wavefoil in the bow, of span 2.34 times the ship beam. In head sea waves of wavelength 3.12 times the ship length (between perpendiculars, L_{PP}), and height 0.10 m, the ship cruised at about 0.7 m/s, powered only by the waves. Almost the same speed was achieved in following seas with the same wave height, but with a wave length of $0.96L_{PP}$. Froude-scaled to full scale, this is equivalent to an 80 m ship sailing at 8.6 knots in waves of 4 m height.

1.2.2 Theoretical studies of wave propulsion

Wu (1972) and Wu and Chwang (1975) studied the thrust generation of an oscillating hydrofoil advancing in waves, but neglected the effect of the free surface and the solid bottom. As Wu (1972) notes, this is a reasonable simplification when the hydrofoil is farther than two chord lengths away from each of these boundaries.

Figure 1.12: Kenichi Horie on board the *Suntory Mermaid II*, which sailed from Hawaii to Japan in 2008. Photo: Reuters/Shigeo Yamada/Handout (Fabre, 2008).

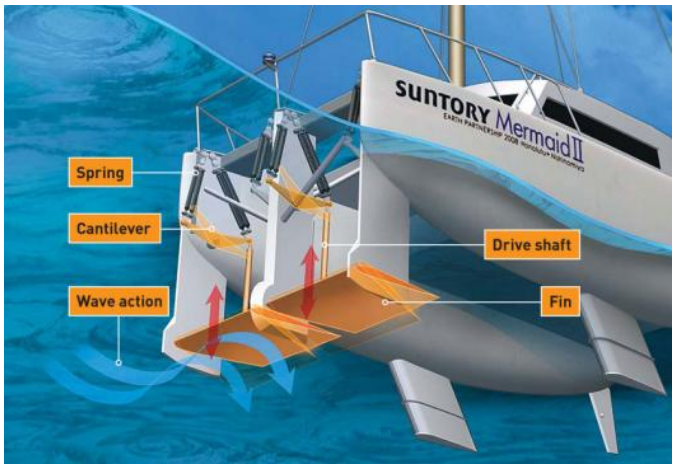

Figure 1.13: Propulsion mechanism of the *Suntory Mermaid II*. Illustration: Kevin Hand (Geoghegan, 2008a).

In four reports, Isshiki (1982a,b) and Isshiki and Murakami (1983, 1984) theoretically and experimentally explored thrust generation of a hydrofoil advancing in waves. In his first report, Isshiki (1982a) improved Wu's theory by including an approximation of the free-surface effect and studied the thrust from a non-oscillating hydrofoil advancing in waves. In his second report, Isshiki (1982b) explored opti-

mized foil motions in heave and pitch given that the power required to heave and pitch the foil was zero. In the third and fourth reports (Isshiki and Murakami, 1983, 1984), thrust generation through absorption of wave energy by an advancing hydrofoil, heaving and pitching passively through a set of springs, was verified experimentally and compared with theory. The effects of foil draft, heave and pitch springs, and an auxiliary float were studied theoretically in the fourth report (Isshiki and Murakami, 1984). When the foil was attached to the float in a suitable position, larger thrust was obtained than without the float. More experimental results are given in Isshiki et al. (1984).

Veritec, a former subsidiary of Det Norske Veritas (today DNV GL Group), analyzed the propulsive effect of wavefoils near the bow of vessels 20 m, 40 m, and 70 m long (Veritec, 1985, 1986) operating in the North Sea. Foil areas of 2%, 4%, and 6% of the vessel water plane area were studied. The fuel saving percentage increased with increasing foil area for all three ships. For the 70 m vessel with a foil of 6% of the vessel water plane area, the fuel saving was 43% at 10.6 knots and 10% at 15.9 knots. The vessel motions were calculated using a strip theory program, but the heave and pitch damping due to the foils was not accounted for. Foil drag and dynamic effects on the foil lift were not accounted for.

Grue et al. (1988) examined the propulsion of a foil moving through water close to a free surface in 2D. They applied a vortex distribution along the centerline of the foil and the wake and solved for the local vortex strength. All equations were linearized. The ability of the foil to propel a ship in waves was studied, and they found that a 40 m long ship in 1 m high regular waves would travel at a speed of 8 knots. They assumed that the foil moved downward when the wave field velocity was upward, and that the heave motion of the ship was of the same order of magnitude as the amplitude of the incoming waves. Finally, the theory was compared with experiments from Isshiki et al. (1984), with mixed degrees of success.

If ships can potentially save large amounts of fuel in waves, whales and dolphins should be able to minimize their energy consumption in waves too. This was studied by Bose and Lien (1990) who showed that in seas corresponding to a windspeed of 20 knots, a 14.5 long fin whale could save about 25% propulsive power in head seas and 33% in following seas, when swimming at a depth of 2.0 m and a forward speed of 2.5 m/s. The power savings dropped with increasing submergence depth.

An actively controlled pitching bow-mounted foil, or bow wing, for auxiliary ship propulsion in waves was studied by Naito and Isshiki (2005). They performed experiments where a ship model was equipped with bow wings that rotated harmonically in pitch, with varying phase relative to the incoming regular head sea waves. Furthermore, they measured the pressure on the bottom surface of the wings, and plotted the amplitude of the bottom pressure against the amplitude of the angle of attack of the bow wings. The result was a nearly linear graph for angles of attack below 20 degrees. Finally, they proposed and simulated a control system, which receives the pressure on the bottom surface of the bow wings as input and returns the optimal bow wing angle as output. Their approach assumes that the horizontal foil force is neglected when calculating the ship motions and that the vertical foil force oscillates with the encounter frequency, so that a

frequency-domain approach can be used. The frequency-domain solution for the optimal foil angle is then Fourier transformed into a time-domain solution in order to study the response in irregular waves.

In two master's theses from the Norwegian University of Science and Technology (Angvik, 2009; Borgen, 2010), the MARINTEK program ShipX Vessel Responses (VERES) was used to calculate heave and pitch response amplitude operators (RAOs) for ships with a fixed foil on each side of the bow. Based on the ship motions, the thrust of actively pitch-controlled foils was calculated, accounting for foil drag and finite span effects on the lift and drag but not dynamic effects. The added resistance in waves was accounted for. Angvik (2009) studied only an offshore supply vessel, whereas Borgen (2010) studied an offshore supply vessel, a coastal tanker, and a purse seiner. The reported fuel savings were very promising.

Politis and Politis (2014) and Belibassakis and Politis (2012, 2013) also studied an actively controlled pitching foil. They used a boundary element method to accurately model the forces on an oscillating foil, assuming attached flow. Furthermore, they set the foil pitch to be linearly proportional to the inflow angle. The drawbacks of this pitch control strategy is discussed in Section 4.6.2. Politis and Politis (2014) showed that the power necessary for active pitch control is only a small percentage of the propulsive power from the actively controlled foil.

Numerical methods have also been applied to study wave energy extraction for marine propulsion. De Silva and Yamaguchi (2012) used the commercially available code FLUENT to study a two-dimensional hydrofoil oscillating harmonically in heave and pitch under the influence of free surface waves. Simulation results were found to be in good agreement with experimental results in Isshiki and Murakami (1984). It was also shown numerically that the thrust and efficiency were highest when the foil oscillation frequency was the same as the wave encounter frequency. When the wave amplitude to foil chord length ratio was less than 1/7, more than 70% of the wave energy could be recovered as useful propulsion energy. The wave energy recovery percentage decreased with increasing wave amplitude, though.

Filippas and Belibassakis (2013, 2014a,b) used a boundary element method and focused on the free-surface effects, by studying a two-dimensional hydrofoil undergoing heaving and pitching oscillations underneath the free surface, with constant forward speed. There was good agreement with results in De Silva and Yamaguchi (2012).

The literature on oscillating foils in general – i.e., not limited to the purpose of wave propulsion of ships – is extensive. A short literature review of unsteady foil theory is given in Section 3.1, and further references to previous work on oscillating foils are given in Chapter 4.

Except for the two studies by Veritec (1985, 1986), and the Master's theses of Angvik (2009), and Borgen (2010), few of the previous theoretical studies of wave propulsion have calculated fuel savings for a given ship in realistic ocean wave conditions. In the present work, practical solutions and actual fuel savings have been in focus.

1.3 Outline of the thesis

Chapter 2 begins with a discussion of frequency-domain vs. time domain analyses and describes the assumptions that must be made to simulate a ship with foils in the frequency domain. Then, a short summary of the seakeeping and maneuvering theory implemented in the ship simulator used in the present work, VeSim, is given. For a detailed exposition of this theory, the reader is advised to consult Fossen (2011).

In Chapter 3, the most important findings of classical unsteady thin-airfoil theory are explained. Then, a slightly modified Leishman-Beddoes dynamic stall model, building on classical unsteady thin-airfoil theory, is presented, along with a correction for finite-span effects.

Chapter 4 describes experiments done with an oscillating foil. This foil was built to be put on a 1:16 scale model of a 90 m long platform supply vessel. It was tested without the ship to validate the dynamic stall model in Chapter 3 and to study the effect of actively controlled and spring-loaded foil pitch on the foil thrust.

Chapter 5 studies the effect of the wavefoil tested in Chapter 4 on the aforementioned platform supply vessel. Two methods of pitch control are studied: one using pressure sensors on and near the leading edge of the foil, and another using angle of attack vanes. The dynamic stall model presented in Chapter 3 was implemented in VeSim to calculate the foil forces. VeSim simulations are compared with experiments for a fixed foil, and the effects of pitch-controlled and spring-loaded foils on the ship are studied numerically. A simplified frequency-domain analysis of a ship with wavefoils in head seas is presented, and the foil thrust from the simplified analysis is compared with the foil thrust from VeSim simulations.

Chapter 6 is devoted to a ship powered purely by renewable energy, exploiting the wind energy with wingsails and the wave energy with wavefoils. Wingsails were implemented in VeSim using the same dynamic stall model as for the wavefoils. The expected speeds of this ship on a given route throughout the year are calculated, along with the corresponding standard deviations.

The experiments presented in Chapter 5 were only done in head seas, and more experiments were needed to validate the numerical results in following seas. Hence, in Chapter 7, experiments with a small radio-controlled ship model employing a spring-loaded bow foil are presented. This model was run in both head and following seas, and the effects of wave period, ship speed, spring stiffness, and regular vs. irregular waves are studied. The experimental results are compared with VeSim simulations and results for the ship in full scale are also presented.

Finally, Chapter 8 summarizes the key findings of the thesis and provides suggestions for future work.

1.4 Main contributions

The main contributions of the present work are:

1. Experiments with an oscillating foil were performed, showing that the phase angle between heave and pitch is crucial for the thrust generation at low for-

ward speed, and that a beneficial phase angle is accomplished with a spring-loaded foil. The experiments also showed that a spring-loaded foil with well-tuned spring stiffness is preferable over a fixed foil and over a pitch-controlled foil where the pitch control is based on vanes for detecting the angle of attack.

2. Experiments with a ship model with a fixed and an actively pitch-controlled wavefoil, using two different pitch-control methods, were performed. The experiments showed that both pitch control using pressure sensors and pitch control using angle of attack vanes can result in lower ship resistance than with a fixed foil.

3. A dynamic stall model for wavefoil and wingsail forces was implemented in the time-domain ship simulator VeSim. This allows for fast and relatively accurate calculations of wavefoil and wingsail forces in a wide range of operating conditions.

4. A ship with fixed, actively pitch-controlled, and spring-loaded wavefoils was simulated in VeSim, and the results for a fixed foil were compared with experiments. These simulations showed that at moderate ship speeds pitching the foil is only necessary for a narrow range of wave periods where the most violent ship motions are found.

5. A ship powered purely by renewable energy was simulated, and a novel method to calculate the wind speed based on wave statistics was presented. The ship was found to have quite low expected ship speeds, with fairly large standard deviations, on a given route throughout the year.

6. Experiments with a free-running ship model with wavefoils for auxiliary propulsion in regular and irregular waves were performed, showing generally positive fuel savings in head seas, but negative fuel savings in following seas. Scaling of these results was discussed, and the wavefoil was found to be significantly more beneficial in full scale.

1.5 Publications

The following publications are directly connected with the work presented in this thesis:

- Bøckmann, E. and Steen, S. (2013). The effect of a fixed foil on ship propulsion and motions. In Third International Symposium on Marine Propulsors, pages 553-561.

- Bøckmann, E., Steen, S., and Myrhaug, D. (2014). Performance of a ship powered purely by renewable energy. In ASME 2014 33rd International Conference on Ocean, Offshore and Arctic Engineering, Volume 8A: Ocean Engineering.

- Bøckmann, E. and Steen, S. (2014). Experiments with actively pitch-controlled and spring-loaded oscillating foils. Applied Ocean Research, 48:227–235.

Bøckmann and Steen (2013) originates from Section 5.1, Bøckmann et al. (2014) is an earlier version of Chapter 6, and Bøckmann and Steen (2014) includes most of Chapter 4 in this thesis.

The observant reader may notice some differences between the content in these papers and this thesis. The wave heights and periods used in Bøckmann and Steen (2013) were based on measurements with a wave probe on the moving carriage. These measurements were, however, quite different from the measurements of wave height and period from the carriage when stationary. In this thesis, the wave measurements from the stationary carriage are used, as they are believed to be more accurate than the measurements from the moving carriage.

The draft of the ship in Chapter 6 is larger than the draft of the ship in Bøckmann et al. (2014). The draft was changed to be able to use ship resistance data from experiments with the hull studied.

Most importantly, a bug in VeSim was fixed in February 2014 after Bøckmann et al. (2014) was submitted. This bug impacted the ship motions with forward speed, particularly in heave. Hence, the results in both Bøckmann and Steen (2013) and Bøckmann et al. (2014) are affected by this bug. The results in this thesis were generated after the bug fix, however, and are therefore more thrustworthy. Comparing the heave RAO for the simulated ship without foil in Bøckmann and Steen (2013) with the corresponding heave RAO in Chapter 5, we see that the heave RAO in Chapter 5 approaches 1 for long waves, as it should, whereas the heave RAO in Bøckmann and Steen (2013) does not. Comparing the ship speed plots in Bøckmann et al. (2014) with the ship speed plots in Chapter 6, we see that there are large differences and that the plots in Chapter 6 looks more reasonable.

Chapter 2

Seakeeping theory

2.1 Frequency-domain vs. time-domain analyses

Seakeeping, in hydrodynamic terminology, is the study of a floating object's response in waves. This can be done in two ways:

1. Studying the object's motions as a function of wave frequency (frequency-domain analysis)

2. Studying the object's motions as a function of time (time-domain analysis)

In a frequency-domain analysis, the ship motion amplitudes and phases are found for a certain encounter frequency, by solving a system of linear equations. This approach assumes that all forces oscillate with the same frequency and are directly proportional, with a possible phase difference, to the wave elevation. By solving the system of equations for all encounter frequencies, the ship motion amplitudes and phases are found in the frequency domain. In an irregular sea consisting of superimposed regular waves, the ship motions can be found by superimposing the responses to the regular waves. In up to moderately high waves and speeds, frequency-domain analyses of a bare hull, i.e., a hull without appendices such as foils, have proven to quite accurately predict the ship motions (McTaggart, 2010).

In a time-domain analysis, a system of differential equations must be formulated and solved numerically, in order to determine the ship motions. Frequency-domain coefficients are often required as input in the system of differential equations, so the frequency-domain problem has to be solved before the time-domain solution can be found. The advantage with this approach is that ship motions can be found even if the ship is subjected to forces varying arbitrarily with time.

At an early stage of the work with this thesis, the author looked into different approaches for simulating the motions of a ship with foils in waves. First, including the foil forces in the equations of motions and solving the linear equations of motions in the frequency domain was considered. Since all forces are assumed to oscillate with the same frequency and be directly proportional to the wave elevation, one must therefore make the following assumptions:

- The foil lift is directly proportional to the angle of attack.
- The angle of attack is directly proportional to the wave elevation.
- The foil lift points along an axis which is vertical relative to the mean position of the ship.
- The foil drag is neglected because it oscillates with twice the frequency of the foil lift.

These assumptions imply that simulating a ship with foils undergoing stall is impossible, as is simulating a ship with foils that non-harmonically adjust their angle of attack to avoid stall. One of the main intentions of the present work, see Section 1.1, was to study both of these features, so time-domain analyses were necessary. Consequently, a model for the foil forces was implemented in the MARINTEK Vessel Simulator (VeSim), which is a time-domain simulation tool. VeSim has been under continuous development since 2004. It is structured so that different subsystems of the vessel, called "federates", connect to the simulation, and share parameters at every time step with the other "federates". In this way, the vessel motion and the foil force, for instance, depend mutually on each other.

2.2 Summary of the unified seakeeping and maneuvering theory implemented in VeSim

In this section, a nonlinear unified seakeeping and maneuvering theory (Fossen, 2005), which VeSim is based on, is summarized. Although not resulting from the work behind this thesis, the theory is briefly presented in order for the reader to understand the fundamentals of how VeSim works.

2.2.1 Reference frames

Before we study how the six degrees of freedom motions of a ship can be calculated, let us first look at the coordinate systems, or reference frames, involved. The following definitions are taken from Fossen (2011).

The *North-East-Down* reference frame $x_n y_n z_n$ with origin o_n is defined relative to the Earth's reference ellipsoid (NIMA, 1997), and is considered inertial. The $x_n y_n$-plane is usually defined as the tangent plane on the surface of the Earth moving with the craft. The x-axis points true *north*, the y-axis points toward *east*, and the z-axis points *downward* normal to the surface of the Earth. The n-frame positions and Euler angles are given by the vector $\boldsymbol{\eta}$.

The *body-fixed* reference frame $x_b y_b z_b$ with origin o_b is a moving reference frame that is fixed to the vessel, and is considered non-inertial. The x_b-axis is positive toward the bow, the y_b-axis is positive toward starboard, and the z_b-axis is positive downward, see Figure 2.1. The origin o_b is located midships at the waterline, with the z_b-axis passing through the center of gravity of the vessel. The b-frame linear velocities and angular velocities are given by the vector $\boldsymbol{\nu}$.

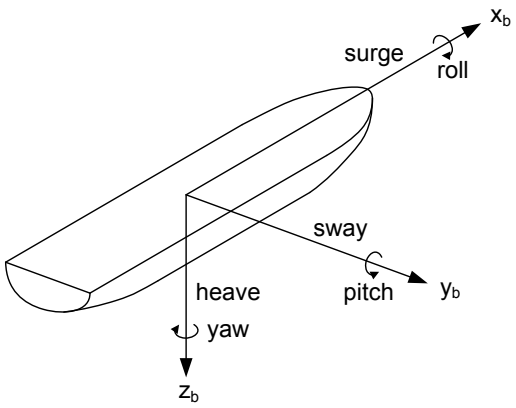

Figure 2.1: Body-fixed reference frame in VeSim

The *seakeeping* reference frame $x_s y_s z_s$ is a reference frame which is fixed to the equilibrium state of the vessel, and is considered inertial. This means that it is non-accelerating, is fixed in orientation with respect to the n-frame, and moves along the path of the vessel with the mean forward speed, U, of the vessel. Consequently, the orientation and U cannot vary, or they must vary very slowly. The x_s-axis is positive forward, the y_s-axis is positive toward starboard, and the z_s-axis is positive downward. In absence of wave excitation, the s-frame origin, o_s, coincides with the b-frame origin, o_b. The s-frame perturbation vector is $\boldsymbol{\xi}$. Like $\boldsymbol{\eta}$ and $\boldsymbol{\nu}$, $\boldsymbol{\xi}$ have six components, and they are perturbations in surge, sway, heave, roll, pitch, and yaw, respectively.

Positions, velocities, and accelerations can be transformed from one reference frame to another using rotation matrices. In Fossen (2005), the rotation matrix used in the transformation from the b-frame to the s-frame assumes that the angles of the b-frame with respect to the s-frame are small. This assumption is not made in VeSim, however, as it is not applicable for small boats in large waves.

2.2.2 Equations of motion

The time-domain seakeeping equations of motion in the s-frame for a vessel with no forward speed can be written, thanks to the works of Cummins (1962) and Ogilvie (1964), as (Fossen, 2011)

$$[\mathbf{M}_{RB} + \mathbf{A}(\infty)]\,\ddot{\boldsymbol{\xi}} + \mathbf{B}_{total}(\infty)\dot{\boldsymbol{\xi}} + \int_0^t \mathbf{K}(t-\tau)\dot{\boldsymbol{\xi}}(\tau)d\tau + \mathbf{G}\boldsymbol{\xi} = \boldsymbol{\tau}_{FK+d}, \qquad (2.1)$$

where the matrix of retardation functions, $\mathbf{K}(t)$, is given as

$$\mathbf{K}(t) = \frac{2}{\pi}\int_0^\infty [\mathbf{B}_{total}(\omega) - \mathbf{B}_{total}(\infty)]\cos(\omega t)d\omega. \qquad (2.2)$$

$\mathbf{M}_{RB}$ is the rigid body mass matrix, $\mathbf{A}(\infty)$ is the added mass matrix for infinite frequency, $\mathbf{B}_{total}$ is a damping matrix including both potential and viscous damping,

$\mathbf{G}$ is the restoring force matrix, and $\boldsymbol{\tau}_{FK+d}$ is a vector containing Froude-Krylov and diffraction forces. A dot over the symbol denotes time differentiation, and two dots imply that time differentiation is done twice.

VeSim needs all external forces to be given in the b-frame. Therefore, the equations of motion, Eq. 2.1, should be transformed from the s-frame to the b-frame. When transforming the equations of motion to the rotating b-frame, Coriolis forces between the s-frame and the b-frame appear when the ship has forward speed. The reason for this is that the velocities and accelerations in the s-frame can be expressed using velocities and accelerations in the b-frame, in Eq. 2.1. This is illustrated in Figure 2.2, where δu and δw are the wave-induced vessel velocities in x_b- and z_b-direction, respectively. If ξ_5 is small and $o_b = o_s$ (assumed in this example, for simplicity),

$$\xi_3 \approx \delta w - U\xi_5, \tag{2.3}$$

where we have assumed that $U \gg \delta u$.

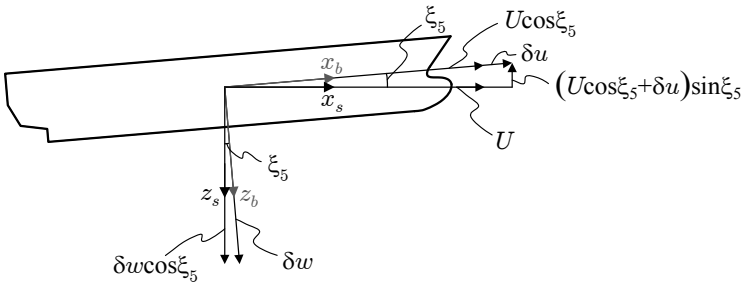

Figure 2.2: Body-fixed vs. seakeeping reference frames

The equations of motion in the b-frame then become (Fossen, 2011)

$$\begin{aligned}&[\mathbf{M}_{RB} + \mathbf{A}_U(\infty, U)]\,\dot{\boldsymbol{\nu}} + \mathbf{C}^*_{RB}\boldsymbol{\nu} + \mathbf{B}_{tot,U}(\infty, U)\boldsymbol{\nu}_r \\ &+ \int_0^t \mathbf{K}_U(t-\tau, U)[\boldsymbol{\nu}(\tau) - U\mathbf{e}_1]d\tau + \mathbf{G}\boldsymbol{\eta} = \boldsymbol{\tau}_{FK+d},\end{aligned} \tag{2.4}$$

where $\mathbf{C}^*_{RB}\boldsymbol{\nu}$ are Coriolis forces and moments due to the rotation of the b-frame about the s-frame, as derived in a linearized version in Fossen (2005), and $\mathbf{e}_1$ is the unit vector in x_b-direction. Subscript U denotes speed-dependence. $\boldsymbol{\nu}_r$ includes ocean currents. Other forces that are not necessarily harmonically varying can be added to the right side of Eq. 2.4, when solving Eq. 2.4 in the time domain. The speed-dependent added mass and damping coefficients are calculated using the strip theory by Salvesen et al. (1970) and transformed to the b-frame. This transformation removes speed-dependent terms with the encounter frequency, ω_e, in the denominator, which is undefined when $\omega_e = 0$. The retardation function is now calculated using the speed-dependent damping matrices, as

$$\mathbf{K}_U(t, U) = \frac{2}{\pi}\int_0^\infty [\mathbf{B}_{total,U}(\omega, U) - \mathbf{B}_{total,U}(\infty, U)]\cos(\omega t)d\omega. \tag{2.5}$$

VeSim first solves Eq. 2.4 for the vessel accelerations in the b-frame. Then, the accelerations are integrated to obtain the vessel velocities in the b-frame. The vessel velocities are then transformed into the n-frame and integrated once again to obtain the vessel positions in the n-frame (Fathi, 2013).

Chapter 3

Unsteady foil theory

3.1 Background

Fuelled by the need to understand the problem of wing flutter, the foundation of unsteady foil theory was laid in the 1920s and 1930s by pioneers such as Wagner (1925), Theodorsen (1935), Küssner (1935), Garrick (1936), and von Kármán and Sears (1938). They all assumed incompressible and inviscid flow, that the effect of airfoil thickness is negligible, and that the shed vortices in the wake remain on a straight line behind the foil, thereby assuming small transverse motions. Despite its simplifying assumptions, this classical unsteady thin-airfoil theory is often used when studying oscillating foils, primarily because of the mathematically elegant analytical solutions. The resulting expression for the unsteady lift in the highly mathematical paper of Theodorsen (1935) can easily be implemented in a computer program like MATLAB, and one can very quickly obtain reasonably accurate values for the unsteady lift, even for transverse oscillation amplitudes of practical size.

There is no need to look to aircraft to find oscillating foils, however. Fish swim by oscillating their tails from side to side, and cetaceans by oscillating their tails up and down. Birds and insects stay aloft and move forward by flapping their wings. Lighthill was a pioneer in studying fish swimming from a hydrodynamic perspective, with his theory for the swimming of slender fish (Lighthill, 1960). Wu (1961) analyzed fish swimming by studying the two-dimensional potential flow over a waving flat plate of finite chord, building on results from classical unsteady thin-airfoil theory. Lighthill (1970) also applied unsteady foil theory to analyze thunniform swimming, i.e., fish locomotion where virtually all lateral motion occurs in the caudal fin and the region connecting the caudal fin to the main body. Lighthill's (1970) theory is extended in Chopra (1974) to account for a finite aspect ratio and in Chopra (1976) to account for large amplitude motion, but still with a low tail angle of attack. As noted by Scherer (1968) and Chopra (1976), large oscillation amplitudes relative to the chord are needed to achieve practical levels of thrust.

The term "dynamic stall" refers to a foil with a continuously changing angle of attack, which at some point passes the static stall angle. Dynamic stall is characterized by lift, drag, and moment curves not following their static equivalents,

but rather some form of loops, if the angle of attack variations are cyclic. Physically, the phenomenon is characterized by (Leishman, 2002) the build-up of a vortex at the leading edge, which detaches and is convected downstream in the wake, see Figure 3.1. When the vortex passes the trailing edge, the flow on the upper surface becomes fully separated, and when the angle of attack becomes low enough again, the flow reattaches back to front. The vortex building up at the leading edge is associated with an increase in lift, as long as the vortex stays over the upper surface, and an increase in nose-down pitching moment, due to the center of pressure moving aft as the vortex is convected downstream. The lift, drag, and nose-down pitch moment become significantly higher than their static values, and they all peak when the vortex passes into the wake – although usually not exactly simultaneously (McCroskey, 1981) – before dropping dramatically.

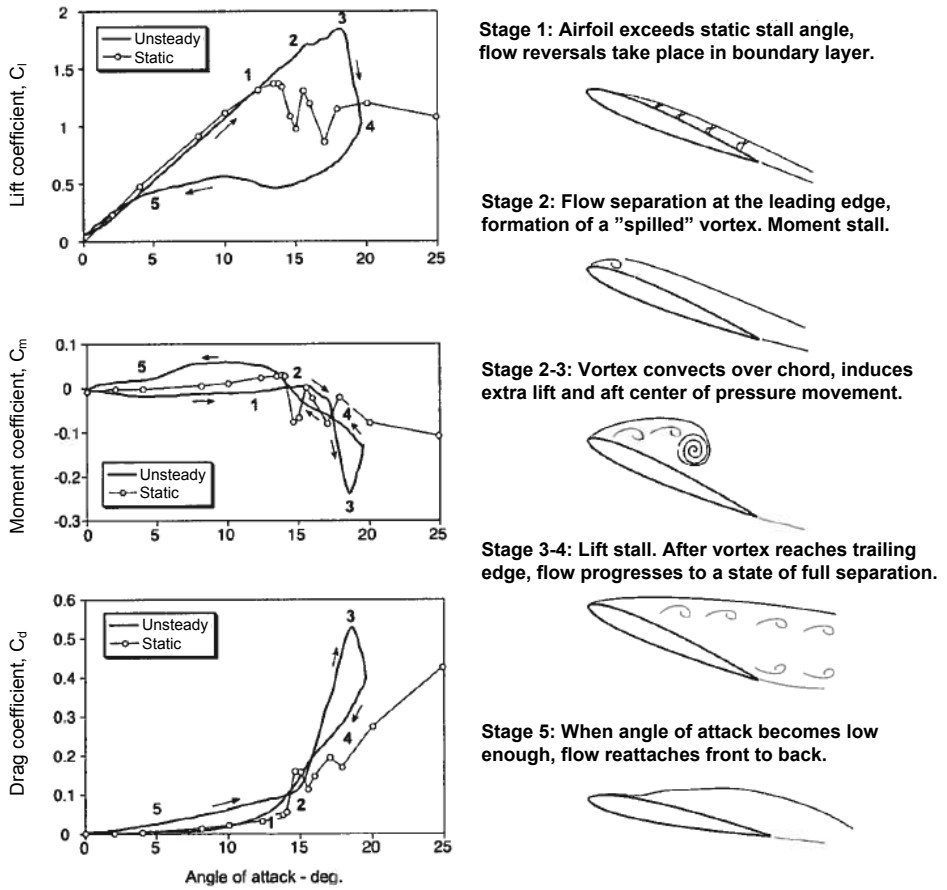

Figure 3.1: Flow features and unsteady airloads during the course of a dynamic stall cycle. Adapted (typed scanned text) from Leishman (2002).

McCroskey et al. (1976) performed dynamic stall experiments on a NACA 0012

airfoil with various leading-edge geometries, and found that although different types of stall occurred, all types were characterized by leading-edge vortex shedding. McCroskey (1981) performed a comprehensive experimental study of dynamic stall, discussing the effects of airfoil geometry, reduced frequency, amplitude, mean angle, Mach number, types of motion, and three-dimensional effects. He also discusses the different calculation methods available at the time. A good review of early dynamic stall research is given by Carr (1988).

Although CFD in principle now can be used to calculate the forces and moments on a foil during dynamic stall, agreement with experiments is still poor in the deep stall regime (Wang et al., 2010; Ol et al., 2010), and the calculations are time-consuming. Several semi-empirical models have been developed (Tarzanin, 1972; Tran and Petot, 1981; Leishman and Beddoes, 1989; Øye, 1991; Hansen et al., 2004; Larsen et al., 2007) that can provide fast results, which for many engineering applications are sufficiently accurate. Such semi-empirical models rely on a varying number of empirical coefficients as input. The well-validated (Pierce, 1996; Gupta and Leishman, 2006; Pereira et al., 2013) Leishman-Beddoes (L-B) dynamic stall model (Leishman and Beddoes, 1989) combines classical unsteady thin-airfoil theory for attached flow with an analytical expression for the separation point on a flat plate (Thwaites, 1960), and it includes dynamic effects through semi-empirical expressions.

In Section 3.2, the assumptions and most important results of classical unsteady thin-airfoil are explained, and an algorithm (Leishman, 2002) for calculating the unsteady lift resulting from arbitrary changes in angle of attack is presented. Then, in Section 3.3, the dynamic stall model used in the present work is presented. This dynamic stall model is a slightly modified version of the L-B dynamic stall model. The author found that some modifications of the L-B model were necessary for low inflow velocities and applied some other useful modifications of the L-B model proposed by Moriarty and Hansen (2005), which are explained in Section 3.3. An extension of the two-dimensional dynamic stall model to account for finite-span effects, proposed by the author, is presented in Section 3.3.5. The final dynamic stall model is compared with experiments in Chapter 4.

3.2 Classical unsteady thin-airfoil theory

3.2.1 The Theodorsen function

In his seminal paper, Theodorsen (1935) provides an analytical expression for the unsteady lift on a harmonically oscillating two-dimensional flat plate. The flow is assumed to be inviscid (i.e., not separating from the plate) and incompressible, and the transverse motion of the plate is assumed to be small so that the vortices shed in the wake remain on a straight line behind the foil, see Figure 3.2. The plate undergoes harmonic heave and pitch oscillations with the frequency ω, and the forward speed is U. The chord length of the plate is $c = 2b$.

As Kelvin's theorem states, the circulation around a closed curve moving with the fluid in an inviscid, barotropic flow with conservative body forces remains constant with time. Hence, if there is an increase in the circulation around the

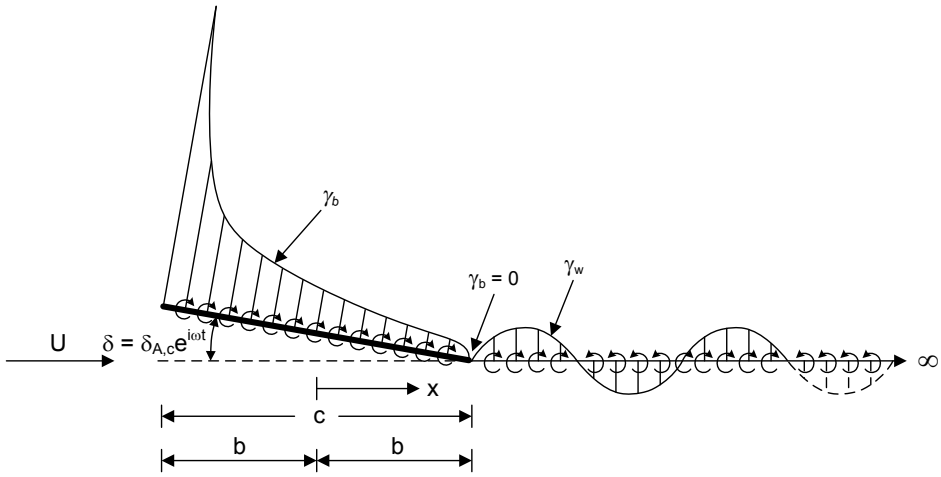

Figure 3.2: Assumptions in Theodorsen's model of unsteady airfoil forces. Modified from Leishman (2002). Although the airfoil is only pitching in this figure, it may undergo heave oscillation of small amplitude as well.

plate, there must be a corresponding decrease in the circulation in the wake. When representing the circulation around the plate by a vortex distribution, as in Figure 3.2, this implies that a change in angle of attack (and hence circulation around the plate) is accompanied by a vortex shed in the wake, with opposite sign of the change in circulation. In Figure 3.2, the vortex distribution on the plate, called the bound vorticity, is denoted γ_b, whereas the wake vorticity is denoted γ_w. The wake vortex sheet extends downstream to infinity. The Kutta condition says that there must be a stagnation point at the sharp trailing edge, or in other words, that the flow at the trailing edge must be tangential to the flat plate. This implies that $\gamma_b = 0$ at the trailing edge.

The important result of Theodorsen's analysis is that the unsteady lift can be written as the sum of two terms: a noncirculatory term due to flow acceleration, called added mass (also known as apparent mass or virtual mass), and a quasi-steady term, due to circulation about the plate, multiplied by the Theodorsen function, $C(k)$. The argument in this function, k, is called the *reduced frequency* and is the angular frequency of oscillation, ω, nondimensionalized by $c/2$ and U:

$$k = \frac{\omega c}{2U}. \tag{3.1}$$

For a plate oscillating harmonically in heave and pitch, the unsteady lift, L, becomes (Leishman, 2002)

$$\begin{aligned} L =& \pi\rho b^2 \left[\ddot{h} + U\dot{\delta} - ba\ddot{\delta}\right] \\ &+ 2\pi\rho U^2 b \left[\delta + \frac{\dot{h}}{U} + \frac{b\dot{\delta}}{U}\left(\frac{1}{2} - a\right)\right] C(k), \end{aligned} \tag{3.2}$$

where ρ is the mass density of the fluid, a is the pitch axis location relative to the mid-chord measured in semi-chords, h is the heave motion, and δ is the pitch motion. The heave and pitch motions must be written as

$$h(t) = h_{A,c}e^{i\omega t}, \tag{3.3}$$

$$\delta(t) = \delta_{A,c}e^{i\omega t}, \tag{3.4}$$

where $h_{A,c}$ and $\delta_{A,c}$ are complex heave and pitch amplitudes, respectively. The time-varying quasi-steady angle of attack term in Eq. 3.2 (due to pitch angle, heave velocity and pitch velocity) multiplied by the Theodorsen function, $C(k)$, is known as the *effective angle of attack*. The lift is given as the real value of Eq. 3.2. The corresponding moment about the mid-chord, $M_{1/2}$, is (Leishman, 2002)

$$\begin{aligned} M_{1/2} = &- \pi\rho b^2 \left[\left(\frac{1}{2} - a \right) Ub\dot{\delta} + b^2 \left(\frac{1}{8} + a^2 \right) \ddot{\delta} - ab\ddot{h} \right] \\ &+ 2\pi\rho U^2 b^2 \left(a + \frac{1}{2} \right) \left[\delta + \frac{\dot{h}}{U} + \frac{b\dot{\delta}}{U} \left(\frac{1}{2} - a \right) \right] C(k). \end{aligned} \tag{3.5}$$

The Theodorsen function, $C(k)$, is given as

$$C(k) = F(k) + iG(k) = \frac{H_1^{(2)}(k)}{H_1^{(2)}(k) + iH_0^{(2)}(k)}, \tag{3.6}$$

where F and G are the real and imaginary parts of $C(k)$. $H_n^{(2)}$ are Hankel functions (Abramowitz et al., 1972) given as

$$H_n^{(2)} = J_n - iY_n, \tag{3.7}$$

where J_n and Y_n are Bessel functions of the first and second kind, respectively. The real and imaginary parts of the Theodorsen function are plotted in Figure 3.3. As seen from the top plot in Figure 3.3, the amplitude of the unsteady lift approaches half the amplitude of the quasi-steady lift as k increases toward infinity.

3.2.2 The Wagner function

Wagner (1925) studied a flat plate that is given a step change in angle of attack while moving at speed U in inviscid and incompressible flow. The lift is instantly affected by the change in angle of attack, but it takes some time for the lift to reach a new steady value. Physically, this can be explained by the influence on the plate from the vortex that is shed at the step change in angle of attack. After some time this vortex is so far downstream of the plate that its effect on the plate is negligible. The lift of a plate with $c = 2b$ that instantly has a change in attack from zero to α at $t = 0$, is given as

$$L(s) = \pi\rho b^2 U\delta(s) + 2\pi\rho U^2 b\alpha\phi(s), \tag{3.8}$$

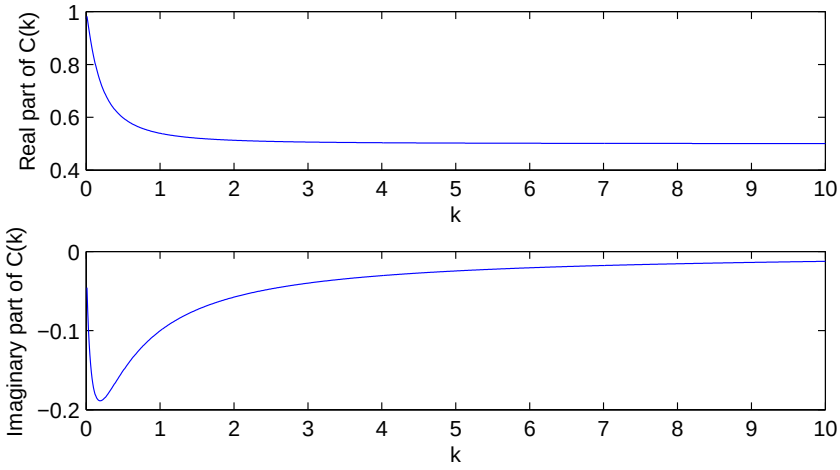

Figure 3.3: Real and imaginary parts of the Theodorsen function

where $\delta(s)$ here is the Dirac delta function, $\phi(s)$ is the Wagner function, and s is the number of semi-chords traveled by the plate at time t, that is,

$$s = \frac{2Ut}{c}. \tag{3.9}$$

The first term in Eq. 3.8 is an added mass term and is responsible for infinitely high lift at $s = 0$. The second term in Eq. 3.8 is the circulatory lift.

Since the Wagner function is not in a convenient analytic form, it is typically replaced by an exponential or algebraic approximation. Jones (1938, 1940) proposed an approximation of the Wagner function:

$$\phi(s) = 1 - A_1 e^{-b_1 s} - A_2 e^{-b_2 s}, \tag{3.10}$$

where $A_1 = 0.165$, $A_2 = 0.335$, $b_1 = 0.0455$, and $b_2 = 0.3$, which agrees with the exact solution to within 1% accuracy. Eq. 3.10 is plotted in Figure 3.4. Jones (1940) also proposed Wagner-like functions for finite aspect ratio wings but provided convenient curve fit expressions only for aspect ratios 3 and 6.

The circulatory part of the lift coefficient due to arbitrary changes in angle of attack, $C_L^C(t)$, can be calculated by using the Wagner function, $\phi(s)$, and superposition of step responses in Duhamel's integral:

$$C_L^C(s) = C_{L_\alpha}\left[\alpha(0)\phi(s) + \int_0^s \frac{d\alpha}{ds}(\sigma)\phi(s-\sigma)d\sigma\right] = C_{L_\alpha}\alpha_E(s), \tag{3.11}$$

where C_{L_α} is the lift coefficient slope ($C_{L_\alpha} = 2\pi$ for a flat plate), σ is a dummy time variable of integration, and α_E is the effective angle of attack.

The following derivation of an algorithm to calculate the unsteady lift due to a time-varying angle of attack is based on Leishman (2002). This algorithm is used in

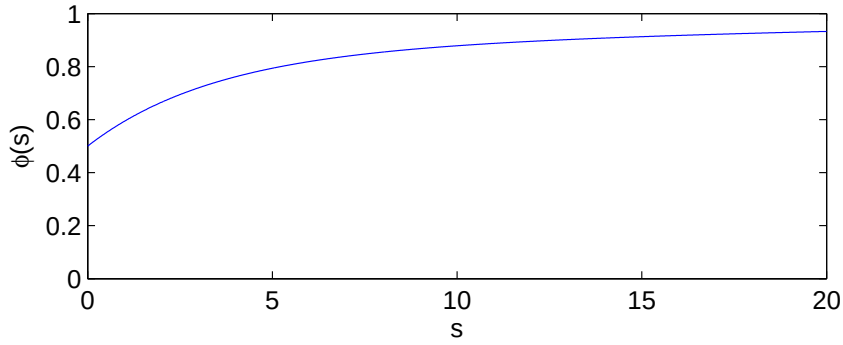

Figure 3.4: The Wagner function based on the approximation of Jones (1938, 1940), Eq. 3.10

the dynamic stall model in Section 3.3. Using the Duhamel integral in Eq. 3.11 to calculate $\alpha_E(t)$, with the Wagner function in the form of Eq. 3.10, $\alpha_E(s)$ becomes

$$\begin{aligned}
\alpha_E(s) &= \alpha(0)\phi(s) + \int_0^s \frac{d\alpha}{ds}(\sigma)\phi(s-\sigma)d\sigma \\
&= \alpha(0)\left(1 - A_1 e^{-b_1 s} - A_2 e^{-b_2 s}\right) \\
&\quad + \int_0^s \frac{d\alpha}{ds}(\sigma)\left(1 - A_1 e^{-b_1(s-\sigma)} - A_2 e^{-b_2(s-\sigma)}\right) d\sigma \\
&= \alpha(0) - A_1\alpha(0)e^{-b_1 s} - A_2\alpha(0)e^{-b_2 s} + \int_0^s d\alpha(s) \\
&\quad - A_1 \int_0^s \frac{d\alpha}{ds}(\sigma)e^{-b_1(s-\sigma)}d\sigma - A_2 \int_0^s \frac{d\alpha}{ds}(\sigma)e^{-b_2(s-\sigma)}d\sigma. \qquad (3.12)
\end{aligned}$$

$A_1\alpha(0)e^{-b_1 s}$ and $A_2\alpha(0)e^{-b_2 s}$ are short-term transients and can be neglected, allowing us to write

$$\alpha_E(s) = \alpha(s) - X(s) - Y(s), \qquad (3.13)$$

where

$$X(s) = A_1 \int_0^s \frac{d\alpha}{ds}(\sigma)e^{-b_1(s-\sigma)}d\sigma, \qquad (3.14)$$

and

$$Y(s) = A_2 \int_0^s \frac{d\alpha}{ds}(\sigma)e^{-b_2(s-\sigma)}d\sigma. \qquad (3.15)$$

Assuming a continuously sampled system with time step ΔS, we have at the

next time step:

$$\begin{aligned} X(s+\Delta S) &= A_1 \int_0^{s+\Delta S} \frac{d\alpha}{ds}(\sigma) e^{-b_1(s+\Delta S-\sigma)} d\sigma \\ &= e^{-b_1 \Delta S} \overbrace{A_1 \int_0^{s} \frac{d\alpha}{ds}(\sigma) e^{-b_1(s-\sigma)} d\sigma}^{X(s)} \\ &\quad + \overbrace{A_1 \int_s^{s+\Delta S} \frac{d\alpha}{ds}(\sigma) e^{-b_1(s+\Delta S-\sigma)} d\sigma}^{I} . \end{aligned} \tag{3.16}$$

The integral, I, can be written as

$$I = A_1 e^{-b_1(s+\Delta S)} \int_s^{s+\Delta S} \frac{d\alpha}{ds}(\sigma) e^{b_1 \sigma} d\sigma. \tag{3.17}$$

Using a simple backward-difference approximation for $d\alpha/ds$ at time $s+\Delta S$, and the midpoint rule for integration, we get

$$\begin{aligned} I &= A_1 e^{-b_1(s+\Delta S)} \frac{\alpha(s+\Delta S) - \alpha(s)}{\Delta S} e^{b_1\left(s+\frac{\Delta S}{2}\right)} \Delta S \\ &= A_1 \left[\alpha(s+\Delta S) - \alpha(s)\right] e^{-b_1 \frac{\Delta S}{2}} . \end{aligned} \tag{3.18}$$

This gives

$$X(s+\Delta S) = X(s) e^{-b_1 \Delta S} + A_1 \left[\alpha(s+\Delta S) - \alpha(s)\right] e^{-b_1 \frac{\Delta S}{2}} \tag{3.19}$$

or

$$X(s) = X(s-\Delta S) e^{-b_1 \Delta S} + A_1 \left[\alpha(s) - \alpha(s-\Delta S)\right] e^{-b_1 \frac{\Delta S}{2}} . \tag{3.20}$$

By following the same analogy,

$$Y(s) = Y(s-\Delta S) e^{-b_2 \Delta S} + A_2 \left[\alpha(s) - \alpha(s-\Delta S)\right] e^{-b_2 \frac{\Delta S}{2}} . \tag{3.21}$$

3.2.3 Other fundamental functions

In addition to the Theodorsen and Wagner functions, there are several other fundamental functions in unsteady thin-airfoil theory. "Fundamental" here refers to the fact that these functions solve mathematically idealized problems, but that does not mean that they are not useful in practice.

Sears (1938) studied a flat plate traveling with constant forward speed U and no vertical motion into a sinusoidal vertical gust. Analogous to the use of the Theodorsen function, the Sears function – see for instance Leishman (2002) for more details – is multiplied with the quasi-steady angle of attack to obtain the unsteady frequency-dependent lift of the plate traveling through the sinusoidal vertical gust. One may wonder what the aerodynamic difference is between two equal plates traveling at the same forward speed, where one plate undergoes sinusoidal vertical

motion and the other plate experiences a sinusoidal vertical gust. The difference is the vertical flow field seen by the two plates, and this is easiest to understand if one considers vertical motion/gust of a short wavelength relative to the plate. The Sears function and the Theodorsen function convergence as k approaches zero, implying that the two problems are mathematically equal for low-frequent oscillations.

The Küssner function – once again, Leishman (2002) is a good source for an introduction to this function – is a time-domain function like the Wagner function, used when calculating the lift on a flat plate traveling at steady forward speed, entering a sharped-edged vertical gust. Unlike the Wagner function, the Küssner function takes a value of 0 for $s = 0$. Similarly to Eq. 3.11, the lift in an arbitrarily varying upwash field can be calculated using the Küssner function in the Duhamel superposition integral.

3.2.4 Relation between the Theodorsen function and the Wagner function

Garrick (1938) showed that the Theodorsen function in the frequency domain and the Wagner function in the time domain are related by a Laplace transform pair, through the following derivation:

Eq. 3.11 can be rewritten as

$$C_L^C(s) = C_{L_\alpha}\left[\alpha(0)\phi(s) + \int_0^s \frac{d\alpha}{ds}(s-\sigma)\phi(s)d\sigma\right]. \tag{3.22}$$

Now, let α be harmonically varying as

$$\alpha(s) = \alpha_{A,c}e^{iks}, \tag{3.23}$$

where $\alpha_{A,c}$ is the complex angle of attack amplitude, so that

$$\frac{d\alpha}{ds}(s-\sigma) = \alpha_{A,c}ike^{ik(s-\sigma)}. \tag{3.24}$$

Eq. 3.22 then becomes

$$\begin{aligned} C_L^C(s) &= C_{L_\alpha}\left[\alpha_{A,c}\phi(s) + \alpha_{A,c}ike^{iks}\int_0^s \phi(s)e^{-ik\sigma}d\sigma\right] \\ &= C_{L_\alpha}\alpha_{A,c}\phi(s) + C_{L_\alpha}\alpha_{A,c}ike^{iks}\int_0^\infty \phi(s)e^{-ik\sigma}d\sigma \\ &\quad -C_{L_\alpha}\alpha_{A,c}ike^{iks}\int_s^\infty \phi(s)e^{-ik\sigma}d\sigma. \end{aligned} \tag{3.25}$$

For the steady-state part only,

$$C_L^C(s) = C_{L_\alpha}\alpha_{A,c}ike^{iks}\int_0^\infty \phi(s)e^{-iks}ds. \tag{3.26}$$

This must be equal to Theodorsen's result,

$$C_L^C(s) = C_{L_\alpha}\alpha_{A,c}C(k)e^{iks}, \tag{3.27}$$

which implies that

$$C(k) = ik \int_0^\infty \phi(s) e^{-iks} ds. \tag{3.28}$$

Using the definition of the Laplace transform, we can then write

$$C(k) = ik\mathcal{L}\{\phi(s)\}. \tag{3.29}$$

The Wagner function can be obtained from the Theodorsen function by using the inverse Laplace transform:

$$\phi(s) = \mathcal{L}^{-1}\left\{\frac{C(k)}{k}\right\}. \tag{3.30}$$

Figure 3.5 shows the original Theodorsen function compared with the Theodorsen function obtained using Eq. 3.29 with Jones's (1938; 1940) approximation of the Wagner function, Eq. 3.10.

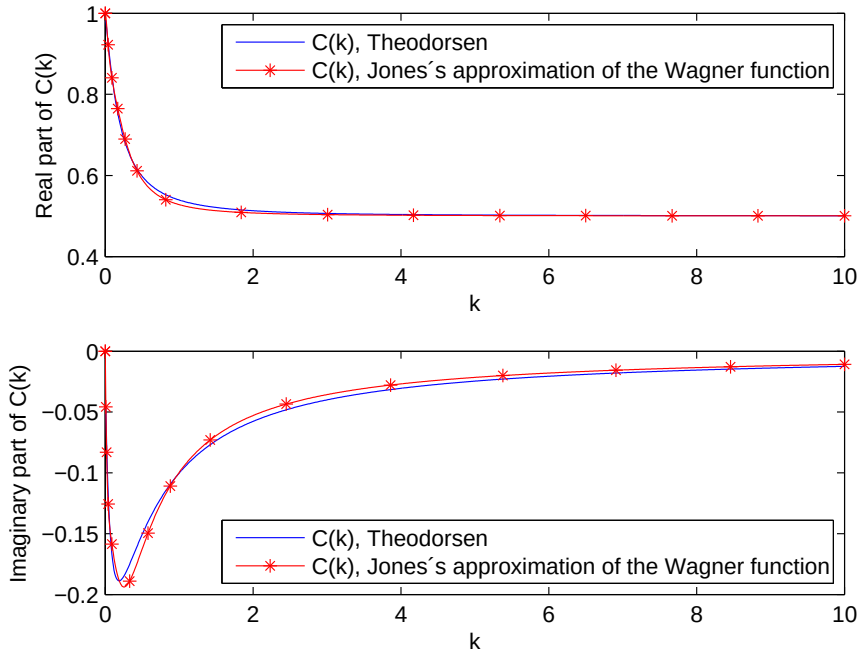

Figure 3.5: Numerically obtained Theodorsen function, based on Jones's approximation of the Wagner function, plotted against the original Theodorsen function

Using Eq. 3.10, Eq. 3.28 can be evaluated by hand to get a simple approximated

expression for the Theodorsen function:

$$\begin{aligned} C(k) &= ik\int_0^\infty \left(1 - A_1 e^{-b_1 s} - A_2 e^{-b_2 s}\right) e^{-iks} ds \\ &= ik\left[-\frac{1}{ik}e^{-iks} + \frac{A_1}{b_1 + ik}e^{-s(b_1+ik)} + \frac{A_2}{b_2+ik}e^{-s(b_2+ik)}\right]_0^\infty \\ &= 1 - \frac{ikA_1}{b_1+ik} - \frac{ikA_2}{b_2+ik}. \end{aligned} \tag{3.31}$$

3.2.5 Leading-edge suction force

A flat plate oscillating harmonically in heave and pitch in an inviscid and incompressible fluid produces forward thrust through two forces: the leading-edge suction force and the horizontal component of the pressure force normal to the plate. The latter can be both a thrust and a drag force, whereas the leading-edge suction force is always a thrust force. Physically, the leading-edge suction force, S, on a thin plate at an inclination to the inflow arises because the flow must accelerate around the leading edge of the plate – given that the the flow is attached – thereby creating a low pressure and a thrust force at the leading edge.

The normal force, N, on an inclined flat plate in steady, inviscid, incompressible flow can be decomposed into a lift force, L, acting perpendicular to the inflow, and a drag force, D, acting parallel to the inflow. This is illustrated in Figure 3.6. Mathematically, it can be shown (see for instance Johnston (2004)) that the component of S acting in the opposite direction of the free-stream velocity, U, is equal in magnitude to D, resulting in zero force in the free-stream direction.

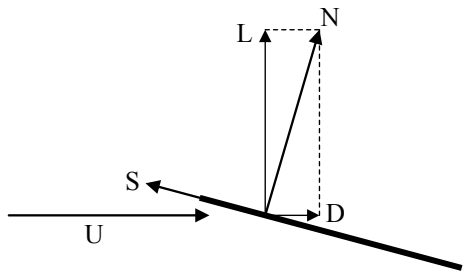

Figure 3.6: Forces on a flat plate in steady flow

3.3 Dynamic stall model

The dynamic stall model implemented in the present work is explained here. Unless otherwise specified, this model is identical to the L-B model (Leishman and Beddoes, 1989). The modifications to the L-B model were found necessary in order to make the model work properly. The noncirculatory normal force is calculated differently and the separation point location are expressed slightly differently in the

present model than in the L-B model. Further details are given where the modifications are described. The dynamic stall model is valid for a two-dimensional foil, but the author has proposed corrections for a finite-span foil in Section 3.3.5.

3.3.1 Attached flow

If there is a small change in angle of attack for fully attached flow, it will take some time before the separation point is reestablished at the trailing edge. The circulatory normal force coefficient due to an accumulating series of step changes in angle of attack can be expressed as

$$\begin{aligned} C_{N,n}^{C} &= C_{N_\alpha}(\alpha_n - \alpha_0 - X_n - Y_n) && (3.32)\\ &= C_{N_\alpha}(\alpha_{E,n} - \alpha_0), && (3.33) \end{aligned}$$

where C_{N_α} is the normal force coefficient curve slope at the zero-lift angle of attack, α_0 is the zero-lift angle of attack, and subscript n denotes time step n. $\alpha_{E,n}$ is then the effective angle of attack at time step n. X and Y are the deficiency functions given in Eqs. 3.20 and 3.21, that is,

$$X_n = X_{n-1}e^{-b_1\Delta S} + A_1(\alpha_n - \alpha_{n-1})e^{-b_1\frac{\Delta S}{2}}, \tag{3.34}$$

$$Y_n = Y_{n-1}e^{-b_2\Delta S} + A_2(\alpha_n - \alpha_{n-1})e^{-b_2\frac{\Delta S}{2}}, \tag{3.35}$$

where A_1, A_2, b_1 and b_2 are profile dependent variables describing the time delay, and ΔS is the distance traveled by the foil in semi-chords during a time interval $\Delta t = t_n - t_{n-1}$. For a flat plate, $A_1 = 0.165$, $A_2 = 0.335$, $b_1 = 0.0455$ and $b_2 = 0.3$ (Jones, 1938, 1940).

The noncirculatory normal force, also known as the added mass force, is given for each chordwise strip of a flat plate as

$$N_{AM} = \frac{\rho\pi c^2}{4} ds \left(-\ddot{h}\cos\delta + U\frac{d}{dt}(\sin\delta) + \left(\frac{c}{2} - x_p\right)\ddot{\delta} \right), \tag{3.36}$$

where ds is the foil strip width, x_p is the distance from the leading edge to the pivot point, and $\dot{\delta}$ and $\ddot{\delta}$ denote the first and second derivatives of δ, respectively. Finding the noncirculatory normal force coefficient without the use of a deficiency function, as done here and in Hansen et al. (2004), is a simplification relative to the original L-B model, which uses a deficiency function to account for time-history effects. For very low Mach numbers, which is the case for the applications in the present work, time-history effects on the noncirculatory normal force are negligible.

In Bøckmann and Steen (2013), the noncirculatory normal force was nondimensionalized by

$$C_N^I = \frac{N_{AM}}{\frac{1}{2}\rho V^2 c}, \tag{3.37}$$

where V is the inflow speed to the foil, which is different from U if the foil is moving vertically in addition to horizontally. The total normal force coefficient

during attached flow conditions, C_N^p, is found by summing the circulatory and noncirculatory coefficients:

$$C_{N,n}^p = C_{N,n}^C + C_{N,n}^I. \tag{3.38}$$

An obvious problem with nondimensionalizing the noncirculatory normal force coefficient as in Eq. 3.37 is the case when V approaches zero. The same problem occurs for the original expression for C_N^I in Leishman and Beddoes (1989). Therefore, in the implementation of the L-B model in the ship simulator VeSim (see Chapter 5), $C_{N,n}^p = C_{N,n}^C$ in Eq. 3.38. This does not imply that the added mass force was neglected in the VeSim simulations, since the added mass force was added at a later stage (see Section 3.3.5). In the plots in Section 4.3, V is not close to zero, and Eq. 3.38 was therefore applied, where C_N^I was calculated using Eq. 3.37.

3.3.2 Trailing edge separation

The basic assumption of the L-B model is that the normal force coefficient, C_N, for separated flow can be found from

$$C_N = C_{N_\alpha} \left(\frac{1 + \sqrt{f}}{2} \right)^2 (\alpha - \alpha_0), \tag{3.39}$$

which is an approximation to the normal force coefficient on a flat plate in a potential Kirchhoff flow (Thwaites, 1960). The degree of attachment, f, is defined as the distance along the chord from the leading edge to the separation point, divided by the chord length, see Figure 3.7. For fully attached flow, $f = 1$, and $C_N = C_{N_\alpha}(\alpha - \alpha_0)$.

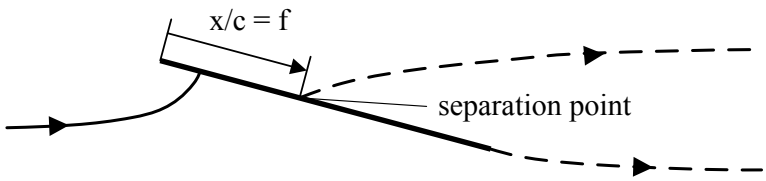

Figure 3.7: The degree of attachment, f, defined in a Kirchhoff flow past a flat plate. Modified from Thwaites (1960) and Hansen et al. (2004).

f is found from Eq. 3.39 by replacing the predicted C_N with the static normal force coefficient, C_N^{static}, found from tables of static lift and drag coefficients, so that

$$f = \left(2\sqrt{\frac{C_N^{static}(\alpha_n)}{C_{N_\alpha}(\alpha_n - \alpha_0)}} - 1 \right)^2. \tag{3.40}$$

For unsteady conditions, there is a lag in the leading-edge pressure response with respect to C_N^p, expressed as

$$C'_{N,n} = C^p_{N,n} - D_{p,n}, \tag{3.41}$$

where D_p is the attached flow deficiency function,

$$D_{p,n} = D_{p,n-1} e^{-\frac{\Delta S}{T_p}} + (C^p_{N,n} - C^p_{N,n-1}) e^{-\frac{\Delta S}{2T_p}}. \tag{3.42}$$

T_p is a nondimensional time constant for the pressure delay of attached flow. An explanation of how a time lag can be expressed as in Eqs. 3.41 and 3.42 is given in Appendix A. An equivalent angle of attack, α_f, is defined as

$$\alpha_{f,n} = \frac{C'_{N,n}}{C_{N_\alpha}} + \alpha_0, \tag{3.43}$$

and the corresponding degree of attachment is calculated using Eq. 3.40 as

$$f'_n = \left(2\sqrt{\frac{C_N^{static}(\alpha_{f,n})}{C_{N_\alpha}(\alpha_{f,n} - \alpha_0)}} - 1 \right)^2. \tag{3.44}$$

The static degree of attachment, f, calculated from Eq. 3.40, was found to reproduce the static normal force coefficient for the NACA 0015 profile only for $|\alpha| < 62°$. The following correction (Moriarty and Hansen, 2005) reproduced the static normal force coefficient for all angles of attack with high accuracy, and was therefore applied:

$$t'_{N,n} = 2\sqrt{\frac{C_N^{static}(\alpha_{f,n})}{C_{N_\alpha}(\alpha_{f,n} - \alpha_0)}} - 1, \tag{3.45}$$

$$f'_n = t'^2_{N,n} \mathrm{sign}(t'_{N,n}). \tag{3.46}$$

In addition to the pressure lag, there is a viscous lag due to the unsteady boundary layer response, represented by a first-order lag in the value of f' as

$$f''_n = f'_n - D_{f,n}, \tag{3.47}$$

where D_f is the deficiency function for the degree of attachment,

$$D_{f,n} = D_{f,n-1} e^{-\frac{\Delta S}{T_f}} + (f'_n - f'_{n-1}) e^{-\frac{\Delta S}{2T_f}}. \tag{3.48}$$

T_f is a nondimensional time constant for the lag in the boundary layer.

In Bøckmann and Steen (2013), the normal force coefficient incorporating both the pressure lag and the viscous lag was computed using Eq. 3.39 as

$$C^f_{N,n} = C_{N_\alpha} \left(\frac{1 + \sqrt{f''_n}}{2} \right)^2 (\alpha_{E,n} - \alpha_0). \tag{3.49}$$

When using the modification by Moriarty and Hansen (2005), however, $C^f_{N,n}$ is given as

$$C^f_{N,n} = C_{N_\alpha}\left(\frac{1+\sqrt{|f''_n|}\text{sign}(f''_n)}{2}\right)^2(\alpha_{E,n}-\alpha_0), \tag{3.50}$$

which is implemented in the present work.

3.3.3 Leading-edge separation

As the absolute value of the angle of attack increases from zero, a vortex builds up at the leading edge. The forces and moments can be represented by ignoring the developing vortex until it detaches and is transported downstream (Leishman and Beddoes, 1989). For a symmetric foil, the leading-edge vortex is assumed to detach when the absolute value of the angle of attack is larger than a certain value, denoted α_v. The vortex then travels downstream at 1/3 of the inflow speed to the foil, V (Green et al., 1992; Beddoes, 1978). α_v can be found from the static moment coefficient curve, where there is a break in the pitching moment (Pereira, 2010). A nondimensional variable τ is introduced to keep track of the position of the traveling vortex. When $\tau = 0$, the vortex is at leading edge, and when $\tau = 1$, the vortex has reached the trailing edge (Larsen et al., 2007). The L-B model says that the vortex has reached the trailing edge when τ is equal to a nondimensional period T_{vl}, which is determined empirically, but in the present work, the vortex travel speed was assumed to be $1/3V$, like in Larsen et al. (2007). $\tau = 0$ unless $|\alpha_n| > \alpha_v$, when τ increases as

$$\tau_n = \tau_{n-1} + \frac{V_n}{3c}\Delta t. \tag{3.51}$$

The increment in the vortex-induced normal force coefficient due to a vortex at the leading edge, C_V, is determined by the difference between the instantaneous linearized value of the unsteady circulatory normal force coefficient and the corresponding unsteady nonlinear normal force coefficient as given by the Kirchhoff approximation:

$$C_{V,n} = C^C_{N,n} - C^f_{N,n}. \tag{3.52}$$

The total accumulated vortex-induced normal force coefficient, C^V_N, is allowed to decay exponentially with time, but may also be updated by a new increment:

$$C^V_{N,n} = C^V_{N,n-1}e^{-\frac{\Delta S}{T_v}} + (C_{V,n} - C_{V,n-1})\,e^{-\frac{\Delta S}{2T_v}}, \tag{3.53}$$

if the vortex is growing in strength and located on the foil surface. T_v is a nondimensional time constant for vortex delay. If the vortex is no longer on the foil surface or it is on the foil surface but decreasing in strength without detaching, Eq. 3.53 reduces to

$$C^V_{N,n} = C^V_{N,n-1}e^{-\frac{\Delta S}{T_v}}. \tag{3.54}$$

Figure 3.8 illustrates this procedure.

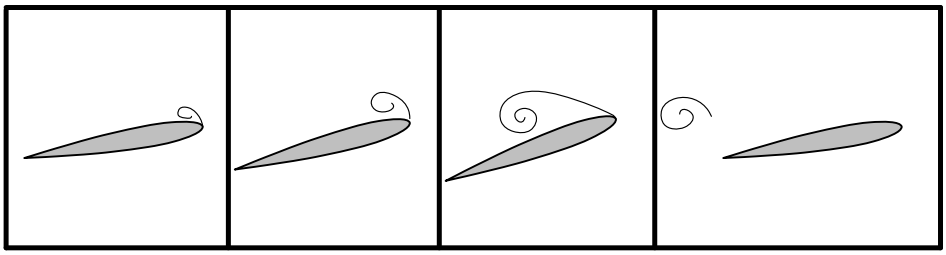

Figure 3.8: Leading-edge separation in the dynamic stall model. The inflow is from right to left.

Finally, the total normal force coefficient becomes

$$C_{N,n} = C_{N,n}^f + C_{N,n}^V + C_{N,n}^I. \tag{3.55}$$

3.3.4 Chordwise force

The chordwise force (i.e., the force in S-direction in Figure 3.6) coefficient is calculated in Leishman and Beddoes (1989) and Bøckmann and Steen (2013) as

$$C_{C,n} = \eta_C C_{N_\alpha}(\alpha_{E,n} - \alpha_0)\alpha_{E,n}\sqrt{f_n''} - C_{D0}, \tag{3.56}$$

where η_C is called the leading-edge suction recovery factor, which accounts for the fact that the foil does not produce 100 percent of the chordwise force attained in potential flow. $\eta_C = 0.95$ is typically used. The first term on the right hand side of Eq. 3.56 represents the leading-edge suction force, as explained in Sec. 3.2.5. $\sqrt{f}$ comes from the Kirchhoff flow model (Thwaites, 1960), and f'' is used instead of f to account for the effects of both pressure and viscous lag. Viscous effects are included through the term C_{D0}, which is the viscous drag coefficient at zero lift. This simplification is assumed to be reasonable, since the pressure drag is already included through the normal force coefficient.

Static C_C values for the NACA 0015 profile were not reproduced by using the static degree of attachment, f, calculated from Eq. 3.40, in Eq. 3.56, except for low angles of attack. The following correction (Moriarty and Hansen, 2005) reproduced the static chordwise force coefficient for all angles of attack with high accuracy, and was therefore applied: A separate degree of attachment, f_C'', based on Eq. 3.56, was found as

$$t'_{C,n} = \frac{C_C^{static}(\alpha_{f,n}) + C_{D0}}{\eta_C C_{N_\alpha}(\alpha_{f,n} - \alpha_0)\alpha_{f,n}}, \tag{3.57}$$

$$f'_{C,n} = \left(t'_{C,n}\right)^2 \operatorname{sign}(t'_{C,n}), \tag{3.58}$$

$$f''_{C,n} = f'_{C,n} - D_{f,n}, \tag{3.59}$$

where C_C^{static} is the static chordwise force coefficient, found from tables of static lift and drag coefficients. $f'_{C,n}$ is set to be 1 if $|\alpha_{f,n}| < 5°$ to avoid the possible singularity when $\alpha_{f,n}$ approaches zero. The chordwise force coefficient was finally obtained as (Moriarty and Hansen, 2005)

$$C_{C,n} = \eta_C C_{N_\alpha}(\alpha_{E,n} - \alpha_0)\alpha_{E,n}\sqrt{|f''_{C,n}|}\operatorname{sign}\left(f''_C\right) - C_{D0}. \tag{3.60}$$

3.3.5 Correcting for finite-span effects

In order to account for the effect of finite span on the foil lift and drag, the following procedure was applied at each time step:

1. The foil was divided into chordwise strips in the spanwise direction. The normal and chordwise forces on each foil strip, N_{strip} and C_{strip}, were calculated using the dynamic stall model described in Sections 3.3.1-3.3.4:

$$N_{strip} = \left(C_N^f + C_N^V\right)\frac{1}{2}\rho V^2 cds, \tag{3.61}$$

$$C_{strip} = C_C\frac{1}{2}\rho V^2 cds. \tag{3.62}$$

   The added mass force was added at a later stage (step 6).

2. The lift and drag of each foil strip, L_{strip} and D_{strip}, were calculated using α_f at each strip:

$$L_{strip} = N_{strip}\cos\alpha_f + C_{strip}\sin\alpha_f, \tag{3.63}$$

$$D_{strip} = N_{strip}\sin\alpha_f - C_{strip}\cos\alpha_f, \tag{3.64}$$

3. When the dynamic stall model was used for foils on a ship, the effect of a finite foil span on the lift was accounted for by multiplying L_{strip} by the factor $1/\left(1+\frac{2}{\Lambda}\right)$ when the wave directions relative to the ship heading were 0° and 180°. Λ is the foil's aspect ratio. This expression for the lift is valid for an elliptical circulation distribution for a large aspect ratio foil below stall. However, the circulation distribution will be far from elliptical if the ship has significant rolling motion. Therefore, the lift correction factor was taken to be 1 when the wave directions relative to the ship heading were ±90°, and linearly interpolated between 1 and $1/\left(1+\frac{2}{\Lambda}\right)$ for other angles.

4. The induced drag coefficient of an elliptical flat foil of large aspect ratio, at angles of attack below stall, is

$$C_{D,i} = \frac{4\pi\alpha_f^2\Lambda}{(\Lambda+2)^2}. \tag{3.65}$$

Although the induced drag is a quantity related to the foil as a whole, each strip's contribution to the total induced drag was calculated as $D_{i,strip} = C_{D,i}\frac{1}{2}\rho V^2 cds$, since α_f in Eq. 3.65 in principle can vary from strip to strip. The induced drag was added to the profile drag of each strip. The induced drag was multiplied by a factor which is 1 in head and following seas, 0 in beam seas, and linearly interpolated between 1 and 0 for other wave directions relative to the ship heading.

5. The lift and drag of all strips at this point accounted for the effect of a finite span and were converted back to normal and chordwise forces by

$$N_{strip} = L_{strip}\cos\alpha_f + D_{strip}\sin\alpha_f, \tag{3.66}$$

$$C_{strip} = L_{strip}\sin\alpha_f - D_{strip}\cos\alpha_f. \tag{3.67}$$

6. Finally, the normal added mass force on the strip, N_{AM}, was added to N_{strip}, and the stripwise forces were summed.

Although these expressions for lift and drag are strictly only valid for an elliptical foil of large aspect ratio, they are quite fair to apply also for a moderately tapered foil (McCormick, 1995) of aspect ratio larger than four (Faltinsen, 2005). The use of these expressions for the lift and induced drag when the foil is stalling is more questionable, but was chosen nevertheless, lacking alternatives.

Chapter 4

Experiments with an oscillating foil

4.1 Experiment setup

A foil of span 1.81 m and max chord length 0.1875 m was tested in a 40 m long, 6.45 m wide, and 1.5 m deep towing tank, see Appendix C.1. The foil sectional form was the NACA 0015 profile. Figure 4.1 is a CAD drawing showing the planform and thickness profile of the foil, with dimensions in mm. The foil was designed with the intention of being mounted on a ship model, see Chapter 5. It was thought to have a telescopic design in full scale, where the outermost parts could be retracted into the center part of the foil. This resulted in the unconventional planform, but no telescope mechanism was built in model scale.

The foil and supporting rig, shown in Figure 4.2, were mounted to the towing tank carriage. The foil was attached to two aluminum struts. On top of the struts was a motor, pitching the foil via two thin rods. As shown in Figure 4.3, the rods rotated a wheel 57 mm above the chord line of the foil, $0.25c$ from the leading edge, thereby pitching the foil about this point. The idea was that, when mounted to the ship, the foil could be swung back and stored in a small compartment of the hull, so that the foil bottom was flush with the hull bottom. For this reason, the foil was designed to pitch about a point above itself, in addition to the fact that it was easier to build such a pitching mechanism. The telescope mechanism was assumed so that the foil could have a span larger than the hull width, without the foil tips sticking out from the ship hull when the foil was stored in the hull bottom.

Above the motor were three vertical force transducers and one horizontal force transducer. The three vertical force transducers were arranged in a triangular pattern, with two force transducers partly in front of the motor, and the third behind the motor. The uppermost item of the foil rig, the horizontal force transducer, was attached to a steel beam connecting the foil rig to two electric actuators on the towing tank carriage. These two electric actuators actuated the entire foil rig in heave. When not heaving, the foil would be approximately 0.75 m from the free

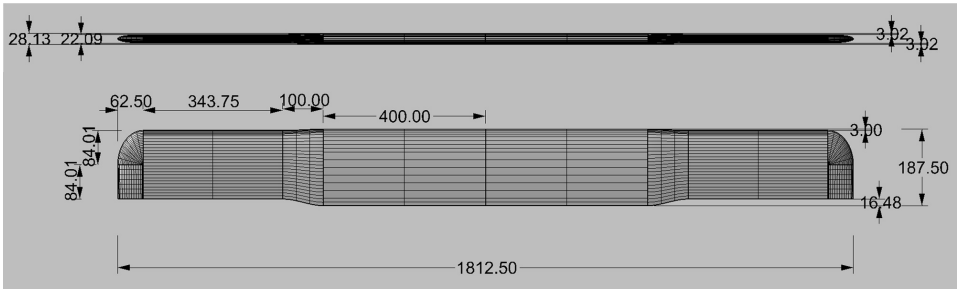

Figure 4.1: The planform and thickness profile of the foil used in the experiments, with dimensions in mm

surface and the solid tank bottom. When heaving, the foil was always at a distance more than three chords away from each of these boundaries, so it is fair to assume that the influence of the free surface and the solid tank bottom on the foil force was negligible (Wu, 1972).

120 mm above the foil's chord line were two vanes, one on each strut, detecting the inflow angle to the foil. Figure 4.3 is a 2D CAD drawing showing the size and location of the vanes, with dimensions in mm, whereas Figure 4.4 shows a close-up view of the vane on the starboard strut. The idea behind these vane locations was that the average of the two vane angles would be little influenced by the upwash and downwash from the foil, yet at the same time capture wave-induced fluid particle motion at the depth of the foil. The vanes were connected to waterproof potentiometers, with the wire from the potentiometers going up to the signal amplifier on the towing tank carriage. Before the basin was filled with water, the signals from the potentiometers were calibrated against the vane angles. To simplify the experiments, it was assumed that oscillating the foil in heave without surface waves would expose the foil to oscillating fluid motion similar to what one would get with surface waves, which supposedly is a good approximation for waves much longer than the foil chord.

4.2 Static angle of attack

Static lift and drag coefficients for the foil are shown in Figure 4.5. The steady forward speed, U, was 1.286 m/s, giving a Reynolds number of $Re = 2.0 \times 10^5$. $U = 1.286$ m/s was chosen because when mounting the same foil to a ship model, see Chapter 5, $U = 1.286$ m/s corresponded to 10 knots forward speed for the full-scale ship. Lift and drag coefficients calculated using a vortex lattice code (Pedersen, 2008) and the two-dimensional lift and drag coefficients for the appropriate Reynolds number from Sheldahl and Klimas (1981) (actually taken from Lazauskas (2004), who corrected anomalies in the original data[1]) are also shown in Figure 4.5, for comparison. We see that the vortex lattice code captured the lift

[1]All the references to Sheldahl and Klimas (1981) in this thesis actually refers to the data taken from Lazauskas (2004)

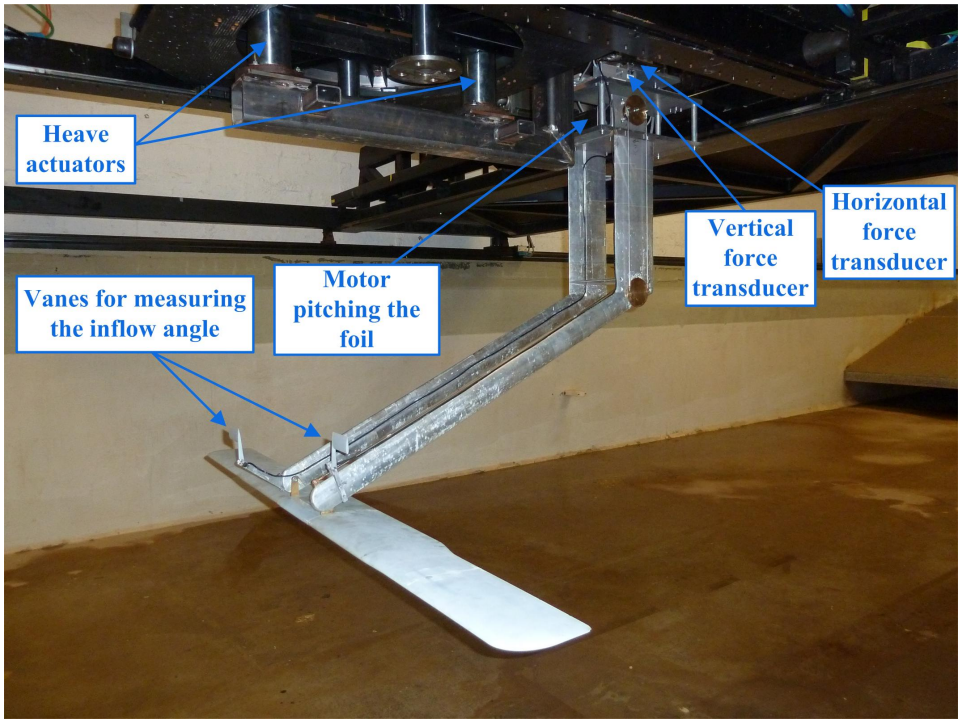

Figure 4.2: Experiment setup for the actively pitch-controlled foil, before the basin was filled with water

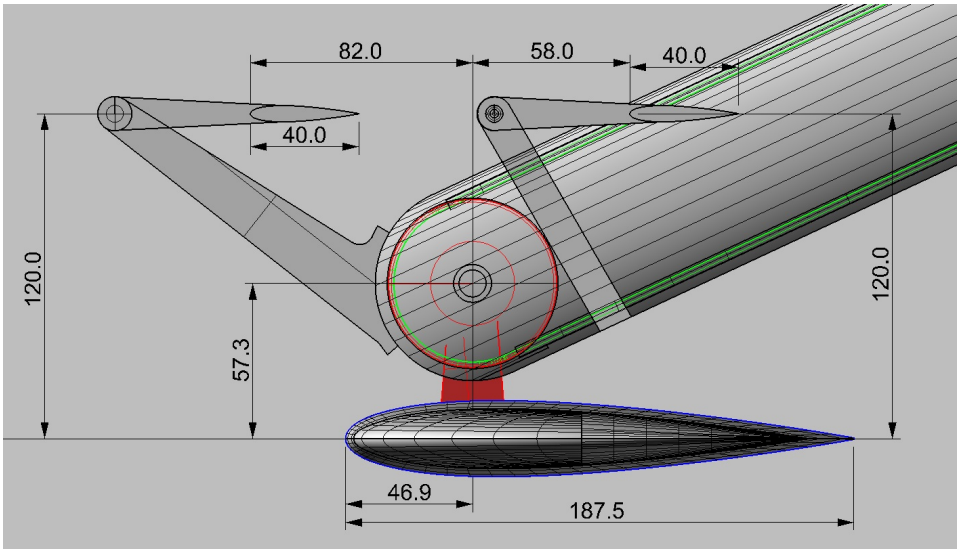

Figure 4.3: 2D CAD drawing of the foil and the vanes, with dimensions in mm. The upstream and downstream vanes were mounted to the starboard and port struts, respectively.

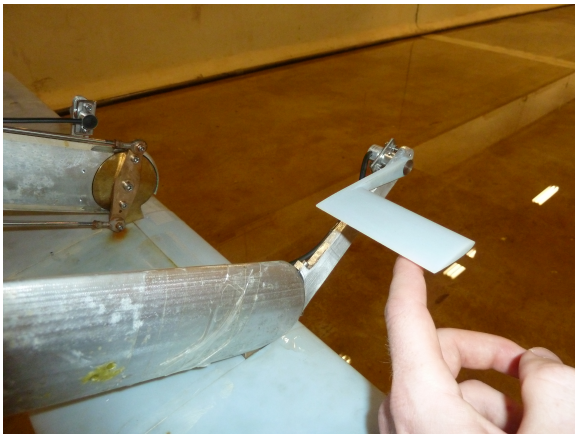

Figure 4.4: Close-up view of the vane on the starboard strut. The vanes would hang down if not supported.

coefficient curve fairly well below stall, whereas the drag coefficient was underestimated by the vortex lattice code, since it did not account for viscous drag. All the foil force coefficient plots in this chapter were corrected for the inertia force on the foil and for hydrodynamic forces on the struts, found from towing the struts without the foil. The hydrodynamic interaction between the foil and the two struts is believed to be the reason why the lift coefficient is not perfectly symmetrical about zero angle of attack. We see that the foil stalled at an angle of attack of about $\pm 12°$, causing a reduction in absolute value of the lift coefficient and a significant increase of the drag coefficient.

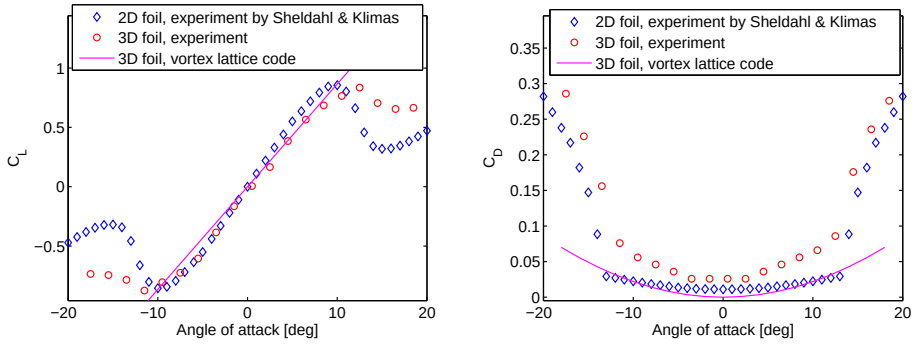

(a) Lift coefficient curve

(b) Drag coefficient curve

Figure 4.5: Lift and drag coefficients. $U = 1.286$ m/s, $Re = 2.0 \times 10^5$.

4.3 Dynamic stall model validation

4.3.1 Pure heave motion with steady forward speed

Simulation results of the dynamic stall model described in Section 3.3 were compared with experimental results. The empirical parameters in the numerical model were tuned based on the experimental results, giving the following parameters: $T_p = 1.5, T_f = 7, \alpha_v = 11^o$, $T_v = 15$ and $\eta_C = 0.95$. For simplicity, the chord lengths along the entire span were assumed to be the same as at the foil center, when calculating the Reynolds number, α_E and τ.

The foil traveled at a constant horizontal speed of $U = 1.286$ m/s, and underwent harmonic heave motion with period $T = 2.375$ s and amplitude $h_A = 0.04$ m. This gives a reduced frequency of $k = 0.193$. α is calculated as, see Figure 4.6,

$$\alpha = \arctan\left(-\frac{\dot{h}}{U}\right) + \delta, \tag{4.1}$$

where $\dot{h}$ is the heave velocity. Figures 4.7a and 4.7b show C_N and C_C vs. α for the foil in pure heave motion with constant pitch, $\delta = 0.5°$. The reason for a nonzero

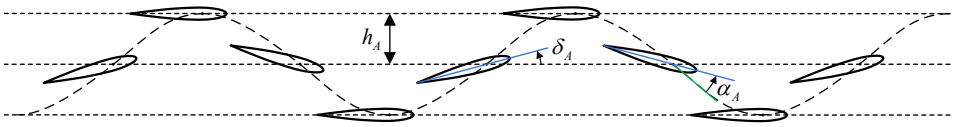

Figure 4.6: A heaving and pitching foil with steady forward speed. h_A is the heave amplitude, δ_A is the pitch amplitude, and α_A is the angle of attack amplitude.

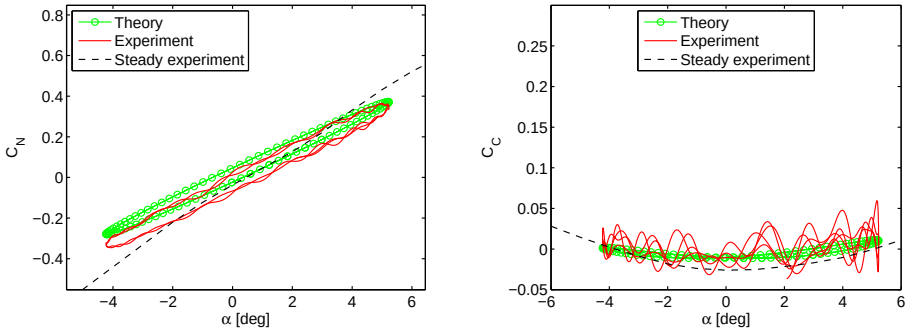

(a) C_N vs. α (b) C_C vs. α

Figure 4.7: C_N vs. α and C_C vs. α for a purely heaving foil with $h_A = 0.04$ m and $k = 0.193$

δ is that, after the experiments were done, the author discovered that what he thought was $\delta = 0°$ was actually $\delta = 0.5°$.

The experimental data signal was filtered using a low-pass filter with cutoff frequency 10 s^{-1}. This filtering was applied for all the experimental results in Section 4.3. The numerical results captures C_N and C_C fairly well, although the C_N values from the experiment are slightly lower than the theoretical values. Note that the experimentally obtained C_C curve is somewhat chaotic, due to the low signal/noise ratio.

4.3.2 Pure pitch motion with steady forward speed

In the following simulations, pure pitch motion about the quarter-chord was assumed and the experiment pitch motion is also referred to as "pure pitch motion". In the experiment, however, the foil pitched about a point located above the chord, as shown in Figure 4.3, so it moved like a pendulum when pitching.

Figure 4.8 shows C_N and C_C vs. α for a purely pitching foil with a constant horizontal speed of $U = 1.286$ m/s and pitch period $T = 1.5$ s. This gives a reduced frequency of $k = 0.305$. In Figure 4.8, $\delta = 3.5^o + 3^o \cos \omega t$. α in this case is given as $\alpha = \delta$.

Figures 4.9 and 4.10 show C_N and C_C vs. α for $\delta = 9.5^o + 5^o \cos \omega t$ and $\delta = 13.5^o + 5^o \cos \omega t$, respectively. Also in Figures 4.9 and 4.10, $U = 1.286$ m/s

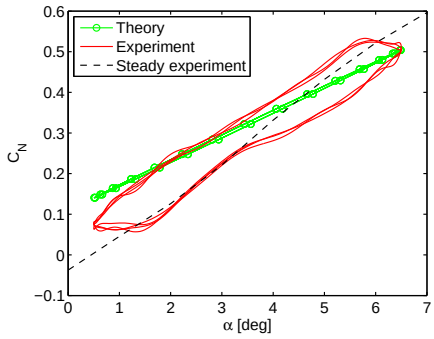

(a) C_N vs. α

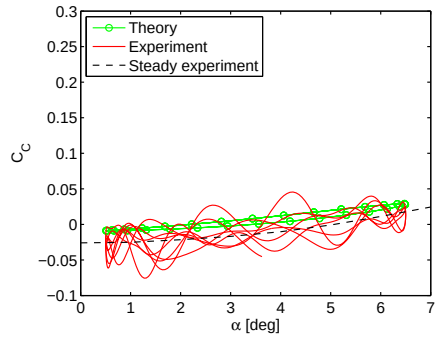

(b) C_C vs. α

Figure 4.8: C_N vs. α and C_C vs. α for a purely pitching foil with $\delta = 3.5^o + 3^o \cos \omega t$ and $k = 0.305$

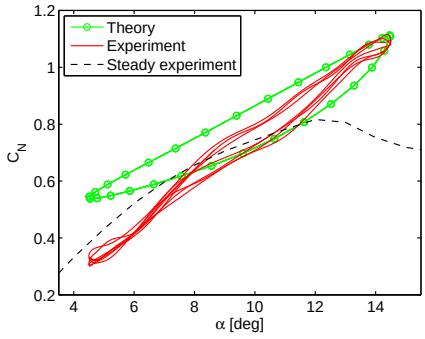

(a) C_N vs. α

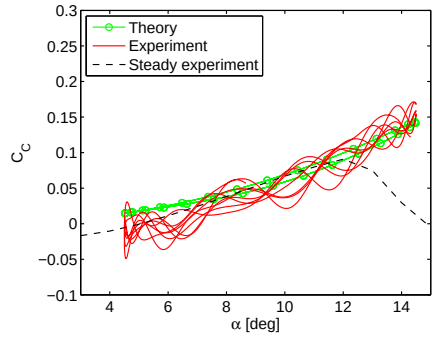

(b) C_C vs. α

Figure 4.9: C_N vs. α and C_C vs. α for a purely pitching foil with $\delta = 9.5^o + 5^o \cos \omega t$ and $k = 0.305$

and $T = 1.5$ s. The agreement between numerical and experimental results is worse for pure pitch motion than for pure heave motion, especially in Figure 4.10. The effect of the pendulum motion on the hydrodynamic foil forces in the pure pitch runs could be the reason for this, although the author attempted to account for this effect by taking the surge motion of the foil into account when calculating the inflow velocity, angle of attack, and added mass force. These considerations had negligible influence on the numerically obtained force, however, and were therefore omitted when generating Figures 4.8-4.10.

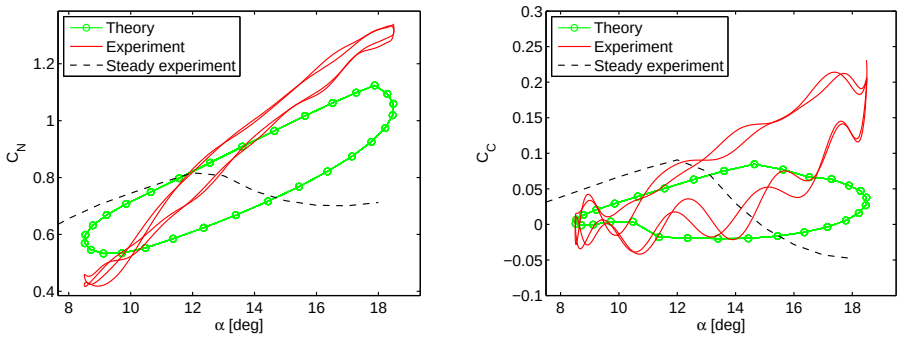

(a) C_N vs. α (b) C_C vs. α

Figure 4.10: C_N vs. α and C_C vs. α for a purely pitching foil with $\delta = 13.5^o + 5^o \cos \omega t$ and $k = 0.305$

4.3.3 Combined heave and pitch motion with steady forward speed

Finally, the dynamic stall model was compared with experiments for combined heave and pitch motion at constant horizontal speed, see Figure 4.6. The horizontal speed was $U = 0.9$ m/s, which was chosen because the runs with combined heave and pitch motion were primarily done to study the effect of dynamic stall on the thrust, see Section 4.4.2, and a lower speed was needed for the foil to stall. The heave amplitude was 0.12 m, and the pitch amplitude was varied in the different runs: $\delta_A = 2°$ in Figure 4.11, $\delta_A = 6°$ in Figure 4.12, and $\delta_A = 10°$ in Figure 4.13. The heave and pitch period, T, was 1.5 s, corresponding to a reduced frequency of $k = 0.436$. The pitch motion was 90 degrees out of phase with the heave motion, so that the foil had zero pitch angle at the bottom and top positions, pitched nose down on its way down and vice versa, as shown in Figure 4.6. We see from Figures 4.11, 4.12, and 4.13 that the agreement between theory and experiment for combined heave and pitch motion is quite good for C_C, and also quite good for C_N in Figure 4.13. The agreement between the theoretical and experimental C_N loops for combined heave and pitch motion appears to improve with increasing pitch amplitudes.

The horizontal force, or thrust, was converted into a force coefficient by dividing the force by $\frac{1}{2}\rho V^2 S$, where S is the projected area of the foil. Table 4.1 shows that the mean horizontal force coefficient, $\overline{C_H}$, peaked for $\delta_A = 6°$ when comparing these three runs, according to experiments, whereas $\overline{C_H}$ was highest for $\delta_A = 10°$ according to the theory. This shows that it is possible to maximize the thrust by adjusting the pitch angle of the foil. The differences between the experimental and theoretical mean horizontal force coefficients are less than 7%. Also shown in Table 4.1 is the mean horizontal force coefficient when two-dimensional quasi-steady theory was used, with no finite-span corrections. In this case, the normal added mass force was ignored. We see that this theory is completely unable to

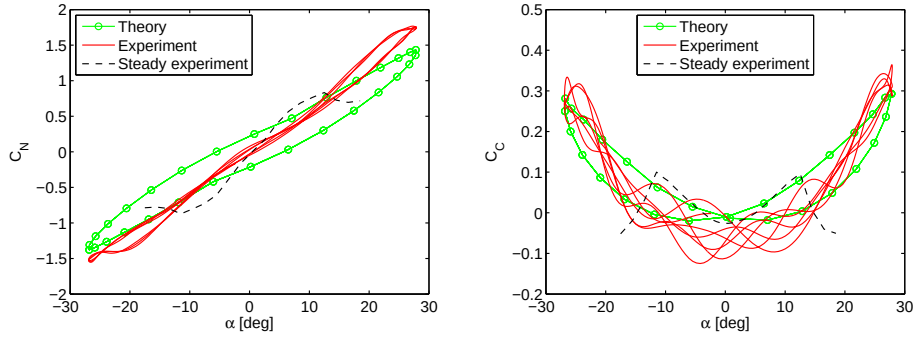

(a) C_N vs. α (b) C_C vs. α

Figure 4.11: C_N vs. α and C_C vs. α for a combined heaving and pitching foil with $\delta = 0.5^o + 2^o \cos\omega t$, $h_A = 0.12$ m, and $k = 0.436$

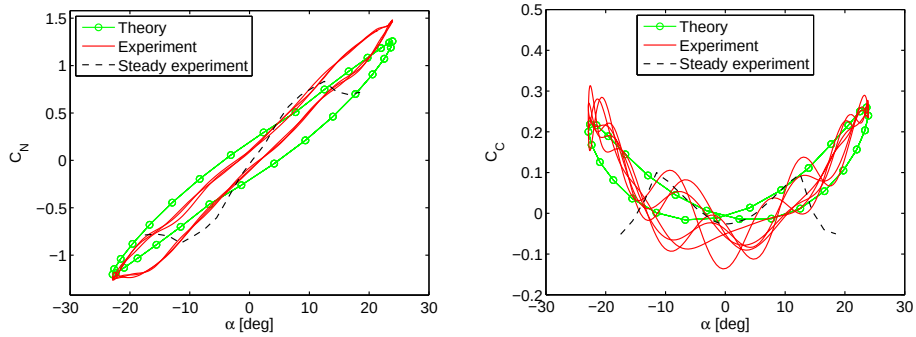

(a) C_N vs. α (b) C_C vs. α

Figure 4.12: C_N vs. α and C_C vs. α for a combined heaving and pitching foil with $\delta = 0.5^o + 6^o \cos\omega t$, $h_A = 0.12$ m, and $k = 0.436$

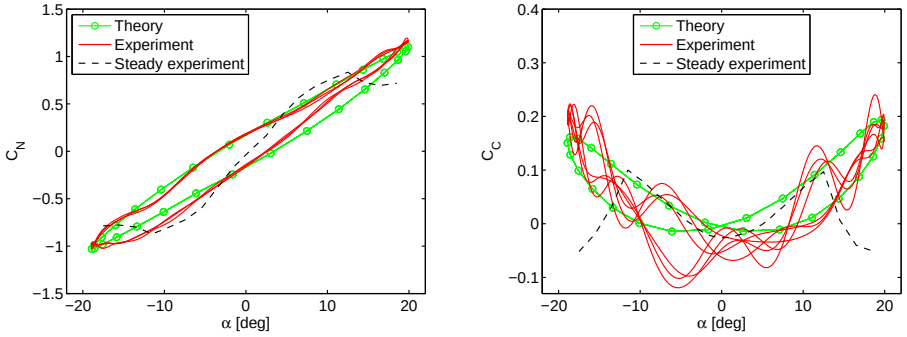

(a) C_N vs. α (b) C_C vs. α

Figure 4.13: C_N vs. α and C_C vs. α for a combined heaving and pitching foil with $\delta = 0.5^o + 10^o \cos\omega t$, $h_A = 0.12$ m, and $k = 0.436$

reproduce the experimental results, primarily due to the calculated drag force. Applying finite-span corrections will make the mean horizontal force coefficient even smaller.

	$\overline{C_H}$, experiment	$\overline{C_H}$, theory	$\overline{C_H}$, 2D quasi-steady theory
$\delta_A = 2°$	0.1620	0.1548	-0.0196
$\delta_A = 6°$	0.1865	0.1746	-0.0071
$\delta_A = 10°$	0.1791	0.1784	0.0113

Table 4.1: Mean horizontal force coefficients, $\overline{C_H}$, for combined harmonic heave and pitch motion

4.4 Forced harmonic heave and pitch oscillations

The foil was made to oscillate harmonically in heave and pitch while traveling at steady forward speeds of 0.7 m/s, 0.9 m/s, and 1.286 m/s. The two lower speeds were chosen so that pitching the foil would have a significant effect on the foil thrust. The heave amplitude was 0.12 m (limited by the experiment setup) and the heave period was 1.5 s. Again, the pitch motion was leading the heave motion with a 90-degree phase angle, so that the foil pitched nose-down when heaving downward and nose-up when heaving upward.

The Strouhal number, St, is a key parameter in oscillating foil propulsion due to its importance for the thrust-producing jet behind the foil, as noted by Triantafyllou et al. (1991, 1993). For oscillating foils, it is defined as

$$St = \frac{\omega A}{\pi U}, \tag{4.2}$$

where A is the width of the wake. In oscillating foil propulsion, the distance traveled by the trailing edge is commonly used for the width of the wake. The Strouhal number is denoted St if the double heave amplitude is used as the width of the wake and St_{TE} if the trailing edge motion is used. Triantafyllou et al. (1991, 1993) performed experiments on a foil oscillating in a combined heave and pitch motion, with the pitch motion 90 degrees out of phase with the heave motion, and found the efficiency to peak at a Strouhal number of 0.25. They also noted that fish and cetaceans varying in size from shark and dolphins to goldfish oscillate their tails at Strouhal numbers that lie almost invariably in the 0.25-0.35 range. Triantafyllou et al. (2000) notes, however, that while "the optimum range of Strouhal number – between 0.25 and 0.35 – is found for certain specific profiles used in Triantafyllou et al. (1993); in other cases, different values may be obtained." With $h_A = 0.12$ m and $T = 1.5$ s, we get St values of 0.23, 0.18, and 0.12, for the three speeds used in the present experiments, in increasing order.

4.4.1 Inflow angle measurements

A measured effective inflow angle, $\phi_{E,measured}$, was found by taking the average of the two vane angles. In Figure 4.14, $\phi_{E,measured}$ is shown for forced harmonic heave and pitch motion with $\delta_A = 8°$. Also shown in Figure 4.14 is the quasi-steady inflow angle, ϕ, obtained as

$$\phi = \arctan\left(-\frac{\dot{h}}{U}\right), \tag{4.3}$$

where $\dot{h}$ was defined to be positive when the foil was heaving upward.

A theoretical effective inflow angle, $\phi_{E,theory}$, is also shown in Figure 4.14 for comparison. $\phi_{E,theory}$ is calculated in a similar manner as the effective angle of attack, α_E, is calculated in Eqs. 3.32 and 3.33, i.e.,

$$\phi_{E,theory,n} = \phi_n - X_n - Y_n, \tag{4.4}$$

where subscript n denotes time step n. X and Y are deficiency functions given, similarly to Eqs. 3.34 and 3.35, by

$$X_n = X_{n-1}e^{-b_1\Delta S} + A_1(\phi_n - \phi_{n-1})e^{-b_1\frac{\Delta S}{2}}, \tag{4.5}$$

$$Y_n = Y_{n-1}e^{-b_2\Delta S} + A_2(\phi_n - \phi_{n-1})e^{-b_2\frac{\Delta S}{2}}. \tag{4.6}$$

We see that the measured and theoretical ϕ_E graphs are fairly similar, although the $\phi_{E,measured}$ amplitudes exceeds the $\phi_{E,theory}$ amplitudes somewhat. Note that the theoretical approach is strictly only valid for attached flow. Especially for $U = 0.7$ m/s, separation is very likely to occur. The theoretical approach also assumes that the vortex wake is flat, which is not the case in reality. It appears that the agreement between $\phi_{E,measured}$ and $\phi_{E,theory}$ is best for low δ_A values for all three speeds. The reason for this may be that the wake is flatter for low δ_A values.

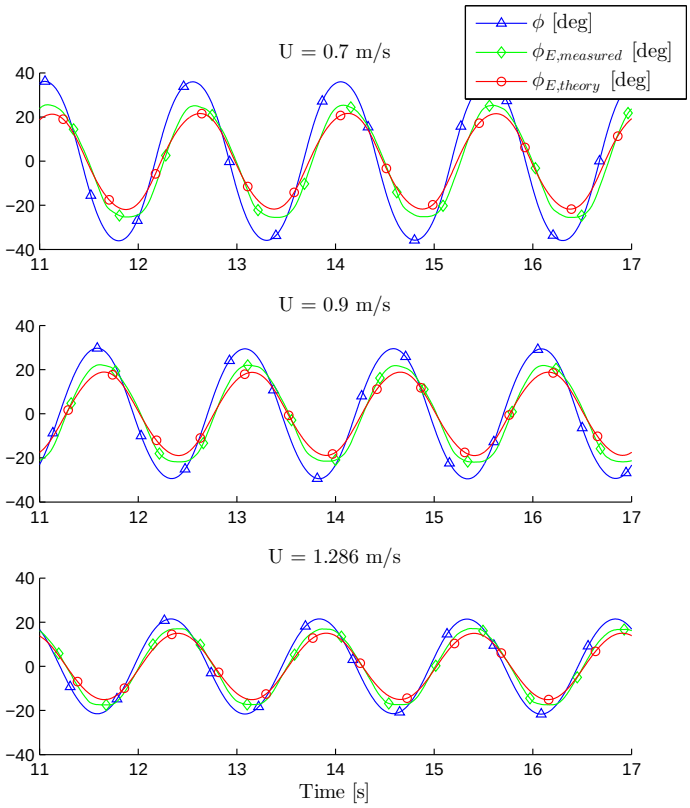

Figure 4.14: Comparison of measured and theoretical inflow angle for forced harmonic heave and pitch motion, $\delta_A = 8°$, $h_A = 0.12$ m, and $T = 1.5$ s.

4.4.2 The effect of pitch amplitude

Figure 4.15 shows the thrust coefficients for varying pitch amplitudes, for the three forward speeds. Larger pitch amplitude means lower angle of attack. We see that there was a pitch amplitude which maximized the thrust, for all the three speeds. For $U = 1.286$ m/s, the thrust coefficient for a non-pitching foil was just slightly lower than the thrust coefficient for a foil with optimal harmonic pitch amplitude. We see that there was not a sudden loss in thrust at a certain pitch amplitude, which one might expect from the shape of the lift and drag coefficient curves, but rather a quite smooth thrust peak.

The measured effective angle of attack, $\alpha_{E,measured}$, was calculated as

$$\alpha_{E,measured} = \phi_{E,measured} + \delta. \tag{4.7}$$

The amplitude of $\alpha_{E,measured}$ is denoted $\alpha_{E,measured,A}$. The theoretical effective angle of attack, $\alpha_{E,theory}$, with amplitude $\alpha_{E,theory,A}$, was calculated using Eqs. 3.32-3.35. Both $\alpha_{E,measured,A}$ and $\alpha_{E,theory,A}$ are given in Figure 4.15 for the pitch amplitudes that gave the highest thrust coefficient values at each forward speed. We see that there are some deviations between $\alpha_{E,measured,A}$ and $\alpha_{E,theory,A}$, especially for $U = 0.7$ m/s, which one might expect since the theory assumes small angle of attack amplitudes.

Table 4.2 gives the thrust coefficient, C_T, power coefficient, C_P, and efficiency, η, of the foil for the pitch amplitudes that gave the highest thrust coefficient values at each forward speed. The reason St_{TE} and St differ by one digit, for $U = 0.7$ m/s and $U = 1.286$ m/s, is slightly inaccurate heave and pitch actuation and rounding of the values. When calculating C_T, C_P, and η, the force on the struts was subtracted from the total force, leaving only the force on the foil alone. The thrust coefficient, C_T, is defined as

$$C_T = \frac{\overline{F_H}}{\frac{1}{2}\rho S U^2}, \tag{4.8}$$

where $\overline{F_H}$ is the average thrust during a cycle. The power coefficient is defined as

$$C_P = \frac{P}{\frac{1}{2}\rho S U^3}. \tag{4.9}$$

P is the average input power during a cycle, given as

$$P = \frac{1}{T}\left(\left|\int_0^T F_V \dot{h} \mathrm{d}t\right| + \int_0^T M\dot{\delta}\mathrm{d}t\right), \tag{4.10}$$

where F_V is the vertical force, M is the moment required to pitch the foil, and $\dot{\delta}$ is the pitch velocity. Unfortunately, M was not recorded in the experiments. Hence, the input power is computed without the last term in the parenthesis in Eq. 4.10. The absolute value sign in Eq. 4.10 is needed to get a positive C_P, because the heave velocity is defined to be positive when the foil is heaving upward, which is when the vertical force points downward and is negative by the present definition. Note that Eq. 4.10 allows for not only an input power to the system, but also

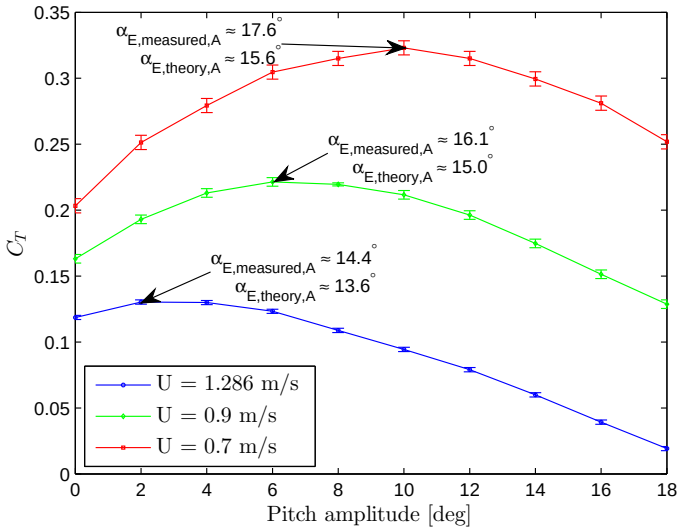

Figure 4.15: Thrust coefficients for forced harmonic pitch motion. $h_A = 0.12$ m and $T = 1.5$ s. Arrows indicate approximate amplitudes (average between trough and crest) of theoretical effective angle of attack amplitude, $\alpha_{E,theory,A}$, and measured effective angle of attack amplitude, $\alpha_{E,measured,A}$.

an output power from the system. This was not possible with the experiment setup, meaning that the calculated efficiency values might be lower in reality. The efficiency of the foil is found from

$$\eta = \frac{C_T}{C_P}. \tag{4.11}$$

U [m/s]	**St**	**$\mathbf{St_{TE}}$**	**δ_A [°]**	**$\mathbf{C_T}$**	**$\mathbf{C_P}$**	η
0.7	0.23	0.24	10	0.32	0.70	0.46
0.9	0.18	0.18	6	0.22	0.48	0.46
1.286	0.12	0.13	2	0.13	0.28	0.47

Table 4.2: Thrust coefficient, power coefficient, and efficiency for the most thrust-producing runs at each forward speed with forced harmonic pitch motion

The error bars in Figures 4.15, 4.16, 4.18, and 4.21 give a 95% confidence interval of the precision error. The thrust coefficients in these figures are calculated based on the mean thrust during five oscillations, except for the spring-loaded foil with $U = 1.286$ m/s, where the thrust is the mean thrust during four oscillations, due to short time series.

4.4.3 The effect of phase between heave and pitch

The phase angle between pitch and heave motions was varied for the two cases $U = 1.286$ m/s, $\delta_A = 4°$ and $U = 0.9$ m/s, $\delta_A = 8°$, and the corresponding thrust coefficients are shown in Figure 4.16. We see that for $U = 1.286$ m/s, the foil thrust was relatively independent of the phase angle. For $U = 0.9$ m/s, however, the foil thrust increased significantly with increasing phase angle, until pitch was leading heave with about 134 degrees. The reason for this is that the normal added mass force becomes increasingly important relative to the circulatory lift force as the forward speed decreases, and when the foil is pitching nose-down at its top position and nose-up at its bottom position the normal added mass force contributes positively to the forward thrust.

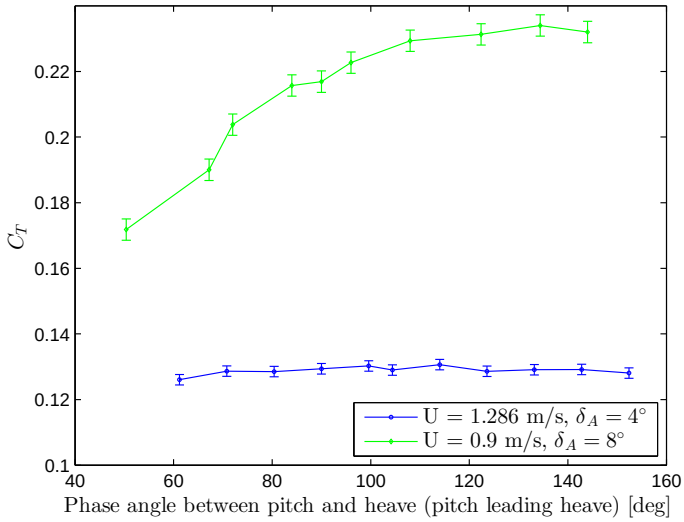

Figure 4.16: The effect of varying phase between pitch and heave. $h_A = 0.12$ m and $T = 1.5$ s.

4.5 Actively pitch-controlled foil

4.5.1 Controlling the foil pitch

The relevant forces and angles of an oscillating foil are shown in Figure 4.17. The normal added mass force is assumed to act at half the chord length from the leading edge. In steady conditions, the lift and drag are assumed to act at the center of pressure, which is x_{cp} from the leading edge. From Figure 4.17 we see that

$$\alpha = \phi + \delta. \tag{4.12}$$

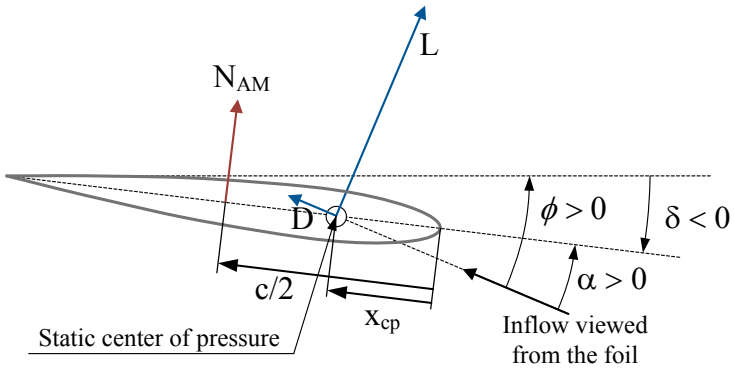

Figure 4.17: Foil forces and angles

As in Politis and Politis (2014) and Belibassakis and Politis (2013), the pitch-controlled angle of attack is taken as a constant times ϕ. This constant is denoted the pitch-control parameter, w_{pc}. The effective inflow angle to the foil, as measured by the small water vanes, is ϕ_E, where ϕ_E is calculated as the average of the two vane angles. A stall criterion can be set so that the angle of attack never exceeds a certain value, α_{max}. The pitch-control algorithm then becomes

$$\delta_{opt} = \begin{cases} -\alpha_{max} - \phi_E, & w_{pc}\phi_E < -\alpha_{max} \\ \phi_E(w_{pc} - 1), & -\alpha_{max} \leq w_{pc}\phi_E \leq \alpha_{max} \\ \alpha_{max} - \phi_E, & w_{pc}\phi_E > \alpha_{max}. \end{cases} \tag{4.13}$$

Results for the pitch-controlled foil with different values of w_{pc} and α_{max} are given in Figure 4.18. A different method of pitch control, using the quasi-steady lift and drag curves to predict the optimal angle of attack and measuring the angle of attack with pressure sensors on the leading edge, is described in Section 5.2.2. This method of pitch control was tested with the foil mounted to the ship model only, and the author have therefore chosen to describe it in Chapter 5, which deals with the ship model tests.

4.5.2 Results

The pitch-controlled foil was also made to oscillate harmonically in heave while traveling at the same steady forward speeds as with forced harmonic pitch motion. The heave amplitude and period were also the same. For the case of active pitch control, the vanes were used to control the foil pitch. It was found that in order to obtain symmetrical pitch about zero, it was necessary to calculate ϕ_E as the average vane angle plus a certain bias. One reason for this is that the weight of the vanes, although low, caused the vanes to hang down when not supported. This would cause the measured angle of attack of the oscillating foil to be slightly asymmetrical.

Figure 4.18 shows the thrust coefficients for varying w_{pc} values for the three different speeds. In order to avoid stall, the maximum angle of attack, α_{max}, was set to be $\alpha_{max} = 13°$ for $U = 1.286$ m/s and $U = 0.9$ m/s, but it was found that $\alpha_{max} = 14°$ gave higher thrust than $\alpha_{max} = 13°$ for $U = 0.7$ m/s. $\alpha_{max} = 50°$ was chosen so that the measured angle of attack would never exceed α_{max}. Note that α_{max} in this context refers to $\alpha_{E,measured}$.

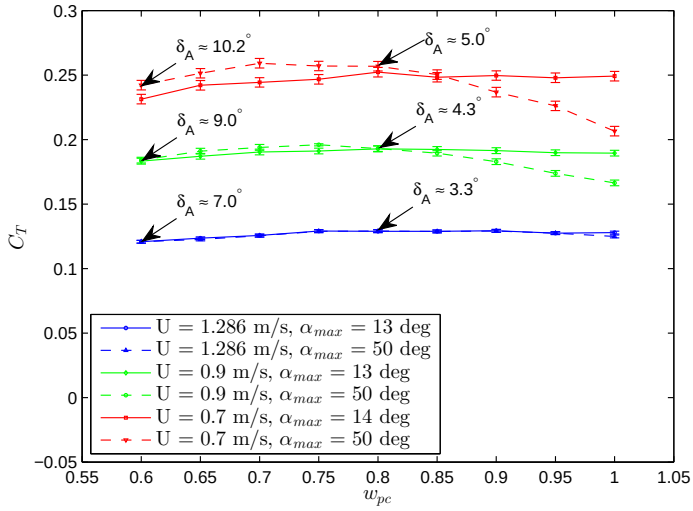

Figure 4.18: Thrust coefficients for controlled pitch motion. Arrows indicate approximate pitch amplitudes for the $\alpha_{max} = 50°$ runs. $h_A = 0.12$ m and $T = 1.5$ s.

We see from Figure 4.18 that the thrust coefficient depended little on the pitch-control parameter, w_{pc}, for the w_{pc} values tested here, when α_{max} was 13° or 14°. For $\alpha_{max} = 50°$, the thrust coefficient was somewhat dependent on w_{pc} for the two lowest speeds. It appears, however, that simply setting α_{max} to 13° or 14° and $w_{pc} = 1$ is a wise choice compared to experimenting with different w_{pc} values, regardless of speed. For lower w_{pc} values than tested here, the foil would have pitched so much that the maximum angle of attack would never have been reached, and the thrust would have decreased.

The maximum thrust coefficient of the pitch-controlled foil was close to the maximum thrust coefficient of the harmonically pitching foil at $U = 1.286$ m/s. As the forward speed decreased, however, the maximum thrust coefficient of the harmonically pitching foil became increasingly higher than the maximum thrust coefficient of the pitch-controlled foil. The reason for this is that the foil's pitch motion was leading the heave motion with down to 49° for the pitch-controlled foil with $U = 0.7$ m/s and $\alpha_{max} = 50°$, and we can see the importance of the phase angle between pitch and heave in Figure 4.16. The phase lag, relative to pitch leading heave with 90 degrees, was mostly due to the effective angle of attack lagging behind the quasi-steady angle of attack, and this effect was detected by the

angle of attack vanes. A small part of this lag was also due to delay in the control system.

4.6 Spring-loaded foil

4.6.1 Experiment setup

The foil rig was modified for the purpose of supporting a spring-loaded foil, see Figure 4.19. The spring-loaded foil was pivoting about a point 26 mm, i.e. $0.14c$, from the leading edge, at the chord line. The spring consisted of a 3 mm diameter piano wire attached to the foil at the pivot point like a cantilever beam. The piano wire was clamped to an aluminum plate on the strut, shown in Figure 4.19, by a magnet connection and a spherical joint so that it could slide and rotate freely. When the foil was pitched, the piano wire would bend, producing a spring moment, M_{spring}, trying to pitch the foil back into its equilibrium position, see Figure 4.20. By changing the position of the magnet clamp, the length of the piano wire cantilever beam would change – in other words, the spring stiffness would change. A waterproof potentiometer at the pivot point measured the foil pitch directly.

Table 4.3 lists the distance from the spring clamp to the pivot point of the foil, marked as d in Figure 4.20. The theoretical spring stiffness, i.e., the required moment in Nm to pitch the foil one degree, is also given. This theoretical spring stiffness was calculated using classical beam theory, assuming zero friction in the system. The spring stiffness was also measured (linear regression through four data points of applied moment and measured foil pitch) when the spring clamp was in position 3 and 4 from the foil. These two measured spring stiffness values are also given in Table 4.3, and they are more than twice the theoretical value, probably due to friction at the pivot point and at the spherical joint at the clamp. Because the spring stiffness was only measured at two spring clamp positions, the theoretical spring stiffness is used as the x-axis in Figure 4.21.

4.6.2 Results

Also for the spring-loaded foil, the foil was made to oscillate harmonically in heave with the same heave amplitude and period as with forced harmonic pitch, while traveling at steady forward speed. The thrust coefficients of the spring-loaded foil for the same three forward speeds as previously tested are shown in Figure 4.21. With the softest spring, the pitch crests were higher than the troughs were deep – see Figure 4.22, which illustrates the clearest case – but with a stiffer spring, the pitch time history was more symmetrical about zero. As with the results for the pitch-controlled foil, the horizontal force on the struts alone was subtracted from the measured force on the foil rig. A higher spring clamp position number gave a softer spring and larger pitch amplitudes. We see that, as was the case with forced harmonic pitch motion, the optimal pitch amplitude increased as the forward speed decreased. The maximum thrust coefficient measured for the spring-loaded foil for $U = 1.286$ m/s was smaller than the maximum thrust coefficient measured for the

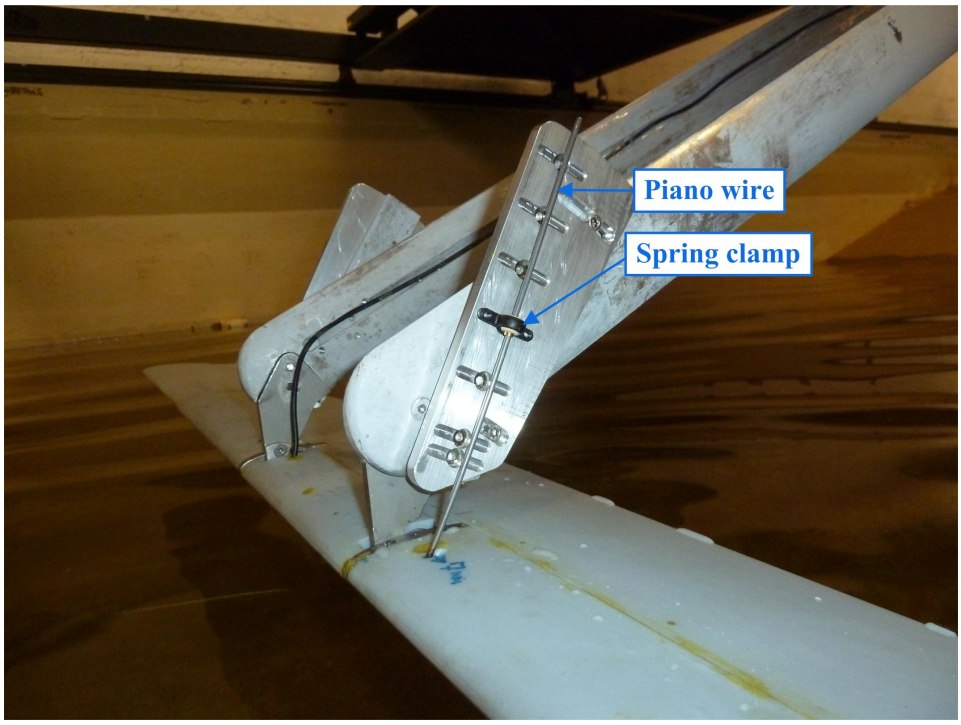

Figure 4.19: Experiment setup for the spring-loaded foil, with the basin half full of water

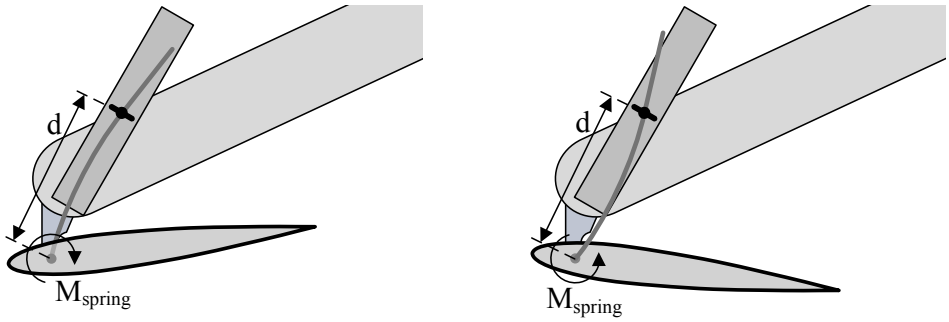

Figure 4.20: Principle drawing of the spring mechanism

Spring clamp position (counted from the foil)	**Distance from spring clamp to foil pivot point (d) [m]**	**Theoretical spring stiffness [Nm/deg]**	**Measured spring stiffness [Nm/deg]**
1	0.06	0.69	-
2	0.07	0.59	-
3	0.10	0.42	0.88
4	0.13	0.32	0.82
5	0.16	0.26	-
6	0.19	0.22	-
7	0.22	0.19	-

Table 4.3: Spring stiffness, i.e., required moment in Nm to pitch the foil one degree

same speed with forced harmonic pitch motion and with actively controlled pitch motion. For both $U = 0.9$ m/s and $U = 0.7$ m/s, however, the maximum measured thrust coefficient was higher for the spring-loaded foil than with forced harmonic pitch motion where pitch was leading heave with 90 degrees, and much higher than for the pitch-controlled foil. Also shown in Figure 4.21 are $\alpha_{E,theory,A}$ values for the spring clamp positions that gave the highest thrust coefficient values. The spring-loaded foil rig had no vanes measuring the inflow angle, which is the reason why there are no $\alpha_{E,measured,A}$ values given in Figure 4.21.

The reason why the spring-loaded foil performed better than the foil with forced harmonic pitch motion and with actively controlled pitch motion for low forward speeds appears to be the phase between heave and pitch, as explained in Section 4.4.3. Figure 4.23 shows the foil pitch and the foil forces, after subtracting the strut force, for the spring-loaded foil, with the spring clamp in position 7, and the pitch-controlled foil, with $w_{pc} = 0.7$ and $\alpha_{max} = 50°$, for $U = 0.7$ m/s. The resultant foil force is drawn at the quarter-chord for simplicity, although it may attack at other positions in reality. The pitch-controlled foil was tilting nose-up at the top position and nose-down at the bottom position, causing the normal added mass force to act against the direction of travel. The spring-loaded foil, however, was tilting slightly nose-down at the top position and slightly nose-up and the bottom position, causing the normal added mass force to act slightly in the direction of travel at these positions. Such a pitch motion resulted in much larger forward thrust than the angle-of-attack-based controlled pitch motion, probably due to the more advantageous direction of the normal added mass force through the whole oscillation cycle. According to Lighthill (1970), aquatic animals are well aware of this effect: "... the 'good hydromechanical shapes' seem to be precisely those which are able to improve greatly their propulsive efficiency η by utilizing this virtual-mass effect."

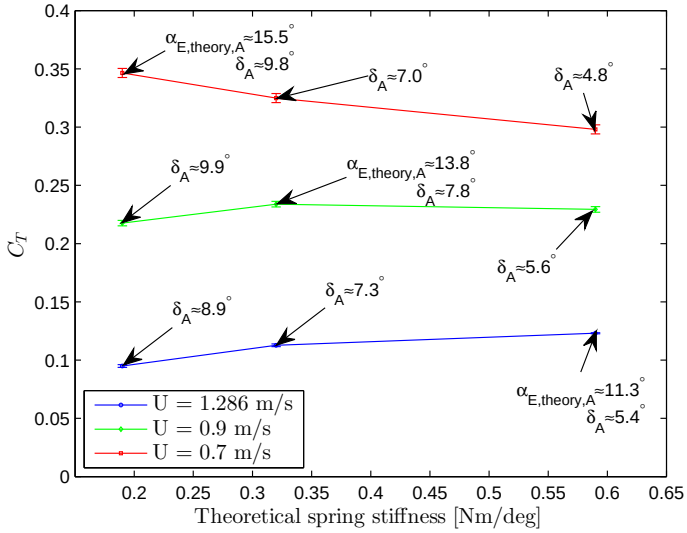

Figure 4.21: Thrust coefficients for the spring-loaded foil. Arrows indicate approximate pitch amplitudes (average between trough and crest) and approximate amplitudes of theoretical effective angle of attack, $\alpha_{E,theory,A}$. $h_A = 0.12$ m and $T = 1.5$ s.

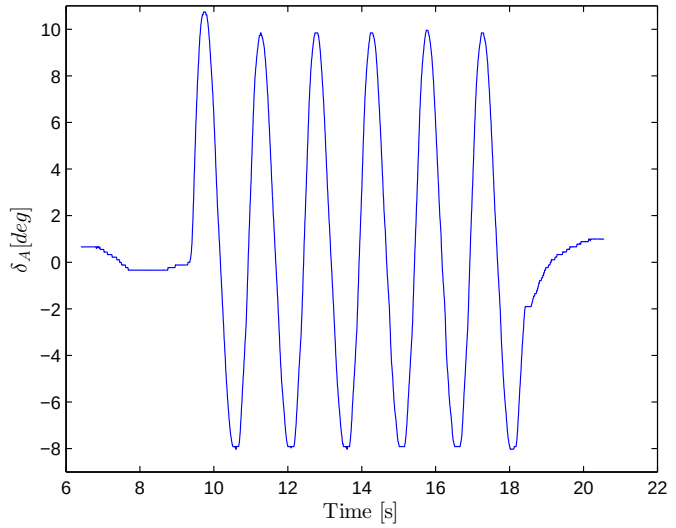

Figure 4.22: Time history of the foil pitch, δ_A, for $U = 1.286$ m/s, with the softest spring (spring clamp in position 7 from the foil). $h_A = 0.12$ m and $T = 1.5$ s.

In Figure 4.23, pitch was leading heave with 97 degrees for the spring-loaded foil, and 56 degrees for the pitch-controlled foil, although neither of the pitch motions were perfectly sinusoidal. The pitch-controlled foil was little influenced by the normal added mass force, since the vanes pitched about a point located far forward of their leading edges. As the ratio between circulatory lift and normal added mass force increased with increasing forward speed, the pitch-controlled foil performed better relative to the spring-loaded foil.

As for the runs with forced harmonic pitch motion, the thrust coefficient, power coefficient, and efficiency were calculated for the spring-loaded foil runs with the highest thrust coefficient values at each forward speed, in Table 4.4. In Tables 4.2 and 4.4, the η values given may differ by one digit from the values obtained using the given C_T and C_P values due to rounding. We see that for $U = 0.9$ m/s and $U = 1.286$ m/s, the efficiencies were clearly higher for the spring-loaded foil than for the foil with forced harmonic pitch motion, due to lower input power. For $U = 0.7$ m/s, both C_T and C_P were higher for the spring-loaded foil, resulting in approximately equal η. If it had been possible to measure M in Eq. 4.10, the efficiencies with forced harmonic pitch motion would have been even lower.

U [m/s]	**St**	**St_{TE}**	**Spring clamp position (counted from the foil)**	**C_T**	**C_P**	η
0.7	0.23	0.24	7	0.35	0.73	0.47
0.9	0.18	0.18	4	0.23	0.44	0.53
1.286	0.12	0.13	2	0.12	0.21	0.58

Table 4.4: Thrust coefficient, power coefficient, and efficiency for the most thrust-producing runs at each forward speed with spring-loaded pitch motion

4.7 Discussion

For both forced harmonic pitch motion and spring-loaded pitch motion, the effective angle of attack – and therefore also the quasi-steady angle of attack – that gave the highest thrust coefficient increased with decreasing forward speed. This implies that the foil could sustain stall for higher angles of attack when the reduced frequency was increased, which is as expected.

The efficiencies calculated for the foil with forced harmonic pitch motion leading the harmonic heave motion with a phase angle of 90 degrees were virtually independent of the Strouhal number. For the spring-loaded foil, however, the efficiency increased with decreasing Strouhal number. As shown by Anderson et al. (1998), the shape of η vs. St curves are very dependent on the foil's pitch amplitude and phase relative to the heave motion.

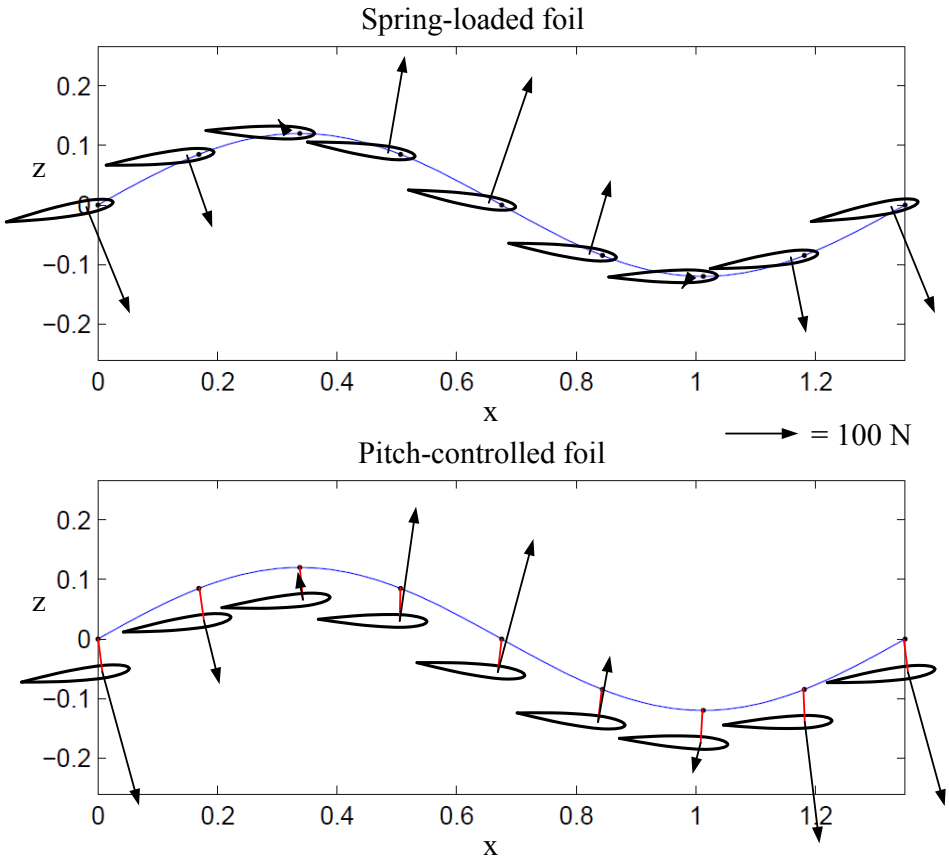

Figure 4.23: Comparison of foil pitch and forces for the spring-loaded foil, with the spring clamp in position 7 from the foil, and the pitch-controlled foil, with $w_{pc} = 0.7$ and $\alpha_{max} = 50°$, for $U = 0.7$ m/s. $h_A = 0.12$ m and $T = 1.5$ s. The spring-loaded foil pitched about a point located at the chord line, whereas the pitch-controlled foil pitched above a point located above the chord line, as shown in the figure by the red line from the foil to the sine curve.

For a harmonically heaving foil, the quasi-steady angle of attack can be expressed as

$$\alpha(t) = -\arctan(\pi St \cos(\omega t)) + \delta, \tag{4.14}$$

through Eq. 4.1 and expressing the heave amplitude with the Strouhal number, using the double heave amplitude as the width of the wake in Eq. 4.2. Because the angle of attack is expressed by an arctan function with St in the argument, the time history of the angle of attack will be further from harmonic, for harmonic heave and pitch, as St increases (Hover et al., 2004). This is also clear from Figure 4.24, which shows the angle of attack time histories for the most thrust-producing runs at each forward speed, with forced harmonic pitch leading heave with a 90-degree phase angle. Also shown in Figure 4.24 are equivalent harmonic angle of attack time histories. We see that even for the highest Strouhal number, $St = 0.23$, the angle of attack time history is fairly close to being harmonic.

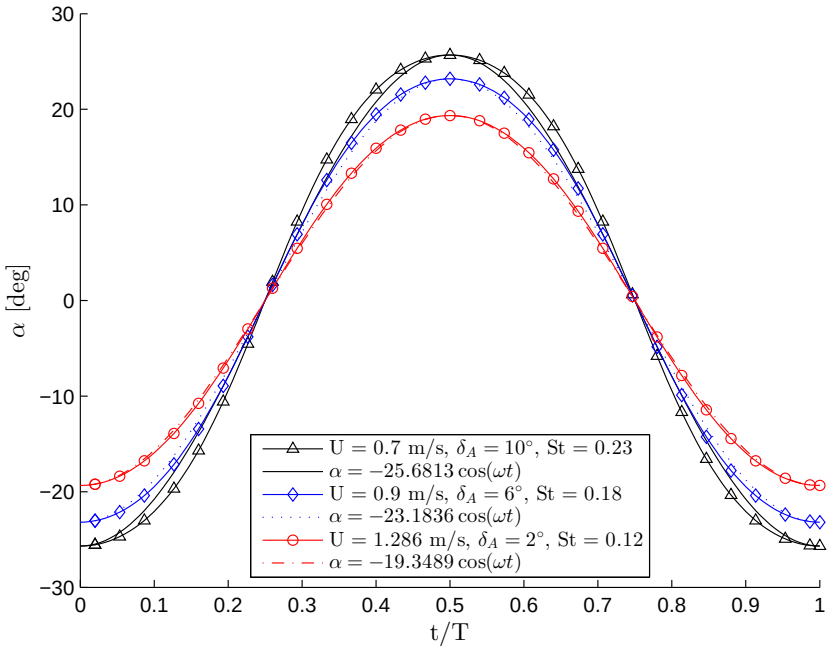

Figure 4.24: Angle of attack vs. time graphs for the most thrust-producing runs at each forward speed, with forced harmonic pitch leading heave with a 90-degree phase angle, compared with their harmonic equivalents

Hover et al. (2004) specified the maximum quasi-steady angle of attack, α_{max}, and adjusted the heave motion to produce four different angle of attack shapes. For harmonic heave and pitch, with the pitch motion leading the heave motion with a 90-degree phase angle, Figures 4.25 and 4.26 show the highest C_T value from the present work and the corresponding η compared with the results in Hover et al.

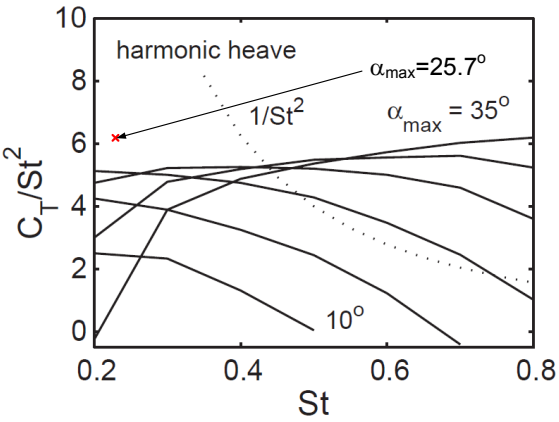

Figure 4.25: The highest C_T with forced harmonic pitch in the present experiments marked with a cross in Figure 5a from Hover et al. (2004). The graphs are for α_{max} values from 10° to 35° in steps of 5°.

(2004). We see that the maximum C_T and the corresponding η in the present work are higher for the same St and α_{max} than the results in Hover et al. (2004). This is probably due to the Reynolds number being approximately 200,000 in the present experiment and 30,000 in Hover et al. (2004).

The thrust coefficient of the pitch-controlled foil depended surprisingly little on the pitch-control parameter, w_{pc}, but there was an optimal w_{pc} value which maximized the thrust coefficient for all forward speeds tested. Setting a limit on the maximum angle of attack had only a significant effect when w_{pc} was very large, i.e., when the foil was close to not pitching except when the maximum angle of attack was exceeded.

Although only three different spring clamp positions were tested, it appears that the pitch amplitudes giving the highest thrust coefficients for the spring-loaded pitch motion are close to the pitch amplitudes giving the highest thrust coefficients for the forced harmonic pitch motion. A good hydrodynamic model of the foil forces should be able to calculate the spring-stiffness which would give the desired pitch amplitude. On the other hand, if one had such a model available, one could have used the model directly to find the spring stiffness giving the highest thrust coefficient. Another approach is to find the optimal effective angle of attack amplitude from Figure 4.15 and tune the spring stiffness to obtain this for a spring-loaded foil, using vanes for measuring the inflow angle. For a ship employing the foil for propulsion, it is also possible to optimize the spring stiffness by measuring the foil thrust directly, or simply the speed of the ship.

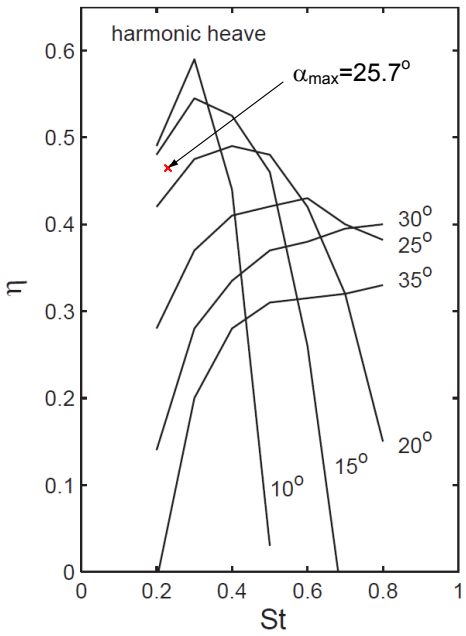

Figure 4.26: η for the highest C_T case with forced harmonic pitch in the present experiments marked with a cross in Figure 6a from Hover et al. (2004). The numbers next to the graphs indicate α_{max} values.

Chapter 5

The effect of a wavefoil on a platform supply vessel

In this chapter, the effect of a wavefoil on a platform supply vessel of the Rolls-Royce UT 751 E design, see Figure 5.1, is examined through simulations and model tests. Two rounds of model tests were done with a 1:16 scale model of the vessel: the first in March 2012 and the second in September 2013, both in the towing tank at the Marine Technology Center in Trondheim, Norway. For more information on the towing tank, see Appendix C.2. The purpose of both rounds of testing was to test the effect of a fixed and an actively controlled wavefoil on the ship model. The location of the foil relative to the ship was the same in the March 2012 and the September 2013 tests, but the foil actuation and pitch-control mechanism were different.

In both the March 2012 and the September 2013 tests, the foil pitched about a wheel located above the the foil, see Figure 4.3. In the March 2012 test, this wheel was actuated via a wire running from the wheel to a motor located above the struts, see Figure 5.2. Although the wire was tightened as much as possible, there was an inherent elasticity in the system. When the motor was supposed to keep the foil fixed, the foil could quite easily be pitched a few degrees by applying hand force on it. Therefore, the wire was replaced with much more rigid rods before the tests that are described in Chapter 4 were done, which improved the foil actuation tremendously.

In the March 2012 test, the leading edge of the foil was equipped with five pressure sensors, see Figure 5.9. These pressure sensors were used to estimate the foil's angle of attack, as explained in Section 5.2.2. Due to a dysfunctional pressure sensor in a test of the foil alone in February 2013 and a desire to measure the angle of attack more directly, the pressure sensor approach to pitch control was abandoned. In the September 2013 test, two vanes were used to measure the inflow angle and thereby estimate the angle of attack, as explained in Chapter 4.

When designing a wavefoil for the Rolls-Royce UT 751 E design, several aspects were taken into consideration. Naito and Isshiki (2005) showed that the wavefoil thrust was highest, of the three wavelengths they studied, when the wavefoil was

located slightly in front of the bow. The foil should be retractable to reduce the calm water resistance. It may also be desirable to retract the foil to protect it in extremely high waves. The intention behind the wavefoil arrangement chosen, shown in Figure 5.2, was to place the foil at a longitudinal position where it would provide large thrust while at the same time allowing for easy retraction by means of the swing-arm mechanism described in Section 4.1.

In its deployed position in full scale, the foil was located 8.761 m below the baseline of the ship, with the quarter-chord located 79.005 m ahead of the aft perpendicular. Placing the foil this far below the hull also greatly reduces the risk of foil slamming. The main particulars of the ship and foil in full and model scales are given in Tables 5.1 and 5.2.

Figure 5.1: The ship used to study the effect of wavefoils: *Far Searcher*, a platform supply vessel of the UT 751 E design. Photo: https://www.farstad.com/fleet/psv-vessels/psv-fleet-list/far-searcher.

Main particulars	**Full scale**	**Model scale**
Waterline length (L_{WL})	90.144 m	5.634 m
Length between perpendiculars (L_{PP})	80.800 m	5.050 m
Beam	21.000 m	1.313 m
Draft used in model tests	4.300 m	0.269 m
Wetted surface area	1865 m^2	7.284 m^2
Displaced volume	4917 m^3	1.201 m^3

Table 5.1: Main particulars of the Rolls-Royce UT 751 E design, in full and model (1:16) scales

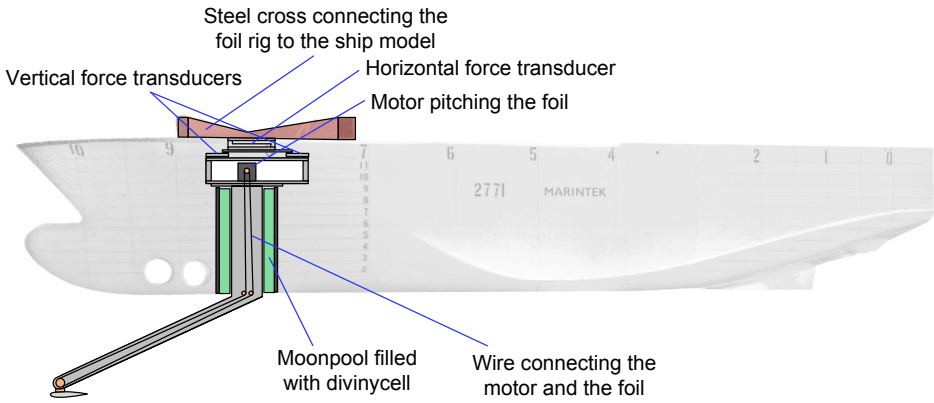

Figure 5.2: The ship model with the foil rig used in the March 2012 test

Main particulars	Full scale	Model scale
Profile	NACA 0015	NACA 0015
Span	28.96 m	1.81 m
Maximum chord	3 m	0.1875 m
Projected area	82 m^2	0.320 m^2
Aspect ratio	10.24	10.24

Table 5.2: Main particulars of the foil used in the simulations and model tests

5.1 Fixed foil

5.1.1 VeSim implementation

The effect of fixed horizontal foils mounted to a ship was implemented in the time-domain MARINTEK Vessel Simulator (VeSim). The user inputs the longitudinal position of the quarter-chord relative to the aft perpendicular (AP), the vertical position of the foil relative to the baseline of the ship, the transverse position of the root and tip of the foil relative to the centerline of the ship, and the chord lengths at the root and tip of the foil. A trapezoidal planform of the foil was assumed. The foil was divided into 10 sections (or strips) of equal width, from the root to the tip. A single foil was composed of two foils, i.e., a starboard foil and a port foil, with adjacent roots.

Fluid velocities parallel and perpendicular to the foil at the $^3/_4$-chord location, and accelerations perpendicular to the foil at the midchord, were obtained at the spanwise center of each section, through linear interpolation between the values at the foil root and tip. The quasi-steady angles of attack for all sections were calculated from these velocities. The effect of the ship hull on the inflow (caused by the wave and ship motions) to the foil was not included in the wavefoil implementation in VeSim. Not including this effect is non-conservative, since the hull generally will reduce the inflow angles to the foil and therefore decrease the foil thrust. The

influence of the free surface on the wavefoil forces was also not included in VeSim. As already mentioned, if the foil is located deeper than two chord lengths from the free surface, the influence of the free surface on the wavefoil is negligible (Wu, 1972).

Dynamic foil forces were calculated using the dynamic stall model described in Section 3.3. Simulating many different wave conditions in real-time or faster was desired, and using a dynamic stall model to calculate the foil forces seemed like a good compromise between speed and accuracy. If, for instance, a panel method had been used to calculate the foil forces, stall could not have been studied, and the simulations would have been more time consuming. Using normal and chordwise forces, instead of lift and drag, is very convenient in the case of fixed foils since VeSim requires the forces acting on the ship to be given in the ship-fixed reference frame.

5.1.2 Model test setup

The same force transducer setup as described in Chapter 4 was used in both the March 2012 and the September 2013 tests. As shown in Figure 5.2, the struts supporting the foil went through a moonpool in the ship model, which was partly filled with divinycell to reduce the moonpool area to a minimum. The foil rig was connected to the ship hull via the red steel cross visible in Figures 5.2 and 5.3. The ship model was towed from wires attached to an aluminum beam, which was mounted perpendicular to the hull, as shown in Figure 5.3. This enabled the ship to move freely in heave and pitch, while constrained in yaw. The surge motion of the model was limited by springs connecting the towing wires to the towing tank carriage.

Originally, the model was supposed to be exposed to head sea regular waves with full-scale wave height 3 m, and full-scale wave periods ranging from 6.5 s to 11.5 s. The actual waves generated were, however, somewhat different, and are given in Table 5.3. To compare model tests and simulations, the same wave conditions were used in the simulations. The ship model was also tested in the same conditions without the foil in order to separate out the effect of the foil.

T [s]	**H [m]**
11.499	2.958
10.513	3.027
9.505	2.911
8.505	3.002
7.504	3.518
6.508	2.973

Table 5.3: Wave periods (T) and heights (H) used in the model tests and simulations, found from surface elevation measurements

Figure 5.3: The setup in the March 2012 towing tank test

5.1.3 Comparison of simulation and experiment

Comparisons of the simulated and experimentally determined ship resistance, foil thrust, and vessel RAOs in heave and pitch are shown in Figure 5.4, for the full scale ship sailing at 12 knots. It is clear that the foil reduced the ship resistance and motions significantly. The agreement between simulated and experimental results is reasonably good for the foil thrust, heave RAO, and pitch RAO, but not so good for the ship resistance. We see that for a wave period of 7.5 s, which is the wave period where the ship motions were most violent, there is a considerable difference in the simulated and experimentally determined ship resistance and heave RAO for a ship without foil. For this wave period, the ship without foil moved so violently (see Figure 5.15) that assuming non-breaking waves, which is done in VeSim, is not recommended and likely to cause deviation between simulated and experimental results.

To compare the simulations, which were done in full scale, with the model tests, the experimentally determined ship resistance and foil thrust were directly Froude-scaled to full scale. A model scale force, F_M, is Froude-scaled to its full scale value, F_S, by

$$F_S = \frac{\rho_S}{\rho_M}\lambda^3, \tag{5.1}$$

where ρ_S and ρ_M are the mass densities of sea water and fresh water, respectively, and λ is the scale factor – in this case, 16.

Because lift and drag coefficients of a foil section depend strongly on the Reynolds

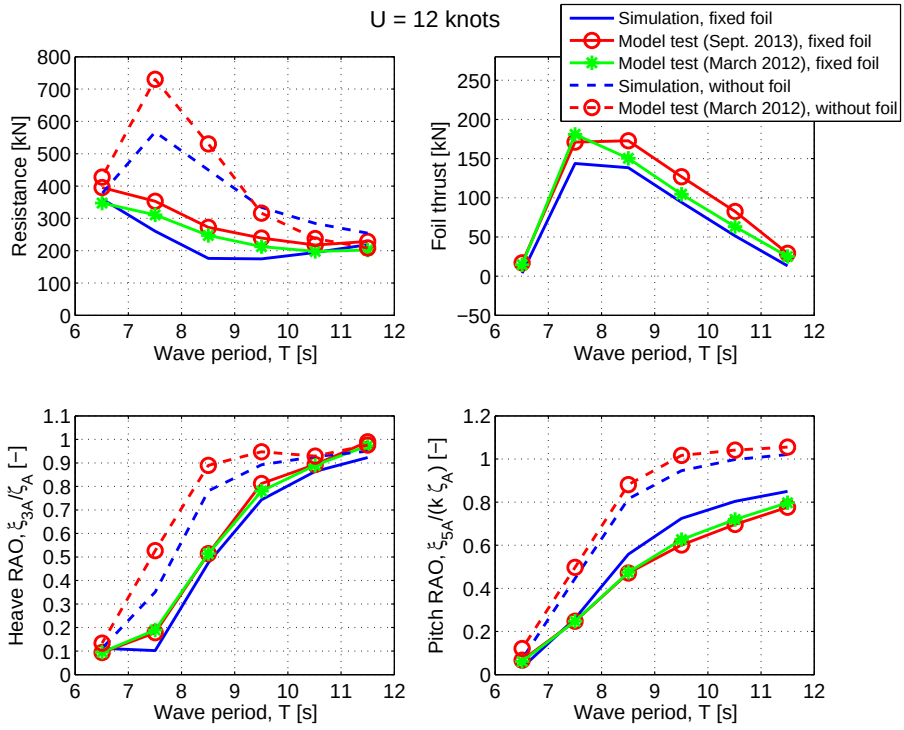

Figure 5.4: Simulation vs. experiment results for regular head sea waves and a forward speed of 12 knots

number, Re, model scale Re was used in the simulations. VeSim needs the calm water resistance graph as input. The experimentally determined calm water resistance graph, directly Froude-scaled to full scale, was used as VeSim input, to obtain the same ratio between horizontal and vertical forces in model and full scale, which is important when comparing the ship motions. Since the frictional resistance coefficient is less in full scale than in model scale, Froude-scaling the resistance directly implies that the resistance is overpredicted in full scale. Therefore, in reality, the foil thrust would be larger compared to the ship resistance in full scale, than what is indicated by Figure 5.4. If only an estimate of the full-scale calm water resistance was desired, the model-scale calm water resistance would have been scaled according to standard procedures (i.e., scaling viscous resistance and wave resistance differently – see for instance Faltinsen (2005)). Furthermore, the simulated ship was towed by a simulated spring system, similar to the one used in the model tests, with the model scale spring stiffness Froude-scaled to full scale.

The forces on the struts were not modeled in VeSim, so the struts' influence on the simulated ship motions was neglected. To compare the simulated and experimentally determined ship resistance and foil thrust, the strut resistance in the September 2013 test were Froude-scaled to full scale and added to the simulated

ship resistance and subtracted from the simulated foil thrust. This was necessary because the force sensor measuring the foil thrust in the experiment was located above the struts – as shown in Figure 5.2 – and therefore measuring also the force on the struts.

Both results from the March 2012 and the September 2013 tests with a fixed foil are shown in Figure 5.4. In September 2013, the calm water resistance was measured with the foil fixed but not without the foil, whereas in March 2012, the calm water resistance was measured only without the foil. At a speed of 12 knots, the calm water resistance without foil was 197 kN, Froude-scaled to full scale, and 254 kN with foil (in the September 2013 test). From testing the foil alone it was found that the strut resistance was 2.3 times higher in the September 2013 test than in the March 2012 test, at 10 knots. Calm water resistance graphs without foil (March 2012) and with fixed foil (September 2013) are shown in Figure 5.5. The reason for the difference in calm water resistance is that the rods pitching the foil in the September 2013 test ran along and outside the port strut (this can be seen in Figure 4.4), whereas the wire pitching the foil in the March 2012 test ran inside the port strut. In addition, the vanes used for pitch control in the September 2013 test contributed with some resistance. The extra strut resistance is clear from both Figures 5.4 and 5.5.

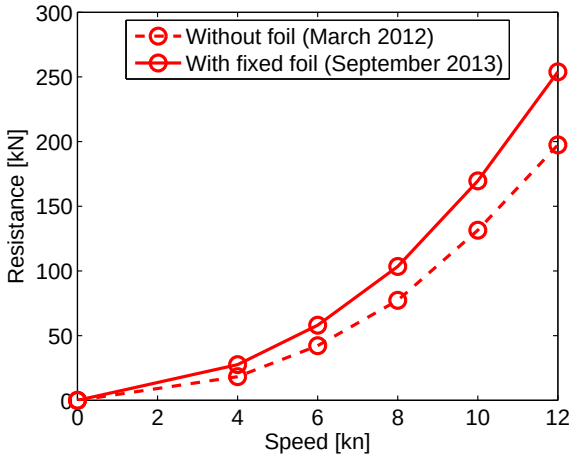

Figure 5.5: Calm water resistance without foil (March 2012) and with fixed foil (September 2013)

Replacing the wire pitching the foil with much more rigid rods, not only improved the foil actuation, as mentioned, but also kept the foil more fixed when it was supposed to be fixed. This is another reason for the difference between the March 2012 and September 2013 results in Figure 5.4.

When performing a VeSim simulation, the added resistance in waves is calculated with the MARINTEK software ShipX Vessel Responses (VERES) (Fathi, 2012). In VERES, dynamic lift on the wavefoil is calculated using the Theodorsen

function and summing up the foil section forces, but no dynamic stall effects are included. Further details on the wavefoil model in VERES is given in Section 5.6.1.

There are two available methods for calculating the added resistance in VERES: "Gerritsma & Beukelman" and "Pressure integration". "Gerritsma & Beukelman" is the extension of the method by Gerritsma and Beukelman (1972) to oblique waves (Loukakis and Sclavounos, 1978), whereas "Pressure integration" is the pressure integration method of Faltinsen et al. (1980). The "Gerritsma & Beukelman" method was applied in the head seas simulations in Sections 5.1.3 and 5.4, whereas the "Pressure integration" method was found to be more robust in following seas and was therefore applied in the simulations in Section 5.5, Chapter 6, and Chapter 7. Both methods are combined with the wave reflection formula of Faltinsen et al. (1980) for short waves (Fathi and Hoff, 2014). When using the "Pressure integration" method, the option "Apply surge, sway and yaw motion limits in following seas (at low encounter freq.)" was ticked off. Selecting this option avoids unphysically large motions in surge, sway and yaw close to zero frequency of encounter in following seas (Fathi and Hoff, 2014).

Figures 5.6 and 5.7 compare experimental and simulated results for 10 knots and 8 knots forward speed, respectively. The agreement between simulations and experiments is at the same level as for a speed of 12 knots, except for the resistance with fixed foil, where the agreement appears to be worse with decreasing speed.

5.2 Actively pitch-controlled foil

5.2.1 VeSim implementation

The simple pitch-control algorithm in Eq. 4.13 was implemented in VeSim, to simulate actively pitch-controlled wavefoils. In the implementation of pitch-controlled foils in VeSim, δ_{opt} was calculated based on ϕ_E at the spanwise center of the foil. ϕ_E was calculated in the same manner as in Eq. 4.4. We assumed perfect actuation, i.e., that the foil immediately took on the calculated δ_{opt}. At every time step, the following procedure was performed:

1. α_n was calculated at the spanwise foil center based on δ from the previous time step.

2. X_n and Y_n were calculated at the spanwise foil center using Eqs. 3.34 and 3.35.

3. $\phi_{E,n}$ was calculated at the spanwise foil center using Eq. 4.4.

4. δ_{opt} was calculated at the spanwise foil center using a modified version of Eq. 4.13, which includes the vessel pitch (see Figure 5.8):

$$\delta_{opt} = \begin{cases} -\alpha_{max} - \phi_E - \xi_5, & w_{pc}\phi_E < -\alpha_{max} \\ \phi_E(w_{pc} - 1) - \xi_5, & -\alpha_{max} \leq w_{pc}\phi_E \leq \alpha_{max} \\ \alpha_{max} - \phi_E - \xi_5, & w_{pc}\phi_E > \alpha_{max}. \end{cases} \tag{5.2}$$

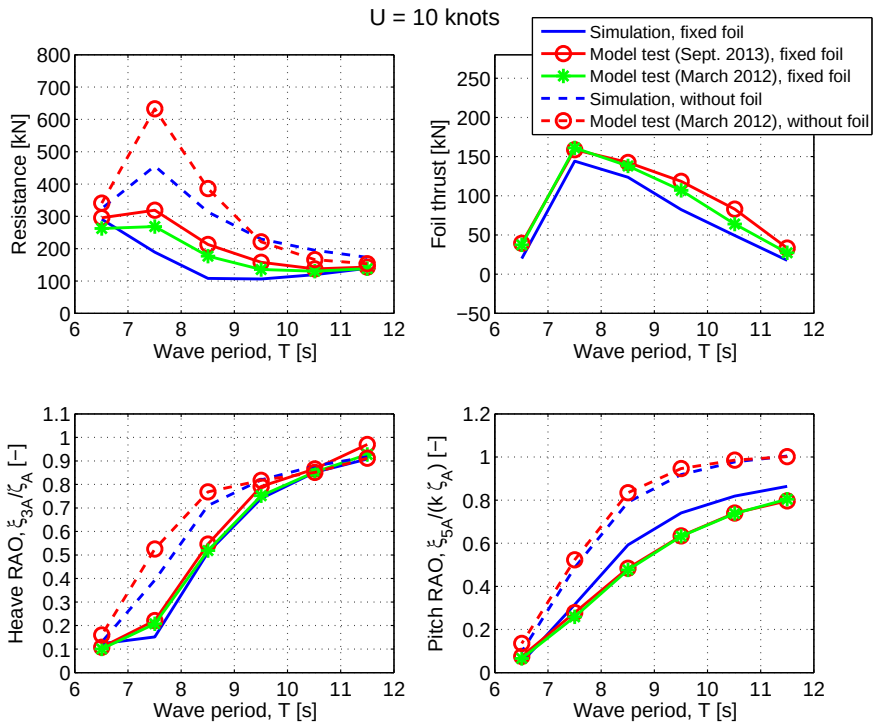

Figure 5.6: Simulation vs. experiment results for regular head sea waves and a forward speed of 10 knots

5. α_n was calculated at the spanwise foil center using the newly found δ_{opt}.

6. Steps 2-5 were repeated until α_n had converged.

After δ was determined by setting $\delta = \delta_{opt}$, new values of α_n, X_n, Y_n and α_E were calculated for all spanwise foil sections. Dynamic foil forces were then calculated using the dynamic stall model described in Section 3.3.

5.2.2 Model test, March 2012

The model test with actively pitch-controlled in March 2012 was partly successful: *successful* since pitch control was slightly beneficial in several runs and clearly beneficial in two runs ($T = 9.5$ s, 8 knots forward speed and $T = 6.5$ s, 10 knots forward speed), and *partly* because of the inherent elasticity in the wire connecting the motor and the foil, see Figure 5.2, which probably is part of the reason why not better results were obtained with the pitch-controlled foil.

In January 2012, the foil alone was tested for the first time in the same basin as described in Section 4.1, see Appendix C.1. The foil was equipped with five pressure sensors located on and near the leading edge, see Figure 5.9. In Figure

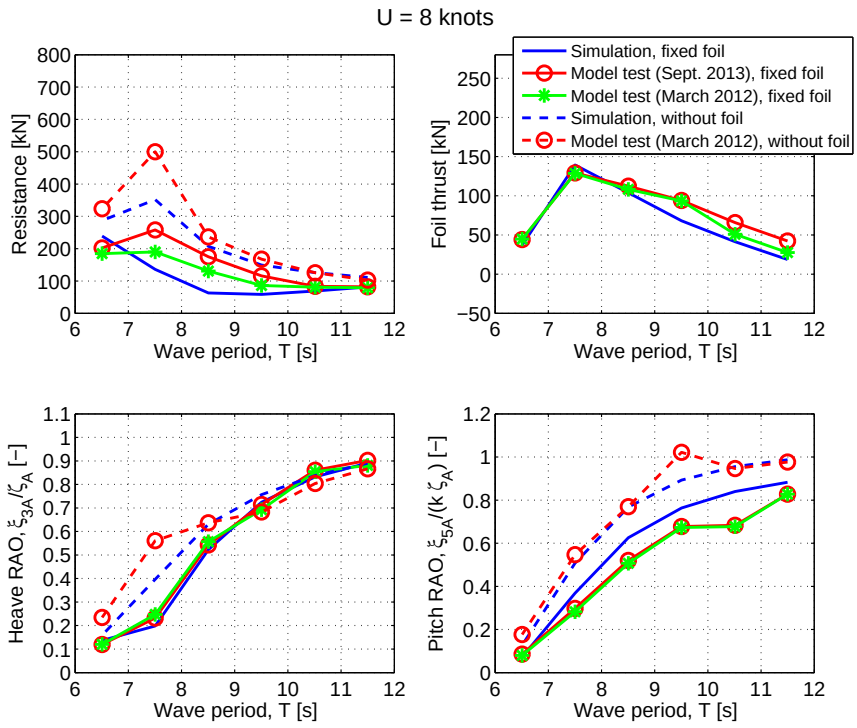

Figure 5.7: Simulation vs. experiment results for regular head sea waves and a forward speed of 8 knots

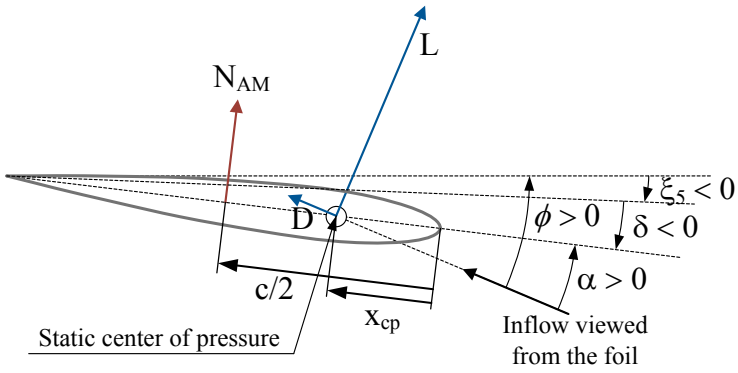

Figure 5.8: Foil forces and angles, including vessel pitch

5.9, p_k denotes the pressure at pressure sensor k. Based on pressure recordings at a range of static angles of attack, Figure 5.10 was generated. When knowing the pressure at sensors 1, 3, and 5, one can interpolate in Figure 5.10 to estimate the

angle of attack. In the March 2012 model test with actively pitch-controlled foil, the four nearest data points in Figure 5.10 to the measured pressure point was found at each time step, and fourth degree polynomial interpolation was applied to estimate the angle of attack. Since each data point corresponds to a forward speed of the foil, U, this method enables us to estimate the angle of attack without knowing the inflow speed to the foil. In Figure 5.10, the different U values corresponds to full scale forward speeds of 6, 8, 10, 12, and 14 knots.

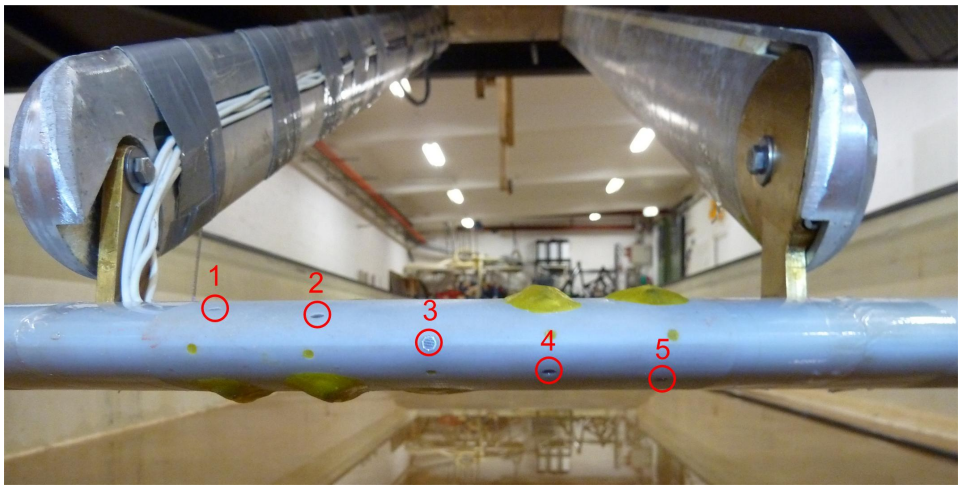

Figure 5.9: The five pressure sensors on and near the leading edge used in the March 2012 test, marked with red circles and numbered

In the March 2012 test with pitch-controlled foil, the optimal foil pitch was determined in a different manner than using Eq. 4.13. Instead of pitching the foil a constant times the angle of attack, up to a maximum angle of attack, as in Eq. 4.13, the static lift and drag curves were used directly to find the optimal angle of atttack at all times. This should in theory eliminate the tuning of a pitch-control parameter, as in Eq. 4.13.

From a quasi-steady point of view, the foil thrust is given by (see Figure 4.17)

$$T = L\sin\phi - D\cos\phi. \tag{5.3}$$

The optimal angle of attack is considered to be the angle of attack that maximizes the propulsive thrust, at a given time instant. This angle of attack can be found by differentiating the expression for the thrust with respect to the angle of attack, and setting this expression equal to zero:

$$\frac{\partial T}{\partial \alpha} = \frac{\partial L}{\partial \alpha}\sin\phi - \frac{\partial D}{\partial \alpha}\cos\phi = 0, \tag{5.4}$$

which gives

$$\phi = \arctan\left(\frac{\frac{\partial D}{\partial \alpha}}{\frac{\partial L}{\partial \alpha}}\right). \tag{5.5}$$

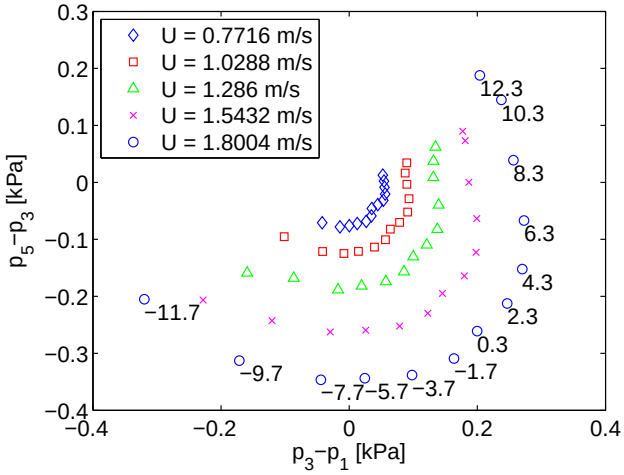

Figure 5.10: Pressure plot used to estimate the angle of attack in the March 2012 model test. Numbers at the data points indicate angle of attack in degrees. For all velocities, the order of the angle of attack relative to the pressure point is the same as the one shown.

The resulting ϕ will be a function of α, which is actually the most thrust-producing angle of attack, denoted α_{opt}. Thus, we also know α_{opt} as a function of ϕ. Figure 5.11 shows the α_{opt} vs. ϕ graph used in the March 2012 test, obtained using Eq. 5.5 and curve-fitted polynomials to experimentally obtained static lift and drag coefficient curves. Finally, the optimal foil pitch is given by

$$\delta_{opt} = \alpha_{opt} - \phi - \xi_5. \tag{5.6}$$

The ship resistance, foil thrust, vessel heave RAO, and vessel pitch RAO for the ship without foil, with fixed foil, and with pitch-controlled foil are shown in Figures 5.12, 5.13 and 5.14 for forward speeds of 12, 10, and 8 knots, respectively. Again, the model scale forces are directly Froude-scaled to full scale. Due to time limitations, not all wave periods were tested for forward speeds of 12 and 8 knots.

At 12 knots, the ship with pitch-controlled foil had slightly lower resistance in waves than the ship with fixed foil, at a wave period of 8.5 s. This is reflected by the foil thrust graph, which shows that the thrust for the pitch-controlled foil was higher than the thrust for the fixed foil at this wave period. For the other wave periods, the resistance and foil thrust values with pitch-controlled foil and with fixed foil are quite similar. The heave and pitch RAOs with fixed foil and with pitch-controlled foil are very similar.

At 10 knots, the ship resistance values with fixed and pitch-controlled foil are very similar, except for a wave period of 6.5 s, where pitch control was clearly beneficial. This is again reflected by the foil thrust graph, but in this case the pitch-controlled foil thrust was significantly higher also for wave periods 8.5 s and

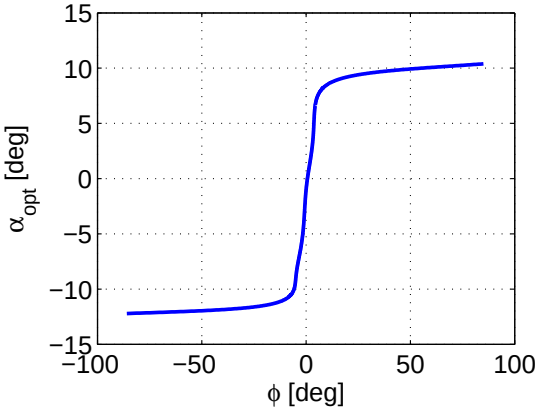

Figure 5.11: α_{opt} vs. ϕ graph used in the March 2012 test

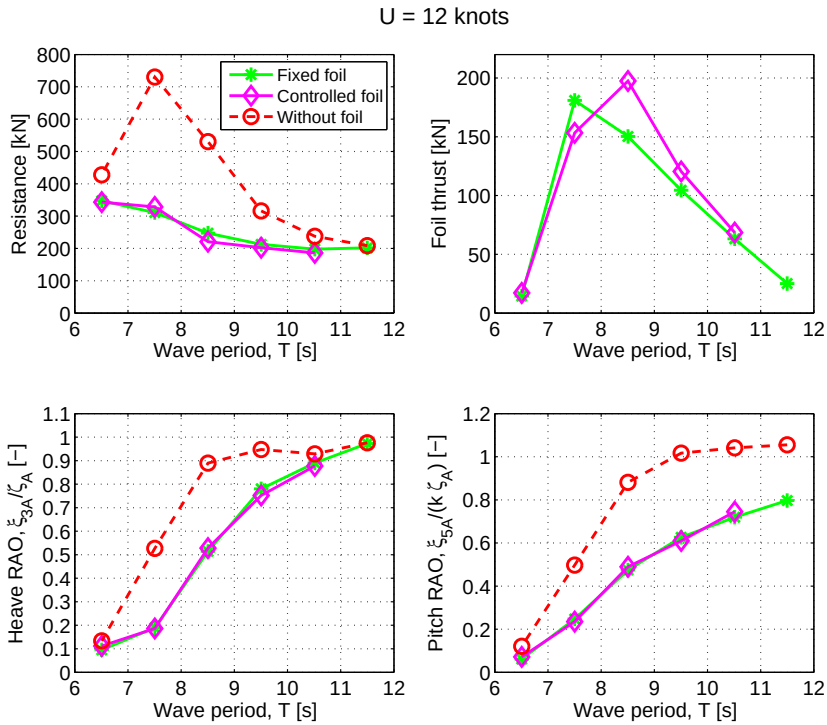

Figure 5.12: Experiment results for the March 2012 test. Regular head sea waves and a forward speed of 12 knots.

9.5 s, and this is not reflected by the ship resistance graph. The reason for this

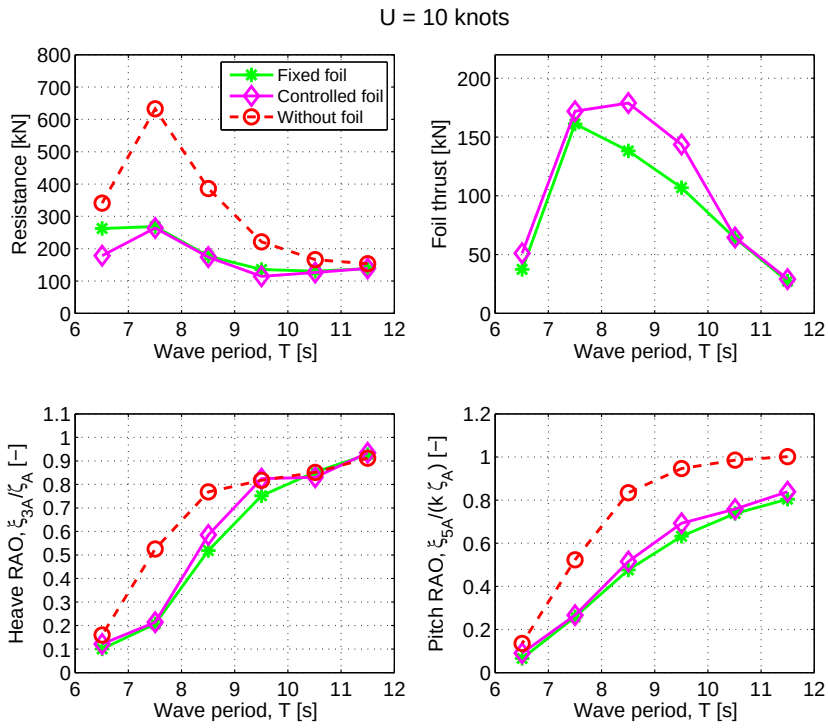

Figure 5.13: Experiment results for the March 2012 test. Regular head sea waves and a forward speed of 10 knots.

is probably that the ship motions with pitch-controlled foil, at these two wave periods, were slightly larger than with fixed foil, causing larger added resistance in waves.

At 8 knots, only three wave periods were tested. The effect of pitch control is clear from the foil thrust graph for all three wave periods, but can only clearly be seen on the resistance graph for a wave period of 9.5 s. Again, the reason for this is probably that the ship motions with pitch-controlled foil were slightly larger than with fixed foil for wave periods 7.5 s and 8.5 s, although the ship motions with fixed foil and with pitch-controlled foil for a wave period of 7.5 s are very similar.

Adding the foil to the ship, whether it was fixed or pitch-controlled, significantly reduced the ship resistance and motions. It is likely that even lower resistance for the pitch-controlled foil, for all three speeds, could have been achieved with a more precise foil actuation mechanism. Tables 5.4, 5.5, and 5.6 give the reduction in ship resistance and motions with fixed foil and with pitch-controlled foil for forward speeds of 12, 10, and 8 knots, respectively. "NaN" means that there was no experimental data to calculate the value. We see that the foil caused a slight increase in heave motion for a few cases in long waves, but that the motion reduction generally was large. Maximum reduction in ship resistance was 67% at

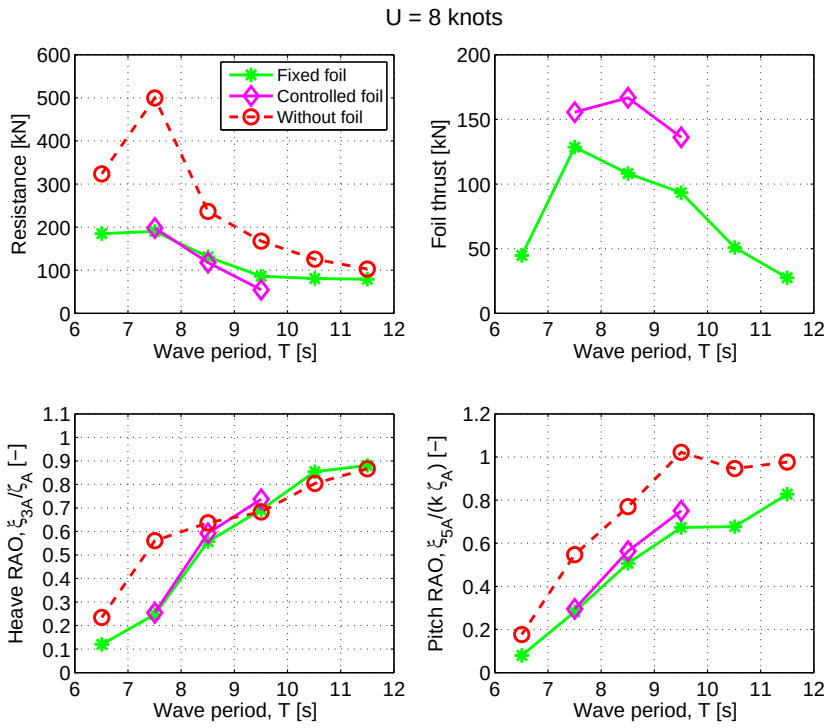

Figure 5.14: Experiment results for the March 2012 test. Regular head sea waves and a forward speed of 8 knots.

a wave period of 9.5 s and a speed of 8 knots for the pitch-controlled foil. The heave motion was reduced by over 60% in several cases, and the pitch motion was reduced by over 50% in several cases.

The motion reduction effect is evident in Figure 5.15, which shows snapshots from videos of the ship model, without foil and with pitch-controlled foil, at the same instant in the wave cycle. The wave height in Figure 5.15 was 3.5 m, the wave period 7.5 s, and the forward speed 12 knots. In fact, the splashing from the ship model without foil was so large that we were a bit worried for the electronic equipment on the towing carriage. Such slamming incidents do occur in real life with this particular ship, as Figure 5.16 shows.

5.2.3 Model test, September 2013

In September 2013, the actively pitch-controlled foil described in Chapter 4 was employed on the same ship model as was tested in March 2012. Due to delays at MARINTEK, five workdays of testing were reduced to two days. Successful runs in calm water and with fixed foil in the same waves as in the March 2012 test were done, and these results are given in Section 5.1.3. Due to time limitations,

	Reduction in ship resistance [%]		Reduction in heave motion [%]		Reduction in pitch motion [%]	
T [s]	**Fixed foil**	**Pitch-controlled foil**	**Fixed foil**	**Pitch-controlled foil**	**Fixed foil**	**Pitch-controlled foil**
11.5	3	NaN	0	NaN	24	NaN
10.5	17	22	4	6	31	28
9.5	33	36	18	21	38	40
8.5	53	58	42	41	46	44
7.5	57	55	64	65	50	53
6.5	19	20	29	16	49	41

Table 5.4: Reduction in ship resistance and motions at 12 knots, from the March 2012 test

	Reduction in ship resistance [%]		Reduction in heave motion [%]		Reduction in pitch motion [%]	
T [s]	**Fixed foil**	**Pitch-controlled foil**	**Fixed foil**	**Pitch-controlled foil**	**Fixed foil**	**Pitch-controlled foil**
11.5	10	9	-2	-2	20	16
10.5	21	24	0	2	25	23
9.5	39	48	8	-1	33	27
8.5	54	55	33	24	43	38
7.5	58	58	61	59	51	49
6.5	23	48	37	24	51	33

Table 5.5: Reduction in ship resistance and motions at 10 knots, from the March 2012 test

only a limited number of cases were tested. Only wave periods 7.504 s and 8.505 s were tested, with the corresponding wave heights from Table 5.3, i.e., 3.518 m and 3.002 m, respectively. Ship speeds of 8, 10, and 12 knots were tested. However, due to various mechanical issues during several of the tests, only two cases are presented here: wave height 3.002 m and wave period 8.505 s for the ship speeds 8 and 10 knots. The foil was controlled using Eq. 5.2, but with setting $\xi_5 = 0$ in this equation for simplicity. Simulations showed that setting $\xi_5 = 0$ in Eq. 5.2 decreased the foil thrust only marginally.

The ship resistance and foil thrust are plotted against w_{pc} for a forward speed of 10 knots in Figure 5.17 and a forward speed of 8 knots in Figure 5.18 together with values for a fixed foil. We see that the benefit of pitch control was larger at 8 knots than at 10 knots and that the pitch-controlled foil resulted in lower ship resistance than a fixed foils only for a few choices of pitch-control parameter.

T [s]	Reduction in ship resistance [%]		Reduction in heave motion [%]		Reduction in pitch motion [%]	
	Fixed foil	Pitch-controlled foil	Fixed foil	Pitch-controlled foil	Fixed foil	Pitch-controlled foil
11.5	23	NaN	-2	NaN	15	NaN
10.5	36	NaN	-6	NaN	28	NaN
9.5	49	67	-1	-8	34	27
8.5	45	50	13	7	34	27
7.5	62	60	56	55	48	46
6.5	43	NaN	49	NaN	55	NaN

Table 5.6: Reduction in ship resistance and motions at 8 knots, from the March 2012 test

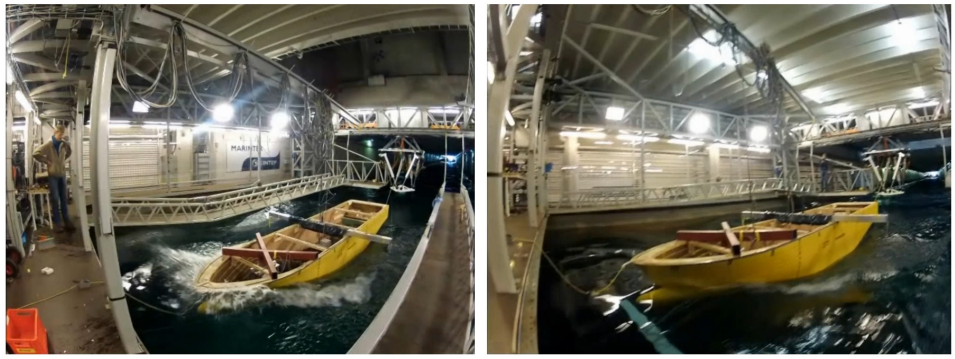

Figure 5.15: Comparison of ship motions, without foil (left) and with controlled foil (right) for 12 knots forward speed, $H = 3.5$ m, and $T = 7.5$ s. The photos were taken at the same instant in the motion cycle.

The foil thrust was significantly higher with pitch control at 8 knots for w_{pc} values from 0.7 to 0.9, but only slightly higher for these w_{pc} values at 10 knots. It is interesting to note that the ship resistance can decrease without a corresponding increase in foil thrust. This can be explained by studying the heave and pitch RAOs, which are plotted in Figures 5.19 and 5.20. Larger w_{pc} implies larger angle of attack, which in turn may give larger damping of the ship motions (and hence less resistance), but less thrust if stall is reached. Indeed, we see that the reduction in ship resistance was accompanied by reduced ship motions, particularly in heave. We also see that when w_{pc} was significantly less than 1, meaning that the angle of attack is significantly reduced compared to a fixed foil, the heave and pitch motions were larger than with a fixed foil, due to reduced foil lift.

Unfortunately, near the end of the last test day, the metal piece connecting the foil to the port strut was torn apart by the hydrodynamic loads on the foil,

Figure 5.16: Bow slamming on *Far Seeker* (Leikarnes, 2011) – a platform supply vessel of the same UT 751 E design as studied in this chapter

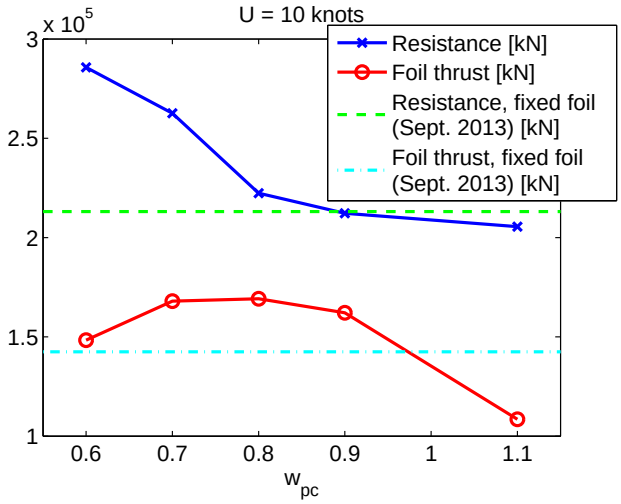

Figure 5.17: Results for pitch-controlled foil, 10 knots, September 2013. $H = 3.002$ m, $T = 8.505$ s.

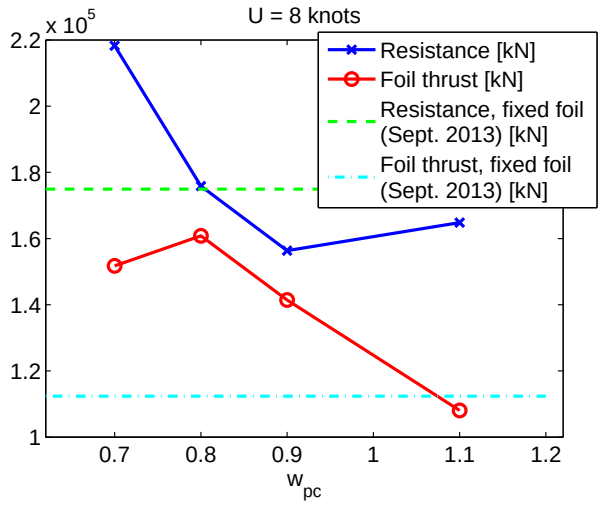

Figure 5.18: Results for pitch-controlled foil, 8 knots, September 2013. $H = 3.002$ m, $T = 8.505$ s.

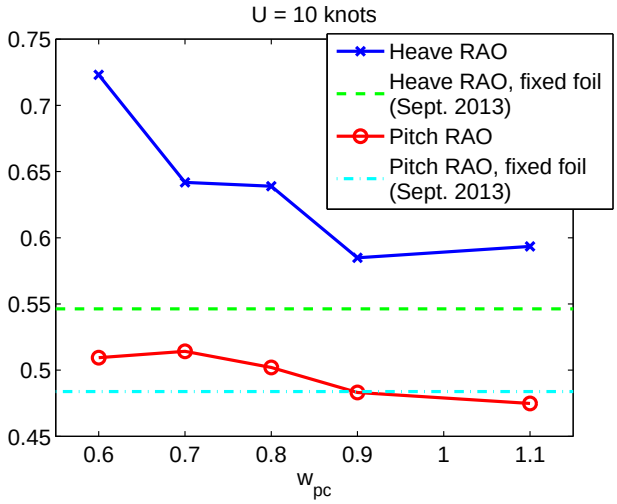

Figure 5.19: RAOs for pitch-controlled foil, 10 knots, September 2013. $H = 3.002$ m, $T = 8.505$ s.

see Figure 5.21, and the testing naturally came to an end. From these tests, and the tests with the same pitch-control mechanism in Section 4.5, controlling the foil pitch using vanes for detecting the inflow does not appear to be the optimal method of pitch control. As discussed in Section 4.6.2, the vanes pitched about a point far forward of their leading edges, implying that the vane angle, and hence the foil pitch, was little influenced by the added mass force on the vanes. This resulted in

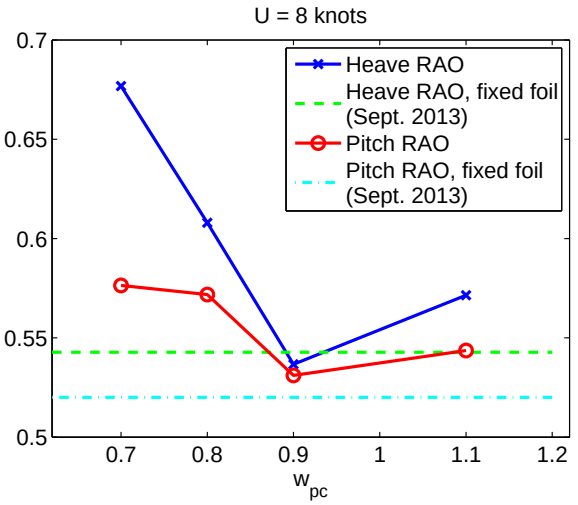

Figure 5.20: RAOs for pitch-controlled foil, 8 knots, September 2013. $H = 3.002$ m, $T = 8.505$ s.

a phase lag of the foil pitch, and lower thrust, relative to the spring-loaded foil in Section 4.6, as shown in Figures 4.16 and 4.23.

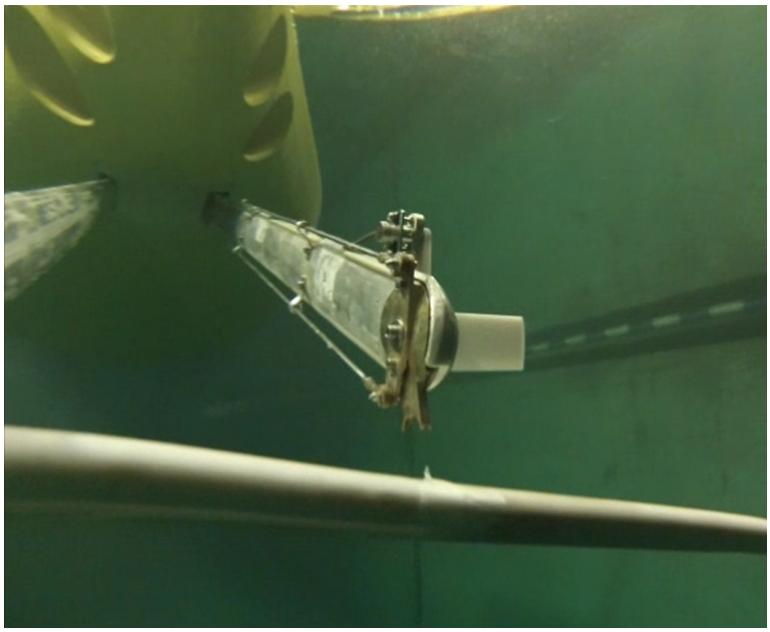

Figure 5.21: Close-up view of the broken connection between the foil and the port strut in the September 2013 test, shortly after the incident

When using pressure sensors for pitch control, the pressure distribution due to fluid accelerations relative to the foil will be captured by the pressure sensors, in addition to the pressure distribution due to circulatory lift. This could lead to a pitch motion of the foil closer to the that of the spring-loaded foil. As already mentioned, the inaccurate foil actuation in the March 2012 tests is likely to have decreased the performance of the pitch-controlled foil using pressure sensors. The inaccurate foil actuation makes it difficult to study the actual foil pitch in the March 2012 tests, since there was no potentiometer at the foil itself measuring the foil pitch directly.

5.3 Spring-loaded foil

For the case of a spring-loaded foil, experiments were done with a foil without the ship, as described in Section 4.6, and spring-loaded wavefoils were implemented in VeSim. There was not available time in the towing tank to test the spring-loaded foil from Section 4.6 on the model of the UT 751 E platform supply vessel. When testing the foil alone in the smaller MC Lab, see Appendix C.1, the author had to wear a drysuit and adjust the position of the magnet clamp determining the stiffness of the spring for the spring-loaded foil, see Figure 4.19, under water. This would have been very difficult to do in the towing tank, which is far too deep to stand on the tank bottom while working on the foil under water. In other words, a different mechanism for adjusting the spring stiffness of a spring-loaded foil must be designed before eventual future tests with a spring-loaded foil in the towing tank.

In the VeSim implementation of spring-loaded foils, we assumed that there is a linear rotation spring which works in both directions, see Figure 5.22. Newton's second law for the spring-loaded foil becomes

$$\int_f \left\{ N_f \left(a + \frac{c}{4} - x_p \right) + N_{AM} \left(\frac{c}{2} - x_p \right) + N_V \left(CP_V c + \frac{c}{4} - x_p \right) \right\} ds$$
$$-k_s \delta = I \ddot{\delta}, \qquad (5.7)$$

where N_f is the normal force associated with C_N^f, a is the distance from where N_f attacks to the quarter-chord (positive when N_f attacks behind the quarter-chord), x_p is the distance from the leading edge to the pivot point of the spring-loaded foil, N_V is the normal force associated with C_N^V, CP_V is the nondimensional center of pressure due to the vortex producing C_N^V, k_s is the spring constant, and I is the moment of inertia for the foil. $\int_f$ means integrating over the foil span.

a is given as

$$a = \frac{M}{N_f}, \qquad (5.8)$$

where M is the pitching moment about the quarter-chord, defined to be positive when it acts to pitch the foil in the nose-up direction. The pitching moment

was found by entering a lookup table of moment coefficients vs. angle of attack (Sheldahl and Klimas, 1981) with α_f.

CP_V is given as (Leishman and Beddoes, 1989)

$$CP_V = 0.20\left(1 - \cos(\pi\tau)\right), \tag{5.9}$$

where τ is the vortex travel parameter explained in Sec. 3.3.3. Leishman and Beddoes (1989) use $\frac{\tau_v}{T_{vl}}$ instead of τ in Eq. 5.9, where τ_v is a nondimensional vortex time, and T_{vl} is a nondimensional vortex passage time constant.

Inserting Eq. 3.36 for N_{AM} in Eq. 5.7 and rewriting, we get

$$\ddot{\delta} = \frac{\int_f \left\{ N_f \left(a + \frac{c}{4} - x_p\right) + \frac{\rho\pi c^2}{4} ds \left(-\ddot{h}\cos\delta + U\frac{d}{dt}\left(\sin\delta\right)\right)\left(\frac{c}{2} - x_p\right)\right\} ds + \int_f N_V \left(CP_V c + \frac{c}{4} - x_p\right) ds - k_s\delta}{I - \int_f \frac{\rho\pi c^2}{4} ds \left(\frac{c}{2} - x_p\right)^2 ds}. \tag{5.10}$$

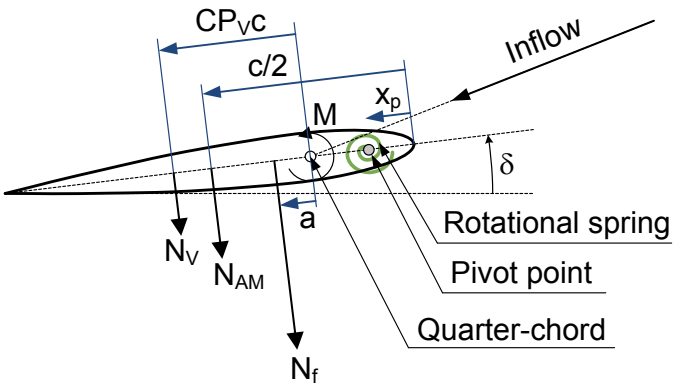

Figure 5.22: Moment balance for a spring-loaded foil

In the Vesim implementation of Eq. 5.10, δ_{n-1} was used when calculating $\ddot{\delta}_n$. N_f was calculated using the dynamic stall model described in Section 3.3, using δ_{n-1} when calculating α_n. After $\ddot{\delta}_n$ was found, $\dot{\delta}_n$ and δ_n were obtained using the backward Euler method for time integration,

$$\dot{\delta}_n = \dot{\delta}_{n-1} + \Delta t\ddot{\delta}_n, \tag{5.11}$$

$$\delta_n = \delta_{n-1} + \Delta t\dot{\delta}_n, \tag{5.12}$$

because this method proved to be stable for sufficiently small time steps and convenient to implement.

5.4 Simulations with pitch-controlled and spring-loaded foils

Simulation results for the ship with a fixed, pitch-controlled, and spring-loaded foil are shown in Figures 5.23 and 5.24 for forward speeds of 12 and 8 knots, respectively, in the same regular head sea waves as in Figures 5.4, 5.6, and 5.7. In Figures 5.23 and 5.24, strut drag was accounted for in the same manner as described in Section 5.1.3. The empirical constants in the dynamic stall model used in the simulations were the same as in Section 4.3: $T_p = 1.5, T_f = 7, \alpha_v = 11^o$, $T_v = 15$ and $\eta_C = 0.95$. For consistency with the simulations in Section 5.1.3, model scale Re was used when calculating the wavefoil forces.

For both pitch-controlled and spring-loaded foils, the added resistance was calculated assuming that the foil was fixed, since neither foils that are controlled to maximize the forward thrust nor spring-loaded foils are currently implemented in VERES. The same assumption is made in the VeSim simulation with spring-loaded wavefoils in Chapters 6 and 7.

For the pitch-controlled foil, $\alpha_{max} = 12^\circ$ was used, with $w_{pc} = 0.55$ for 12 knots and $w_{pc} = 0.60$ for 8 knots forward speed. For the spring-loaded foil, $k_s = 3,000,000$ Nm/rad was used for each foil half at 12 knots forward speed, and $k_s = 1,000,000$ Nm/rad was used for each foil half at 8 knots forward speed. These values were chosen because they resulted in the lowest sum of ship resistance values for all wave periods, with the belief that setting $\alpha_{max} = 12^\circ$ was reasonable based on the static lift and drag coefficient curves in Figure 4.5. The moment of inertia, I, of the semi-span of the foil (assuming that the foil halves could pitch independently of each other) was estimated to be 11,000 kgm^2 in full scale. I is needed when using Eq. 5.10 for the spring-loaded foil.

From Figures 5.23 and 5.24 we see that the effect of pitching the foil was only significant for wave periods 7.5 s and 8.5 s. These wave periods were seen from the model test to be the wave periods that gave the most violent ship motions, and hence they also produced the largest foil thrust, as the foil thrust plots show. According to these simulations, the optimized pitch-controlled and spring-loaded foils performed very similarly.

5.5 Fuel savings with fixed foil in irregular waves

Simulations with the same ship and foil were done in short-crested irregular waves to calculate how much fuel the wavefoil would save the ship in realistic ocean wave conditions. A significant wave height (H_s) of 2.5 m is typical in the North Sea and the North Atlantic and was therefore applied in the simulations, with a Pierson-Moskowitz wave spectrum. The wave direction was varied between 0 (head seas) and 180 (following seas) degrees, in steps of 45 degrees, and the peak periods (T_p) were 7.5, 9, and 10.5 seconds. The calm water resistance polynomial used as input in these simulations was based on correctly scaling the calm water resistance from model tests, using the standard procedure where viscous resistance and wave resistance are scaled differently – see for instance Faltinsen (2005).

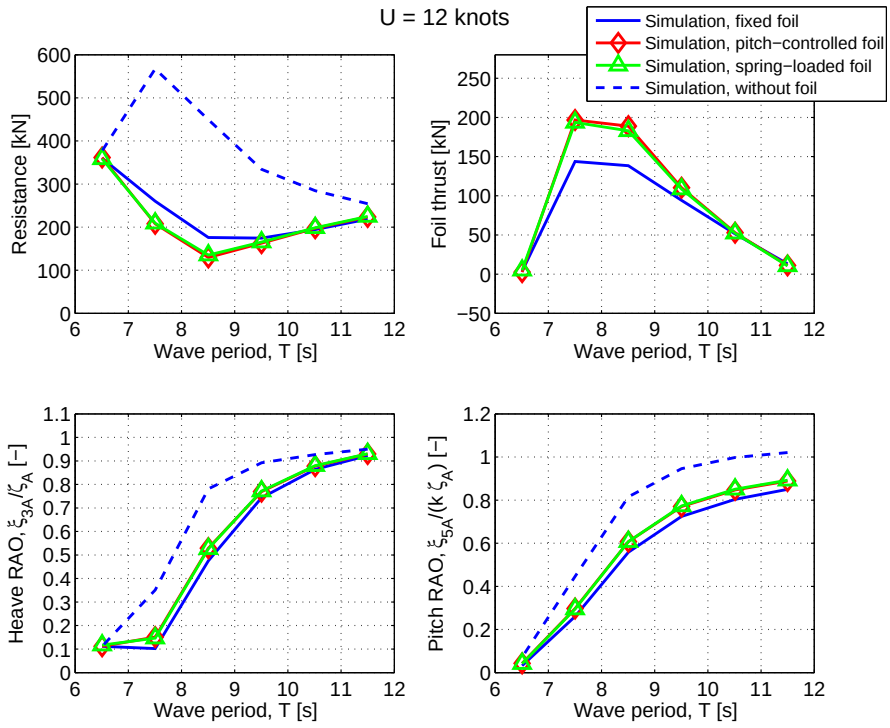

Figure 5.23: Simulation results for fixed, pitch-controlled, and spring-loaded foils in regular head sea waves, with a forward speed of 12 knots

The simplest wavefoil is fixed relative to the ship, so a fixed foil was used in the irregular waves simulations to provide a measure of minimum wavefoil performance. When the ship has rolling motion, which it will have in the wave directions simulated, the strut forces may dampen the ship motions and provide thrust, just like the horizontal wavefoil. Hence, the strut forces were modeled using the same dynamic stall model as described in Sec. 3.3, but without corrections for finite-span effects, since the strut is attached to the ship at its upper end and the foil at its lower end.

The ship was propelled using two azimuthing pod propulsors with a propeller diameter of 3.2 m. The maximum continuous rating (MCR) of each pod was increased from 200 to 1200 kW, in steps of 250 kW, and the corresponding ship speeds were found based on the mean speed of 5 min simulations at each engine setting, after the speed had stabilized. For wave directions 135° and 180°, an additional run with MCR 100 kW for each pod was done, to make sure that the lowest MCR gave a ship speed well below 8 knots. The power needed to obtain various ship speeds was found from fitting a curve on the form $P = aU^b + c$ to the power vs. speed plot, where P is total engine power, U is speed, and a, b, and c are curve fit coefficients, and interpolating. An example of such curve fits for head

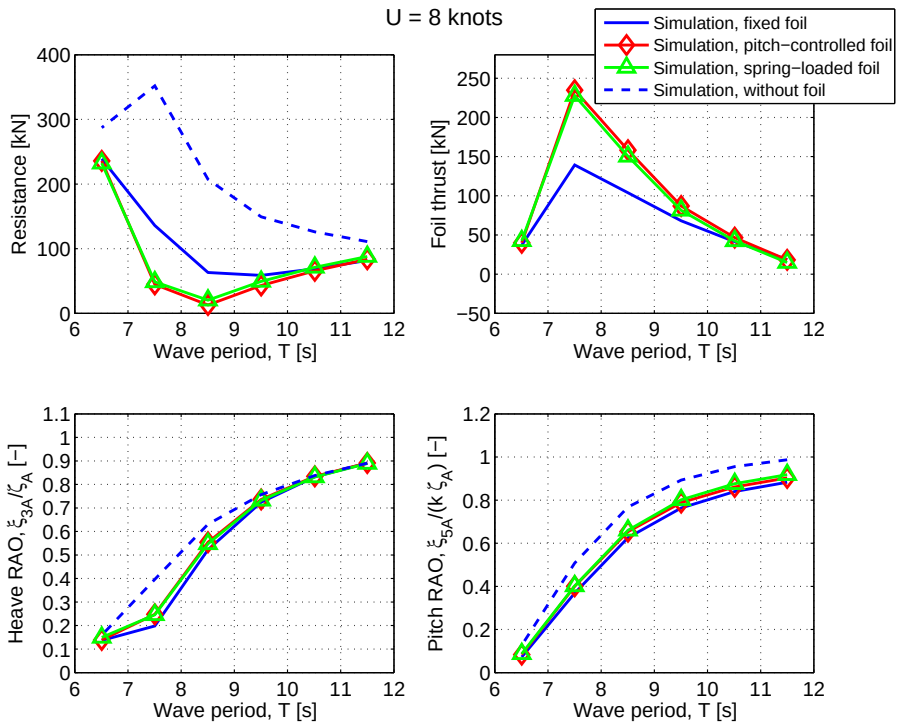

Figure 5.24: Simulation results for fixed, pitch-controlled, and spring-loaded foils in regular head sea waves, with a forward speed of 8 knots

sea waves and $T_p = 7.5$ s is shown in Figure 5.25. The complete set of power vs. speed graphs is given in Appendix D.

Assuming that the fuel consumption is linearly proportional to the engine power, Table 5.7 gives the fuel savings for the different combinations of sea states and wave directions, for ship speeds of 8, 10, and 12 knots. At 8 knots, the fuel savings are in the range 23-39%, except in following seas, where the fuel savings are 9-14%. For all combinations of wave direction and T_p, except from 10 to 12 knots in following seas for $T_p = 7.5$ s, the fuel savings decrease with increasing speed. At 12 knots, the fuel savings are in the range 2-15%. In following seas, the ship moved little relative to the waves, resulting in low benefit of the wavefoil.

5.6 Frequency-domain analysis in head seas

5.6.1 Ship motions

Although VeSim can be used to study ships with wavefoils, a simpler frequency-domain analysis is a good alternative to get a decent estimate on the effect of the

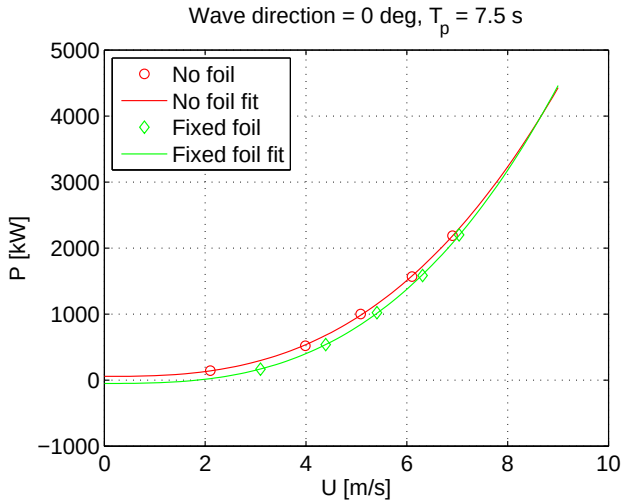

Figure 5.25: Total engine power vs. ship speed, head sea waves, $H_s = 2.5$ m, $T_p = 7.5$ s

Wave direction [°]	**T_p** [s]	**Fuel saving at 8 knots** [%]	**Fuel saving at 10 knots** [%]	**Fuel saving at 12 knots** [%]
0	7.5	24	14	8
0	9	35	24	13
0	10.5	31	20	10
45	7.5	33	19	10
45	9	39	27	15
45	10.5	33	20	11
90	7.5	37	23	14
90	9	35	21	12
90	10.5	30	17	9
135	7.5	23	14	8
135	9	30	16	5
135	10.5	27	15	5
180	7.5	9	5	7
180	9	14	10	7
180	10.5	12	6	2
Average		**27**	**17**	**9**

Table 5.7: Fuel savings with a fixed wavefoil in short-crested irregular waves, with $H_s = 2.5$ m

wavefoils (see for instance Belibassakis and Politis (2013)). A frequency-domain analysis is particularly useful if one wants to optimize the wavefoil by varying location, span, chord length, etc. In the following frequency-domain analysis, we

assume head seas for simplicity, but the procedure outlined can be expanded to cover all wave directions. Such a wavefoil model in the frequency-domain is implemented in the frequency-domain program VERES (Fathi, 2012) and was used by Angvik (2009) and Borgen (2010). For consistency with VERES, the coordinate system for the ship motions that is used in VERES is adopted here, see Figure 5.26. In the following analysis, a fixed wavefoil is assumed. In VERES, it is possible to select a control system for the foils that aims to minimize the ship motions, but it is currently not possible to control the foil pitch for maximum thrust.

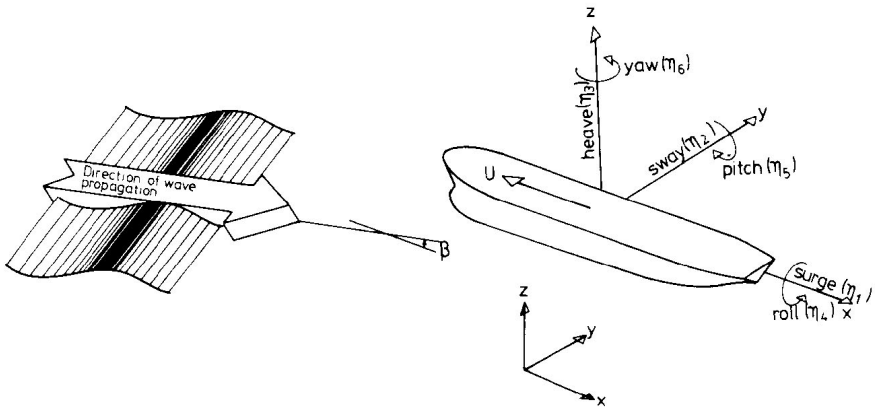

Figure 5.26: Coordinate system in VERES (Fathi, 2012)

Assuming that the ship motions and the wave excitation forces vary harmonically, the equations of motions can be written as (Faltinsen, 1993)

$$\left[(\underline{\underline{M}} + \underline{\underline{A}})(-\omega_e^2) + \underline{\underline{B}} i\omega_e + \underline{\underline{C}}\right] \underline{\xi_A} = \underline{F_A}, \tag{5.13}$$

where $\underline{\underline{M}}$ is the mass matrix, $\underline{\underline{A}}$ is the added mass matrix, $\underline{\underline{B}}$ is the damping matrix, $\underline{\underline{C}}$ is the restoring matrix, $\underline{\xi_A}$ is a vector containing complex motion amplitudes, and $\underline{F_A}$ is a vector containing complex amplitudes of the wave excitation forces and moments. Adding harmonically varying foil forces to Eq. 5.13, we get

$$\left[(\underline{\underline{M}} + \underline{\underline{A}})(-\omega_e^2) + \underline{\underline{B}} i\omega_e + \underline{\underline{C}}\right] \underline{\xi_A} = \underline{F_A} + \underline{F_{foil}}, \tag{5.14}$$

where $\underline{F_{foil}}$ is a vector containing complex amplitudes of the foil forces. In linear theory, as explained in Section 2.1, the foil force is assumed to be vertical, so the only nonzero elements in $\underline{F_{foil}}$ are $F_{foil,3}$ and $F_{foil,5}$, where $F_{foil,5} = -F_{foil,3} x_f$.

The vertical foil force is found by summing up the forces on spanwise sections of width ds:

$$F_{foil,3} \approx \int_f C_{L_\alpha} \alpha C(\omega_{e,r}) \frac{1}{2} \rho U^2 c ds + \int_f N_{AM} ds, \tag{5.15}$$

where C is the Theodorsen function with the reduced frequency of encounter, $\omega_{e,r}$, as argument. $\omega_{e,r}$ is used for reduced frequency here instead of k, as in Section 3.2.1, because k in this section is the wave number. In Eq. 5.15 it is assumed that the vertical foil velocity is much smaller than the horizontal, and that the horizontal foil motion is unaffected by the waves, so that $V \approx U$. The angle of attack, α, is given as

$$\alpha \approx \frac{w - (\dot{\xi}_3 - x_f \dot{\xi}_5)}{U} + \xi_5, \tag{5.16}$$

where w is the vertical wave particle vertical velocity. For regular waves with amplitude ζ_A in infinitely deep water,

$$w = i\omega\zeta_A e^{k(z_f - ix_f)} e^{i\omega_e t}. \tag{5.17}$$

Assuming that the foil is a flat plate, N_{AM} is given as

$$N_{AM} = \rho\pi \left(\frac{c}{2}\right)^2 \ddot{z}, \tag{5.18}$$

where $\ddot{z}$ is the acceleration perpendicular to the plate, which in head seas is

$$\ddot{z} \approx \dot{w} - \ddot{\xi}_3 + x_f \ddot{\xi}_5 + U\dot{\xi}_5. \tag{5.19}$$

x_f and z_f are horizontal and vertical locations of the foil, respectively, with respect to the center of gravity of the ship.

To solve Eq. 5.14, we must move the foil force terms depending on the ship motions to the left side of the equation, so that Eq. 5.14 can be written as

$$\left[(\underline{\underline{M}} + \underline{\underline{A}} + \underline{\underline{A_f}})(-\omega_e^2) + (\underline{\underline{B}} + \underline{\underline{B_f}})i\omega_e + (\underline{\underline{C}} + \underline{\underline{C_f}})\right] \underline{\xi_A} = \underline{F_A} + \underline{F_{fA}}, \tag{5.20}$$

where subscript f implies that the quantities are related to the foil, so that $\underline{\underline{A_f}}$, $\underline{\underline{B_f}}$, $\underline{\underline{C_f}}$, and $\underline{F_{fA}}$ are added mass matrix, damping matrix, restoring matrix and wave excitation force amplitude vector, respectively, for the foil. Using Eqs. 5.15-5.19, we get

$$A_{f,33} = \int_f \rho\pi \left(\frac{c}{2}\right)^2 ds, \tag{5.21}$$

$$A_{f,35} = -\int_f \rho\pi \left(\frac{c}{2}\right)^2 x_f ds, \tag{5.22}$$

$$B_{f,33} = \int_f C_{L_\alpha} \Re(C(\omega_{e,r})) \frac{\rho}{2} U c ds, \tag{5.23}$$

$$\begin{aligned} B_{f,35} = \quad & - \int_f C_{L_\alpha} \Re(C(\omega_{e,r})) \frac{\rho}{2} U c x_f ds \\ & - \int_f C_{L_\alpha} \Im(C(\omega_{e,r})) \frac{\rho}{2\omega_e} U^2 c ds - \int_f \rho\pi \left(\frac{c}{2}\right)^2 U ds, \end{aligned} \tag{5.24}$$

$$C_{f,33} = -\int_f C_{L_\alpha} \Im(C(\omega_{e,r})) \frac{\rho}{2} U c \omega_e ds, \tag{5.25}$$

$$C_{f,35} = \int_f C_{L_\alpha} \Im(C(\omega_{e,r})) \frac{\rho}{2} U c x_f \omega_e ds - \int_f C_{L_\alpha} \Re(C(\omega_{e,r})) \frac{\rho}{2} U^2 c ds, \tag{5.26}$$

$$F_{fA,3} = \int_f C_{L_\alpha} C(\omega_{e,r}) \frac{\rho}{2} U c i \omega \zeta_A e^{k(z_f - i x_f)} ds \tag{5.27}$$

$$- \int_f \rho \pi \left(\frac{c}{2}\right)^2 \omega \omega_e \zeta_A e^{k(z_f - i x_f)} ds. \tag{5.28}$$

Since $F_{foil,5}$ = -$F_{foil,3} x_f$, we get

$$A_{f,53} = -A_{f,33} x_f, \tag{5.29}$$
$$A_{f,55} = -A_{f,35} x_f, \tag{5.30}$$
$$B_{f,53} = -B_{f,33} x_f, \tag{5.31}$$
$$B_{f,55} = -B_{f,35} x_f, \tag{5.32}$$
$$C_{f,53} = -C_{f,33} x_f, \tag{5.33}$$
$$C_{f,55} = -C_{f,35} x_f, \tag{5.34}$$
$$F_{fA,5} = -F_{f,3} x_f. \tag{5.35}$$

5.6.2 Foil thrust

After the ship motions are found in the frequency domain, the foil thrust at each section can be calculated, see Figure 5.8, as

$$T = L(\alpha_E) ds \sin(\alpha_E - \delta - \xi_5) - D(\alpha_E) ds \cos(\alpha_E - \delta - \xi_5) + \Re(N_{AM}) ds \sin(-\delta - \xi_5), \tag{5.36}$$

where

$$\alpha_E = \Re(\alpha C(\omega_{e,r})), \tag{5.37}$$

$$L \approx C_{L_\alpha} \alpha_E \frac{1}{2} \rho U^2 c, \tag{5.38}$$

and

$$D \approx \left(C_{D,v}(\alpha_E) + C_{D,i}(\alpha_E)\right) \frac{1}{2} \rho U^2 c. \tag{5.39}$$

For a fixed foil, $\delta = 0$, in Eq. 5.36. In Eq. 5.39, $C_{D,v}$ is the viscous drag coefficient and $C_{D,i}$ is the induced drag coefficient. For an elliptical flat wing, which is the foil planform generating the least induced drag, with maximum chord length denoted c_{max},

$$C_{L_\alpha} = \frac{2\pi}{1 + \frac{2}{\Lambda}} \tag{5.40}$$

and

$$C_{D,i} = \frac{4\pi\alpha_E^2\Lambda}{(\Lambda+2)^2}, \tag{5.41}$$

where the aspect ratio, Λ, is

$$\Lambda = \frac{4s}{\pi c_{max}}. \tag{5.42}$$

For a comparison of the foil thrust obtained with the frequency-domain method and the foil thrust obtained with VeSim, see Figure 5.31.

5.7 The effect of foil location and size

A naval architect considering installing wavefoils on a ship would need to know how large the wavefoils must be, and where the wavefoils must be placed, to achieve a desired foil thrust. This can be answered by simulating varying wavefoil sizes and locations in VeSim, but a simpler method is proposed in the following, based on the frequency-domain analysis in Section 5.6. Knowing the frequency-domain properties of the ship with forward speed, the procedure described here can be implemented in, e.g., MATLAB, to obtain the optimal wavefoil location and size. The frequency-domain analysis is compared here with VeSim simulations for a ship speed of 12 knots and a wave height of 2 m. This ship speed and wave height was used in all the following plots. For simplicity and computational speed (a lookup table for C_{Dv} as a function of α and Re is computationally slow), $C_{Dv} = 0.01$ was used in the calculations.

In Figure 5.27, the foil thrust, nondimensionalized by $\rho g \zeta_A^2 L_{PP}$, is plotted against the longitudinal distance from AP to the foil divided by L_{PP} and the wave-length-to-L_{PP} ratio, λ/L_{PP}. The foil was assumed to have the same vertical location, span, and maximum chord length as the foil studied in this chapter, but an elliptical planform was assumed for simplicity. The λ/L_{PP} resulting in the highest foil thrust is about 1.5, giving a wave period of approximately 9 s. Of course, it is difficult to place the foil far ahead of the bow or far aft of the stern in reality. Interestingly, the foil does not need to be placed as far ahead of the bow as aft of the stern to produce the same foil thrust, and the thrust peak ahead of the bow is also higher than the thrust peak aft of the stern.

For a wave period of 9 s, the nondimensional foil thrust is plotted against both longitudinal and vertical foil position nondimensionalized by L_{PP} in Figure 5.28. We see that the vertical position of the foil is secondary, compared to the longitudinal foil position. Figure 5.28 should be used with care since neither the foil's interaction with the free surface nor the hull is included in the simulation model. As Wu (1972) notes, neglecting free-surface interaction is a reasonable simplification when the foil is farther than two chord lengths below the free surface, or $z_f/L_{PP} = 0.021$ in this case.

Figure 5.29 shows the same as Figure 5.27, but with the wave length, λ, replaced by the foil span, s, for a wave period of 9 s. Note that for a nondimensional longitudinal foil position between -0.3 and 1, the effect of increasing the nondimensional foil span above 0.3 is small.

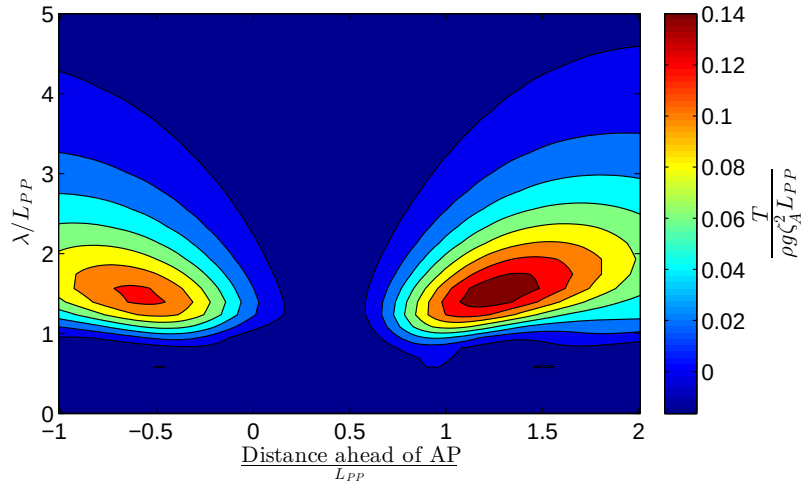

Figure 5.27: Nondimensional foil thrust vs. nondimensional longitudinal foil position and wave-length-to-L_{PP} ratio

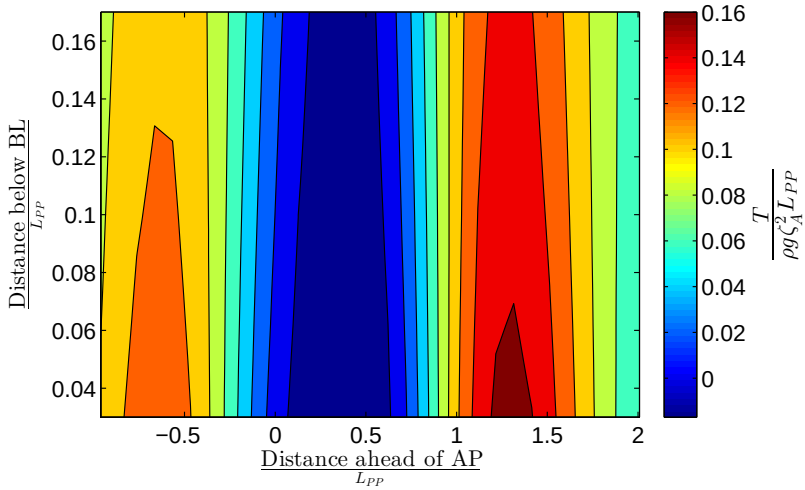

Figure 5.28: Nondimensional foil thrust vs. nondimensional longitudinal and vertical foil positions for a wave period of 9 s

For the foil location and span of the foil used in the experiments in this chapter and in Chapter 4, the aspect ratio (assuming elliptical planform) was varied in Figure 5.30, by varying the maximum chord length only. We see that the highest foil thrust does not change much when the aspect ratio is larger than about 13. Note that Figure 5.30 is based on lifting line theory which, for a steady foil, is 20%

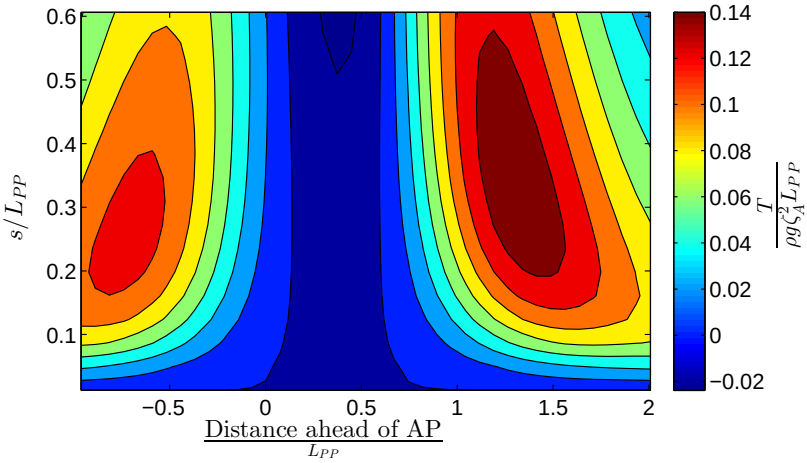

Figure 5.29: Nondimensional foil thrust vs. longitudinal foil position and span-to-L_{PP} ratio for a wave period of 9 s

inaccurate for an aspect ratio of two (Faltinsen, 2005).

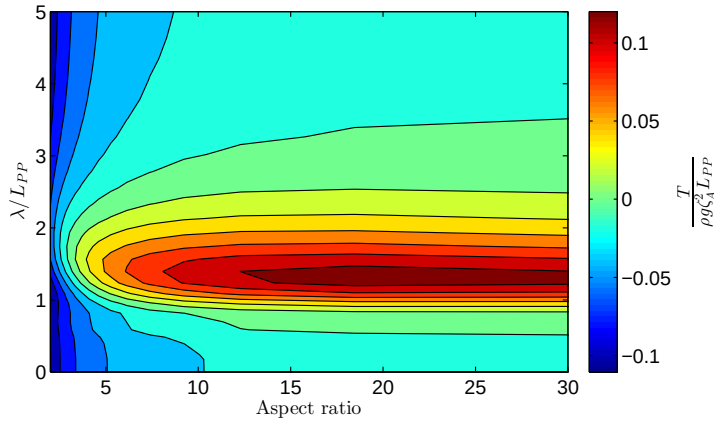

Figure 5.30: Nondimensional foil thrust vs. aspect ratio and wave-length-to-L_{PP} ratio

In Figure 5.31, the wavefoil model in VeSim is compared to the simpler frequency-domain model. The same foil at the same vertical location as in the experiments in this chapter was used, and the longitudinal foil position was varied for λ/L_{PP} values 0.6, 1.2 and 2.0. In other words, the frequency-domain graphs are horizontal cuts in Figure 5.27. The frequency-domain model predicts the peaks in foil thrust at the same longitudinal foil locations as the VeSim model, but overpredicts the magnitude of the foil thrust peaks relative to the VeSim model. Figure 5.31

bears striking resemblance to Figure 9 in Naito et al. (1986), which is reproduced as Figure 13 in Naito and Isshiki (2005), except the thrust peak magnitude for $\lambda/L_{PP} = 2.0$ is closer to that of $\lambda/L_{PP} = 1.2$ in Figure 5.31 than in Naito and Isshiki (2005). Based on Figure 5.31, the simpler frequency-domain model appears to be safe to use for fast calculations of the effect of fixed wavefoils on the ship in the given conditions.

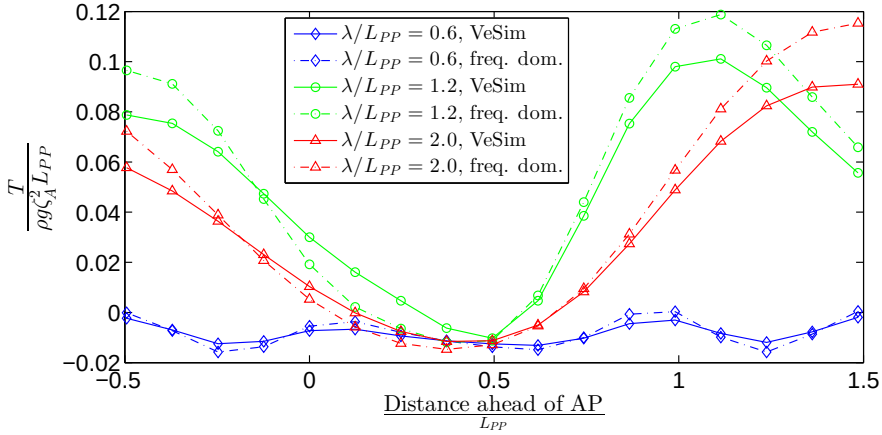

Figure 5.31: Comparison of foil thrust from VeSim and from the simpler frequency-domain analysis

To provide an indication of when the simplified model for wavefoil forces can be used to calculate the wavefoil force with reasonable accuracy, this model was used to simulate a single harmonically heaving foil, with $\delta = 0$. The foil was assumed to have elliptical span, with the same maximum chord length, span, and foil profile as the foil tested in Chapter 4 and in this chapter. Instead of setting $C_{D,v}$ in Eq. 5.39 to a constant, $C_{D,v}$ was in this case found by interpolating in a table of $C_{D,v}$ vs. angle of attack and Reynolds number (Sheldahl and Klimas, 1981). Figure 5.32 shows C_T, C_P, η, and maximum quasi-steady angle of attack, α_{max}, calculated using the simplified model, against the Strouhal number. The Strouhal number was varied by keeping the heave amplitude fixed at 0.12 m and varying the forward speed. In Figure 5.32, the α_{max} graph is linear for the simplified model, because the expression for angle of attack, Eq. 5.16, is based on linear theory. When calculating C_P, the vertical force was calculated as

$$F_V = \int_f [L\cos(\alpha_E) + D\sin(\alpha_E) + N_{AM}]\, ds. \tag{5.43}$$

Also shown in Figure 5.32 are C_T, C_P, η, and α_{max} vs. Strouhal number, for the same foil, calculated using the dynamic stall model from Section 3.3. Since the forward speed for the highest St is quite low, in this implementation, $C^p_{N,n} = C^C_{N,n}$ was used in Eq. 3.38 (see discussion in Section 3.3.1). We see that the difference

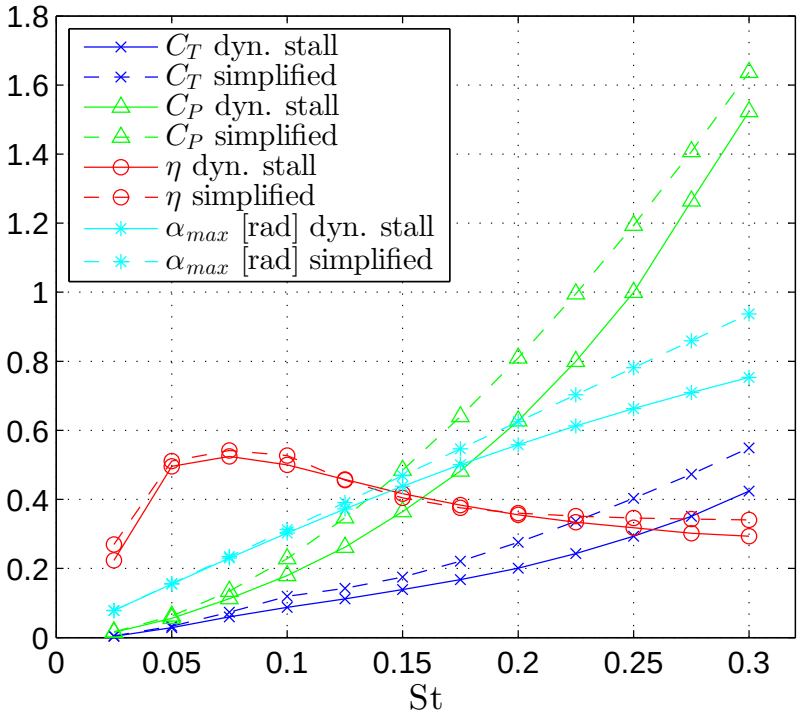

Figure 5.32: Theoretical C_T, C_P, η, and α_{max} for a non-pitching foil

between the two models increases for increasing Strouhal numbers, which is as expected, since the simplified model does not account for stall. The C_T and C_P curves for the simplified model start deviating from the curves for the dynamic stall model already at $St = 0.075$. Note that the relative deviation between the two C_P curves does not increase with increasing St.

Chapter 6

Performance of a ship powered purely by renewable energy

6.1 Motivation

Whereas Chapter 5 studied a particular ship's benefits of employing a wavefoil for *auxiliary* propulsion and motion reduction in waves, the present chapter is devoted to studying the performance a ship harnessing *all* its propulsive power from renewable energy. As concerns over global warming grow, the shipping community must take its share of responsibility to reduce greenhouse gas emissions. Shipping is currently responsible for 3.3% of the global CO_2 emissions. If the global temperature is to be stabilized at no more than 2°C warmer than pre-industrial levels by the year 2100, however, and emissions from shipping continue as projected, shipping would constitute between 12% and 18% of the global total CO_2 emissions in 2050 that would be required to achieve stabilization (by 2100) with a 50% probability of success (International Maritime Organization, 2009).

It is clear that radical measures are required if we are serious about cutting greenhouse gas emissions. A natural solution is going back to sail ships. Before the industrial revolution, square rigs ruled the world's oceans. At optimal wind conditions, these ships did not sail much slower than today's slow steaming cargo ships, which typically sail at 18 knots. *Cutty Sark*, for instance, logged a maximum speed of 17.5 knots and her 24-hour average speed record was 15 knots (Lubbock, 1924). With modern advances in sail technology, specifically with the advent of wingsails, it seems obvious that modern wind-powered cargo ships could have outraced *Cutty Sark*.

This chapter studies the performance of a ship exploiting the wind energy with wingsails, wave energy with wavefoils, and solar energy with solar panels. The route chosen is Ponta Delgada, Azores - Funchal, Madeira, round-trip, see Figure 6.1. The main reason for choosing this route is that free wind and wave statistics

were available for the route from `www.globalwavestatisticsonline.com`. Furthermore, the route has good wind, wave and sun conditions, making it ideal for a ship powered purely by renewable energy. For simplicity, the ship is assumed to travel in a straight line, perfectly southeast from Ponta Delgada to Funchal – although the route in reality curves along the Madeiran coast the very last part. Vice versa, the ship is assumed to travel perfectly northwest from Funchal to Ponta Delgada.

Figure 6.1: The route from Ponta Delgada to Funchal

6.2 The ship

6.2.1 Design specifications

A commonly studied container/cargo ship hull, the Series 60 $C_B = 0.6$ (Todd, 1963), was selected for the ship. Its length was chosen with wave propulsion in mind, i.e. L_{PP} being somewhat shorter than typical ocean waves, as was found preferable in Section 5.7. Main particulars of the ship are given in Table 6.1.

The ship was equipped with five wingsails and two wavefoils: one slightly ahead of the bow, and the other astern of the stern. An illustration of the ship, showing the locations of the wingsails and wavefoils, is given in Figure 6.2.

The residual resistance coefficient (due to wave generation), C_R, of the hull was calculated from

$$C_R = C_T - (1 + k)C_F, \tag{6.1}$$

where the total resistance coefficient, C_T, was taken from model tests with the Series 60 hull (Longo and Stern, 2002), and the frictional resistance, C_F, was

Length overall	80.000 m
Length on waterline	79.999 m
Length between perpendiculars	78.999 m
Breadth at waterline	11.434 m
Draught	4.278 m
Volume displacement	2330 m^3
Wetted surface area	1127 m^2
Block coefficient (C_B)	0.5955
Prismatic coefficient	0.6097

Table 6.1: Main particulars of the ship.

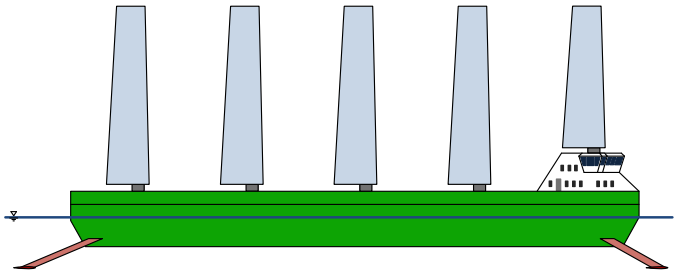

Figure 6.2: Illustration of the ship, showing the locations of the wingsails and the wavefoils

calculated from

$$C_F = \frac{0.075}{(\log Re - 2)^2}. \tag{6.2}$$

The form factor, k, was calculated to be 0.0741 by using MARINTEK's expression for the form factor (Steen and Minsaas, 2012):

$$k = 0.6\Phi + 75\Phi^3, \tag{6.3}$$

where

$$\Phi = \frac{C_B}{L_{WL}}\sqrt{2BT}. \tag{6.4}$$

In Eq. 6.4, B is the breadth, and T is the draft. The total resistance coefficient for the ship in the scale used in this chapter was then obtained from Eq. 6.1:

$$C_T = C_R + (1 + k)C_F, \tag{6.5}$$

where C_F is different in the scale used in this chapter than in Longo and Stern (2002).

The polynomial

$$R = 485.93U^3 - 1957.7U^2 + 10124U, \tag{6.6}$$

where R is the resistance in Newton and U is the ship speed in m/s, was a good fit to the calculated resistance curve and used as calm water input in the simulations, since a resistance polynomial is needed as input in VeSim.

6.2.2 Wingsails

Five wingsails having the NACA 0015 profile were mounted on the ship's deck, with their quarter chords 9.42 m, 25.26 m, 41.10 m, 56.94 m, and 72.78 m ahead of the aft perpendicular, as shown in Figure 6.2. The root chord length was 6 m and the tip chord length was 4 m. The aft four wingsails roots were 8.66 m above the baseline, whereas the front wingsail root was 13.73 m above the baseline. All wingsails tips were 33.41 m above the baseline. Since the gaps between the wingsails and the ship deck were less than 0.06 of the wingsail height, it is fair to assume that the induced drag is that of a wing with the same planform and half-span equal to the wingsail height (Hoerner and Borst, 1975).

The wingsails were divided into 10 spanwise strips. The chordwise and normal forces on each wingsail strip were calculated using the dynamic stall model described in Section 3.3. Aerodynamic interaction between the wingsails was neglected in this analysis. The interaction effect is dependent on the apparent wind angle, β. Miyasaka et al. (2013) showed that the average thrust per wingsail in a group of three wingsails can exceed the thrust of one wingsail in close reach ($\beta = 60°$) and broad reach ($\beta = 120°$) conditions. In wind abeam ($\beta = 90°$) condition, however, Miyasaka et al. (2013) found that the average thrust per wingsail was slightly lower than the thrust of one wingsail. Therefore, it appears that neglecting aerodynamic wingsail interaction is a reasonable simplification.

The angle of attack (α), the apparent wind angle (β), and the wingsail angle (δ_{ws}) are related through

$$\alpha = \beta - \delta_{ws}. \tag{6.7}$$

Based on varying δ_{ws} for all β values to optimize the forward thrust for a wind speed of 10 m/s and a ship speed of 12 knots, yet avoiding rapid changes in wingsail angle, δ_{ws} was set to be

$$\delta_{ws} = \begin{cases} 0, & 0° \leq \beta \leq 14°. \\ \beta - 14°, & 14° < \beta < 104°. \\ 90°, & \beta \geq 104°. \end{cases} \tag{6.8}$$

This procedure is illustrated in Figure 6.3. In following wind and waves, it was possible in a few sea states that the ship was propelled by the wavefoils at a speed fast enough for the apparent wind speed to be close to zero, or even head wind. To avoid very rapid wingsail motion, the wingsail angle was forced to remain at 90° in these cases. Since the ship is rolling and pitching, β will vary along the wingsail. β at the wingsails' lower tip was used when calculating the optimal wingsail angle in the simulations. Although only wind directions between 0° and 180° were simulated, the apparent wind angle could be negative for short amounts of time due to the ship motion. To avoid rapid changes in wingsail angle in these cases, the wingsail angle was programmed to remain unchanged in these cases, i.e., remain at 0° or 90°. $\dot{\delta}$ and $\ddot{\delta}$ in Eq. 3.36 were calculated by subtracting the value at the previous time step from the value at the current time step and dividing by the time step, since values at even earlier time steps were not easily available in VeSim. This led to unphysical wingsail forces when the wingsail angle changed

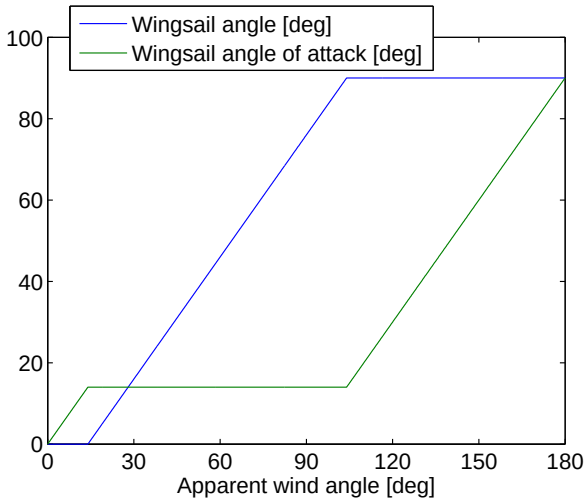

Figure 6.3: Wingsail angle and corresponding angle of attack applied in the simulations

abruptly. To overcome this, the terms in Eq. 3.36 proportional to $\dot{\delta}$ and $\ddot{\delta}$ were simply ignored when calculating the wingsail forces.

6.2.3 Wavefoils

Two spring-loaded wavefoils, also having the NACA 0015 profile, provided propulsive thrust for the ship in waves. Each wavefoil consisted of two halves, with trapezoidal planform, which could rotate in pitch independently of each other. The inner tip chord length of each half was 3 m, the outer tip chord length was 2 m, and the semi-span of each wavefoil was 12 m. The front wavefoil's quarter chord was located 2.21 m ahead of the fore perpendicular, whereas the aft wavefoil's quarter-chord was located 5.65 m aft of the aft perpendicular. The wavefoils were located 3 m below the baseline. The moment of inertia, I, of the semi-span of the foil (assuming that the foil halves could pitch independently of each other) was estimated to be 6,300 kgm^2.

The wavefoils were supported by struts, also assumed to be of the NACA 0015 profile, with longitudinal orientations shown in Figure 6.2. The struts had a chord length of 1.96 m. The roots of the front struts were 0.465 m from the centerline of the ship, and the roots of the aft struts were 0.407 m from the centerline of the ship. These distances were determined by the hull shape of the vessel. All strut tips were 4 m from the centerline of the ship.

It was found that when reducing the spring stiffness so that the angle of attack approached zero, the wavefoil thrust decreased but the thrust from the struts that supported the wavefoils increased, due to increased ship motions. When the significant wave height, H_s, was below 3 m, the spring stiffness was set to 500,000 Nm/rad, when H_s was between 3 and 5 m the spring stiffness was set

to 1,000,000 Nm/rad, and when H_s was above 5 m the spring stiffness was set to 2,000,000 Nm/rad. For head sea waves with $H_s = 0.5$ m, it was found that a spring stiffness of 500,000 Nm/rad gave unphysical foil behavior, with very rapid foil pitch oscillations. Setting the spring stiffness to 200,000 Nm/rad for these runs solved this problem.

6.2.4 Solar power

The ship was assumed to use solar power only to provide the necessary electricity needed on board. It was assumed that the ship has 400 m^2 of the deck area covered by solar panels which are completely exposed to the sun. This is, of course, a simplification, as the wingsails will shade the solar panels, but can be compensated by a larger solar panel area.

6.3 Weather assumptions

6.3.1 Calculating wind speed from sea state

To limit the number of simulations, the wind and waves were assumed to come from the same direction. From available scatter diagrams of H_s and spectral peak period, T_p, a corresponding wind speed was calculated. In order to do so, the simplified form of the two-peaked Torsethaugen wave spectrum (Det Norske Veritas, 2010) was used, which gives two H_s and T_p pairs – one due to wind-dominated sea, $H_{s,w}$ and $T_{p,w}$, and the other due to swell-dominated sea, $H_{s,sw}$ and $T_{p,sw}$. Assuming that $H_{s,w}$ and $T_{p,w}$ were due to fully developed wind-generated sea with unlimited fetch, the following relation (Tucker and Pitt, 2001) was used,

$$H_{s,w} = 0.025 V_W^2, \tag{6.9}$$

which is based on the JONSWAP spectrum, to calculate the wind speed at 10 m elevation above the sea surface, V_W, corresponding to a given $H_{s,w}$. Furthermore, T_p was calculated from the mean zero-up-crossing period, T_{m02}, through

$$\frac{T_p}{T_{m02}} = 1.41, \tag{6.10}$$

which is valid for a Pierson-Moskowitz spectrum. When using the Torsethaugen spectrum, Eq. 6.10 will be an approximation, as T_p/T_{m02} strictly depends on the spectral shape. Figure 6.4 shows the resulting V_W as a function of H_s and T_{m02}. We see that the wind speed increases with the wave height in the wind-dominated sea region. In the swell-dominated sea region, however, both H_s and T_{m02} must increase for the wind speed to increase. At the intersection between wind-dominated sea and swell-dominated sea, there is a marked "trench" with zero wind, which has no physical justification. The Harris wind gust spectrum was used in the simulations, based on V_W as the 10-minute mean wind speed.

Wave scatter tables for the ocean region between the Azores and Madeira were available at `www.globalwavestatisticsonline.com` for all wave directions

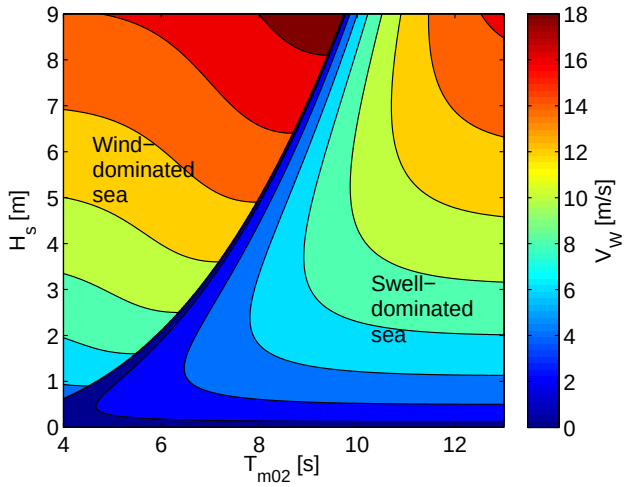

Figure 6.4: Wind speed (V_W) as a function of significant wave height (H_s) and mean zero-crossing period (T_{m02})

in 45-degree intervals and all four seasons, and also a table covering all directions and all year. Using the all-directions-all-year wave scatter table and Figure 6.4, a cumulative distribution function (CDF) for the wind speed was generated and compared with a CDF based on observed wind speeds from `www.globalwavestatisticsonline.com` in Figure 6.5. Note that the approach described here gives a CDF that is relatively consistent with observed data, despite the unphysical zero wind "trench".

6.3.2 Solar intensity

An average yearly solar intensity of 190 W/m^2 (International Renewable Energy Agency, 2013) and a photovoltaic panel efficiency of 18.8% (PlanetSolar, 2013) were assumed, giving the ship solar power of 35.72 W/m^2. With 400 m^2 of completely exposed solar panels, 14.3 kW of power was generated on average for use on board the ship. This should be sufficient for the moderate-sized ship, especially considering that with a battery, energy can be stored when little power is consumed.

6.4 Ship speed calculations

In order to calculate the expected ship speed and corresponding standard deviation for all seasons and both legs, the ship speed was first calculated for all sea states and all wave directions relative to the ship heading. The wind direction was, as mentioned earlier, the same as the wave direction. To limit the number of simulations, the ship was exposed to waves and wind from head to following seas

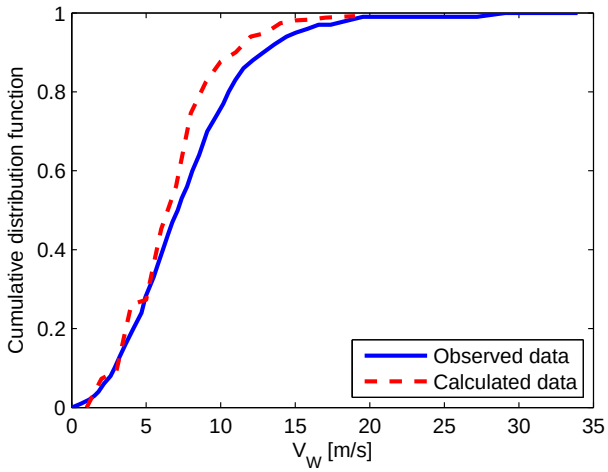

Figure 6.5: Cumulative distribution function (CDF) for wind speed from `www.globalwavestatisticsonline.com` (Observed data) compared with the CDF for the wind speed calculated from the wave scatter table (Calculated data)

in steps of 45°. Since the ship is symmetrical about the centerline, it was sufficient to simulate waves and wind from starboard side only. The available wave scatter diagrams were given for H_s in the range 0-14 m in steps of 1 m, and >14 m, and T_{m02} in the range <4 s, 4-14 s in steps of 1 s, and >14 s. It is not likely that the ship would sail if $H_s > 7$ m, so only H_s values from 0.5 m to 6.5 m in steps of 1 m and T_{m02} values from 3.5 s to 14.5 s in steps of 1 s were simulated. Figures 6.6-6.10 show the mean ship speed as a function of sea state for all wind and wave directions. We see that the highest ship speeds occur in beam wind and waves, and the "trench" with zero wind can be recognized in the ship speed plots. Figures 6.6-6.10 were generated based on 1500 s simulations, where the ship speed was calculated based on the distance covered the last 800 s. If another wave seed had been used, or the simulation time had been different, the mean ship speeds would have changed somewhat.

VeSim generates realistic short-crested waves by multiplying the wave spectrum by a spreading function, $D(\theta)$, where θ is the primary direction of wave propagation. The spreading function used in VeSim has the form (Fathi, 2013)

$$D(\theta) = \begin{cases} d\cos^2\left(\frac{\theta\pi}{2\delta}\right), & -\delta \le \theta \le \delta. \\ 0, & \theta < -\delta \text{ or } \theta > \delta. \end{cases} \tag{6.11}$$

where

$$d = 1/\left(\int_{-\delta}^{\delta} \cos^2\left(\frac{\theta\pi}{2\delta}\right) \mathrm{d}\theta\right). \tag{6.12}$$

δ can take any value between 0 (long-crested waves) and $\pi/2$ (most short-crested waves). $\delta = \pi/2$ was used in the simulations. The effect of short-crestedness and

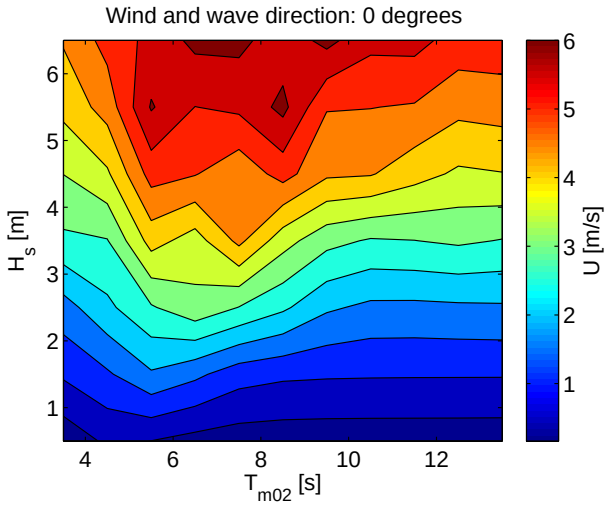

Figure 6.6: Ship speed plot, wind and wave direction 0 degrees (head sea)

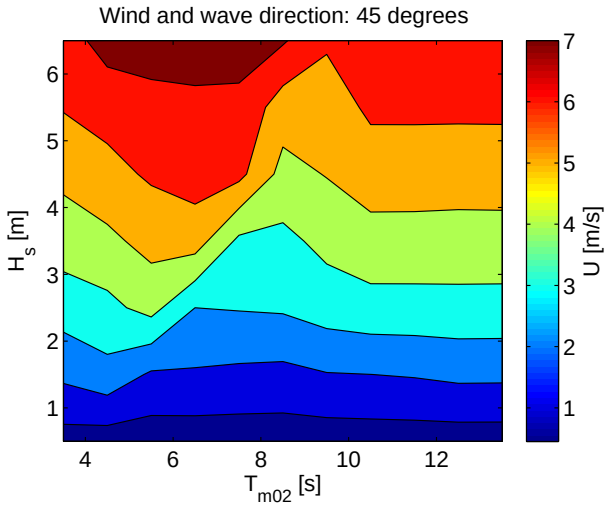

Figure 6.7: Ship speed plot, wind and wave direction 45 degrees (head quartering seas)

irregular waves was also studied, and is worth noting: For head sea waves and wind with $H_s = 3.5$ m, $T_{m02} = 6.5$ s, $V_W = 11.7$ m/s, the ship speed was 3.77 m/s for short-crested irregular waves, 2.57 m/s for almost long-crested irregular waves $\left(\delta = \frac{10}{180}\pi\right)$, and as fast as 7.15 m/s for long-crested regular waves.

For all seasons and both legs, the wind direction relative to the ship heading was calculated. Since the wind directions with available statistics were north, northeast, east, etc., and the ship was assumed to sail directly southeast when sailing toward

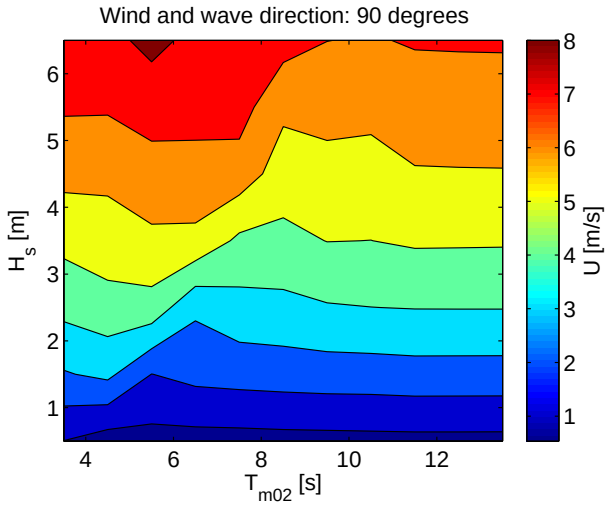

Figure 6.8: Ship speed plot, wind and wave direction 90 degrees (beam seas)

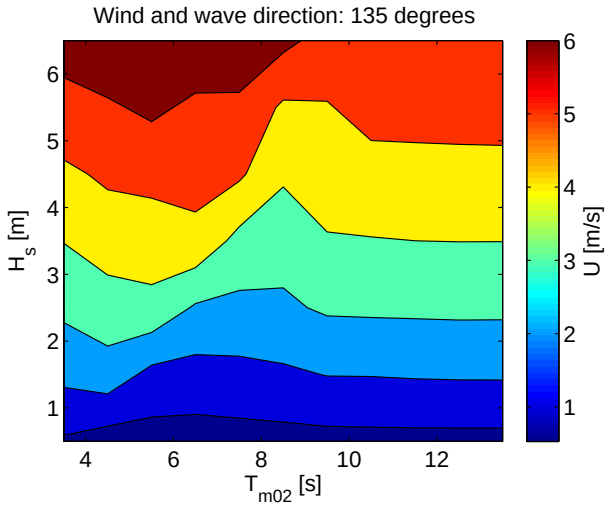

Figure 6.9: Ship speed plot, wind and wave direction 135 degrees (following quartering seas)

Funchal and directly northwest when sailing toward Ponta Delgada, the calculated wind directions relative to the ship heading conveniently turned up to be covered by the range the ship speed was calculated for.

The probability of a combination of a certain sea state and wind direction was calculated by multiplying the probability of the sea state given the wind direction by the probability of that wind direction occurring. For a given season and leg, the CDF value for a certain U value was calculated by summing up the probabilities of

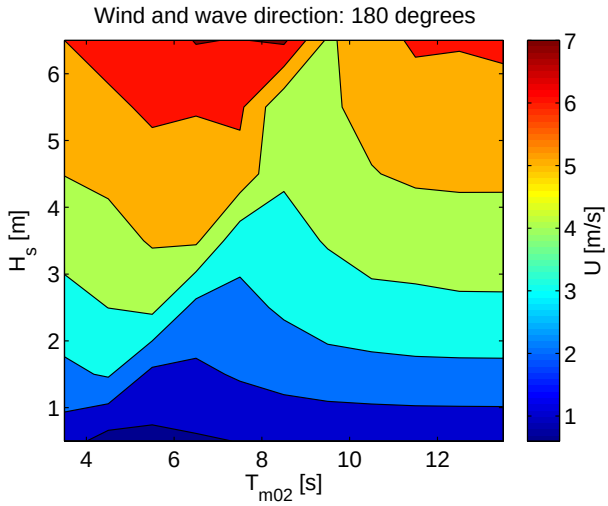

Figure 6.10: Ship speed plot, wind and wave direction 180 degrees (following seas)

the sea state and direction combinations giving lower values of U. The CDF of U for the ship traveling toward Ponta Delgada in the winter is shown in Figure 6.11.

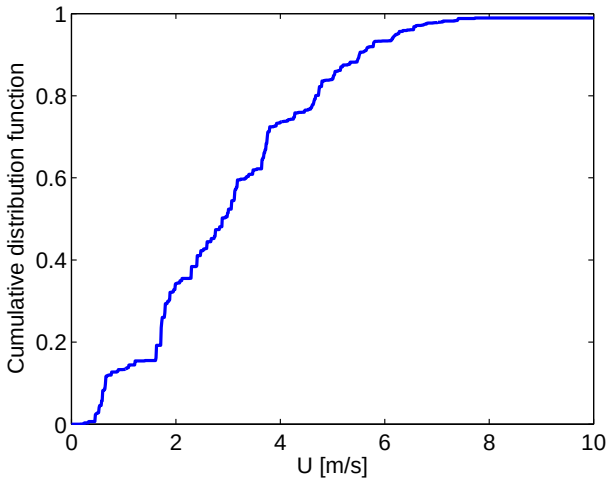

Figure 6.11: CDF for the ship speed when traveling toward Ponta Delgada in the winter

Knowing the CDF for the vessel speed, $F(u)$, the expected value, $E[U]$, was calculated from

$$E[U] = \int_0^\infty (1 - F(u))\, du. \tag{6.13}$$

The variance, σ^2, was calculated from

$$\sigma^2 = 2\int_0^\infty u\,(1 - F(u))\,du - (E[U])^2\,, \tag{6.14}$$

where σ is the standard deviation.

The resulting expected values and standard deviations of the ship speed, for both legs and all four seasons, are shown in Table 6.2. Since sea states with $H_s > 6.5$ m were not simulated, the CDFs were modified so that the cumulative probability of all combinations of wave directions and sea states with $H_s \leq 6.5$ m was 1. In the table of wind direction probabilities for the area from `www.globalwavestatisticsonline.com`, the sum of the probabilities of all the wind directions is not entirely 1, however, resulting in the cumulative probability of all combinations of wave directions and sea states with $H_s \leq 6.5$ m being marginally less than 1. The probability of $H_s > 6.5$ m occurring is small: 4.41%.

Season	**Expected value of ship speed [m/s]** Toward Funchal / Toward Ponta Delgada	**Standard deviation of ship speed [m/s]** Toward Funchal / Toward Ponta Delgada
Spring	2.90 / 2.90	2.06 / 2.11
Summer	2.47 / 2.50	2.19 / 2.22
Fall	2.78 / 2.79	2.14 / 2.17
Winter	3.16 / 3.16	2.04 / 2.07

Table 6.2: Ship speed statistics for all four seasons

To illustrate the distribution of propulsive force between the wingsails and the wavefoils, let us consider the sea state $H_s = 3.5$ m, $T_{m02} = 8.5$ s, $V_W = 7.2$ m/s. In this sea state, the wavefoils contributed to 100%, 58%, 56%, 67%, and 52% of the propulsive force, for wind and wave directions 0, 45, 90, 135, and 180 degrees, respectively. The rest of the propulsive force came from the wingsails. For the sea state $H_s = 1.5$ m, $T_{m02} = 11.5$ s, $V_W = 6.8$ m/s, the contribution from the wavefoils were 100%, 37%, 17%, 29%, and 7% for the same wind and wave directions.

6.5 Discussion

A ship whose speed is utterly dependent on the local weather conditions will not surprisingly see huge variations in the ship speed. The expected speeds of the ship described in this chapter are 5-6 knots, when sailing the route from Ponta Delgada to Funchal and back in all four seasons. The standard deviations of the ship speed are large: about 4 knots. The ship sailed over 14 knots in favorable wind and wave conditions, but such conditions are rare. The seasonal variations are quite small: The maximum seasonal difference in expected ship speed is the summer/winter difference of 1.3 knots when sailing toward Funchal.

If the ship is to keep a minimum speed of 5 knots, regardless of weather conditions, a propeller running on an auxiliary power source must be used when the

waves are small and the wind speed is low. When sailing toward Ponta Delgada in the winter, for instance, this means 43% of the time. A fair part of this required energy can probably be harvested by employing water turbines when the ship speed is higher than 5 knots and stored for later use with batteries.

Chapter 7

Experiments with a free-running ship model

7.1 Motivation

Although the model tests and simulations described in Chapter 5 showed the benefit of the wavefoil on ship resistance, more model tests were needed, for the following reasons:

- The model tests described in Chapter 5 were only done in head seas. The low fuel savings in following seas, found in Section 5.5, seemed worthy of further investigation.
- The model tests described in Chapter 5 were only done in regular waves. Based on the experiences with the simulations in Chapter 6, using regular waves would produce overly optimistic results compared to using irregular waves.
- A ship with a spring-loaded wavefoil had not been tested so far in the present work.
- A ship powered by a propeller, with the wavefoil providing auxiliary propulsion, had not been tested so far in the present work. Previous model tests of ships with wavefoils in the literature have mainly studied a ship entirely powered by the waves (e.g., Kjærland (1979); Kjærland (1980); Nagata et al. (2010)). In the model tests described in the following, however, the more commercially interesting case of a ship using wavefoils as auxiliary propulsion would be tested.

In addition, a new round of model tests with a smaller ship model would be a good opportunity to apply the optimization method described in Section 5.7 and build a physical model with – presumably – an optimal wavefoil.

For these reasons, a small radio-controlled ship model, powered by a propeller, seemed desirable to test. A ship model with a length of about 1 m would be suitable

to test in the frequently available basin described in Appendix C.1. Such a model can easily be taken in and out of water to remove the foil or to modify the spring stiffness, and the wavefoil would be small enough to be produced relatively cheap by a 3D-printer.

7.2 The ship

The ship selected for the experiments was a roll-on/roll-off (RORO) ship, with main particulars given in Table 7.1. It was chosen for this study because a working remote-controlled model in a suitable scale (1:101) for free-running tests was available to the author, and because it has a fairly general cargo ship shape. Lines plans of the ship are shown in Figure 7.1.

Main particulars	Full scale	Model scale
Design length	90.431 m	0.895 m
Length over all	98.079 m	0.971 m
Design beam	17.049 m	0.169 m
Beam over all	17.271 m	0.171 m
Design draft	3.830 m	0.038 m
Wetted surface area	1614 m^2	0.1582 m^2
Displaced volume	3601 m^3	3.4946E-3 m^3

Table 7.1: Main particulars of the RORO ship

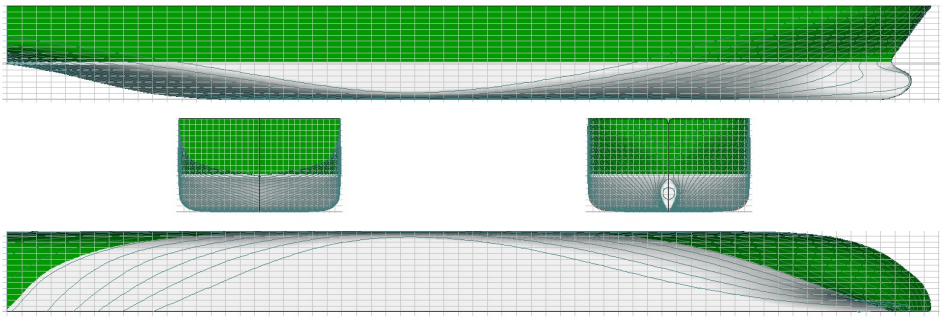

Figure 7.1: Linesplan of the RORO ship

7.3 Optimal foil size and location, design stage

When finding the optimal foil size and location, the procedure outlined in Section 5.6 was used to try multiple foil combinations and see which combination gave the highest foil thrust. $C_{Dv} = 0.01$ was used in the calculations. There are many parameters that be can be varied but to limit the scope of the analysis the foil

configuration that gave the highest thrust for a ship speed of 12 knots and a wave height of 2 m was sought. First, the ship was assumed to have two fixed wavefoils, one near the bow and the other near the stern, where both foils were of equal elliptical planform, chord, and span, and both foils were located at the same z_f-coordinate. To reduce the risk of foil slamming, the foils' vertical position was chosen to be 5 m below the baseline of the ship, i.e., z_f = -8.83 m. The spanwise center of both foils were located at the ship's centerline.

The front foil was located at x_f = -50 m, and the stern foil was located x_f = 50 m, with the foil's maximum chord length and span being 4 m and 15 m, respectively. The corresponding total foil thrust as a function of wave period is shown in Figure 7.2.

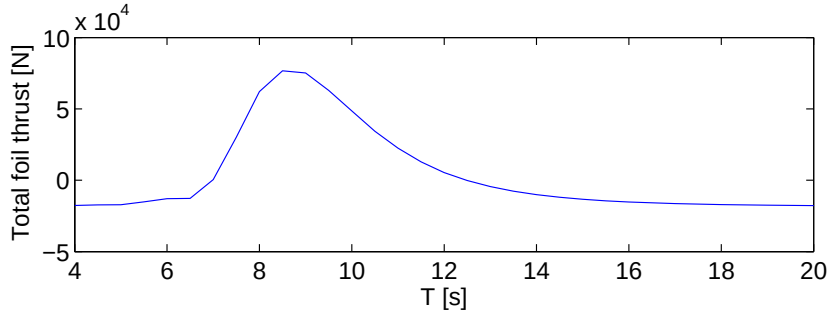

Figure 7.2: Total foil thrust vs. wave period with bow foil located at x_f = -50 m and stern foil located at x_f = 50 m

Next, the wave period that gave the highest total foil thrust was chosen, i.e., T = 8.5 s, the same foil chord and span was kept, and the corresponding total foil thrust as a function of the longitudinal location of both foils was plotted, see Figure 7.3. x_f = -61 m for the bow foil, and x_f = 53 m for the stern foil was selected as a compromise between high total foil thrust and the foils not located too far forward or aft of the ship. For this foil location combination, the foil thrust is plotted against the foil span in Figure 7.4. For the same foil dimensions and foil locations, a similar plot as Figure 7.2 now showed that the maximum total foil thrust was found for a wave period of 9 s. Using this wave period, the foil span was varied again, and the optimal foil span was now found to be 26 m, see Figure 7.4.

Using the same maximum chord length and foil positions, with T = 9 s and a foil span of 26 m, z_f was varied to study the effect of vertical foil location on the foil thrust, see Figure 7.5. We see that the foil thrust increases with decreasing foil depth because of higher water velocity relative to the foil. This is also the case with bow foil only, whereas with stern foil only, the foil thrust increases with increasing foil depth.

It is interesting to note that for the maximum total foil thrust in Figure 7.4, the bow foil thrust was 103 kN while the stern foil thrust was only 4 kN. When the bow foil was removed, the stern foil thrust increased to 25 kN, whereas when the stern foil was removed, the bow foil thrust increased to 111 kN. Considering

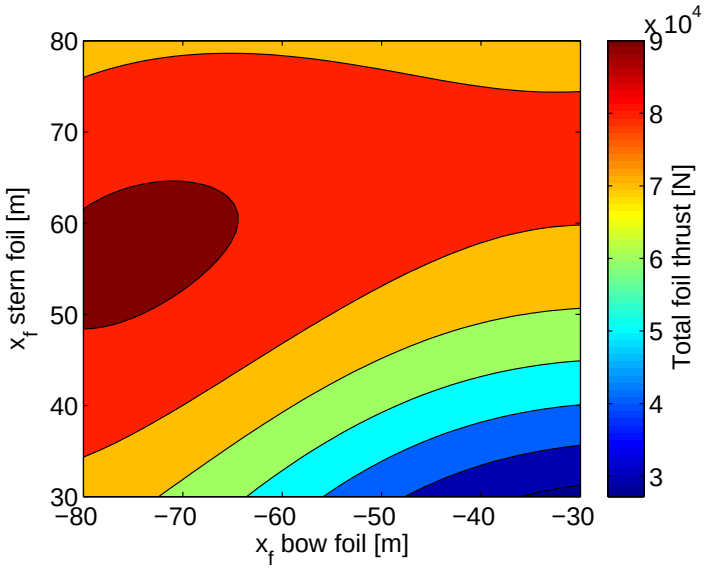

Figure 7.3: Total foil thrust vs. longitudinal location of foils for $T = 8.5$ s

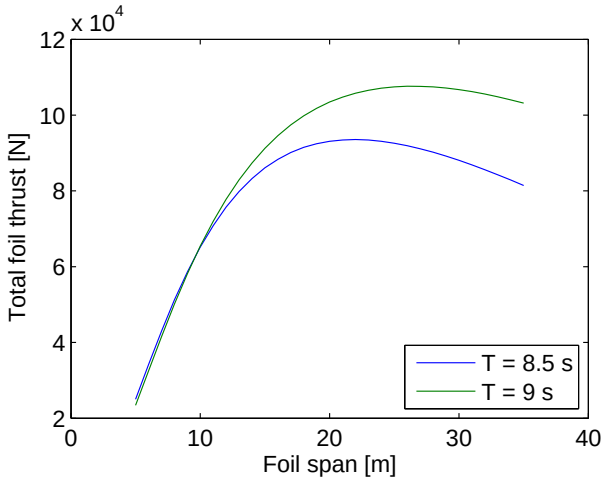

Figure 7.4: Total foil thrust vs. foil span. x_f = -61 m for the bow foil and x_f = 53 m for the stern foil.

the foil thrust, there appears to be no need for a stern foil if a bow foil is already installed, according to the frequency-domain model. The span maximizing the foil thrust was found to be 27 m for both the case of bow foil only and the case of stern foil only. The final foil design therefore ended up having a span of 27 cm.

Figure 7.6 shows the total foil thrust when the spans of the bow foil and the stern foil are different. The foil locations were the same as in Figures 7.4 and 7.5,

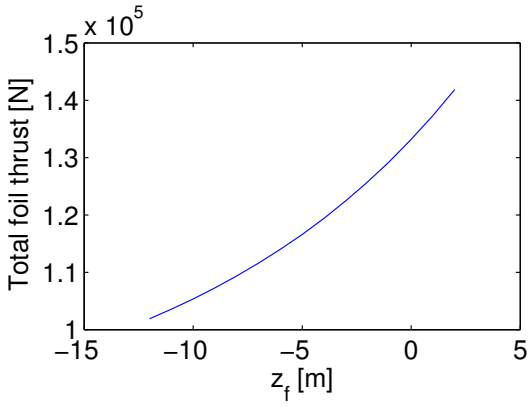

Figure 7.5: Total foil thrust vs. vertical location of foils. $T = 9$ s, x_f = -61 m for the bow foil, $x_f = 53$ m for the stern foil, and the foil span was 26 m.

and the wave period was $T = 9$ s. We see that when the bow foil span is larger than approximately 5 m, there is no need to employ a stern foil in order to maximize the foil thrust.

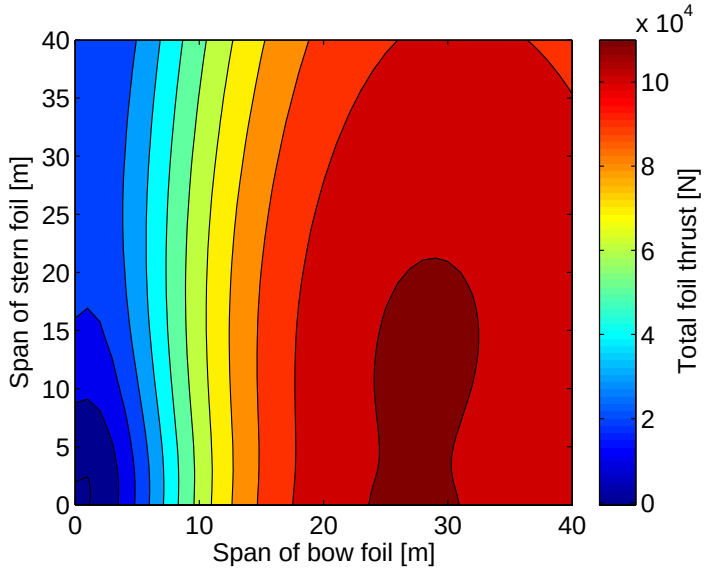

Figure 7.6: Total foil thrust vs. bow and stern foil span. $T = 9$ s, x_f = -61 m for the bow foil, and $x_f = 53$ m for the stern foil.

7.4 Foils and struts

The foils and struts, see Figure 7.7 for a 3D-rendering, were designed by the author and 3D-printed by the 3D-printing company Shapeways. A picture of the foils and struts is given in Figure 7.8. A piano wire inside the foil acted as a torsion spring between the foil and the strut. Due to the strength of the material and the 3D-printing accuracy, a certain thickness of the foil was required. The required thickness was obtained with a maximum chord length of 4 cm and the foil profile being NACA 0017.

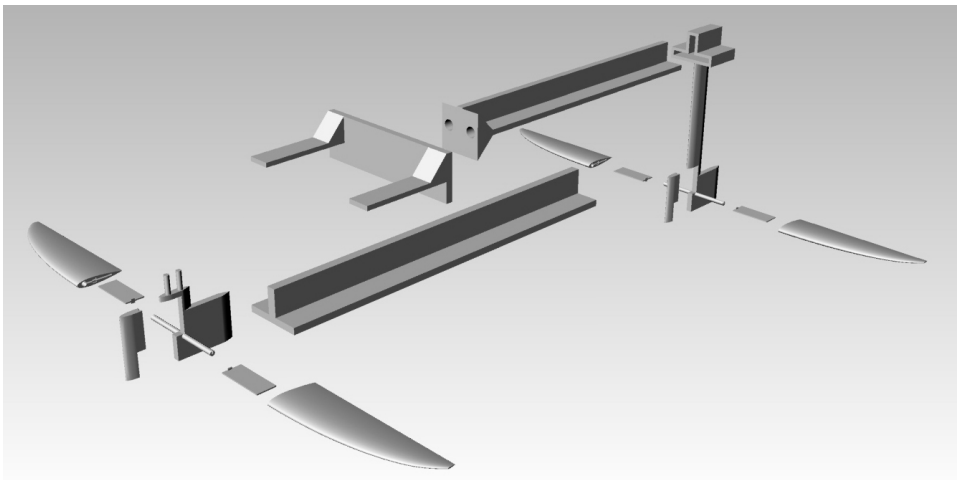

Figure 7.7: 3D-rendering of the foils, struts, and supporting parts

When outfitting the model for wave propulsion, the author wanted to have the possibility of mounting the wavefoils at different longitudinal positions. Therefore, the ship was equipped with a rail extending forward from the bow, and another rail extending astern of the stern, which a strut supporting the foil could be mounted on, see Figure 7.9. The shortest strut in Figures 7.7 and 7.8 was mounted underneath the bulb (see Figure 7.10), which was considered to be the most realistic position for a full-scale vessel yet at the same time hydrodynamically advantageous. During the tests, only the strut that could be mounted underneath the bulb was used. The rails extending forward and aft were still present during the tests, however, to give the ship a more realistic radius of gyration in pitch, since the mass of the model was mostly located near the longitudinal center of the model. The idea behind the dividing wall between the two foil halves was to reduce induced drag from the foil roots, since the two foil halves could pitch independently of each other.

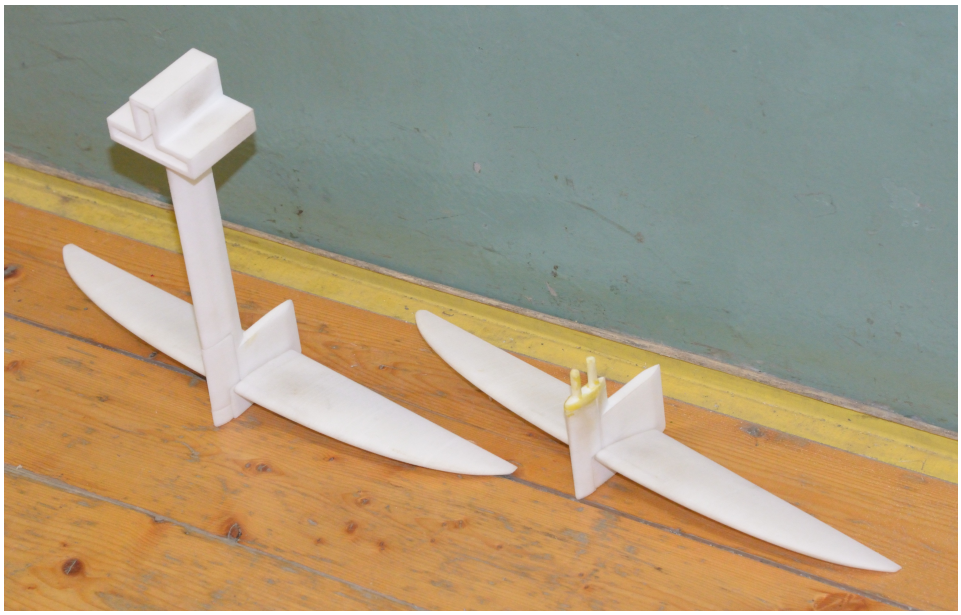

Figure 7.8: Picture of the foils and the struts. Only the short strut, to be mounted underneath the bulb, was used in the experiments.

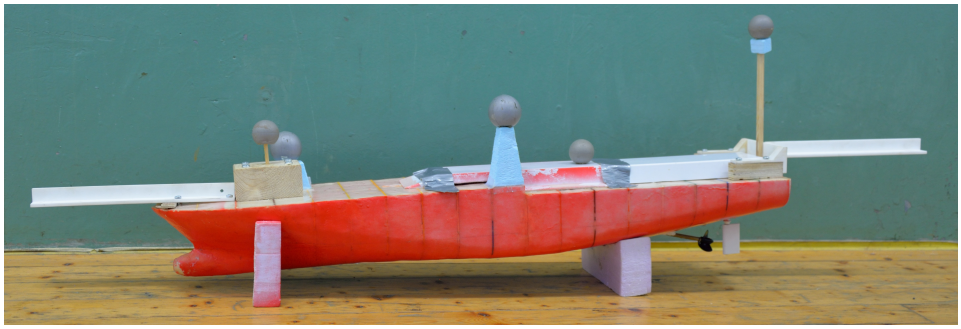

Figure 7.9: The free-running ship model on land, showing the front and back rail which the longer strut could be mounted on and the grey motion tracking balls. The front rail is bent up to avoid hitting the water.

7.5 Calm water performance

7.5.1 Experiment setup

The ship model was powered by a 3000 mAh battery, powering both the rudder servo and the motor to the propeller. Also powered by the same battery was an Arduino Uno R3 microcontroller. Connected to the motor and the Arduino was a voltage and current sensor (AttoPilot Voltage and Current Sense Breakout - 45A)

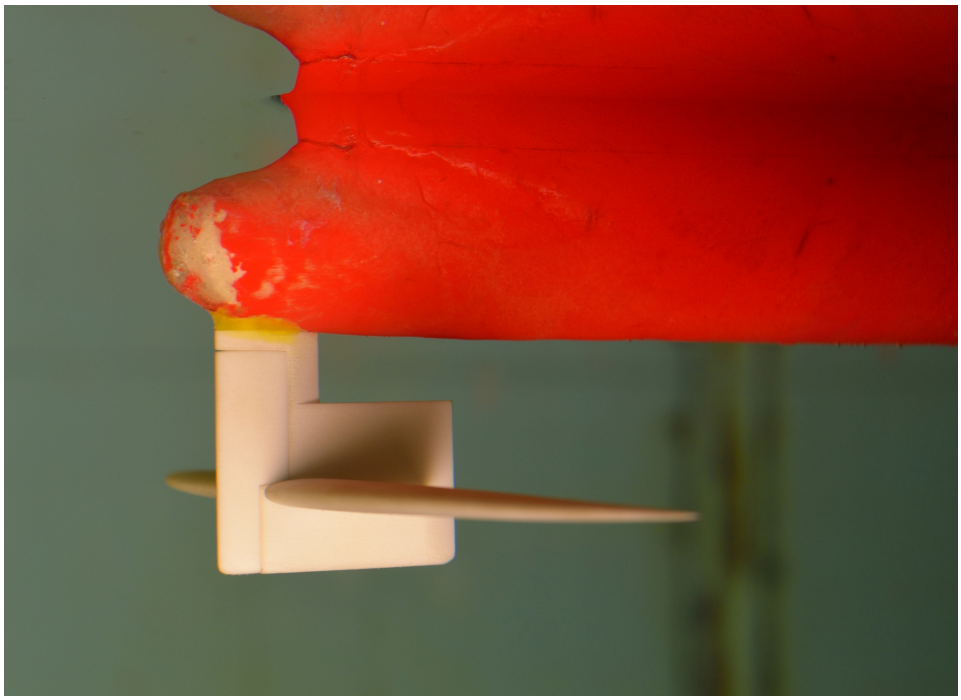

Figure 7.10: Underwater image (taken through glass) of the free-running ship model showing the foils on the small strut attached to the bulb

which measured the voltage and the current going to the motor and sent the signals to the Arduino. The current and voltage information was then transmitted from the Arduino, via a Bluetooth receiver/transmitter called Bluetooth Mate Silver, to a computer logging the motor power, see Figures 7.11 and 7.16. All the electronics on the ship model were covered by a plastic cover, visible in Figure 7.9.

To avoid unnecessary fluctuations in the motor power when trying to keep the remote control's throttle stable manually, the throttle signal was routed to a Variref external power source, see Figure 7.12. This setup made it possible to set the exact throttle voltage and keep it constant. Although the throttle voltage was constant, the motor power would fluctuate due to varying propeller loading and battery conditions, so measuring the motor power was still necessary.

Figure 7.13 shows the bare hull being towed in calm water. Since the motion tracking balls were not in use during towing, the front ball was replaced by a rod, which the model was towed from. The rod was connected to a force sensor via perforated strip, which allowed the model to move freely in yaw, heave, and pitch, while keeping the model fixed in surge, sway, and roll. The force sensor was mounted to a wooden beam which was attached to the carriage in the small towing tank, as shown in Figure 7.13. For more information on the small towing tank, see Appendix C.3.

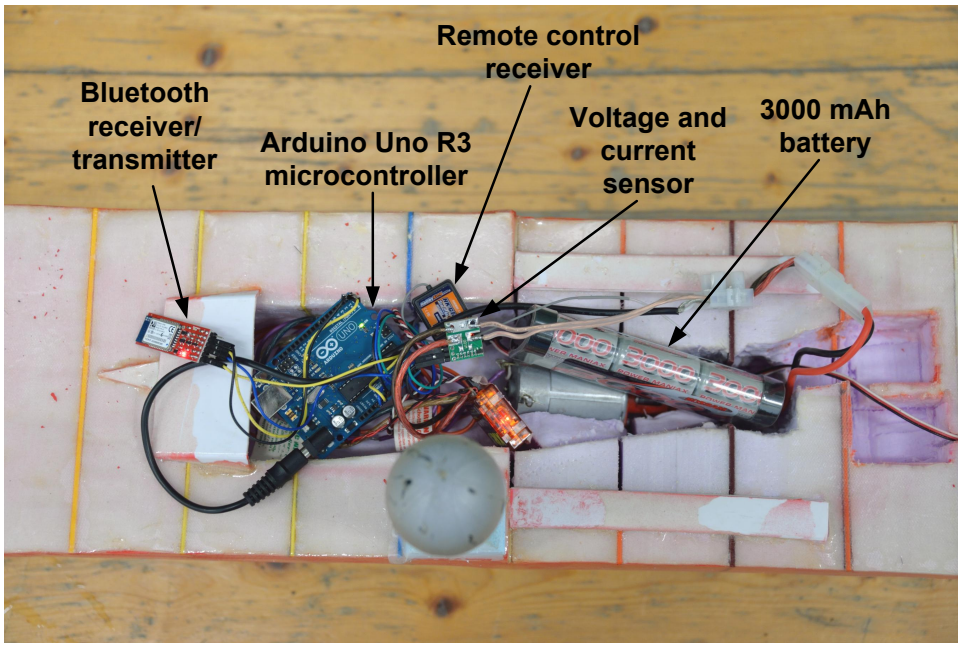

Figure 7.11: The electronics inside the free-running ship model

7.5.2 Calm water resistance

Figure 7.14 shows the model scale calm water resistance without foil and with the foil on a small strut mounted underneath the bulb, as shown in Figure 7.10. The strut and foil increased the resistance with 59% at a speed of 0.31 m/s, but only with 33% at 0.92 m/s. The reason for this decrease in strut resistance relative to the total resistance with increasing speed is that the ship generated waves at higher speeds, causing additional wave resistance, whereas the strut did not pierce the free surface and hence generated minimal wave resistance at the same speeds.

7.5.3 Propulsion characteristics

To determine the propulsion characteristics of the ship model, it was towed in the small towing tank at speeds from 0.20 to 0.82 m/s – corresponding to 4-16 knots in full scale – with varying motor power. The propeller thrust was determined by subtracting the ship resistance with a running propeller from the ship resistance in calm water without foil. Denoting the propeller power, which is the propeller thrust multiplied with the ship speed, P_T, and the power consumed by the electric motor, P_M, Figure 7.15 shows P_T vs. P_M for the ship speeds that were tested. We see that linear regression describes the relation between P_T and P_M fairly well, at all speeds. The slope of the P_T vs. P_M curve is the total propulsive efficiency of the propulsion system, and we see that it is very low – about 0.09 for the highest speed. It is likely that the vast majority of the propulsion losses are due to friction

Figure 7.12: The remote control of the free-running ship model, with the throttle controlled by an external power source

in the propeller shaft and losses in the electric system.

7.6 Performance in waves

7.6.1 Experiment setup

The model's motions were tracked using Qualisys Oqus motion tracking cameras and Qualisys software. Five motion tracking balls were used for the Qualisys Oqus cameras to see the model when it was free-running in waves, visible in Figure 7.9. Figure 7.16 shows the model sailing in head sea regular waves, and this view is close to the view from one of the Oqus cameras. The water surface elevation was measured using an electrical resistance-based wave sensor mounted on a wooden beam to get some clearance from the tank wall, see Figure 7.16.

First, the performance of the ship model was tested in regular waves with height 3.0 cm and periods 0.70 s, 0.90 s, and 1.09 s, corresponding to a full-scale wave height of 3 m and to full-scale periods of 7 s, 9 s, and 11 s. Then, the model was tested in irregular waves of the Pierson-Moskowitz spectrum with $H_s = 3.0$ cm and $T_p = 0.70$ s, 0.90 s, and 1.09 s. The model was manually steered via the remote control up and down the basin. The ship was seen by the Oqus cameras for a distance of approximately 12 m. When post-processing, the average speed and power consumption were found for a slightly shorter distance.

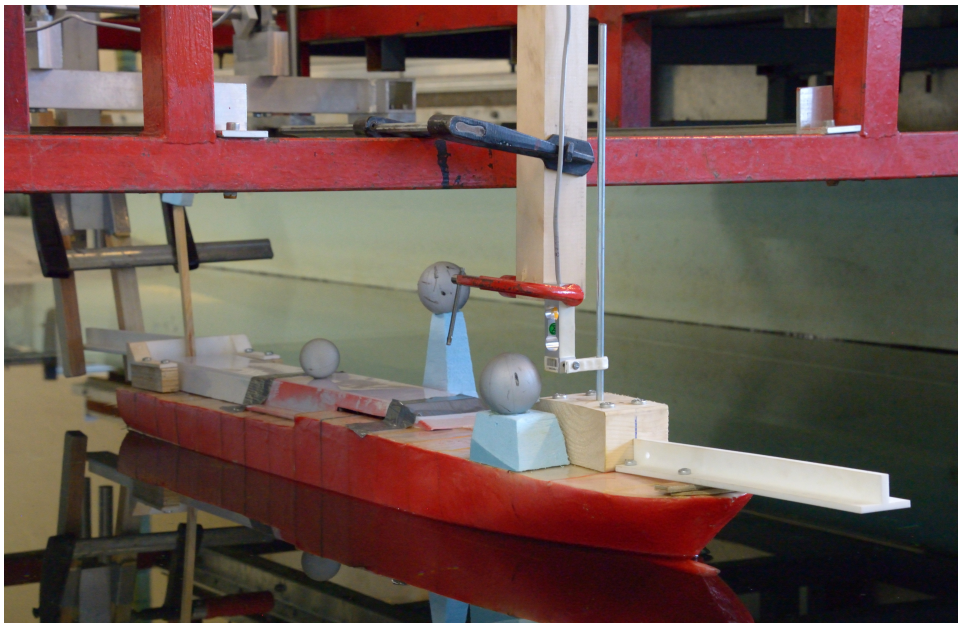

Figure 7.13: Towing the free-running ship model from the carriage in the small towing tank, see Appendix C.3

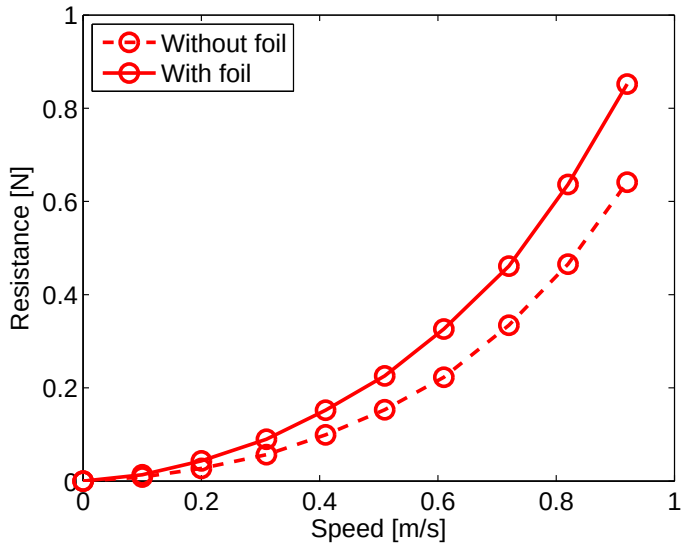

Figure 7.14: Calm water resistance for the free-running ship model, with and without foil, in model scale

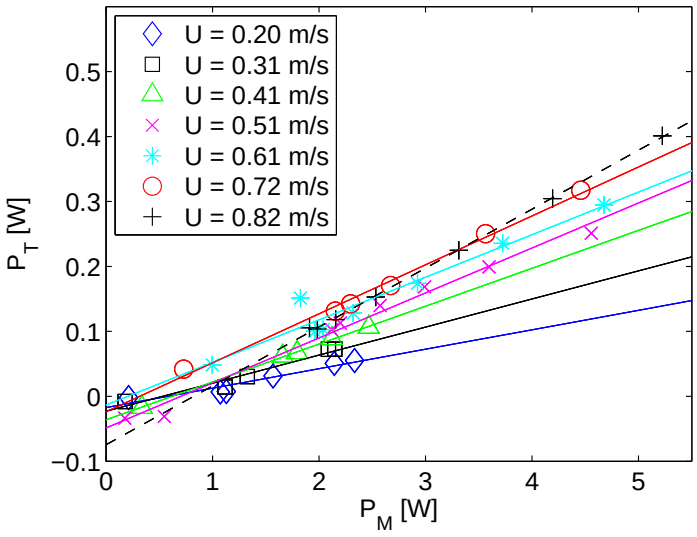

Figure 7.15: Propulsion characteristics in calm water for the free-running ship model. The solid lines are linear regression lines corresponding to the data points of the same color.

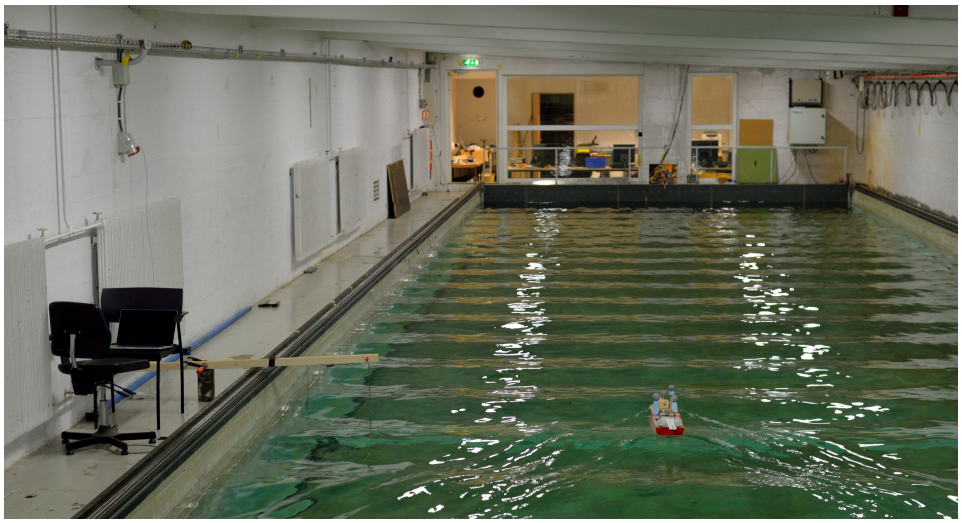

Figure 7.16: Experiment setup of the free-running ship model in waves, showing the computer logging the motor power via a Bluetooth connection on the chair to the left, the wave sensor mounted to the wooden beam, and the ship model sailing in head sea regular waves

In regular waves, only one run in head and following seas were done, for five different throttle settings. In irregular waves, four runs in head seas and four runs in following seas were done, to get reasonably large time series. In full scale, this corresponds to measuring data for a distance slightly shorter shorter than 4.85 km at each throttle setting and heading, in a particular sea state.

Two different springs were used in the foil, both in regular and in irregular waves: one with diameter 0.5 mm and the other with diameter 0.7 mm. A close-up view of the free-running ship model is shown in Figure 7.17.

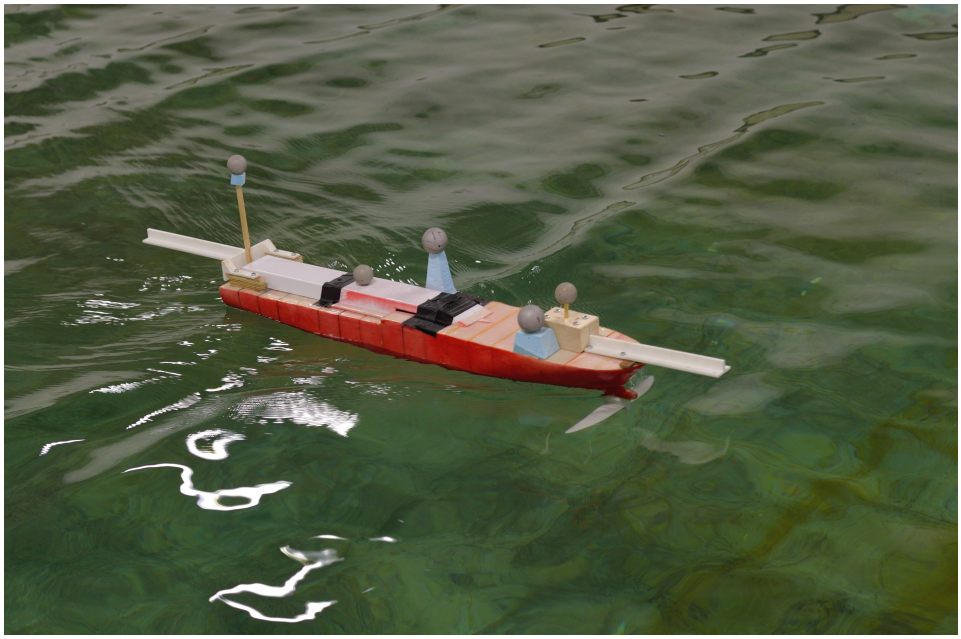

Figure 7.17: Close-up view of the free-running ship model propelling itself in following seas

7.6.2 Regular waves

The average speed and P_T in regular waves for the three wave periods, two headings, and five different throttle settings are shown in Figures 7.18, 7.19, and 7.20. P_T was found from measurement of P_M during the tests, and using linear interpolation in Figure 7.15 to relate P_M to P_T. This method was used because the experiment propeller was so small that it was not possible to measure the propeller thrust directly when the model was self-propelled in waves. We see that when employing the wavefoil, the ship required less P_T to sail at a particular speed only for the two lowest wave periods in head seas than when not employing the wavefoil. In Section 5.5, it was found through full-scale simulations – although with a different ship – that the benefit of the wavefoil in following seas was low. The present model test results are even more discouraging, showing negative effect of the foil at all wave

periods. As we shall see in Section 7.7, however, scale effects are important, and the results in full scale are much more uplifting.

The influence of the spring stiffness on the ship speed was small, although it appears from Figures 7.18, 7.19, and 7.20 that the softest spring (diameter 0.5 mm) was beneficial in regular waves, particularly in following seas.

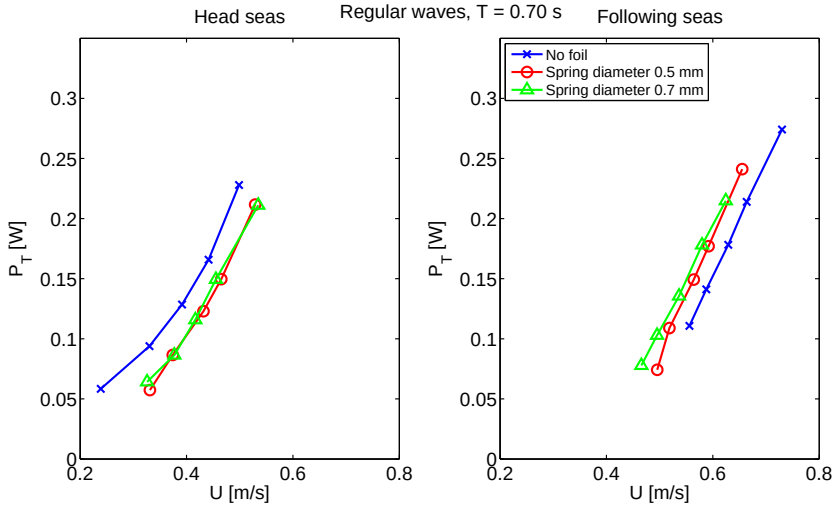

Figure 7.18: Results for the free-running ship model in regular waves, $T = 0.70$ s, head and following seas. $H = 3.0$ cm.

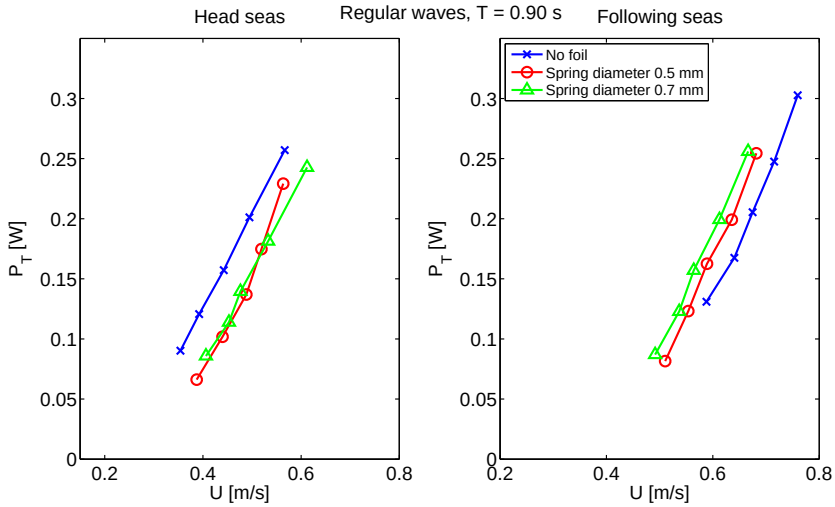

Figure 7.19: Results for the free-running ship model in regular waves, $T = 0.90$ s, head and following seas. $H = 3.0$ cm.

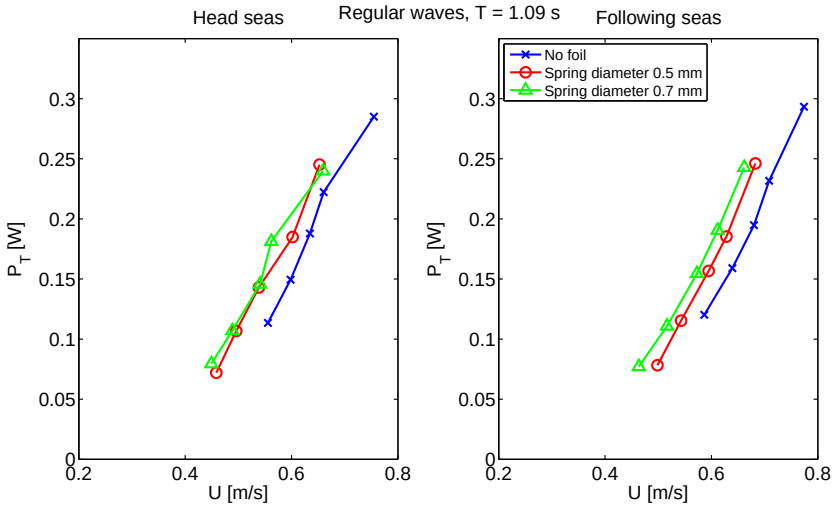

Figure 7.20: Results for the free-running ship model in regular waves, $T = 1.09$ s, head and following seas. $H = 3.0$ cm.

7.6.3 Irregular waves

Figures 7.21, 7.22, and 7.23 show the average speeds and P_T in irregular waves. In these figures, the speed and motor power were averaged over one run up or down the basin, and the average values for four runs up and down the basin values were then averaged.

As Figures 7.21, 7.22, and 7.23 show, the ship with wavefoil generally required less P_T to sail at a given speed in head seas than the ship without wavefoil. As was the case for regular waves, when employing the wavefoil, the ship required higher P_T to sail at a given speed in following seas. The influence of the spring stiffness on the ship speed was small also for irregular waves, but based on Figures 7.21, 7.22, and 7.23, the stiffest spring (diameter 0.7 mm) appears to have been weakly preferable. The opposite was concluded for regular waves, which one may expect, since the ship motions – and hence inflow angles to the foil – were generally larger in regular waves.

7.7 Comparison with simulations and scaling

Simulations were done in VeSim in both model and full scales. The model scale resistance curve for the bare hull was used as input in the model scale VeSim simulations, and model scale Reynolds number was used when calculating the foil forces. The strut resistance found from experiments was used in the simulations.

Figures 7.24, 7.25, and 7.26 show the experimental and simulated results compared, in regular waves. It is clear that there is not a good agreement between

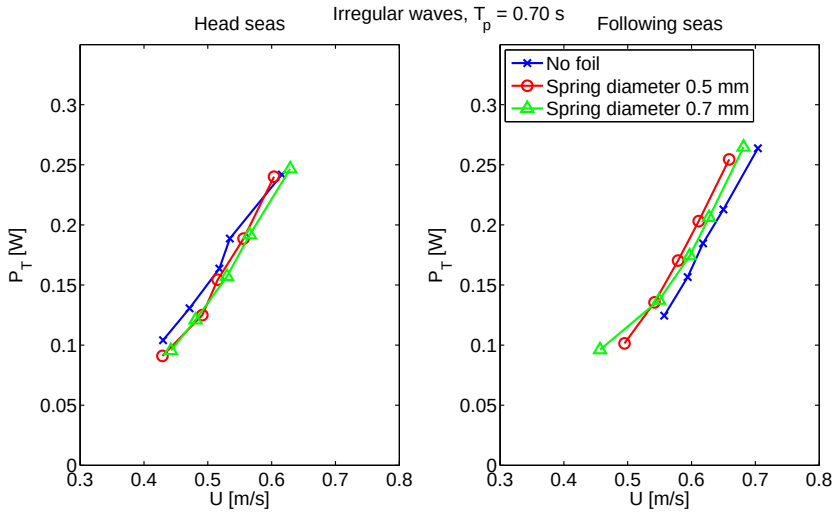

Figure 7.21: Results for the free-running ship model in irregular waves, $T_p = 0.70$ s, head and following seas. $H_s = 3.0$ cm.

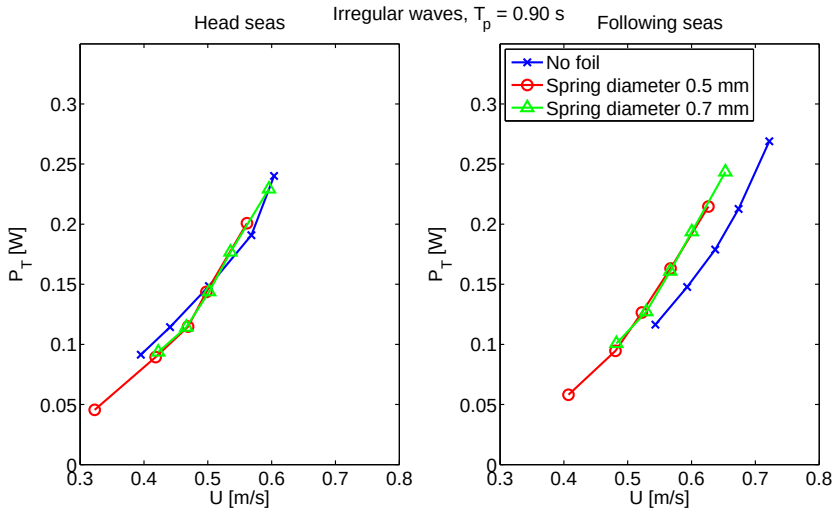

Figure 7.22: Results for the free-running ship model in irregular waves, $T_p = 0.90$ s, head and following seas. $H_s = 3.0$ cm.

experimental and simulated results, although two conclusions drawn from the experiments apply to the simulations as well: the influence of the spring stiffness on the ship speed was small, and the wavefoil was more beneficial in head than in following seas.

One reason for the discrepancies between the experimental and simulated re-

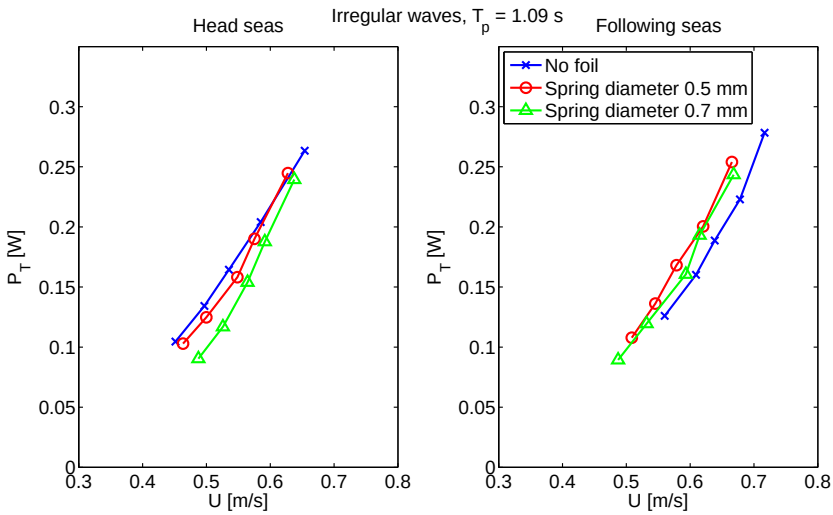

Figure 7.23: Results for the free-running ship model in irregular waves, $T_p = 1.09$ s, head and following seas. $H_s = 3.0$ cm.

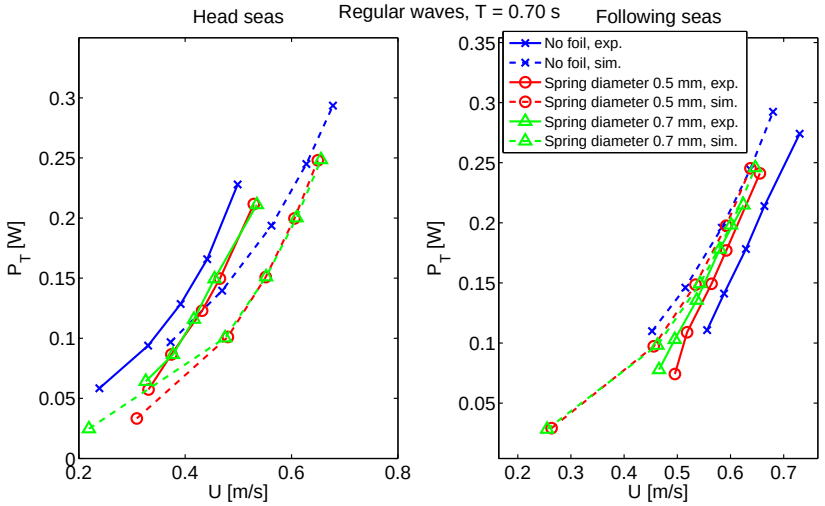

Figure 7.24: Comparison of simulations and experiments for the free-running ship model. Regular waves, $T = 0.70$ s, $H = 3.0$ cm.

sults is that the assumption that the propeller power in the experiments was a speed-dependent constant times the motor power (Figure 7.15) might be questionable. In other words, the propeller thrust, and hence P_T, in the experiments is uncertain. It was not possible to measure the propeller thrust directly using a conventional propeller dynamometer due to the size of the propeller, however, so

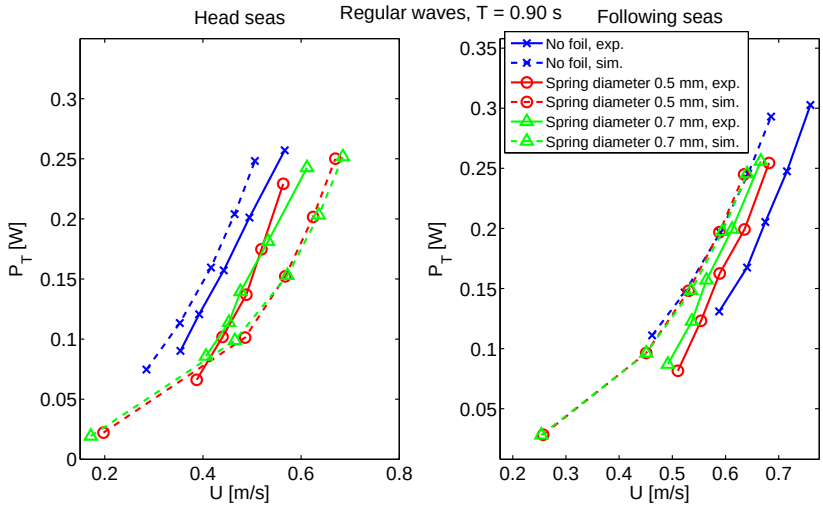

Figure 7.25: Comparison of simulations and experiments for the free-running ship model. Regular waves, $T = 0.90$ s, $H = 3.0$ cm.

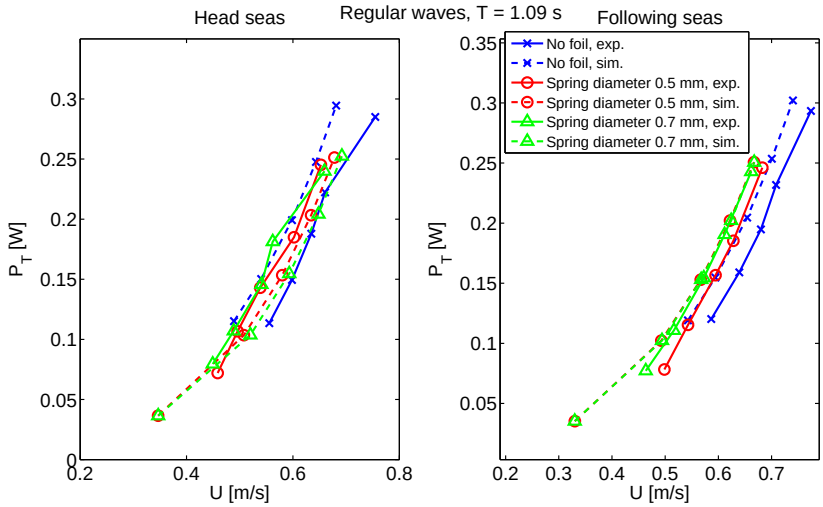

Figure 7.26: Comparison of simulations and experiments for the free-running ship model. Regular waves, $T = 1.09$ s, $H = 3.0$ cm.

this assumption had to be made in order to estimate the propeller thrust when the ship model was self-propelled in waves. Considering that there is a significant difference between experimental and simulated results without foil, the uncertainty in the actual propeller thrust in the experiments appears to be large.

Another reason for the discrepancies is that the foils in VeSim are a little differ-

ent from the actual foils used in the experiment. In VeSim, the wavefoil is assumed to be of the NACA 0015 profile and tapered, whereas the experiment foil was of the NACA 0017 profile and elliptical. It was convenient to assume the same foil profile in the present simulations as in the simulations in Chaper 5 since data tables of lift and drag coefficients were available for the NACA 0015 profile in Sheldahl and Klimas (1981), but not for NACA 0017. The difference in lift and drag coefficients between the two foil profiles were assumed to be small, since the foil was spring-loaded and therefore should avoid stall. In VeSim, the spring-loaded foils pitched about a point located $0.15c$ from the leading edge at the foil root. The experiment foil also pitched about a point located $0.15c$ from the leading edge at the foil root, but the elliptical and swept planform of the experiment foil implies that the hydrodynamic moment about the pivot point in the experiments was not directly comparable to that of the simulations.

To study if the discouraging low benefit of the wavefoil in the experiment was due to scale effects, let us assume that the foil forces are independent of Reynolds number. If the angle of attack is well below stall, this is almost correct for the foil lift. Froude's hypothesis says that the residual resistance coefficient is the same in model and full scale. The frictional resistance coefficient, however, decreases with Reynolds number, as is shown by Eq. 6.2. The total resistance coefficient will therefore be smaller in full scale than in model scale, and the wavefoil thrust will be larger relative to the resistance in full scale than in model scale.

Simulations were also done with full-scale calm water resistance as input, and using full-scale Reynolds number when calculating the foil forces. The full-scale resistance was obtained using the built-in method (based on the method by Holtrop (1984)) in the MARINTEK software ShipX HullVisc, and can be described by the polynomial

$$R = 65.854U^4 - 439.33U^3 + 6012U^2 + 3216U. \tag{7.1}$$

The strut was assumed to consist of two NACA 0015 foils of the same chord lengths as the two streamlined parts forming the experiment strut. Simulation results in full scale with regular waves are shown in Figures 7.27, 7.28, and 7.29. Simulation results in irregular waves are shown in Figures 7.30, 7.31, and 7.32. In the irregular waves simulations, the Pierson-Moskowitz spectrum was used with a wave spreading angle of 90°, i.e., maximum short-crestedness.

We see from Figures 7.30, 7.31, and 7.32 that the wavefoil was indeed much more beneficial in full scale than in model scale. The effect of spring stiffness was generally small, particularly in irregular waves. In regular head sea waves with period 9 s, the benefit of the wavefoil was enormous, with fuel savings over 80% at 10 knots. The reason for this is that the added resistance in head sea waves peaked at about 8-9 s, depending on the speed, and the wavefoil significantly reduced the added resistance. Of course, regular waves will never occur in reality in full scale.

Fuel savings for the full-scale ship – assuming that the fuel consumption is a constant times the propeller power – were calculated based on interpolating in Figures 7.27-7.32, and are presented in Tables 7.2, 7.3, and 7.4. "NaN" implies that linear interpolation was not possible from the data points in Figures 7.27-7.32. The fuel savings in irregular waves are somewhat lower than in regular waves, except in following seas for $T_p = 11$ s, where the fuel savings are negative for a ship speed

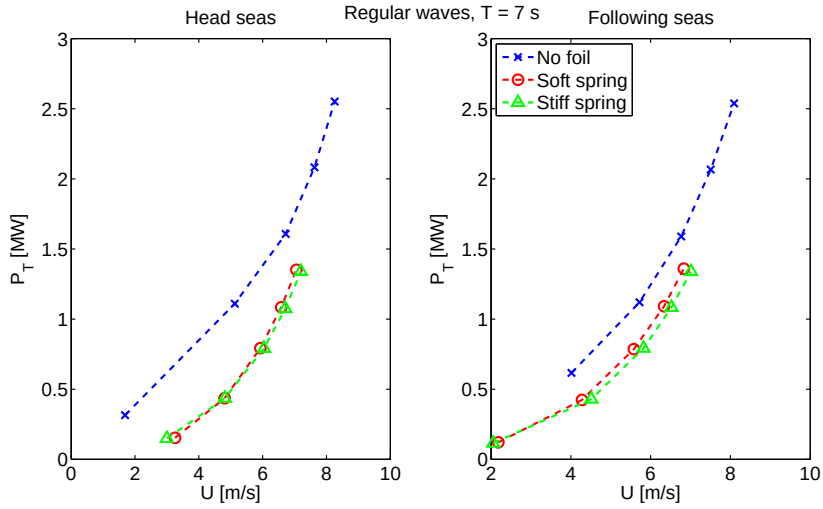

Figure 7.27: Simulations of the free-running ship model in full scale. Regular waves, $T = 7$ s, $H = 3$ m.

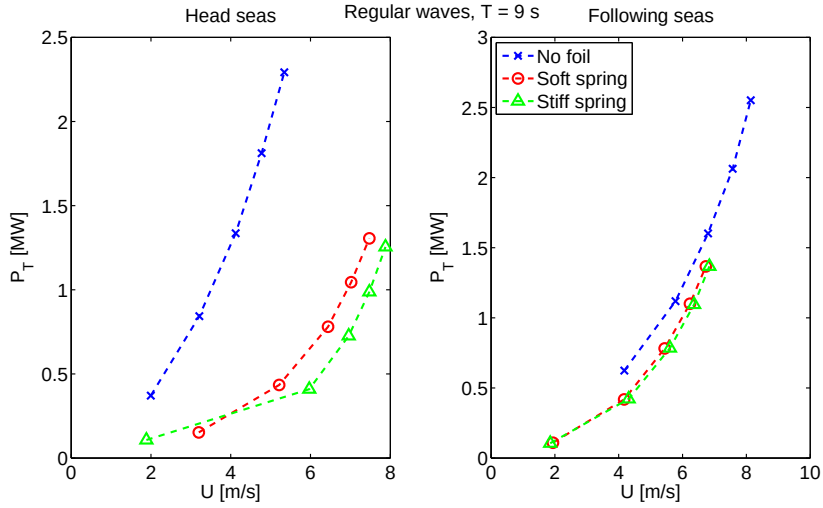

Figure 7.28: Simulations of the free-running ship model in full scale. Regular waves, $T = 9$ s, $H = 3$ m.

of 13 knots in regular waves. Interestingly, there are no negative fuel savings – of the speeds there are fuel saving values for – in irregular following waves. The calculated fuel savings decrease with increasing ship speed as expected, but for a ship speed of 13 knots, they are still fairly large, varying from 22-43% in irregular head seas and 4-12% in irregular following seas.

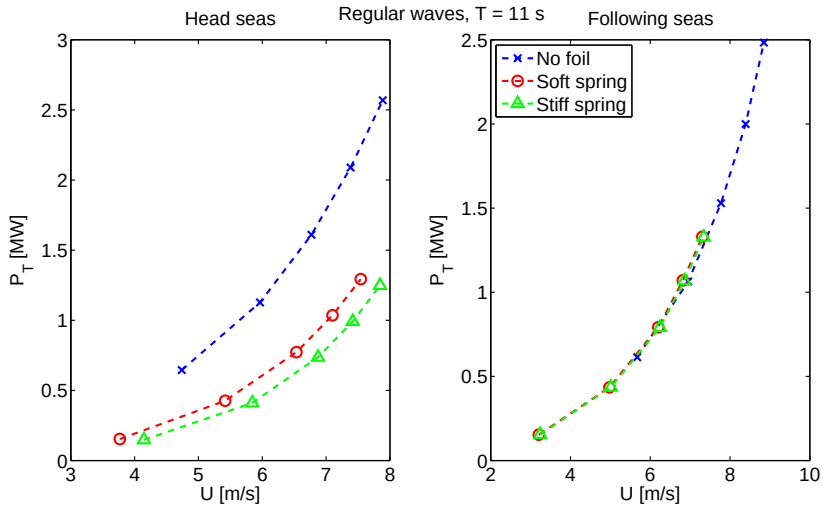

Figure 7.29: Simulations of the free-running ship model in full scale. Regular waves, $T = 11$ s, $H = 3$ m.

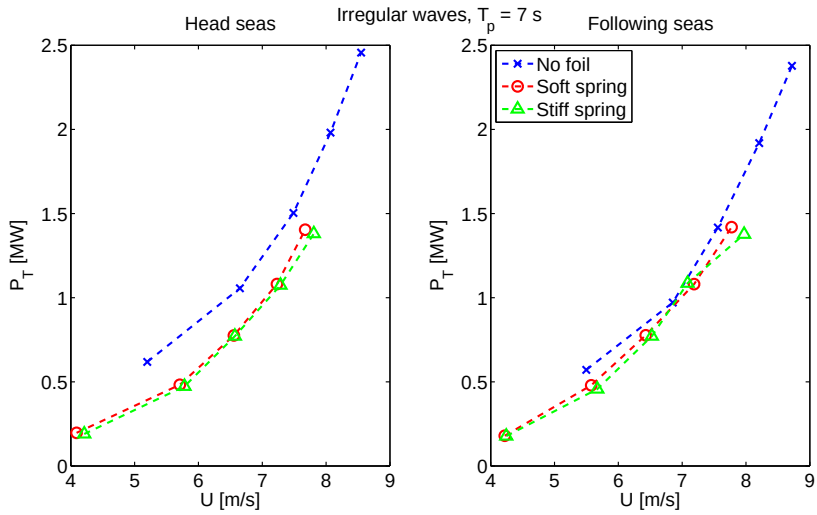

Figure 7.30: Simulations of the free-running ship model in full scale. Irregular waves, $T_p = 7$ s, $H_s = 3$ m.

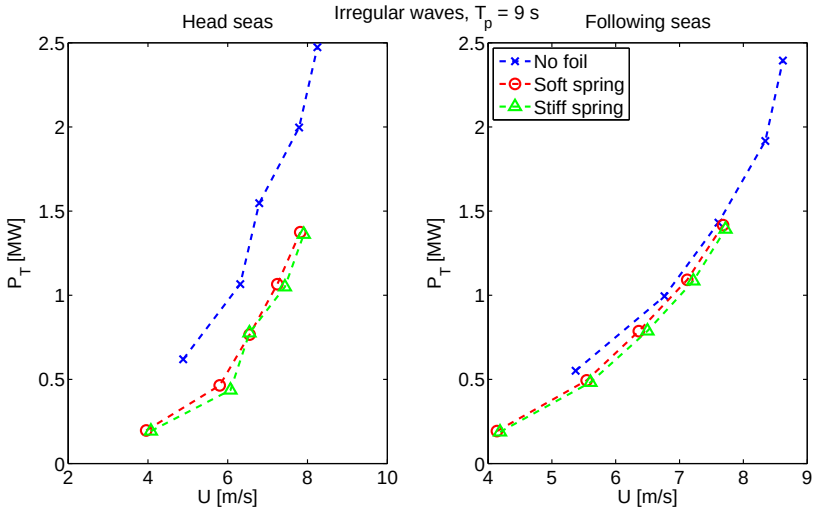

Figure 7.31: Simulations of the free-running ship model in full scale. Irregular waves, $T_p = 9$ s, $H_s = 3$ m.

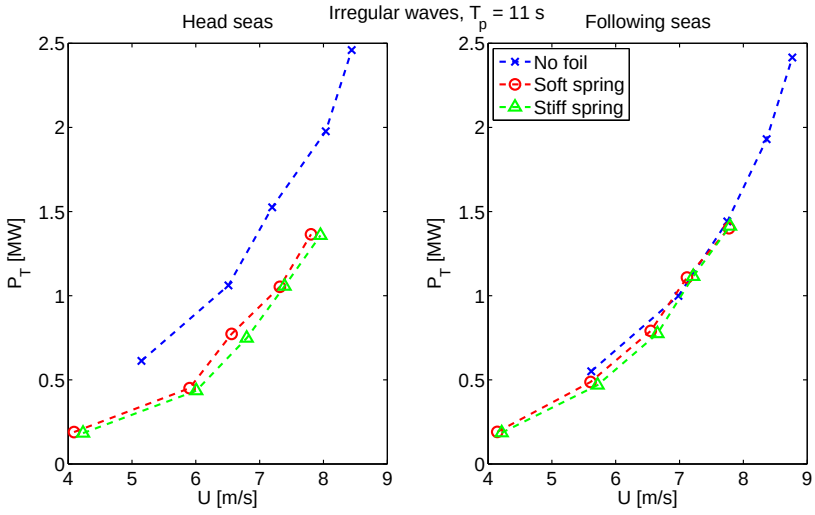

Figure 7.32: Simulations of the free-running ship model in full scale. Irregular waves, $T_p = 11$ s, $H_s = 3$ m.

	Regular waves				Irregular waves			
	Head seas		Following seas		Head seas		Following seas	
Speed [kn]	*Soft spring*	*Stiff spring*	*Soft spring*	*Stiff spring*	*Soft spring*	*Stiff spring*	*Soft spring*	*Stiff spring*
10	51	52	30	36	NaN	NaN	NaN	NaN
11	45	47	26	32	37	40	18	27
12	37	41	23	29	29	32	11	17
13	28	33	18	25	22	24	5	7

Table 7.2: Table of the fuel savings in percent for the free-running ship model in full scale. $T_p = 7$ s, $H_s = 3$ m.

	Regular waves				Irregular waves			
	Head seas		Following seas		Head seas		Following seas	
Speed [kn]	*Soft spring*	*Stiff spring*	*Soft spring*	*Stiff spring*	*Soft spring*	*Stiff spring*	*Soft spring*	*Stiff spring*
10	80	84	24	29	47	54	NaN	NaN
11	NaN	NaN	20	25	49	55	17	22
12	NaN	NaN	18	22	40	50	11	16
13	NaN	NaN	13	17	43	43	5	11

Table 7.3: Table of the fuel savings in percent for the free-running ship model in full scale. $T_p = 9$ s, $H_s = 3$ m.

	Regular waves				Irregular waves			
	Head seas		Following seas		Head seas		Following seas	
Speed [kn]	*Soft spring*	*Stiff spring*	*Soft spring*	*Stiff spring*	*Soft spring*	*Stiff spring*	*Soft spring*	*Stiff spring*
10	53	62	NaN	NaN	NaN	NaN	NaN	NaN
11	50	62	NaN	NaN	47	51	11	19
12	47	59	1	2	39	47	9	16
13	46	57	-4	-2	31	40	4	12

Table 7.4: Table of the fuel savings in percent for the free-running ship model in full scale. $T_p = 11$ s, $H_s = 3$ m.

Chapter 8

Conclusions and suggestions for future work

8.1 Conclusions

This thesis examined the benefits of employing fixed, pitch-controlled, and spring-loaded foils, so-called wavefoils, on a ship for propulsion and motion reduction in waves. The approach was both theoretical and experimental, and experiments and theory were compared when possible. Below, the main conclusions of the present work and some suggestions for future research and commercial development are given.

Experiments with a foil traveling at a constant horizontal speed with harmonic heave motion were performed to study how the foil thrust depended on the foil pitch. The motivation for doing these experiments was to study the effect of pitching wavefoils on a ship in a controlled environment, that is, a basin with an oscillating foil alone. A slightly modified version of the Leishman-Beddoes dynamic stall model was implemented, and results from this model were compared with experimental results. There was fairly good agreement between the theoretical and experimental results for pure harmonic heave motion with no pitch motion and for combined harmonic heave and pitch motion with a large pitch amplitude. For pure pitch motion with no heave motion, the model did not perform well compared with experiments. The fact that the foil was pitching about a point located about $1/3$ chord length above the chord line might be the reason for this, although correcting the inflow velocity, angle of attack, and added mass force for this pendulum motion had negligible effect on the agreement between theory and experiments.

In the experiments with an oscillating foil, both active pitch control using vanes for detecting the inflow angle, and spring-loaded pitch were tested. It was found that spring-loaded pitch resulted in a more thrust-producing pitch motion than setting the foil pitch to be linearly proportional to the inflow angle detected by the vanes. This was explained by the direction of the added mass force through the oscillation cycle.

Wavefoils were implemented in the time-domain ship simulator VeSim from MARINTEK. Wavefoil forces were calculated by using the aforementioned dynamic stall model. The idea behind this was to develop an efficient and reliable tool for predicting the performance of ships with wavefoils where dynamic stall could occur. Short computational time was essential for simulating long time series in irregular waves, and the dynamic stall model fulfilled this requirement. Model tests with a 1:16 scale model of a 90 m long platform supply vessel were performed and compared with experiments for the case of fixed foils. It was found that the simulation tool can be used to give reasonably accurate predictions of the effect of the wavefoil, although there is still room for improvement, particularly in the calculation of ship resistance in waves. Pitch control using pressure sensors on and near the leading edge, to relate the pressure on the foil to the angle of attack, was also tried, when the foil was mounted to the platform supply vessel model. Significantly reduced ship resistance with pitch control was only achieved for two different wave periods at different speeds. Unfortunately, the foil pitch actuation in these experiments was not sufficiently stiff to provide precise foil pitch.

When studying multiple wavefoil locations or sizes, time-domain studies are impractical. For this purpose, a frequency-domain approach is much more efficient to get a decent estimate of the wavefoil effect if the assumptions of linear theory are satisfied. Based on frequency-domain analyses of the foil thrust, it does not appear that a stern foil is worth installing if a bow foil has already been installed. Both frequency-domain and time-domain analyses show the importance of installing the wavefoil far forward on the ship – ideally slightly in front of the bow.

A ship harnessing all of its propulsive power from the wind with wingsails and from the waves with wavefoils was proposed. Such a ship will have quite low expected values of the ship speed, with fairly large standard deviations, even on a route where wind and waves are abundant.

Simulations showed that fuel savings for the platform supply vessel, with the fixed foil tested, were in the range 2-15% (depending on the wave direction) in typical North Sea waves, when sailing at a speed of 12 knots. For slightly larger waves and foil span, compared to the ship beam, simulations predicted fuel savings in the range 29-50% in head seas and 9-17% in following seas, for a similarly sized RORO ship with a spring-loaded foil. The simulation model did not account for flow interaction between the ship hull and the foil. Accounting for this will reduce the predicted fuel savings, because the hull will generally reduce the inflow angles to the foil. The spring stiffness was found, both through model tests with a small model of the RORO ship and through simulations, to be of surprisingly little importance to the wavefoil performance.

For the waves producing the most violent ship motions, simulations showed that pitching foils can reduce the ship resistance significantly relative to a fixed foil, particularly if the forward speed is not too high. Until an actively pitch-controlled wavefoil producing a pitch motion similar to that of the spring-loaded foil has been designed, however, the author recommends a spring-loaded wavefoil with variable spring stiffness.

8.2 Suggestions for future work

8.2.1 Suggestions for future research

Future research could try to find a pitch-control method that gives a more beneficial phase of the pitch motion at low forward speeds. One alternative is to let the inflow angle vanes pivot about a point closer to their leading edges in order to be more influenced by the normal added mass force, like the spring-loaded foil. The pressure distribution around the foil will certainly be influenced by the added mass effect, so using pressure sensors like Naito and Isshiki (2005), or as described in Section 5.2.2, may be another way of obtaining a more beneficial phase of the pitch motion after all.

The experiments with pressure sensors for active pitch control in this thesis suffered from an imprecise pitch actuation mechanism, which likely means that the foil thrust can be further increased relative to the fixed foil. The problem with the pressure sensors used in this thesis was that they were not built to sustain water submersion for several weeks, so a robust set of pressure sensors is recommended. If using pressure sensors to control the foil, one should try to include the effect of the added mass force on the foil thrust when determining the optimal foil pitch.

Further studies of the effect of phase angle on the thrust of an harmonically heaving and pitching foil could be carried out and related to the optimal spring stiffness of a spring-loaded foil. For the case of a spring-loaded foil, a control algorithm which adjusts the spring stiffness to maximize the ship speed over a certain time interval may be worth studying. For the case of an actively pitch-controlled foil, a control mechanism which maximizes the foil thrust at all times, based on direct measurement of the foil thrust, may also be worth looking into.

The effect of the hull on the inflow to the foil should be studied, since neglecting this effect is non-conservative. It would be interesting to investigate if the hull shape can be optimized for either wave propulsion alone or combined wind and wave propulsion. For combined wind and wave propulsion, wingsail interaction should be studied.

Other suggested topics for future work are interaction effects of multiple wavefoils in various arrangements and hydroelasticity effects due to flexibility of the foils.

Finally, this thesis has only looked into hydrodynamic aspects of a ship with wavefoils. Before building full-scale wavefoils for a ship, a structural analysis of the foils subjected to worst-case-scenario loads needs to be done. An economic analysis investigating the return on investment for a ship owner deciding to outfit a vessel with wavefoils is also necessary before commercial development.

8.2.2 Suggestions regarding commercial development of wavefoils

As concluded above, a spring-loaded wavefoil with variable spring stiffness appears – to the author – to be the best solution for a full-scale ship, until further progress has been made on active pitch control. The spring stiffness could be adjusted based

on measurements of the ship speed. One could also mount a vane detecting the foil's angle of attack and use the measured angle of attack to ensure that the foil does not stall, when selecting the spring stiffness.

Regarding retracting a foil into the hull, there are a number of possibilities. Perhaps the easiest is to use the same mechanism as on retractable roll stabilizer fins, where the horizontally aligned foils swing 90 degrees into cavities in the hull. Another option related to existing solutions is lowering two foils down from a cavity in the hull bottom, like a retractable thruster, and then folding one foil to starboard side and the other foil to port side. If struts are used, they should be designed as streamlined and thin as structural limitations allow, because of the extra resistance they introduce. The author found that a strut in the bow made the free-running ship model in Chapter 7 more difficult to maneuver, and the ship designer should have this in mind if considering a strut-mounted wavefoil.

References

Abramowitz, M., Stegun, I. A., et al. (1972). Handbook of mathematical functions, volume 1. Dover New York.

Anderson, J. M., Streitlien, K., Barrett, D. S., and Triantafyllou, M. S. (1998). Oscillating foils of high propulsive efficiency. Journal of Fluid Mechanics, 360:41–72.

Angvik, I. (2009). Application of an active foil propeller on an offshore vessel. Master's thesis, Norwegian University of Science and Technology.

Anon. (1983). Wave power for ship propulsion. The Motor Ship, 64(757):67, 69.

Ashburton Guardian (1897). A boat with fins. XVIII(4281):1. 30 August.

Beddoes, T. (1978). Onset of leading edge separation effects under dynamic conditions and low Mach numbers. In Proceedings of the 34th Annual Forum of the American Helicopter Society.

Belibassakis, K. A. and Politis, G. K. (2012). Hydrodynamic analysis of flapping wing systems for augmenting ship propulsion in rough sea. In Proceedings of the Twenty-second (2012) International Offshore and Polar Engineering Conference, pages 929–936.

Belibassakis, K. A. and Politis, G. K. (2013). Hydrodynamic performance of flapping wings for augmenting ship propulsion in waves. Ocean Engineering, 72:227–240.

Berg, A. (1985). Trials with passive foil propulsion on M/S "Kystfangst". Project no. 672.138. Fiskeriteknologisk Forskningsinstitutt, Trondheim, Norway.

Bøckmann, E. and Steen, S. (2013). The effect of a fixed foil on ship propulsion and motions. In Proceedings of the Third International Symposium on Marine Propulsors, pages 553–561.

Bøckmann, E. and Steen, S. (2014). Experiments with actively pitch-controlled and spring-loaded oscillating foils. Applied Ocean Research, 48:227–235.

Bøckmann, E., Steen, S., and Myrhaug, D. (2014). Performance of a ship powered purely by renewable energy. In ASME 2014 33rd International Conference on Ocean, Offshore and Arctic Engineering, Volume 8A: Ocean Engineering.

Borgen, C. T. (2010). Application of an active foil propeller. Master's thesis, Norwegian University of Science and Technology.

Bose, N. and Lien, J. (1990). Energy absorption from ocean waves: a free ride for cetaceans. Proceedings of the Royal Society of London. B. Biological Sciences, 240(1299):591–605.

Burnett, R. F. (1979). Wave energy for propelling craft - nothing new. The Naval Architect, Nov.:239.

Carr, L. W. (1988). Progress in analysis and prediction of dynamic stall. Journal of Aircraft, 25(1):6–17.

Chopra, M. G. (1974). Hydromechanics of lunate-tail swimming propulsion. Journal of Fluid Mechanics, 64(02):375–392.

Chopra, M. G. (1976). Large amplitude lunate-tail theory of fish locomotion. Journal of Fluid Mechanics, 74(01):161–182.

Cummins, W. E. (1962). The impulse response function and ship motions. Schiffstechnik, 9(47):101–109.

De Silva, L. W. A. and Yamaguchi, H. (2012). Numerical study on active wave devouring propulsion. Journal of Marine Science and Technology, 17(3):261–275.

Det Norske Veritas (2010). Recommended practice, DNV-RP-C205.

Dybdahl, K. (1988). Foilpropellen kan revolusjonere skipsfarten. Teknisk Ukeblad/Teknikk, 135(39):10–11. 27. Oktober.

Fabre, O. (2008). Sailor takes on Pacific in wave-powered boat. Reuters, March 17, 2008. Retrieved October 19, 2014 from `http://www.reuters.com/article/2008/03/17/us-wavepower-idUSKUA76174820080317`.

Faltinsen, O. (1993). Sea loads on ships and offshore structures, volume 1. Cambridge university press.

Faltinsen, O., Minsaas, K., Liapis, N., and Skjørdal, S. (1980). Prediction of resistance and propulsion of a ship in a seaway. In 13th Symposium on Naval Hydrodynamics.

Faltinsen, O. M. (2005). Hydrodynamics of High-Speed Marine Vehicles. Cambridge University Press.

Fathi, D. (2012). ShipX Vessel Responses (VERES), Ship Motions and Global Loads, User's Manual. MARINTEK.

Fathi, D. (2013). MARINTEK Vessel Simulator (VeSim), Vessel Model. MARINTEK. Rev. 5.

Fathi, D. and Hoff, J. R. (2014). ShipX Vessel Responses (VERES), Theory Manual. MARINTEK.

Filippas, E. S. and Belibassakis, K. A. (2013). Free surface effects on hydrodynamic analysis of flapping foil thrusters in waves. In Proceedings of the ASME 2013 32nd International Conference on Ocean, Offshore and Arctic Engineering, Volume 5: Ocean Engineering.

Filippas, E. S. and Belibassakis, K. A. (2014a). A boundary element method for the hydrodynamic analysis of flapping-foil thrusters operating beneath the free surface and in waves. In Developments in Maritime Transportation and Exploitation of Sea Resources, volume 1, pages 3–11. CRC Press.

Filippas, E. S. and Belibassakis, K. A. (2014b). Hydrodynamic analysis of flapping-foil thrusters operating beneath the free surface and in waves. Engineering Analysis with Boundary Elements, 41:47–59.

Fossen, T. I. (2005). A nonlinear unified state-space model for ship maneuvering and control in a seaway. International Journal of Bifurcation and Chaos, 15(09):2717–2746.

Fossen, T. I. (2011). Handbook of Marine Craft Hydrodynamics and Motion Control. John Wiley & Sons, Ltd, first edition.

Garrick, I. E. (1936). Propulsion of a flapping and oscillating airfoil. NACA Report No. 567.

Garrick, I. E. (1938). On some reciprocal relations in the theory of nonstationary flows. NACA Tech. Rep. 629.

Gause, J. A. (1966). Flexible fin propulsion member and vessels incorporated same. GB Patent 1176559. Filed Sept. 7, 1966. Patented Jan. 7, 1970.

Gause, J. A. (1967). Water-borne vessel comprising propulsion system incorporating flexible fin propulsion members. US Patent 3,453,981. Filed Apr. 24, 1967. Patented Jul. 8, 1969.

Geoghegan, J. (2008a). Wave runner. Popular Science. February 22. Retrieved October 19, 2014 from `http://www.popsci.com/gear-gadgets/article/2008-02/wave-runner`.

Geoghegan, J. J. (2008b). Boat, moved only by waves, sails to a seafaring first. The New York Times. July 8, 2008. Retrieved June 29, 2011 from `http://www.nytimes.com/2008/07/08/science/08wave.html`.

Gerritsma, J. and Beukelman, W. (1972). Analysis of the resistance increase in waves of a fast cargo ship. International Shipbuilding Progress, 19(217):285–293.

Green, R. B., Galbraith, R. A., and Niven, A. J. (1992). Measurements of the dynamic stall vortex convection speed. Aeronautical Journal, 96(958):319–325.

Grue, J., Mo, A., and Palm, E. (1988). Propulsion of a foil moving in water waves. Journal of Fluid Mechanics, 186:393–417.

Gupta, S. and Leishman, J. G. (2006). Dynamic stall modelling of the S809 aerofoil and comparison with experiments. Wind Energy, 9(6):521–547.

Hansen, M. H., Gaunaa, M., and Madsen, H. A. (2004). A Beddoes-Leishman type dynamic stall model in state-space and indicial formulations. Risø-R-1354(EN), Risø National Laboratory, Roskilde, Denmark.

Hoerner, S. F. and Borst, H. V. (1975). Fluid-Dynamic Lift. Hoerner Fluid Dynamics.

Holtrop, J. (1984). A statistical re-analysis of resistance and propulsion data. International Shipbuilding Progress, 31(363):272–276.

Hover, F. S., Haugsdal, Ø., and Triantafyllou, M. S. (2004). Effect of angle of attack profiles in flapping foil propulsion. Journal of Fluids and Structures, 19(1):37–47.

International Maritime Organization (2009). Second IMO GHG Study 2009. `http://www.imo.org/blast/blastDataHelper.asp?data_id=27795&filename=GHGStudyFINAL.pdf`. Retrieved November 12, 2013.

International Renewable Energy Agency (2013). Global solar and wind atlas. `http://irena.masdar.ac.ae/`. Retrieved August 21, 2013.

Isshiki, H. (1982a). A theory of wave devouring propulsion (1st Report) - Thrust generation by a linear Wells turbine. J. Soc. Naval Arch. Japan, 151:54–64.

Isshiki, H. (1982b). A theory of wave devouring propulsion (2nd Report) - Optimized foil motions for a passive-type wave devouring propulsor. J. Soc. Naval Arch. Japan, 152:89–100.

Isshiki, H. and Murakami, M. (1983). A theory of wave devouring propulsion (3rd Report) - An experimental verification of thrust generation by a passive-type hydrofoil propulsor. J. Soc. Naval Arch. Japan, 154:118–128.

Isshiki, H. and Murakami, M. (1984). A theory of wave devouring propulsion (4th Report) - A comparison between theory and experiment in case of a passive-type hydrofoil propulsor. J. Soc. Naval Arch. Japan, 156:102–114.

Isshiki, H., Murakami, M., and Terao, Y. (1984). Utilization of wave energy into propulsion of ships - wave devouring propulsion. In 15th Symp. on Naval Hydrodyn., pages 31–44.

Jakobsen, E. (1981). The foilpropeller, wave power for propulsion. In Papers Presented at the Second International Symposium on Wave & Tidal Energy, pages 363–369.

Johnston, C. O. (2004). Review, extension, and application of unsteady thin airfoil theory. Center for Intelligent Material Systems and Structures (CIMSS), Virginia Polytechnic Institute and State University, Blacksburg, VA, 24060. CIMSS Report No. 04-101.

Jones, R. T. (1938). Operational treatment of the nonuniform-lift theory in airplane dynamics. NACA Tech. Note 667.

Jones, R. T. (1940). The unsteady lift of a wing of finite aspect ratio. NACA Tech. Rep. 681.

Kjærland, O. (1979). Model tests with a wave propulsion system. Com. R. SMT 43.8 4344006, The Ship Research Institute of Norway, Trondheim, Norway.

Kjærland, O. (1980). Model tests with a foil propeller. Com. R. SMT 43.0 4344010, The Ship Research Institute of Norway, Trondheim, Norway.

Küssner, H. (1935). Augenblicklicher Entwicklungs-stand der Frage des Flügelflatterns. Luftfahrtforschung, 6:193–209.

Lai, P. S. K., Bose, N., and McGregor, R. C. (1993). Wave propulsion from a flexible-armed, rigid-foil propulsor. Mar. Technol. Soc. J, 30(1):30–38.

Larsen, J. W., Nielsen, S. R. K., and Krenk, S. (2007). Dynamic stall model for wind turbine airfoils. Journal of Fluid and Structures, 23(7):959–982.

Lazauskas, L. (2004). Airfoil data. `http://www.cyberiad.net/foildata.htm`. Retrieved August 15, 2012.

Leikarnes, M. (2011). I storm med Far Seeker. `http://www.youtube.com/watch?v=cVvleU9Q5TY`. Retrieved May 9, 2014.

Leishman, J. G. (2002). Principles of Helicopter Aerodynamics. Cambridge Aerospace Series.

Leishman, J. G. and Beddoes, T. S. (1989). A semi-empirical model for dynamic stall. Journal of the American Helicopter Society, 34(3):3–17.

Lighthill, M. J. (1960). Note on the swimming of slender fish. J. Fluid Mech, 9(02):305–317.

Lighthill, M. J. (1970). Aquatic animal propulsion of high hydromechanical efficiency. Journal of Fluid Mech, 44(02):265–301.

Linden, H. (1895). Improved combination with floating bodies, of fins adapted to effect their propulsion. GB Patent 14,630. Filed Aug. 1, 1895. Patented Jul. 18, 1896.

Longo, J. and Stern, F. (2002). Effects of drift angle on model ship flow. Experiments in fluids, 32(5):558–569.

Loukakis, T. A. and Sclavounos, P. D. (1978). Some extensions of the classical approach to strip theory of ship motions, including the calculation of mean added forces and moments. Journal of Ship Research, 22(1):1–19.

Lubbock, B. (1924). The Log of the Cutty Sark. James Brown & Son, Glasgow, Scotland.

McCormick, B. W. (1995). Aerodynamics, aeronautics, and flight mechanics. John Wiley & Sons, Inc., New York, second edition.

McCroskey, W. J. (1981). The phenomenon of dynamic stall. NASA Technical Memorandum 81264.

McCroskey, W. J., Carr, L. W., and McAlister, K. W. (1976). Dynamic stall experiments on oscillating airfoils. AIAA Journal, 14(1):57–63.

McTaggart, K. A. (2010). Verification and validation of shipmo3d ship motion predictions in the time and frequency domains. In ITTC Workshop on Seakeeping, Seoul, Korea, Oct. 19-21, 2010, pages 160–174.

Mechanix Illustrated (1972). Mr. Gause's incredible self-propelled boat! Oct.:22, 179.

Mitsui O.S.K. Lines (2012). World's First Hybrid Car Carrier Emerald Ace Completed. `http://www.mol.co.jp/en/pr/2012/12035.html`. Press release, June 29, 2012. Retrieved November 12, 2013.

Miyasaka, T., Nakashima, T., Nihei, Y., and Doi, Y. (2013). Prediction and improvement of propulsive performance of wing sails considering their aerodynamic interaction. In Proceedings of the Twenty-third (2013) International Offshore and Polar Engineering Conference, volume 4, pages 800–807.

Moriarty, P. J. and Hansen, A. C. (2005). AeroDyn theory manual. NREL/TP-500-36881, National Renewable Energy Laboratory, Golden, Colorado.

Nagata, S., Imai, Y., Toyota, K., and Isshiki, H. (2010). Thrust generation by waves. In Proc. of the Ninth (2010) ISOPE Pacific/Asia Offshore Mechanics Symposium, pages 155–162.

Naito, S. and Isshiki, H. (2005). Effect of bow wings on ship propulsion and motions. Applied Mechanics Reviews, 58(4):253–268.

Naito, S., Isshiki, H., and Fujimoto, K. (1986). Thrust generation of a fin attached to a ship in waves. Journal of the Kansai Society of Naval Architects, Japan, (202):23–28. In Japanese.

NIMA (1997). Department of Defense World Geodetic System 1984. NIMA Technical Report TR8350.2.

Ogilvie, T. F. (1964). Recent progress toward the understanding and prediction of ship motions. In 5th Symposium on Naval Hydrodynamics, pages 3–80.

Ol, M. V., Bernal, L., Kang, C.-K., and Shyy, W. (2010). Shallow and deep dynamic stall for flapping low Reynolds number airfoils. In Animal Locomotion, pages 321–339. Springer.

Øye, S. (1991). Dynamic stall simulated as time lag of separation. In Proceedings of the 4th IEA Symposium on the aerodynamics of wind turbines.

Pedersen, M. D. (2008). Unsteady lifting-surface solution for rigid sails. Project work TTK4530, Norwegian University of Science and Technology.

Pereira, R., Schepers, G., and Pavel, M. D. (2013). Validation of the Beddoes–Leishman dynamic stall model for horizontal axis wind turbines using MEXICO data. Wind Energy, 16(2):207–219.

Pereira, R. B. d. S. (2010). Validating the Beddoes-Leishman dynamic stall model in the horizontal axis wind turbine environment. Master's thesis, University of Lisbon.

Pierce, K. G. (1996). Wind turbine load prediction using the Beddoes-Leishman model for unsteady aerodynamics and dynamic stall. Master's thesis, The University of Utah.

PlanetSolar (2013). The boat, technical details. `http://www.planetsolar.org/the-boat/technical/`. Retrieved August 21, 2013.

Politis, G. and Politis, K. (2014). Biomimetic propulsion under random heaving conditions, using active pitch control. Journal of Fluid and Structures, 47:139–149.

Popular Science (1935). Wave power runs model boat. April 1935, p. 26.

Popular Science (1950). Waves serve as boat's engine. February 1950, p. 224.

Salvesen, N., Tuck, E. O., and Faltinsen, O. M. (1970). Ship motions and sea loads. Transactions SNAME, 78:250–287.

Scherer, J. O. (1968). Experimental and theoretical investigation of large amplitude oscillating foil propulsion systems. Tech. Rep. 662-1, Hydronautics, Inc., Laurel, Maryland.

Schulze, O. (1911). Wave-motor. US Patent 1,033,476. Filed Jan. 5, 1911. Patented Jul. 23, 1912.

Sears, W. R. (1938). A systematic presentation of the theory of thin airfoils in non-uniform motion. PhD thesis, California Institute of Technology.

Sheldahl, R. E. and Klimas, P. C. (1981). Aerodynamic characteristics of seven symmetrical airfoil sections through 180-degree angle of attack for use in aerodynamic analysis of vertical axis wind turbines. SAND80-2114, Sandia National Laboratories, Albuquerque, New Mexico.

Smulders, F. (1985). Exposition of calculation methods to analyse wind-propulsion on cargo ships. Journal of Wind Engineering and Industrial Aerodynamics, 19(1):187–203.

Steen, S. and Minsaas, K. (2012). Ship resistance. Lecture notes, TMR4220 Naval Hydrodynamics, Norwegian University of Science and Technology.

Tarzanin, F. J. (1972). Prediction of control loads due to blade stall. Journal of the American Helicopter Society, 17(2):33–46.

Terao, Y. (1982). A floating structure which moves toward the waves (possibility of wave devouring propulsion). Journal of the Kansai Society of Naval Architects, Japan, (184):51–54. In Japanese.

Terao, Y. and Isshiki, H. (1991). Wave devouring propulsion sea trial. In Eighteenth Symposium on Naval Hydrodynamics, pages 287–296.

The New York Times (1898). A self-propelling boat. December 18, 1898.

Theodorsen, T. (1935). General theory of aerodynamic instability and the mechanism of flutter. NACA Tech. Rep. 496.

Thwaites, B. (1960). Incompressible Aerodynamics. Clarendon Press, Oxford.

Todd, F. H. (1963). Series 60 methodical experiments with models of single-screw merchant ships. David Taylor Model Basin Report 1712.

Tran, C. T. and Petot, D. (1981). Semi-empirical model for the dynamic stall of airfoils in view of the application to the calculation of responses of a helicopter blade in forward flight. Vertica, 5(1):35–53.

Triantafyllou, G. S., Triantafyllou, M. S., and Grosenbaugh, M. A. (1993). Optimal thrust development in oscillating foils with application to fish propulsion. Journal of Fluids and Structures, 7(2):205–224.

Triantafyllou, M. S., Triantafyllou, G. S., and Gopalkrishnan, R. (1991). Wake mechanics for thrust generation in oscillating foils. Physics of Fluids A: Fluid Dynamics, 3(12):2835–2837.

Triantafyllou, M. S., Triantafyllou, G. S., and Yue, D. K. P. (2000). Hydrodynamics of fishlike swimming. Annual Review of Fluid Mechanics, 32:33–53.

Tucker, M. J. and Pitt, E. G. (2001). Waves in ocean engineering, volume 5 of Elsevier ocean engineering book series. Elsevier, Amsterdam.

Veritec (1985). Analysis of a foil propeller as an auxiliary propulsion system. Veritec report 85-3326.

Veritec (1986). Analysis of a foil propeller as an auxiliary propulsion system. Veritec report 86-3413.

von Kármán, T. and Sears, W. R. (1938). Airfoil theory for non-uniform motion. Journal of the Aeronautical Sciences, 5(10):379–390.

Vrooman, D. (1858). Vibrating propeller. US Patent 22,097. Patented Nov. 15, 1858.

Wagner, H. (1925). Über die Entstehung des dynamischen Auftriebes von Tragflügeln. ZAMM-Journal of Applied Mathematics and Mechanics/Zeitschrift für Angewandte Mathematik und Mechanik, 5(1):17–35.

Wang, S., Ingham, D. B., Ma, L., Pourkashanian, M., and Tao, Z. (2010). Numerical investigations on dynamic stall of low reynolds number flow around oscillating airfoils. Computers & Fluids, 39(9):1529–1541.

Wu, T. Y. (1961). Swimming of a waving plate. Journal of Fluid Mech, 10(03):321–344.

Wu, T. Y. (1972). Extraction of flow energy by a wing oscillating in waves. Journal of Ship Research, 16(1):66–78.

Wu, T. Y. and Chwang, A. T. (1975). Extraction of flow energy by fish and birds in a wavy stream. In Swimming and flying in nature, pages 687–702. Springer.

Appendix A

Time lags in the dynamic stall model

A central idea in the Leishman-Beddoes dynamic stall model is giving a time lag to a quantity by using a deficiency function. Denoting the quantity f and the deficiency function D (these names are just for illustration purposes), the time-lagged value at time s, $f_{lag}(s)$, can be written as

$$f_{lag}(s) = f(s) - D(s), \tag{A.1}$$

where $D(s)$ is given as

$$D(s) = \int_0^s \frac{df}{ds}(\sigma) e^{-\frac{s-\sigma}{T}} d\sigma. \tag{A.2}$$

In Eq. A.2, T is a nondimensional time constant determining the time lag of f.

Figure A.1 shows f and f_{lag} for different values of T, using numerical integration of Eq. A.2, where

$$f(s) = \begin{cases} 0 & \text{if } s < 0 \\ 1 & \text{if } s \geq 10. \end{cases} \tag{A.3}$$

We see that it takes longer time for f_{lag} to approach f when T increases. If f is periodically oscillating, f_{lag} would get both an amplitude reduction and a phase lag.

Analogous to the derivation in Eqs. 3.16-3.20, we can express $D(s)$ using the values of f and D at the previous time step, i.e., $f(s - \Delta s)$ and $D(s - \Delta s)$. This is done several times in the Leishman-Beddoes dynamic stall model. Evaluating D

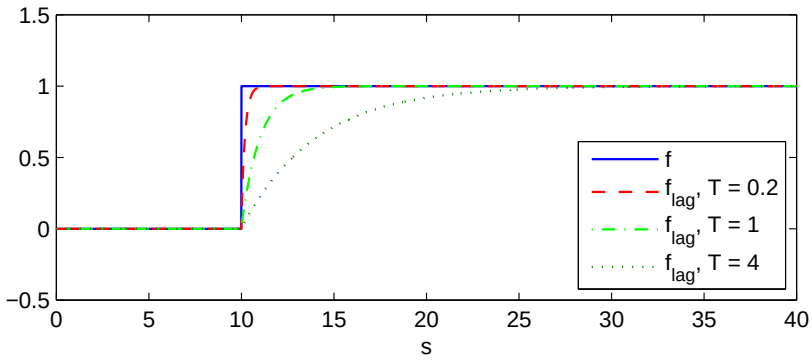

Figure A.1: The effect of varying the nondimensional time constant on the time lag of a step function

at the next time step, $s + \Delta S$, we get

$$\begin{aligned} D(s+\Delta s) &= \int_0^{s+\Delta s} \frac{df}{ds}(\sigma) e^{-\frac{s+\Delta s-\sigma}{T}} d\sigma \\ &= e^{-\frac{\Delta s}{T}} \overbrace{\int_0^{s} \frac{df}{ds}(\sigma) e^{-\frac{s-\sigma}{T}} d\sigma}^{D(s)} \\ &\quad + \overbrace{\int_s^{s+\Delta s} \frac{df}{ds}(\sigma) e^{-\frac{s+\Delta s-\sigma}{T}} d\sigma}^{I} . \end{aligned} \tag{A.4}$$

The integral, I, can be written as

$$I = e^{-\frac{s+\Delta s}{T}} \int_s^{s+\Delta s} \frac{df}{ds}(\sigma) e^{\frac{\sigma}{T}} d\sigma. \tag{A.5}$$

Using a simple backward-difference approximation for df/ds at time $s + \Delta s$, and the midpoint rule for integration, we get

$$\begin{aligned} I &= e^{-\frac{s+\Delta s}{T}} \frac{f(s+\Delta s) - f(s)}{\Delta s} e^{\frac{s+\frac{\Delta s}{2}}{T}} \Delta s \\ &= \left[f(s+\Delta s) - f(s) \right] e^{-\frac{\Delta s}{2T}} . \end{aligned} \tag{A.6}$$

This gives

$$D(s+\Delta s) = D(s) e^{-\frac{\Delta s}{T}} + \left[f(s+\Delta s) - f(s) \right] e^{-\frac{\Delta s}{2T}} \tag{A.7}$$

or

$$D(s) = D(s-\Delta s) e^{-\frac{\Delta s}{T}} + \left[f(s) - f(s-\Delta s) \right] e^{-\frac{\Delta s}{2T}} . \tag{A.8}$$

Appendix B

Uncertainty in the experiments

The error bars in the figures in Chapter 4 were obtained by repeating one condition and calculating the precision limit for the thrust coefficient, P_{C_T}, as

$$P_{C_T} = t\sigma_{C_T}, \tag{B.1}$$

where t is the t-value in the Student's t-distribution, and σ_{C_T} is the standard deviation of the thrust coefficient for the repeated condition. The standard deviation of the mean value for the repeated condition is calculated as

$$\sigma_{\overline{C_T}} = \frac{\sigma_{C_T}}{\sqrt{N}}, \tag{B.2}$$

where N is the number of repeated tests. The precision limit for the mean is then

$$P_{\overline{C_T}} = t\sigma_{\overline{C_T}}. \tag{B.3}$$

This gives a smaller error bar for the test condition that was repeated.

The biggest uncertainty of the bias error is the calibration of the force transducers. The force transducers at the top of the foil rig, measuring the horizontal and vertical foil forces, were calibrated using a rope, a pulley, and weights, as shown in Figure B.1. Weights were added in three load steps and the corresponding voltage was recorded. Linear regression was used to establish the relation between force and voltage. The foil was loaded horizontally and vertically, in both positive and negative directions. The calibration factor would typically vary a few percent when done some months apart.

Also, calibration of the foil pitch is an important uncertainty factor. Calibration of the foil pitch consisted of holding the foil at a steady angle by hand, reading off the foil pitch from a digital protractor (see Figure B.2), and recording the voltage to the motor in the experiments where the motor was used to pitch the foil and the voltage to the potentiometer measuring the foil pitch for the spring-loaded foil. It was quite difficult to keep the foil steady when reading off the foil pitch and

Figure B.1: Calibrating the force transducers using a rope, a pulley, and weights

recording the motor voltage or potentiometer voltage. The foil pitch angles used in the calibration are assumed to be within $\pm 0.15°$ accuracy with a 95% confidence interval.

Figure B.2: Calibrating the foil pitch using a digital protractor. The digital protractor was placed on top of a removable part, fitting perfectly to the foil shape.

Another uncertainty factor is the post-processing procedure. The mean value of a periodic force would vary with the number of periods used to calculate the mean. Figure B.3 shows the mean foil thrust for the spring-loaded foil for $U = 0.9$ m/s, $\xi_{3A} = 0.12$ m, T = 1.5 s, with the spring clamp at position four from the foil. There is no clear convergence of the mean foil thrust with increasing number of oscillation periods, but the variation in mean foil thrust using four oscillation periods and using one oscillation period is only 0.4%.

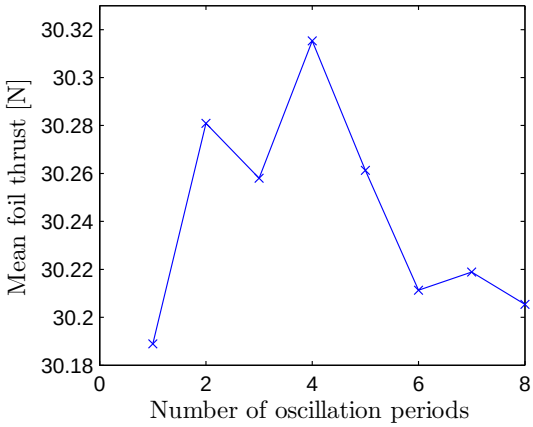

Figure B.3: The effect of varying number of oscillation periods when calculating the mean foil thrust

Appendix C

Laboratory facilities

C.1 The Marine Cybernetics Laboratory (MC Lab)

The Marine Cybernetics Laboratory, or MC Lab, as it is commonly called, is a quite small wave basin at the Marine Technology Center in Trondheim, Norway. It is 40 m long, 6.45 m wide, and 1.5 m deep, making it suitable for ship models up to 3 m long. The basin is equipped with a carriage, which can actuate models in 5 degrees of freedom: surge, sway, heave, yaw and pitch. Maximum surge velocity is 2 m/s. The wave maker can generate regular waves up to 0.25 m high and irregular waves up to 0.15 m high, with periods in the range 0.3-3 s, and 0.6-1.5 s, respectively. In the end of the tank, opposite the wave maker, is a beach to dampen the waves. The MC Lab is mainly used by students and PhD students. A panorama photo of the MC Lab, with the carriage visible at the right side of the picture, is given in Figure C.1.

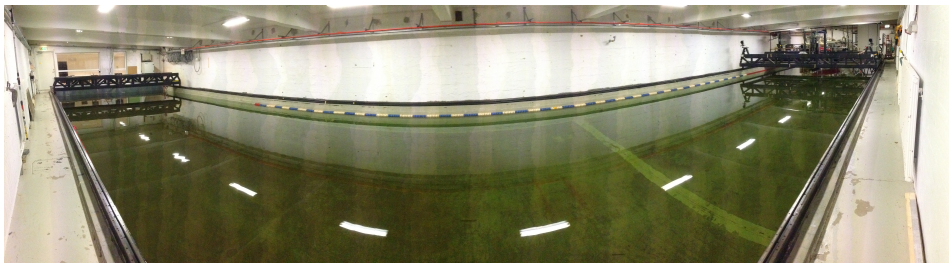

Figure C.1: Panorama view of the MC Lab

C.2 The towing tank

The towing tank at the Marine Technology Center is a 260 m long and 10.5 m wide basin. The depth of the basin is 5.6 m for the first 175 m, and 10 m for the last

85 m. The maximum carriage speed is 12 m/s, and the wave maker can generate waves up to 0.9 m high and wave periods in the range 0.8-5 s. A picture taken down the length of the towing tank is given in Figure C.2. There is a beach in the end of the towing tank opposite to the wave maker, and there are also wave dampers along the side of the towing tank, visible in Figure C.2, which can be elevated up and down when needed.

Figure C.2: The towing tank

C.3 The small towing tank

The small towing tank at the Marine Technology Center, see Figure C.3, is a 25 m long, 2.8 m wide, and 1.0 m deep towing tank, mainly used by students and PhD students. It is equipped with a towing carriage, capable of speeds in the range 0.05 m/s to 1.75 m/s. There is a beach in one tank end and a wave maker in the other end, capable of generating waves with a height up to 0.3 m and periods in the range 0.25-3 s.

Figure C.3: The small towing tank

Appendix D

Power vs. speed, irregular waves simulations

The following figures are power vs. speed graphs from simulations with the platform supply vessel in irregular waves, as described in Section 5.5. $H_s = 2.5$ m in all plots.

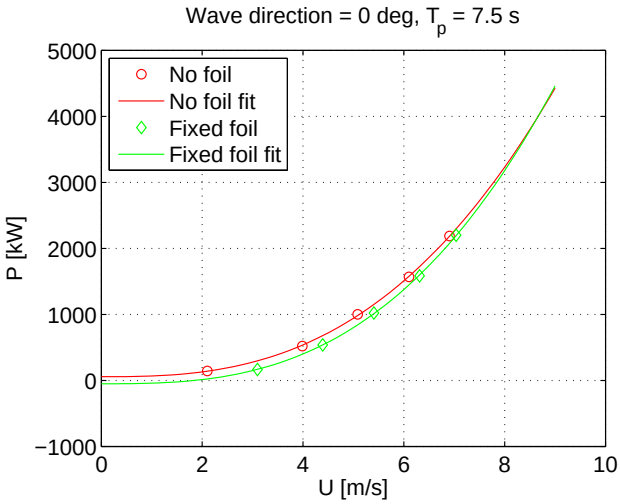

Figure D.1: Total engine power vs. ship speed, wave direction 0°, $T_p = 7.5$ s

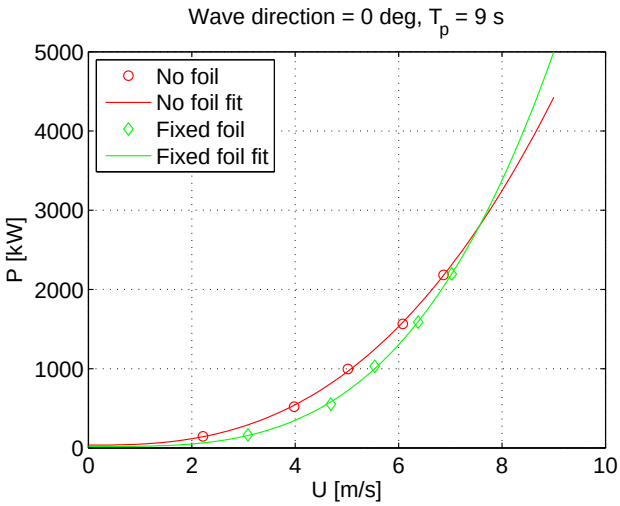

Figure D.2: Total engine power vs. ship speed, wave direction 0°, $T_p = 9$ s

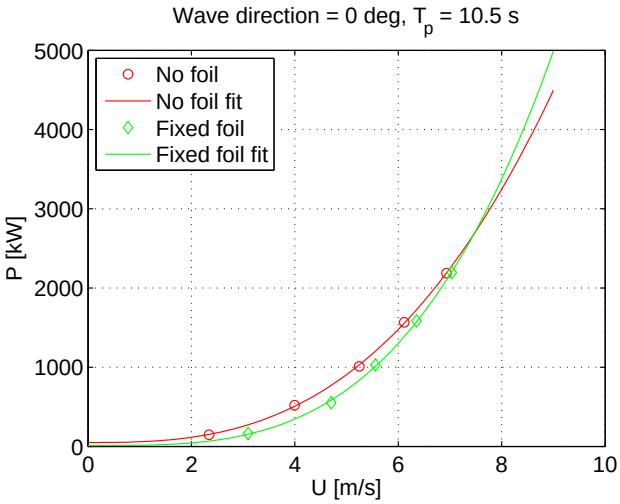

Figure D.3: Total engine power vs. ship speed, wave direction 0°, $T_p = 10.5$ s

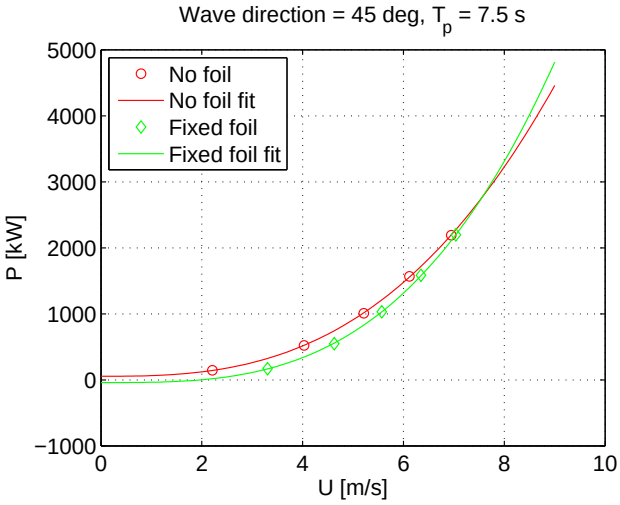

Figure D.4: Total engine power vs. ship speed, wave direction 45°, $T_p = 7.5$ s

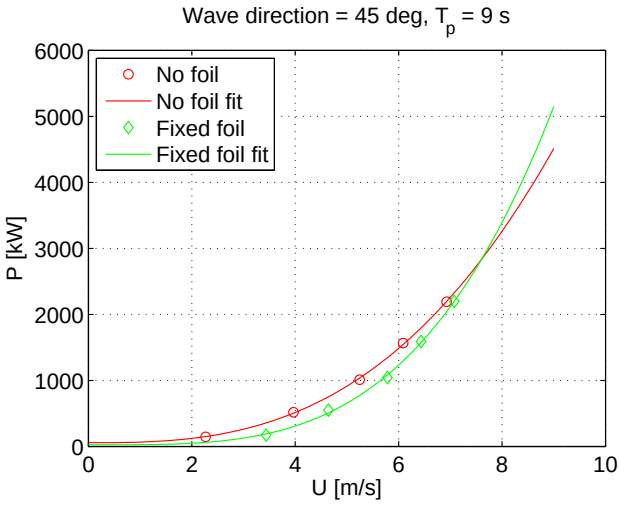

Figure D.5: Total engine power vs. ship speed, wave direction 45°, $T_p = 9$ s

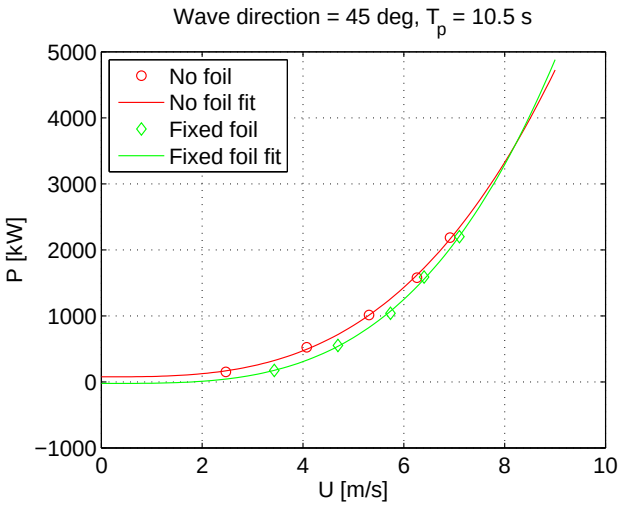

Figure D.6: Total engine power vs. ship speed, wave direction 45°, $T_p = 10.5$ s

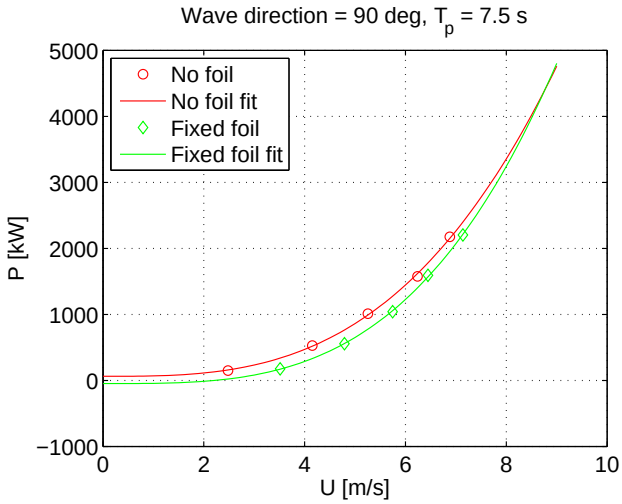

Figure D.7: Total engine power vs. ship speed, wave direction 90°, $T_p = 7.5$ s

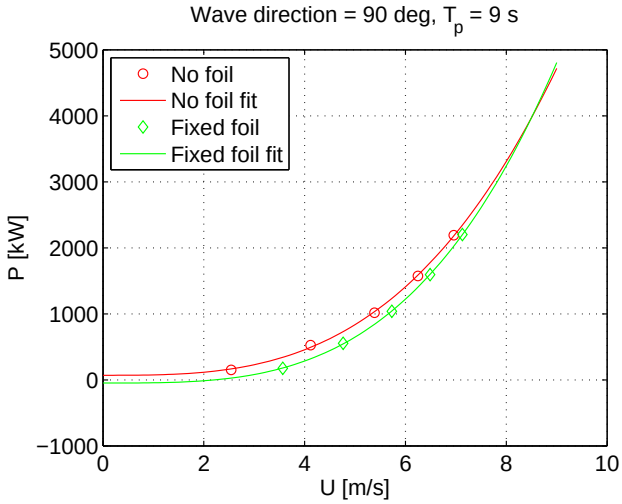

Figure D.8: Total engine power vs. ship speed, wave direction 90°, $T_p = 9$ s

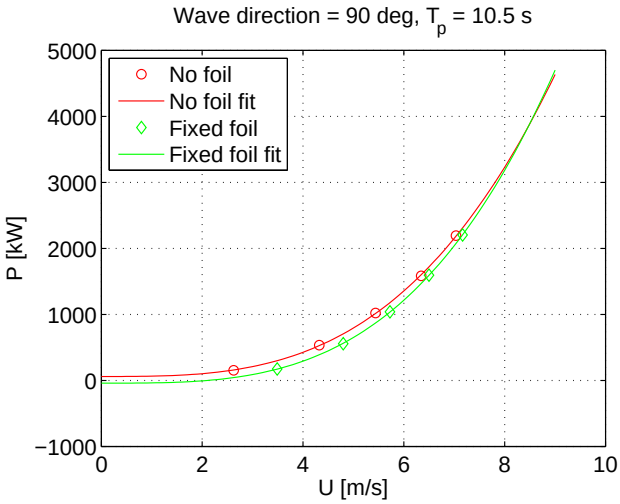

Figure D.9: Total engine power vs. ship speed, wave direction 90°, $T_p = 10.5$ s

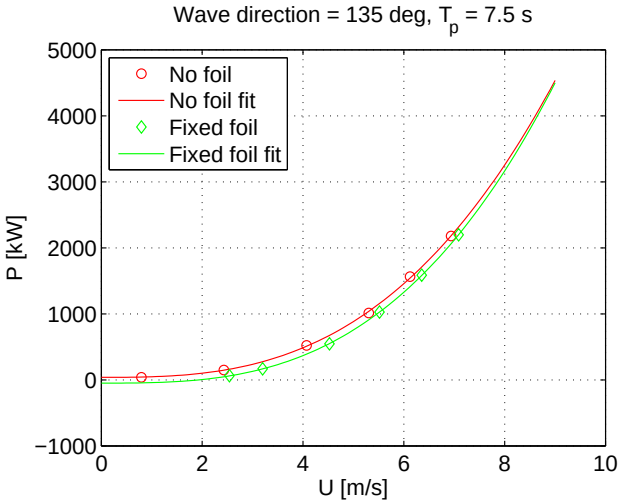

Figure D.10: Total engine power vs. ship speed, wave direction 135°, $T_p = 7.5$ s

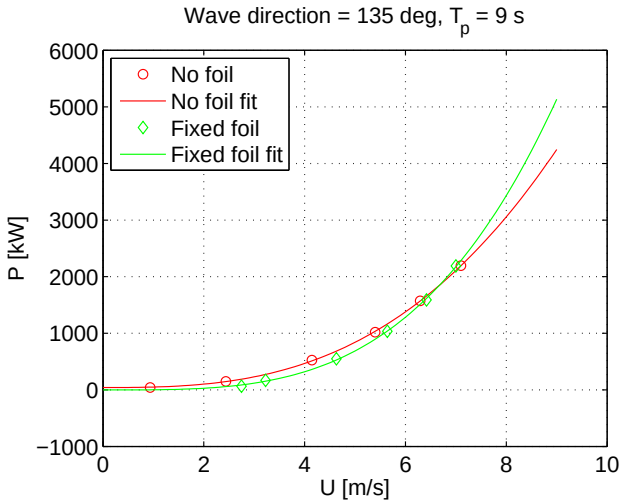

Figure D.11: Total engine power vs. ship speed, wave direction 135°, $T_p = 9$ s

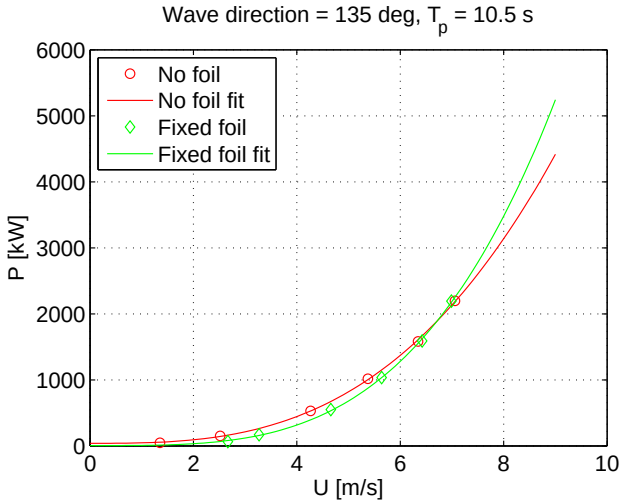

Figure D.12: Total engine power vs. ship speed, wave direction 135°, $T_p = 10.5$ s

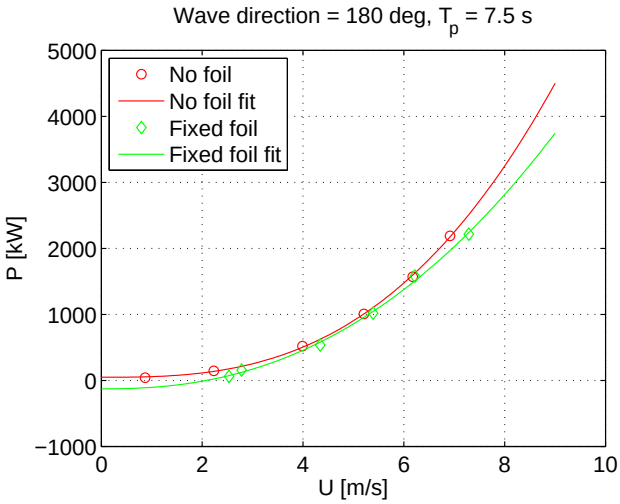

Figure D.13: Total engine power vs. ship speed, wave direction 180°, $T_p = 7.5$ s

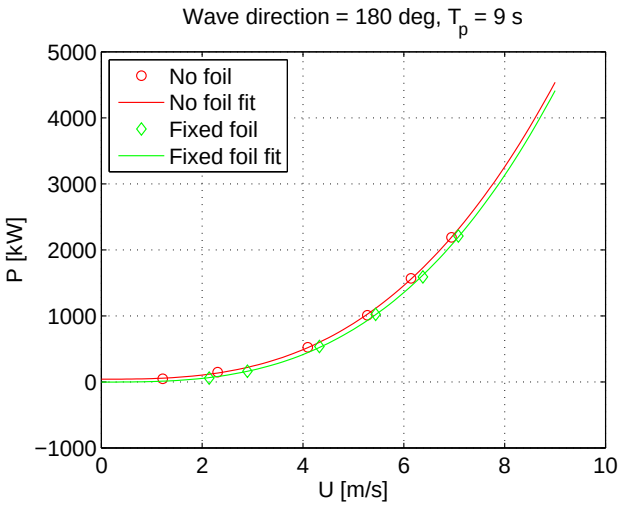

Figure D.14: Total engine power vs. ship speed, wave direction 180°, $T_p = 9$ s

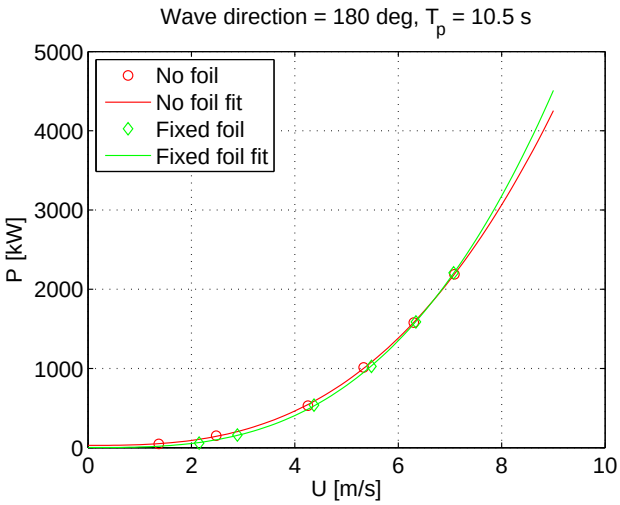

Figure D.15: Total engine power vs. ship speed, wave direction 180°, $T_p = 10.5$ s

Previous PhD theses published at the Departement of Marine Technology
(earlier: Faculty of Marine Technology)
NORWEGIAN UNIVERSITY OF SCIENCE AND TECHNOLOGY

Report No.	Author	Title
	Kavlie, Dag	Optimization of Plane Elastic Grillages, 1967
	Hansen, Hans R.	Man-Machine Communication and Data-Storage Methods in Ship Structural Design, 1971
	Gisvold, Kaare M.	A Method for non-linear mixed -integer programming and its Application to Design Problems, 1971
	Lund, Sverre	Tanker Frame Optimalization by means of SUMT-Transformation and Behaviour Models, 1971
	Vinje, Tor	On Vibration of Spherical Shells Interacting with Fluid, 1972
	Lorentz, Jan D.	Tank Arrangement for Crude Oil Carriers in Accordance with the new Anti-Pollution Regulations, 1975
	Carlsen, Carl A.	Computer-Aided Design of Tanker Structures, 1975
	Larsen, Carl M.	Static and Dynamic Analysis of Offshore Pipelines during Installation, 1976
UR-79-01	Brigt Hatlestad, MK	The finite element method used in a fatigue evaluation of fixed offshore platforms. (Dr.Ing. Thesis)
UR-79-02	Erik Pettersen, MK	Analysis and design of cellular structures. (Dr.Ing. Thesis)
UR-79-03	Sverre Valsgård, MK	Finite difference and finite element methods applied to nonlinear analysis of plated structures. (Dr.Ing. Thesis)
UR-79-04	Nils T. Nordsve, MK	Finite element collapse analysis of structural members considering imperfections and stresses due to fabrication. (Dr.Ing. Thesis)
UR-79-05	Ivar J. Fylling, MK	Analysis of towline forces in ocean towing systems. (Dr.Ing. Thesis)
UR-80-06	Nils Sandsmark, MM	Analysis of Stationary and Transient Heat Conduction by the Use of the Finite Element Method. (Dr.Ing. Thesis)
UR-80-09	Sverre Haver, MK	Analysis of uncertainties related to the stochastic modeling of ocean waves. (Dr.Ing. Thesis)
UR-81-15	Odland, Jonas	On the Strength of welded Ring stiffened cylindrical Shells primarily subjected to axial Compression
UR-82-17	Engesvik, Knut	Analysis of Uncertainties in the fatigue Capacity of

		Welded Joints
UR-82-18	Rye, Henrik	Ocean wave groups
UR-83-30	Eide, Oddvar Inge	On Cumulative Fatigue Damage in Steel Welded Joints
UR-83-33	Mo, Olav	Stochastic Time Domain Analysis of Slender Offshore Structures
UR-83-34	Amdahl, Jørgen	Energy absorption in Ship-platform impacts
UR-84-37	Mørch, Morten	Motions and mooring forces of semi submersibles as determined by full-scale measurements and theoretical analysis
UR-84-38	Soares, C. Guedes	Probabilistic models for load effects in ship structures
UR-84-39	Aarsnes, Jan V.	Current forces on ships
UR-84-40	Czujko, Jerzy	Collapse Analysis of Plates subjected to Biaxial Compression and Lateral Load
UR-85-46	Alf G. Engseth, MK	Finite element collapse analysis of tubular steel offshore structures. (Dr.Ing. Thesis)
UR-86-47	Dengody Sheshappa, MP	A Computer Design Model for Optimizing Fishing Vessel Designs Based on Techno-Economic Analysis. (Dr.Ing. Thesis)
UR-86-48	Vidar Aanesland, MH	A Theoretical and Numerical Study of Ship Wave Resistance. (Dr.Ing. Thesis)
UR-86-49	Heinz-Joachim Wessel, MK	Fracture Mechanics Analysis of Crack Growth in Plate Girders. (Dr.Ing. Thesis)
UR-86-50	Jon Taby, MK	Ultimate and Post-ultimate Strength of Dented Tubular Members. (Dr.Ing. Thesis)
UR-86-51	Walter Lian, MH	A Numerical Study of Two-Dimensional Separated Flow Past Bluff Bodies at Moderate KC-Numbers. (Dr.Ing. Thesis)
UR-86-52	Bjørn Sortland, MH	Force Measurements in Oscillating Flow on Ship Sections and Circular Cylinders in a U-Tube Water Tank. (Dr.Ing. Thesis)
UR-86-53	Kurt Strand, MM	A System Dynamic Approach to One-dimensional Fluid Flow. (Dr.Ing. Thesis)
UR-86-54	Arne Edvin Løken, MH	Three Dimensional Second Order Hydrodynamic Effects on Ocean Structures in Waves. (Dr.Ing. Thesis)
UR-86-55	Sigurd Falch, MH	A Numerical Study of Slamming of Two-Dimensional Bodies. (Dr.Ing. Thesis)
UR-87-56	Arne Braathen, MH	Application of a Vortex Tracking Method to the Prediction of Roll Damping of a Two-Dimension Floating Body. (Dr.Ing. Thesis)

UR-87-57	Bernt Leira, MK	Gaussian Vector Processes for Reliability Analysis involving Wave-Induced Load Effects. (Dr.Ing. Thesis)
UR-87-58	Magnus Småvik, MM	Thermal Load and Process Characteristics in a Two-Stroke Diesel Engine with Thermal Barriers (in Norwegian). (Dr.Ing. Thesis)
MTA-88-59	Bernt Arild Bremdal, MP	An Investigation of Marine Installation Processes – A Knowledge - Based Planning Approach. (Dr.Ing. Thesis)
MTA-88-60	Xu Jun, MK	Non-linear Dynamic Analysis of Space-framed Offshore Structures. (Dr.Ing. Thesis)
MTA-89-61	Gang Miao, MH	Hydrodynamic Forces and Dynamic Responses of Circular Cylinders in Wave Zones. (Dr.Ing. Thesis)
MTA-89-62	Martin Greenhow, MH	Linear and Non-Linear Studies of Waves and Floating Bodies. Part I and Part II. (Dr.Techn. Thesis)
MTA-89-63	Chang Li, MH	Force Coefficients of Spheres and Cubes in Oscillatory Flow with and without Current. (Dr.Ing. Thesis
MTA-89-64	Hu Ying, MP	A Study of Marketing and Design in Development of Marine Transport Systems. (Dr.Ing. Thesis)
MTA-89-65	Arild Jæger, MH	Seakeeping, Dynamic Stability and Performance of a Wedge Shaped Planing Hull. (Dr.Ing. Thesis)
MTA-89-66	Chan Siu Hung, MM	The dynamic characteristics of tilting-pad bearings
MTA-89-67	Kim Wikstrøm, MP	Analysis av projekteringen for ett offshore projekt. (Licenciat-avhandling)
MTA-89-68	Jiao Guoyang, MK	Reliability Analysis of Crack Growth under Random Loading, considering Model Updating. (Dr.Ing. Thesis)
MTA-89-69	Arnt Olufsen, MK	Uncertainty and Reliability Analysis of Fixed Offshore Structures. (Dr.Ing. Thesis)
MTA-89-70	Wu Yu-Lin, MR	System Reliability Analyses of Offshore Structures using improved Truss and Beam Models. (Dr.Ing. Thesis)
MTA-90-71	Jan Roger Hoff, MH	Three-dimensional Green function of a vessel with forward speed in waves. (Dr.Ing. Thesis)
MTA-90-72	Rong Zhao, MH	Slow-Drift Motions of a Moored Two-Dimensional Body in Irregular Waves. (Dr.Ing. Thesis)
MTA-90-73	Atle Minsaas, MP	Economical Risk Analysis. (Dr.Ing. Thesis)
MTA-90-74	Knut-Aril Farnes, MK	Long-term Statistics of Response in Non-linear Marine Structures. (Dr.Ing. Thesis)
MTA-90-75	Torbjørn Sotberg, MK	Application of Reliability Methods for Safety Assessment of Submarine Pipelines. (Dr.Ing.

		Thesis)
MTA-90-76	Zeuthen, Steffen, MP	SEAMAID. A computational model of the design process in a constraint-based logic programming environment. An example from the offshore domain. (Dr.Ing. Thesis)
MTA-91-77	Haagensen, Sven, MM	Fuel Dependant Cyclic Variability in a Spark Ignition Engine - An Optical Approach. (Dr.Ing. Thesis)
MTA-91-78	Løland, Geir, MH	Current forces on and flow through fish farms. (Dr.Ing. Thesis)
MTA-91-79	Hoen, Christopher, MK	System Identification of Structures Excited by Stochastic Load Processes. (Dr.Ing. Thesis)
MTA-91-80	Haugen, Stein, MK	Probabilistic Evaluation of Frequency of Collision between Ships and Offshore Platforms. (Dr.Ing. Thesis)
MTA-91-81	Sødahl, Nils, MK	Methods for Design and Analysis of Flexible Risers. (Dr.Ing. Thesis)
MTA-91-82	Ormberg, Harald, MK	Non-linear Response Analysis of Floating Fish Farm Systems. (Dr.Ing. Thesis)
MTA-91-83	Marley, Mark J., MK	Time Variant Reliability under Fatigue Degradation. (Dr.Ing. Thesis)
MTA-91-84	Krokstad, Jørgen R., MH	Second-order Loads in Multidirectional Seas. (Dr.Ing. Thesis)
MTA-91-85	Molteberg, Gunnar A., MM	The Application of System Identification Techniques to Performance Monitoring of Four Stroke Turbocharged Diesel Engines. (Dr.Ing. Thesis)
MTA-92-86	Mørch, Hans Jørgen Bjelke, MH	Aspects of Hydrofoil Design: with Emphasis on Hydrofoil Interaction in Calm Water. (Dr.Ing. Thesis)
MTA-92-87	Chan Siu Hung, MM	Nonlinear Analysis of Rotordynamic Instabilities in Highspeed Turbomachinery. (Dr.Ing. Thesis)
MTA-92-88	Bessason, Bjarni, MK	Assessment of Earthquake Loading and Response of Seismically Isolated Bridges. (Dr.Ing. Thesis)
MTA-92-89	Langli, Geir, MP	Improving Operational Safety through exploitation of Design Knowledge - an investigation of offshore platform safety. (Dr.Ing. Thesis)
MTA-92-90	Sævik, Svein, MK	On Stresses and Fatigue in Flexible Pipes. (Dr.Ing. Thesis)
MTA-92-91	Ask, Tor Ø., MM	Ignition and Flame Growth in Lean Gas-Air Mixtures. An Experimental Study with a Schlieren System. (Dr.Ing. Thesis)
MTA-86-92	Hessen, Gunnar, MK	Fracture Mechanics Analysis of Stiffened Tubular Members. (Dr.Ing. Thesis)

MTA-93-93	Steinebach, Christian, MM	Knowledge Based Systems for Diagnosis of Rotating Machinery. (Dr.Ing. Thesis)
MTA-93-94	Dalane, Jan Inge, MK	System Reliability in Design and Maintenance of Fixed Offshore Structures. (Dr.Ing. Thesis)
MTA-93-95	Steen, Sverre, MH	Cobblestone Effect on SES. (Dr.Ing. Thesis)
MTA-93-96	Karunakaran, Daniel, MK	Nonlinear Dynamic Response and Reliability Analysis of Drag-dominated Offshore Platforms. (Dr.Ing. Thesis)
MTA-93-97	Hagen, Arnulf, MP	The Framework of a Design Process Language. (Dr.Ing. Thesis)
MTA-93-98	Nordrik, Rune, MM	Investigation of Spark Ignition and Autoignition in Methane and Air Using Computational Fluid Dynamics and Chemical Reaction Kinetics. A Numerical Study of Ignition Processes in Internal Combustion Engines. (Dr.Ing. Thesis)
MTA-94-99	Passano, Elizabeth, MK	Efficient Analysis of Nonlinear Slender Marine Structures. (Dr.Ing. Thesis)
MTA-94-100	Kvålsvold, Jan, MH	Hydroelastic Modelling of Wetdeck Slamming on Multihull Vessels. (Dr.Ing. Thesis)
MTA-94-102	Bech, Sidsel M., MK	Experimental and Numerical Determination of Stiffness and Strength of GRP/PVC Sandwich Structures. (Dr.Ing. Thesis)
MTA-95-103	Paulsen, Hallvard, MM	A Study of Transient Jet and Spray using a Schlieren Method and Digital Image Processing. (Dr.Ing. Thesis)
MTA-95-104	Hovde, Geir Olav, MK	Fatigue and Overload Reliability of Offshore Structural Systems, Considering the Effect of Inspection and Repair. (Dr.Ing. Thesis)
MTA-95-105	Wang, Xiaozhi, MK	Reliability Analysis of Production Ships with Emphasis on Load Combination and Ultimate Strength. (Dr.Ing. Thesis)
MTA-95-106	Ulstein, Tore, MH	Nonlinear Effects of a Flexible Stern Seal Bag on Cobblestone Oscillations of an SES. (Dr.Ing. Thesis)
MTA-95-107	Solaas, Frøydis, MH	Analytical and Numerical Studies of Sloshing in Tanks. (Dr.Ing. Thesis)
MTA-95-108	Hellan, Øyvind, MK	Nonlinear Pushover and Cyclic Analyses in Ultimate Limit State Design and Reassessment of Tubular Steel Offshore Structures. (Dr.Ing. Thesis)
MTA-95-109	Hermundstad, Ole A., MK	Theoretical and Experimental Hydroelastic Analysis of High Speed Vessels. (Dr.Ing. Thesis)
MTA-96-110	Bratland, Anne K., MH	Wave-Current Interaction Effects on Large-Volume Bodies in Water of Finite Depth. (Dr.Ing. Thesis)
MTA-96-111	Herfjord, Kjell, MH	A Study of Two-dimensional Separated Flow by a Combination of the Finite Element Method and

		Navier-Stokes Equations. (Dr.Ing. Thesis)
MTA-96-112	Æsøy, Vilmar, MM	Hot Surface Assisted Compression Ignition in a Direct Injection Natural Gas Engine. (Dr.Ing. Thesis)
MTA-96-113	Eknes, Monika L., MK	Escalation Scenarios Initiated by Gas Explosions on Offshore Installations. (Dr.Ing. Thesis)
MTA-96-114	Erikstad, Stein O., MP	A Decision Support Model for Preliminary Ship Design. (Dr.Ing. Thesis)
MTA-96-115	Pedersen, Egil, MH	A Nautical Study of Towed Marine Seismic Streamer Cable Configurations. (Dr.Ing. Thesis)
MTA-97-116	Moksnes, Paul O., MM	Modelling Two-Phase Thermo-Fluid Systems Using Bond Graphs. (Dr.Ing. Thesis)
MTA-97-117	Halse, Karl H., MK	On Vortex Shedding and Prediction of Vortex-Induced Vibrations of Circular Cylinders. (Dr.Ing. Thesis)
MTA-97-118	Igland, Ragnar T., MK	Reliability Analysis of Pipelines during Laying, considering Ultimate Strength under Combined Loads. (Dr.Ing. Thesis)
MTA-97-119	Pedersen, Hans-P., MP	Levendefiskteknologi for fiskefartøy. (Dr.Ing. Thesis)
MTA-98-120	Vikestad, Kyrre, MK	Multi-Frequency Response of a Cylinder Subjected to Vortex Shedding and Support Motions. (Dr.Ing. Thesis)
MTA-98-121	Azadi, Mohammad R. E., MK	Analysis of Static and Dynamic Pile-Soil-Jacket Behaviour. (Dr.Ing. Thesis)
MTA-98-122	Ulltang, Terje, MP	A Communication Model for Product Information. (Dr.Ing. Thesis)
MTA-98-123	Torbergsen, Erik, MM	Impeller/Diffuser Interaction Forces in Centrifugal Pumps. (Dr.Ing. Thesis)
MTA-98-124	Hansen, Edmond, MH	A Discrete Element Model to Study Marginal Ice Zone Dynamics and the Behaviour of Vessels Moored in Broken Ice. (Dr.Ing. Thesis)
MTA-98-125	Videiro, Paulo M., MK	Reliability Based Design of Marine Structures. (Dr.Ing. Thesis)
MTA-99-126	Mainçon, Philippe, MK	Fatigue Reliability of Long Welds Application to Titanium Risers. (Dr.Ing. Thesis)
MTA-99-127	Haugen, Elin M., MH	Hydroelastic Analysis of Slamming on Stiffened Plates with Application to Catamaran Wetdecks. (Dr.Ing. Thesis)
MTA-99-128	Langhelle, Nina K., MK	Experimental Validation and Calibration of Nonlinear Finite Element Models for Use in Design of Aluminium Structures Exposed to Fire. (Dr.Ing. Thesis)
MTA-99-	Berstad, Are J., MK	Calculation of Fatigue Damage in Ship Structures.

129		(Dr.Ing. Thesis)
MTA-99-130	Andersen, Trond M., MM	Short Term Maintenance Planning. (Dr.Ing. Thesis)
MTA-99-131	Tveiten, Bård Wathne, MK	Fatigue Assessment of Welded Aluminium Ship Details. (Dr.Ing. Thesis)
MTA-99-132	Søreide, Fredrik, MP	Applications of underwater technology in deep water archaeology. Principles and practice. (Dr.Ing. Thesis)
MTA-99-133	Tønnessen, Rune, MH	A Finite Element Method Applied to Unsteady Viscous Flow Around 2D Blunt Bodies With Sharp Corners. (Dr.Ing. Thesis)
MTA-99-134	Elvekrok, Dag R., MP	Engineering Integration in Field Development Projects in the Norwegian Oil and Gas Industry. The Supplier Management of Norne. (Dr.Ing. Thesis)
MTA-99-135	Fagerholt, Kjetil, MP	Optimeringsbaserte Metoder for Ruteplanlegging innen skipsfart. (Dr.Ing. Thesis)
MTA-99-136	Bysveen, Marie, MM	Visualization in Two Directions on a Dynamic Combustion Rig for Studies of Fuel Quality. (Dr.Ing. Thesis)
MTA-2000-137	Storteig, Eskild, MM	Dynamic characteristics and leakage performance of liquid annular seals in centrifugal pumps. (Dr.Ing. Thesis)
MTA-2000-138	Sagli, Gro, MK	Model uncertainty and simplified estimates of long term extremes of hull girder loads in ships. (Dr.Ing. Thesis)
MTA-2000-139	Tronstad, Harald, MK	Nonlinear analysis and design of cable net structures like fishing gear based on the finite element method. (Dr.Ing. Thesis)
MTA-2000-140	Kroneberg, André, MP	Innovation in shipping by using scenarios. (Dr.Ing. Thesis)
MTA-2000-141	Haslum, Herbjørn Alf, MH	Simplified methods applied to nonlinear motion of spar platforms. (Dr.Ing. Thesis)
MTA-2001-142	Samdal, Ole Johan, MM	Modelling of Degradation Mechanisms and Stressor Interaction on Static Mechanical Equipment Residual Lifetime. (Dr.Ing. Thesis)
MTA-2001-143	Baarholm, Rolf Jarle, MH	Theoretical and experimental studies of wave impact underneath decks of offshore platforms. (Dr.Ing. Thesis)
MTA-2001-144	Wang, Lihua, MK	Probabilistic Analysis of Nonlinear Wave-induced Loads on Ships. (Dr.Ing. Thesis)
MTA-2001-145	Kristensen, Odd H. Holt, MK	Ultimate Capacity of Aluminium Plates under Multiple Loads, Considering HAZ Properties. (Dr.Ing. Thesis)
MTA-2001-146	Greco, Marilena, MH	A Two-Dimensional Study of Green-Water Loading. (Dr.Ing. Thesis)

MTA-2001-147	Heggelund, Svein E., MK	Calculation of Global Design Loads and Load Effects in Large High Speed Catamarans. (Dr.Ing. Thesis)
MTA-2001-148	Babalola, Olusegun T., MK	Fatigue Strength of Titanium Risers – Defect Sensitivity. (Dr.Ing. Thesis)
MTA-2001-149	Mohammed, Abuu K., MK	Nonlinear Shell Finite Elements for Ultimate Strength and Collapse Analysis of Ship Structures. (Dr.Ing. Thesis)
MTA-2002-150	Holmedal, Lars E., MH	Wave-current interactions in the vicinity of the sea bed. (Dr.Ing. Thesis)
MTA-2002-151	Rognebakke, Olav F., MH	Sloshing in rectangular tanks and interaction with ship motions. (Dr.Ing. Thesis)
MTA-2002-152	Lader, Pål Furset, MH	Geometry and Kinematics of Breaking Waves. (Dr.Ing. Thesis)
MTA-2002-153	Yang, Qinzheng, MH	Wash and wave resistance of ships in finite water depth. (Dr.Ing. Thesis)
MTA-2002-154	Melhus, Øyvin, MM	Utilization of VOC in Diesel Engines. Ignition and combustion of VOC released by crude oil tankers. (Dr.Ing. Thesis)
MTA-2002-155	Ronæss, Marit, MH	Wave Induced Motions of Two Ships Advancing on Parallel Course. (Dr.Ing. Thesis)
MTA-2002-156	Økland, Ole D., MK	Numerical and experimental investigation of whipping in twin hull vessels exposed to severe wet deck slamming. (Dr.Ing. Thesis)
MTA-2002-157	Ge, Chunhua, MK	Global Hydroelastic Response of Catamarans due to Wet Deck Slamming. (Dr.Ing. Thesis)
MTA-2002-158	Byklum, Eirik, MK	Nonlinear Shell Finite Elements for Ultimate Strength and Collapse Analysis of Ship Structures. (Dr.Ing. Thesis)
IMT-2003-1	Chen, Haibo, MK	Probabilistic Evaluation of FPSO-Tanker Collision in Tandem Offloading Operation. (Dr.Ing. Thesis)
IMT-2003-2	Skaugset, Kjetil Bjørn, MK	On the Suppression of Vortex Induced Vibrations of Circular Cylinders by Radial Water Jets. (Dr.Ing. Thesis)
IMT-2003-3	Chezhian, Muthu	Three-Dimensional Analysis of Slamming. (Dr.Ing. Thesis)
IMT-2003-4	Buhaug, Øyvind	Deposit Formation on Cylinder Liner Surfaces in Medium Speed Engines. (Dr.Ing. Thesis)
IMT-2003-5	Tregde, Vidar	Aspects of Ship Design: Optimization of Aft Hull with Inverse Geometry Design. (Dr.Ing. Thesis)
IMT-2003-6	Wist, Hanne Therese	Statistical Properties of Successive Ocean Wave Parameters. (Dr.Ing. Thesis)

IMT-2004-7	Ransau, Samuel	Numerical Methods for Flows with Evolving Interfaces. (Dr.Ing. Thesis)
IMT-2004-8	Soma, Torkel	Blue-Chip or Sub-Standard. A data interrogation approach of identity safety characteristics of shipping organization. (Dr.Ing. Thesis)
IMT-2004-9	Ersdal, Svein	An experimental study of hydrodynamic forces on cylinders and cables in near axial flow. (Dr.Ing. Thesis)
IMT-2005-10	Brodtkorb, Per Andreas	The Probability of Occurrence of Dangerous Wave Situations at Sea. (Dr.Ing. Thesis)
IMT-2005-11	Yttervik, Rune	Ocean current variability in relation to offshore engineering. (Dr.Ing. Thesis)
IMT-2005-12	Fredheim, Arne	Current Forces on Net-Structures. (Dr.Ing. Thesis)
IMT-2005-13	Heggernes, Kjetil	Flow around marine structures. (Dr.Ing. Thesis
IMT-2005-14	Fouques, Sebastien	Lagrangian Modelling of Ocean Surface Waves and Synthetic Aperture Radar Wave Measurements. (Dr.Ing. Thesis)
IMT-2006-15	Holm, Håvard	Numerical calculation of viscous free surface flow around marine structures. (Dr.Ing. Thesis)
IMT-2006-16	Bjørheim, Lars G.	Failure Assessment of Long Through Thickness Fatigue Cracks in Ship Hulls. (Dr.Ing. Thesis)
IMT-2006-17	Hansson, Lisbeth	Safety Management for Prevention of Occupational Accidents. (Dr.Ing. Thesis)
IMT-2006-18	Zhu, Xinying	Application of the CIP Method to Strongly Nonlinear Wave-Body Interaction Problems. (Dr.Ing. Thesis)
IMT-2006-19	Reite, Karl Johan	Modelling and Control of Trawl Systems. (Dr.Ing. Thesis)
IMT-2006-20	Smogeli, Øyvind Notland	Control of Marine Propellers. From Normal to Extreme Conditions. (Dr.Ing. Thesis)
IMT-2007-21	Storhaug, Gaute	Experimental Investigation of Wave Induced Vibrations and Their Effect on the Fatigue Loading of Ships. (Dr.Ing. Thesis)
IMT-2007-22	Sun, Hui	A Boundary Element Method Applied to Strongly Nonlinear Wave-Body Interaction Problems. (PhD Thesis, CeSOS)
IMT-2007-23	Rustad, Anne Marthine	Modelling and Control of Top Tensioned Risers. (PhD Thesis, CeSOS)
IMT-2007-24	Johansen, Vegar	Modelling flexible slender system for real-time simulations and control applications
IMT-2007-25	Wroldsen, Anders Sunde	Modelling and control of tensegrity structures. (PhD Thesis, CeSOS)
IMT-	Aronsen, Kristoffer Høye	An experimental investigation of in-line and

2007-26		combined inline and cross flow vortex induced vibrations. (Dr. avhandling, IMT)
IMT-2007-27	Gao, Zhen	Stochastic Response Analysis of Mooring Systems with Emphasis on Frequency-domain Analysis of Fatigue due to Wide-band Response Processes (PhD Thesis, CeSOS)
IMT-2007-28	Thorstensen, Tom Anders	Lifetime Profit Modelling of Ageing Systems Utilizing Information about Technical Condition. (Dr.ing. thesis, IMT)
IMT-2008-29	Berntsen, Per Ivar B.	Structural Reliability Based Position Mooring. (PhD-Thesis, IMT)
IMT-2008-30	Ye, Naiquan	Fatigue Assessment of Aluminium Welded Box-stiffener Joints in Ships (Dr.ing. thesis, IMT)
IMT-2008-31	Radan, Damir	Integrated Control of Marine Electrical Power Systems. (PhD-Thesis, IMT)
IMT-2008-32	Thomassen, Paul	Methods for Dynamic Response Analysis and Fatigue Life Estimation of Floating Fish Cages. (Dr.ing. thesis, IMT)
IMT-2008-33	Pákozdi, Csaba	A Smoothed Particle Hydrodynamics Study of Two-dimensional Nonlinear Sloshing in Rectangular Tanks. (Dr.ing.thesis, IMT/ CeSOS)
IMT-2007-34	Grytøyr, Guttorm	A Higher-Order Boundary Element Method and Applications to Marine Hydrodynamics. (Dr.ing.thesis, IMT)
IMT-2008-35	Drummen, Ingo	Experimental and Numerical Investigation of Nonlinear Wave-Induced Load Effects in Containerships considering Hydroelasticity. (PhD thesis, CeSOS)
IMT-2008-36	Skejic, Renato	Maneuvering and Seakeeping of a Singel Ship and of Two Ships in Interaction. (PhD-Thesis, CeSOS)
IMT-2008-37	Harlem, Alf	An Age-Based Replacement Model for Repairable Systems with Attention to High-Speed Marine Diesel Engines. (PhD-Thesis, IMT)
IMT-2008-38	Alsos, Hagbart S.	Ship Grounding. Analysis of Ductile Fracture, Bottom Damage and Hull Girder Response. (PhD-thesis, IMT)
IMT-2008-39	Graczyk, Mateusz	Experimental Investigation of Sloshing Loading and Load Effects in Membrane LNG Tanks Subjected to Random Excitation. (PhD-thesis, CeSOS)
IMT-2008-40	Taghipour, Reza	Efficient Prediction of Dynamic Response for Flexible amd Multi-body Marine Structures. (PhD-thesis, CeSOS)
IMT-2008-41	Ruth, Eivind	Propulsion control and thrust allocation on marine vessels. (PhD thesis, CeSOS)
IMT-2008-42	Nystad, Bent Helge	Technical Condition Indexes and Remaining Useful Life of Aggregated Systems. PhD thesis, IMT

IMT-2008-43	Soni, Prashant Kumar	Hydrodynamic Coefficients for Vortex Induced Vibrations of Flexible Beams, PhD thesis, CeSOS
IMT-2009-43	Amlashi, Hadi K.K.	Ultimate Strength and Reliability-based Design of Ship Hulls with Emphasis on Combined Global and Local Loads. PhD Thesis, IMT
IMT-2009-44	Pedersen, Tom Arne	Bond Graph Modelling of Marine Power Systems. PhD Thesis, IMT
IMT-2009-45	Kristiansen, Trygve	Two-Dimensional Numerical and Experimental Studies of Piston-Mode Resonance. PhD-Thesis, CeSOS
IMT-2009-46	Ong, Muk Chen	Applications of a Standard High Reynolds Number Model and a Stochastic Scour Prediction Model for Marine Structures. PhD-thesis, IMT
IMT-2009-47	Hong, Lin	Simplified Analysis and Design of Ships subjected to Collision and Grounding. PhD-thesis, IMT
IMT-2009-48	Koushan, Kamran	Vortex Induced Vibrations of Free Span Pipelines, PhD thesis, IMT
IMT-2009-49	Korsvik, Jarl Eirik	Heuristic Methods for Ship Routing and Scheduling. PhD-thesis, IMT
IMT-2009-50	Lee, Jihoon	Experimental Investigation and Numerical in Analyzing the Ocean Current Displacement of Longlines. Ph.d.-Thesis, IMT.
IMT-2009-51	Vestbøstad, Tone Gran	A Numerical Study of Wave-in-Deck Impact usin a Two-Dimensional Constrained Interpolation Profile Method, Ph.d.thesis, CeSOS.
IMT-2009-52	Bruun, Kristine	Bond Graph Modelling of Fuel Cells for Marine Power Plants. Ph.d.-thesis, IMT
IMT 2009-53	Holstad, Anders	Numerical Investigation of Turbulence in a Sekwed Three-Dimensional Channel Flow, Ph.d.-thesis, IMT.
IMT 2009-54	Ayala-Uraga, Efren	Reliability-Based Assessment of Deteriorating Ship-shaped Offshore Structures, Ph.d.-thesis, IMT
IMT 2009-55	Kong, Xiangjun	A Numerical Study of a Damaged Ship in Beam Sea Waves. Ph.d.-thesis, IMT/CeSOS.
IMT 2010-56	Kristiansen, David	Wave Induced Effects on Floaters of Aquaculture Plants, Ph.d.-thesis, CeSOS.
IMT 2010-57	Ludvigsen, Martin	An ROV-Toolbox for Optical and Acoustic Scientific Seabed Investigation. Ph.d.-thesis IMT.
IMT 2010-58	Hals, Jørgen	Modelling and Phase Control of Wave-Energy Converters. Ph.d.thesis, CeSOS.
IMT 2010- 59	Shu, Zhi	Uncertainty Assessment of Wave Loads and Ultimate Strength of Tankers and Bulk Carriers in a

		Reliability Framework. Ph.d. Thesis, IMT/ CeSOS
IMT 2010-60	Shao, Yanlin	Numerical Potential-Flow Studies on Weakly-Nonlinear Wave-Body Interactions with/without Small Forward Speed, Ph.d.thesis,CeSOS.
IMT 2010-61	Califano, Andrea	Dynamic Loads on Marine Propellers due to Intermittent Ventilation. Ph.d.thesis, IMT.
IMT 2010-62	El Khoury, George	Numerical Simulations of Massively Separated Turbulent Flows, Ph.d.-thesis, IMT
IMT 2010-63	Seim, Knut Sponheim	Mixing Process in Dense Overflows with Emphasis on the Faroe Bank Channel Overflow. Ph.d.thesis, IMT
IMT 2010-64	Jia, Huirong	Structural Analysis of Intect and Damaged Ships in a Collission Risk Analysis Perspective. Ph.d.thesis CeSoS.
IMT 2010-65	Jiao, Linlin	Wave-Induced Effects on a Pontoon-type Very Large Floating Structures (VLFS). Ph.D.-thesis, CeSOS.
IMT 2010-66	Abrahamsen, Bjørn Christian	Sloshing Induced Tank Roof with Entrapped Air Pocket. Ph.d.thesis, CeSOS.
IMT 2011-67	Karimirad, Madjid	Stochastic Dynamic Response Analysis of Spar-Type Wind Turbines with Catenary or Taut Mooring Systems. Ph.d.-thesis, CeSOS.
IMT - 2011-68	Erlend Meland	Condition Monitoring of Safety Critical Valves. Ph.d.-thesis, IMT.
IMT – 2011-69	Yang, Limin	Stochastic Dynamic System Analysis of Wave Energy Converter with Hydraulic Power Take-Off, with Particular Reference to Wear Damage Analysis, Ph.d. Thesis, CeSOS.
IMT – 2011-70	Visscher, Jan	Application of Particla Image Velocimetry on Turbulent Marine Flows, Ph.d.Thesis, IMT.
IMT – 2011-71	Su, Biao	Numerical Predictions of Global and Local Ice Loads on Ships. Ph.d.Thesis, CeSOS.
IMT – 2011-72	Liu, Zhenhui	Analytical and Numerical Analysis of Iceberg Collision with Ship Structures. Ph.d.Thesis, IMT.
IMT – 2011-73	Aarsæther, Karl Gunnar	Modeling and Analysis of Ship Traffic by Observation and Numerical Simulation. Ph.d.Thesis, IMT.
Imt – 2011-74	Wu, Jie	Hydrodynamic Force Identification from Stochastic Vortex Induced Vibration Experiments with Slender Beams. Ph.d.Thesis, IMT.
Imt – 2011-75	Amini, Hamid	Azimuth Propulsors in Off-design Conditions. Ph.d.Thesis, IMT.
IMT – 2011-76	Nguyen, Tan-Hoi	Toward a System of Real-Time Prediction and Monitoring of Bottom Damage Conditions During

		Ship Grounding. Ph.d.thesis, IMT.
IMT-2011-77	Tavakoli, Mohammad T.	Assessment of Oil Spill in Ship Collision and Grounding, Ph.d.thesis, IMT.
IMT-2011-78	Guo, Bingjie	Numerical and Experimental Investigation of Added Resistance in Waves. Ph.d.Thesis, IMT.
IMT-2011-79	Chen, Qiaofeng	Ultimate Strength of Aluminium Panels, considering HAZ Effects, IMT
IMT-2012-80	Kota, Ravikiran S.	Wave Loads on Decks of Offshore Structures in Random Seas, CeSOS.
IMT-2012-81	Sten, Ronny	Dynamic Simulation of Deep Water Drilling Risers with Heave Compensating System, IMT.
IMT-2012-82	Berle, Øyvind	Risk and resilience in global maritime supply chains, IMT.
IMT-2012-83	Fang, Shaoji	Fault Tolerant Position Mooring Control Based on Structural Reliability, CeSOS.
IMT-2012-84	You, Jikun	Numerical studies on wave forces and moored ship motions in intermediate and shallow water, CeSOS.
IMT-2012-85	Xiang ,Xu	Maneuvering of two interacting ships in waves, CeSOS
IMT-2012-86	Dong, Wenbin	Time-domain fatigue response and reliability analysis of offshore wind turbines with emphasis on welded tubular joints and gear components, CeSOS
IMT-2012-87	Zhu, Suji	Investigation of Wave-Induced Nonlinear Load Effects in Open Ships considering Hull Girder Vibrations in Bending and Torsion, CeSOS
IMT-2012-88	Zhou, Li	Numerical and Experimental Investigation of Station-keeping in Level Ice, CeSOS
IMT-2012-90	Ushakov, Sergey	Particulate matter emission characteristics from diesel enignes operating on conventional and alternative marine fuels, IMT
IMT-2013-1	Yin, Decao	Experimental and Numerical Analysis of Combined In-line and Cross-flow Vortex Induced Vibrations, CeSOS
IMT-2013-2	Kurniawan, Adi	Modelling and geometry optimisation of wave energy converters, CeSOS
IMT-2013-3	Al Ryati, Nabil	Technical condition indexes doe auxiliary marine diesel engines, IMT
IMT-2013-4	Firoozkoohi, Reza	Experimental, numerical and analytical investigation of the effect of screens on sloshing, CeSOS
IMT-2013-5	Ommani, Babak	Potential-Flow Predictions of a Semi-Displacement Vessel Including Applications to Calm Water Broaching, CeSOS

IMT-2013-6	Xing, Yihan	Modelling and analysis of the gearbox in a floating spar-type wind turbine, CeSOS
IMT-7-2013	Balland, Océane	Optimization models for reducing air emissions from ships, IMT
IMT-8-2013	Yang, Dan	Transitional wake flow behind an inclined flat plate----Computation and analysis, IMT
IMT-9-2013	Abdillah, Suyuthi	Prediction of Extreme Loads and Fatigue Damage for a Ship Hull due to Ice Action, IMT
IMT-10-2013	Ramìrez, Pedro Agustìn Pèrez	Ageing management and life extension of technical systems- Concepts and methods applied to oil and gas facilities, IMT
IMT-11-2013	Chuang, Zhenju	Experimental and Numerical Investigation of Speed Loss due to Seakeeping and Maneuvering. IMT
IMT-12-2013	Etemaddar, Mahmoud	Load and Response Analysis of Wind Turbines under Atmospheric Icing and Controller System Faults with Emphasis on Spar Type Floating Wind Turbines, IMT
IMT-13-2013	Lindstad, Haakon	Strategies and measures for reducing maritime CO2 emissons, IMT
IMT-14-2013	Haris, Sabril	Damage interaction analysis of ship collisions, IMT
IMT-15-2013	Shainee, Mohamed	Conceptual Design, Numerical and Experimental Investigation of a SPM Cage Concept for Offshore Mariculture, IMT
IMT-16-2013	Gansel, Lars	Flow past porous cylinders and effects of biofouling and fish behavior on the flow in and around Atlantic salmon net cages, IMT
IMT-17-2013	Gaspar, Henrique	Handling Aspects of Complexity in Conceptual Ship Design, IMT
IMT-18-2013	Thys, Maxime	Theoretical and Experimental Investigation of a Free Running Fishing Vessel at Small Frequency of Encounter, CeSOS
IMT-19-2013	Aglen, Ida	VIV in Free Spanning Pipelines, CeSOS
IMT-1-2014	Song, An	Theoretical and experimental studies of wave diffraction and radiation loads on a horizontally submerged perforated plate, CeSOS
IMT-2-2014	Rogne, Øyvind Ygre	Numerical and Experimental Investigation of a Hinged 5-body Wave Energy Converter, CeSOS
IMT-3-2014	Dai, Lijuan	Safe and efficient operation and maintenance of offshore wind farms ,IMT
IMT-4-2014	Bachynski, Erin Elizabeth	Design and Dynamic Analysis of Tension Leg Platform Wind Turbines, CeSOS
IMT-5-2014	Wang, Jingbo	Water Entry of Freefall Wedged – Wedge motions

		and Cavity Dynamics, CeSOS
IMT-6-2014	Kim, Ekaterina	Experimental and numerical studies related to the coupled behavior of ice mass and steel structures during accidental collisions, IMT
IMT-7-2014	Tan, Xiang	Numerical investigation of ship's continuous- mode icebreaking in leverl ice, CeSOS
IMT-8-2014	Muliawan, Made Jaya	Design and Analysis of Combined Floating Wave and Wind Power Facilities, with Emphasis on Extreme Load Effects of the Mooring System, CeSOS
IMT-9-2014	Jiang, Zhiyu	Long-term response analysis of wind turbines with an emphasis on fault and shutdown conditions, IMT
IMT-10-2014	Dukan, Fredrik	ROV Motion Control Systems, IMT
IMT-11-2014	Grimsmo, Nils I.	Dynamic simulations of hydraulic cylinder for heave compensation of deep water drilling risers, IMT
IMT-12-2014	Kvittem, Marit I.	Modelling and response analysis for fatigue design of a semisubmersible wind turbine, CeSOS
IMT-13-2014	Akhtar, Juned	The Effects of Human Fatigue on Risk at Sea, IMT
IMT-14-2014	Syahroni, Nur	Fatigue Assessment of Welded Joints Taking into Account Effects of Residual Stress, IMT
IMT-1-2015	Bøckmann, Eirik	Wave Propulsion of Ships, IMT